Université de Strasbourg

Ecole doctorale 269 Mathématiques, Sciences de l'Information et de l'Ingénieur

Thèse présentée par

Mehdi SAHLI

Soutenue le : 24/10/2019

Pour l'obtention du grade de : Docteur de l'Université de Strasbourg

Simulation and modelling of thermal and mechanical behaviour of Silicon photovoltaic panels under nominal and real-time conditions

Thèse dirigée par

Pr. AHZI Saïd	ICube, Université de Strasbourg
Dr. TOUCHAL Siham	ICube, Université de Strasbourg
Dr. DE MAGALHÃES CORREIA João Pedro	ICube, Université de Strasbourg

Rapporteurs

Dr. DOLLET Alain	PROMES, Université de Perpignan, UPR CNRS 8521
Pr. MERCIER Sébastien	LEM3, Université de Lorraine

Examinateur

Pr. OUGAZZADEN Abdallah	GTL, Georgia Institute of technology

To my family,

To my friends

Résumé

Le travail présenté dans cette thèse porte sur le développement d'un modèle multi-physique numérique, destiné à étudier le comportement optique, électrique et thermique d'un module photovoltaïque. Le comportement optique a été évalué en utilisant des chaines de Markov. Le comportement électrique est obtenu pour les panneaux en Silicium à l'aide d'une méthode d'optimisation numérique. Le comportement thermique est développé en 1D sur l'épaisseur du module, et le modèle multi-physique a été faiblement couplé sous MATLAB. Le comportement sous des conditions nominales d'opération a été validé en utilisant les données déclarées par les constructeurs. Ce modèle a été utilisé pour effectuer une étude paramétrique sur l'effet des irradiances solaires en régime permanent. Le modèle a été validé pour des conditions d'utilisations réelles en comparant avec des mesures expérimentales de température et de puissance électrique. Une étude thermomécanique en 2D sous ABAQUS/CAE et se basant sur le modèle multi-physique a été effectué en conditions nominales d'opération, ainsi qu'en cycle de fatigue selon la norme 61215 pour prédire les contraintes qui sont imposées sur le panneau dans les deux cas mentionnés précédemment.

Abstract

The work presented in this thesis deals with the development of a numerical multi-physics model, designed to study the optical, electrical and thermal behaviour of a photovoltaic module. The optical behaviour was evaluated using stochastic modelling based on Markov chains, whereas the electrical behaviour was drawn specifically for Silicon based photovoltaic panels using numerical optimization methods. The thermal behaviour was developed in 1D over the thickness of the module, and the multi-physics module was weakly coupled in MATLAB. The behaviour of commercial panels under nominal operation conditions was validated using data declared by the manufacturers. This model was used to perform a parametric study on the effect of solar irradiances in steady state. It was also validated for real use conditions by comparing it to experimental temperature and electrical power output. A thermomechanical study in 2D in ABAQUS/CAE based in the multi-physics model was carried out in nominal operating conditions, as well as in fatigue thermal cycling according to the IEC 61215 Standard to predict the stresses that are imposed on the panel.

Acknowledgment

First of all, I would like to thank Pr. Saïd Ahzi, my thesis director for his confidence and belief in me. He was instrumental to guiding me into this field of research, and allowed me to rediscover my passion for numerical modelling.

I also would like to thank Dr. Siham Touchal, my co-director in Strasbourg. She had the biggest role of helping me focus on what's important in the thesis, and allowed me to work in the best conditions possible.

A huge acknowledgment is reserved to Dr. João Pedro De Magalhães Correia, who had the biggest contribution scientifically. His work ethics, scientific vision and process helped forge this work into its final shape, and I can only be thankful for his patience and help.

My laboratory director, Pr. Nadia Bahlouli was the best director I could ask for. She helped my work by providing the best conditions in the laboratory, providing funding for my conference in Morroco, and helping me find new perspectives in research.

I would also like to thank the doctoral school *Mathématiques, Sciences de l'Information et de l'Ingénieur* (MSII) for the funding they provided for this thesis, and the conferences abroad. I'd especially like to thank the previous director Pr Yves Rémond for his guidance and input.

Words are not enough my thanks and gratitude to the whole ICube research team at the *Boussingault* site. I spent the last 4 years with the kindest and most warm-hearted persons I ever had the pleasure to encounter. The scientific, but most importantly personal growth I have experienced there will forever inspire and motivate me, and our friendship will far outlive our work time together. Thank you Ahmed, Ali, Apolline, Camille, Chrystelle, Delphine, Hamdi… the list goes on.

I would also like thank the Qatar Environment and Energy Research Institute (QEERI) for their cooperation, whether by inviting me to their Solar Test Facility, or allowing me to use their data in my research. I'd like to especially thank Drs. Barth, Figgis and Abdallah for their collaboration and input.

My friends of past and present, that the beautiful city of Strasbourg allowed me to meet, were an integral part of this work. Their presence in my life made this journey possible, and for that, I’m forever grateful.

Finally, I want to thank the people who contributed to this present work by being there for me and assisting me: My family, whose unconditional support is my fuel. Mom, Dad, Amer, Wafa, Ines, Mariem and Zeineb; this is for you.

Publications and scientific contributions:

[Poster] Thermal modelling of photovoltaic panels, *1ère journée « Matériaux et Nanosciences d'Alsace »*, October 17th 2014.

[Poster] Multi-physics and coupled modeling of photovoltaic panels, *Journée doctorale MSII*, October 12th 2015.

[Poster] Absorption prediction by Markov chains modelling in photovoltaic panels, *Journée de la mécanique*, May 12th 2016.

[conference] Multi-physics Modelling of PV panels : A computational Analysis of Heat Generation, 4th International Renewable and Sustainable Energy Conference, Marrakech Morrocco, November 14-17th 2016.

[Paper] Multi-Physics Modelling and Simulation of Heat and Electrical Yield Generation in Photovoltaics, Solar Energy Materials and Solar Cells, Available online July 29th 2017 (IF: 5.018).

[conference] Thermomechanical investigation of PV panels behaviour under NOCT conditions, International Renewable and Sustainable Energy Conference, Tangier, Morroco, 4-7th December 2017.

Résumé de thèse

Simulation et modélisation du comportement thermique et mécanique des panneaux photovoltaïques en Silicium sous conditions nominales et réelles.

Mehdi Sahli

Introduction :

Depuis plusieurs décennies, le développement des énergies renouvelables est devenu crucial afin de réduire les effets négatifs causés par les autres sources d'énergies (fossiles ou nucléaires) mais également pour garantir une indépendance énergétique.

L'évolution de la demande mondiale de l'énergie, les réserves estimées des énergies fossiles et nucléaires, ainsi que le potentiel annuel des énergies renouvelables sont présentés sur la figure 1.

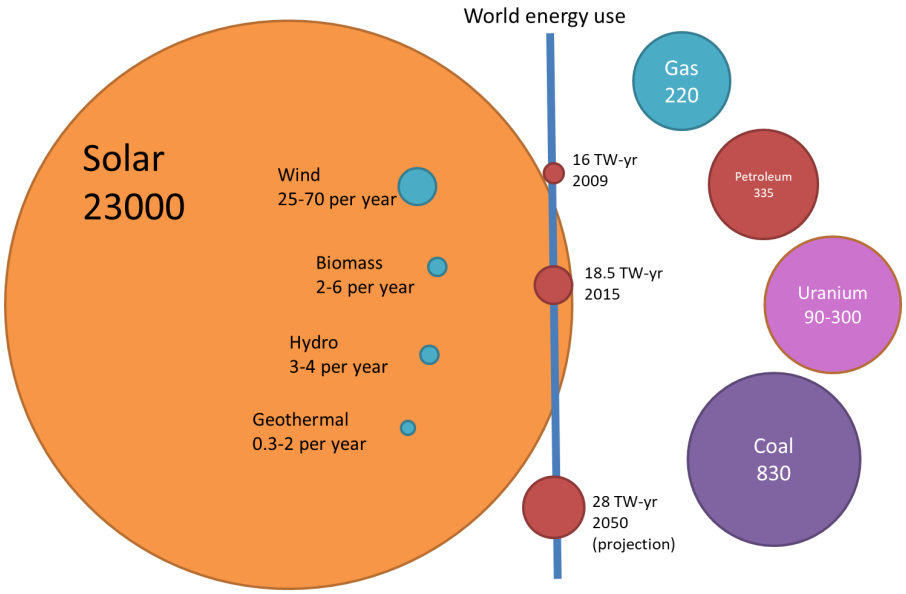

Figure 1 Comparaison des ressources d'énergies ainsi que la demande mondiale énergétique (TW/année) [1]

La source la plus abondante parmi ces énergies renouvelables est le soleil. Une des technologies utilisées pour récolter l'énergie solaire est basée sur l'utilisation des panneaux photovoltaïques. L'effet photoélectrique permet de transformer le rayonnement solaire en un courant électrique continu. La technologie la plus répandue pour la fabrication des panneaux solaires est celle utilisant les cellules photovoltaïques (PV) à base de Silicium, vu l'abondance de cet élément dans la croûte

terrestre, et la facilité de fabrication des cellules. Mais ces avantages s'accompagnent d'un inconvénient majeur : les modules photovoltaïques basés sur le silicium ont un rendement qui diminue lorsque la température augmente, de l'ordre de 0.5% pour chaque degré supplémentaire. De nombreux travaux de la littérature se sont ainsi concentrés sur la modélisation multi-physiques des panneaux [2]–[5]. Dans ces travaux, les modélisations multi-physiques comportaient au moins un modèle thermique et un modèle électrique, et parfois un modèle optique.

Pour pouvoir étudier et prévoir la température ainsi que le rendement en temps réel d'un panneau, l'étude de son comportement thermique est nécessaire. Le panneau est généralement constitué de plusieurs couches ; leur empilement varie selon les différentes technologies employées. Une représentation d'un panneau usuel avec des cellules en Silicium est représenté sur la figure 2.

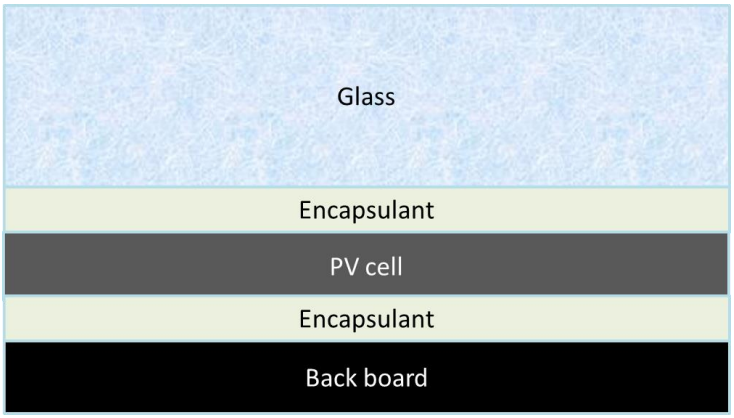

Figure 2 Coupe d'un panneau typique avec des cellules photovoltaïques en Silicium

Les couches constituant le panneau ont des propriétés thermiques bien différentes. De plus, les échanges thermiques entre les différentes couches doivent être pris en compte pour pouvoir prévoir la température à travers son épaisseur. Les échanges thermiques avec l'environnement extérieur doivent être également considérés comme décrit sur la figure 3.

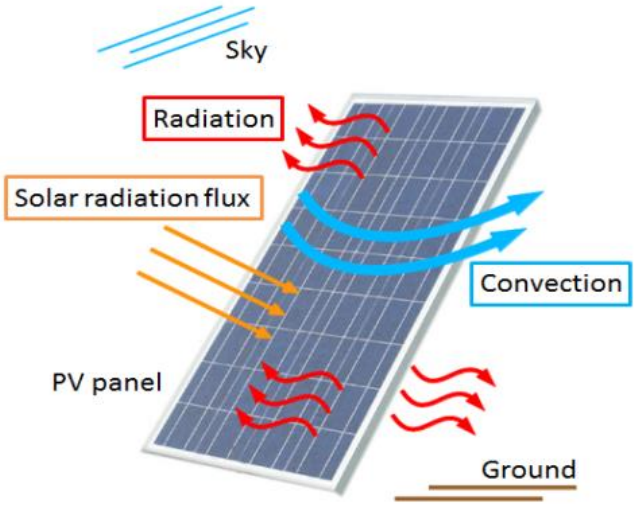

Figure 3 Représentation des échanges thermiques avec l'entourage du panneau.

La production de chaleur et d'électricité par conversion photovoltaïque sont dues au rayonnement solaire. Un modèle optique tenant compte des différentes couches est nécessaire pour déterminer la partie des radiations solaires qui seront absorbées par le panneau, ce qui influence directement les termes sources de chaleur générées dans le panneau à prendre en compte dans le modèle thermique.

Pour compléter la modélisation multi-physiques, il est nécessaire d'estimer la quantité d'électricité produite à partir du rayonnement solaire et de la température du panneau. Le comportement électrique d'un panneau peut être décrit assez fidèlement par des circuits électriques équivalents ; comme le modèle à une diode [6], [7].

Par ailleurs, les effets environnementaux (variations journalières et annuelles de la température et d'humidité) ont aussi un impact sur le vieillissement des matériaux composants le panneau qui induisent une dégradation de son rendement. Ce phénomène est d'autant plus vrai lorsque les panneaux sont en fonction sous des latitudes proches des tropiques ou de l'équateur. Dans ces zones, les températures ambiantes élevées accélèrent la détérioration des panneaux comme indiqué dans le tableau 1.

Tableau 1: Durée de vie moyenne en fonction de la température ambiante [8]**.**

Température ambiante (°C)	Durée de vie moyenne (années)
25	9.6
30	7.5
35	6.1
40	5.1
45	4.3

Une des explications pour comprendre les pertes de performance présentées dans le tableau 1 pourrait être, entre autres, l'apparition et le développement de microfissures ou des effets de délamination. Ces phénomènes sont liés à la dégradation des propriétés mécaniques et d'adhésion des différents matériaux. Cette dégradation est aussi bien due à l'humidité importante qu'à l'alternance des chargements thermomécaniques. L'apparition de contraintes internes est due aux variations de températures combinés à la différence entre les coefficients d'expansion thermique des différentes couches constituant les panneaux photovoltaïques.

Une étude thermique des modules photovoltaïques nous paraît donc nécessaire pour, tout d'abord, pouvoir estimer leur rendement sur le court terme (une journée à quelques journées), puis pour compléter la compréhension de la perte de rendement aperçu à la fin de cycle de vie. Cette étude thermique est complétée par une étude mécanique prenant en compte les contraintes internes au panneau induites par les changements de température. Cette approche nous apportera peut-être des indications plausibles sur les causes de ce vieillissement.

Objectifs :

Le premier objectif de cette thèse est de développer un modèle couplé (optique-électrique-thermique) prédictif qui permet de décrire la réponse thermique des panneaux photovoltaïques en silicium en tenant compte des effets de longueurs d'ondes de la lumière. Ce modèle est validé par rapport aux données mises à disposition par les constructeurs, puis par rapport à des résultats recueillis en temps réel sur un site de test situé au Qatar.

Le second objectif est de développer un modèle numérique du comportement thermomécanique à l'aide du logiciel commercial de calcul ABAQUS. Ce second modèle a pour objet d'estimer les contraintes subies par les panneaux sous différentes conditions de fonctionnement :

- Conditions nominales d'utilisations :
    - Irradiance=800 W/m²,
    - Température ambiante=20°C,
    - Vitesse du vent=1m/s,
    - Conditions du circuit ouvert.
- Dans les conditions cycliques de test de fatigue thermique selon la norme IEC 61215.

Ce modèle permettra également l'étude du comportement thermomécanique (vieillissement, endommagement, fatigue…) des différents composants du panneau sur des longues durées.

Modèle optique, électrique et thermique couplé :

Pour l'élaboration et la validation de ce modèle multi-physique, plusieurs panneaux PV commerciaux ont été étudiés : BP350 et BP585 qui sont des panneaux en Silicium monocristallin, et également un panneau de Voltec Solar VSMS275 qui est un panneau en Silicium polycristallin. Les résultats présentés pour la validation du modèle seront basés sur ces panneaux et leurs fiches constructeurs.

Modèle thermique :

Pour prévoir la distribution de température à l'intérieur du panneau photovoltaïque, celui-ci a été modélisé comme un milieu à une dimension (suivant l'épaisseur du panneau). Le modèle thermique s'appuie sur l'équation classique de la chaleur écrite ci-dessous :

$$\rho C_p \frac{\partial T(x,t)}{\partial t} = k \frac{\partial^2 T(x,t)}{\partial x^2} + Q \qquad (1)$$

où ρ est la densité, C_p la chaleur spécifique, k la conductivité, t le temps, x la distance de la surface, $T(x,t)$ la température et Q la source de chaleur.

Cette équation peut être résolue en différence fini en implicite dans le cas 1D. Les propriétés thermiques des différents matériaux qui composent le panneau sont issus de la littérature et ont été utilisées pour ce calcul. Cependant, la source de chaleur Q reste une quantité à déterminer pour pouvoir résoudre l'équation de la chaleur (1) et déterminer la température sur tous les nœuds de l'épaisseur du panneau. Dans la littérature, l'estimation de la source de chaleur au niveau de la cellule photovoltaïque est effectuée à partir de l'équation suivante :

$$Q = P_{électrique} \times (1 - \eta) \quad (2)$$

Où $P_{électrique}$ est la puissance électrique générée par le panneau et η le rendement du panneau photovoltaïque. Le rendement est défini comme le rapport de la puissance solaire reçue sur la puissance électrique générée. L'utilisation de l'équation (2) implique que le rendement et la puissance électrique du panneau PV doivent être connus pour pouvoir déterminer la source de la chaleur dans la cellule. Ces données sont fournies par le constructeur. Par conséquent, cette équation ne peut être utilisée que pour des panneaux PV connus. Dans ce travail de thèse, nous nous proposons d'estimer la source de chaleur produite par les cellules PV comme la différence entre la puissance solaire reçue et la puissance électrique produite. Pour définir la puissance électrique produite, il nous faut tout d'abord définir la quantité (ou pourcentage) de photons absorbés à l'aide d'un modèle optique.

Modèle optique :

La propagation des photons dans la première couche est représentée dans la figure 4. Elle permet de voir que les photons peuvent être réfléchis, transmis dans le panneau vers l'autre couche ou absorbés dans ladite couche.

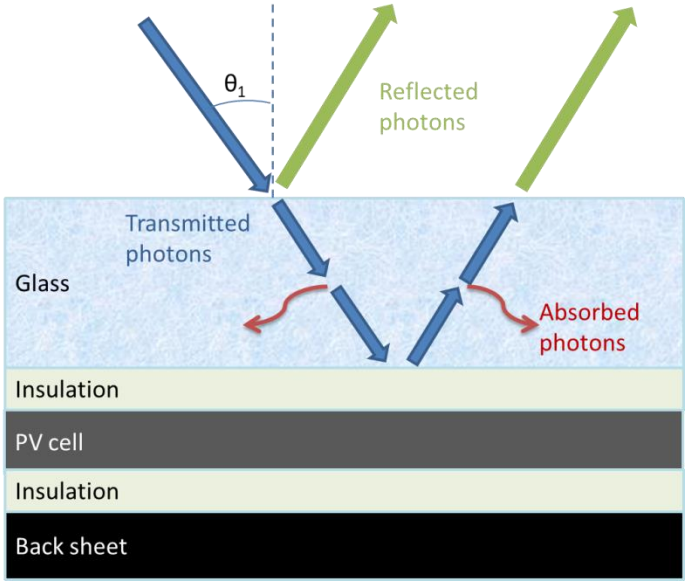

Figure 4 Diagramme de la propagation des photons dans l'épaisseur de la première couche de verre dans le panneau

Le modèle optique développé dans ce travail de thèse s'appuie sur les chaînes de Markov. Ce modèle permet de déterminer les probabilités d'absorption des photons en fonction de leurs longueurs

d'ondes. Il prend en compte les différentes interactions des photons dès leur entrée dans le panneau PV en utilisant seulement les différentes propriétés optiques intrinsèques des matériaux composant celui-ci, à savoir l'indice de réfraction, le taux d'absorption et la réflectance des matériaux.

Les quantités (ou pourcentages) de photons absorbés, transmis ou réfléchis à chaque interface du panneau PV sont estimées et représentées dans la figure 5 ? en fonction des données environnementales (localisation géographique, météorologie, conditions d'installation…).

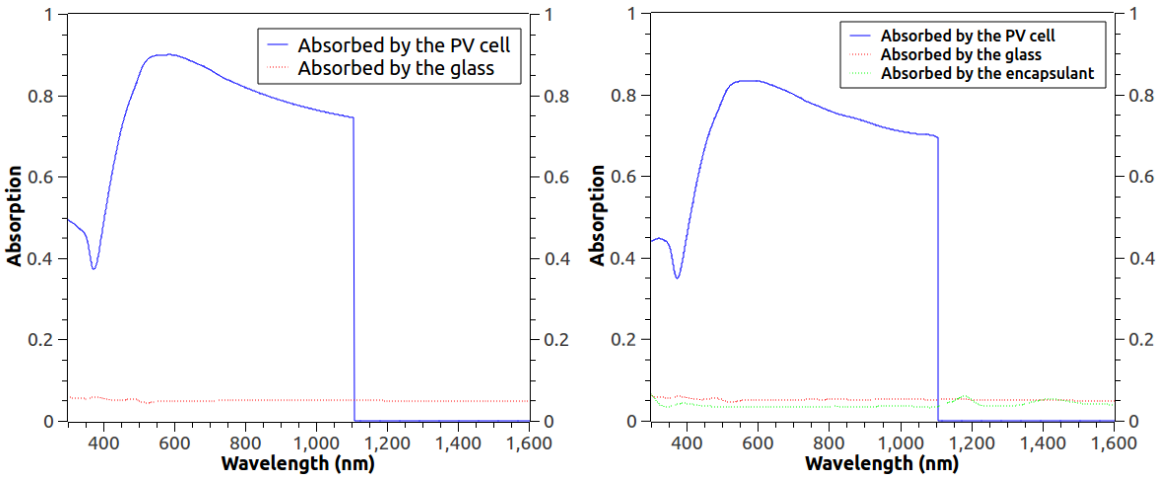

(a) (b)

Figure 5 Pourcentage des photons absorbés par les couches du panneau photovoltaïque en fonction de la longueur d'onde pour les panneaux : BP 350 et BP 585(a) et VSMS275 (b).

Nous supposerons dans ce travail que les photons absorbés dans les couches autres que les cellules PV sont totalement transformés en chaleur, alors que les photons absorbés par les cellules PV seront convertis soit en énergie électrique soit en chaleur (les proportions étant fonction des longueurs d'ondes). Pour calculer la puissance électrique produite, un modèle électrique basé sur les propriétés électriques du silicium a été développé.

Modèle électrique :

Le modèle électrique utilisé s'appuie sur le circuit électrique équivalent à une diode classiquement utilisé pour décrire le comportement électrique des cellules et panneaux PV comme décrit dans la figure 6.

La relation régissant le circuit électrique équivalent s'écrit :

$$I = I_{ph} - I_0 \left(\exp\left(\frac{q_e(V + IR_s)}{k_B X T} \right) - 1 \right) - \frac{V + IR_s}{R_{sh}} \quad (3)$$

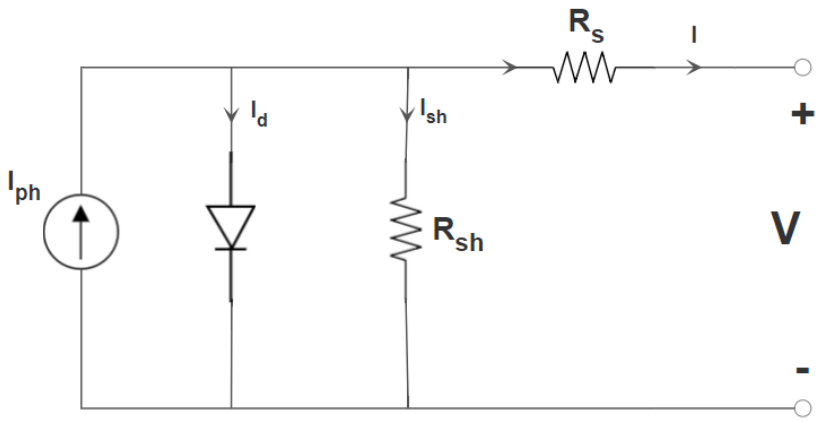

Figure 6 Modèle 1-diode équivalent.

où I_{ph} est appelé l'intensité photo-générée, I_0 l'intensité de saturation de la diode, R_{sh} la résistance de court-circuit, R_s la résistance correspondant aux résistivités des contacts entre les différents régions constitutives de la cellule, k_B la constante de Boltzmann, X un facteur d'idéalité, T la température de la cellule PV et q est la charge élémentaire d'un électron.

L'intensité photo-générée a été déterminée à partir de l'absorption au niveau de la cellule trouvée dans la partie optique, en utilisant l'équation :

$$I_{ph} = eA \int \Phi(\lambda) \times \alpha(\lambda) \times IQE(\lambda) d\lambda \quad (1)$$

où IQE est le rendement quantique interne.

Pour valider le modèle électrique, les courbes Intensité-Voltage $I - V$ (courant en fonction de la tension) ont été tracées dans la figure 7 pour les cas étudiés, et comparées avec celles fournies par le constructeur. Il est à noter que la réponse électrique prévue par le modèle ne dépend que des propriétés électriques intrinsèques des matériaux constitutifs des cellules PV.

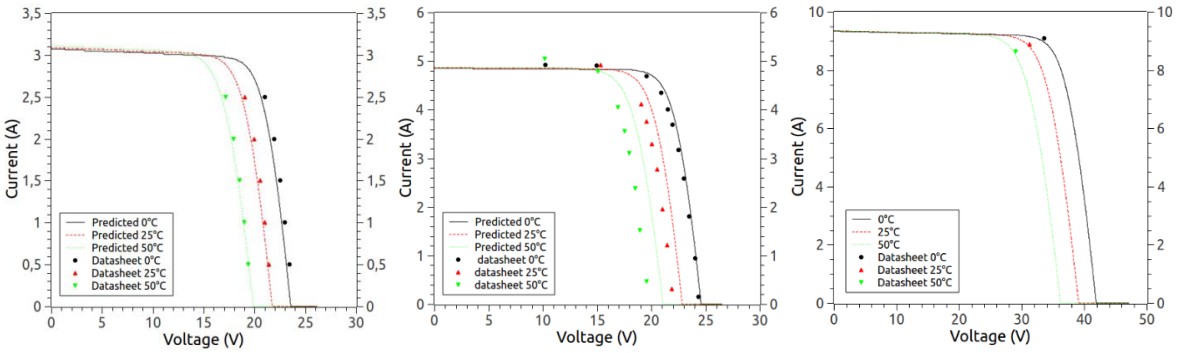

(a) (b) (c)

Figure 7 Courbes $I-V$ pour différents températures d'opération pour les panneaux: BP350 (a), BP585 (b) et VSMS275 (c) avec les données partagées par les constructeurs.

Implémentation numérique et résultats

Implémentation sous MATLAB et validation :

Les différents modèles ont été programmés sous l'environnement de calcul du logiciel commercial MATLAB selon la figure 8. Dans ce travail, nous avons opté pour un couplage faible entre les différents modèles physiques.

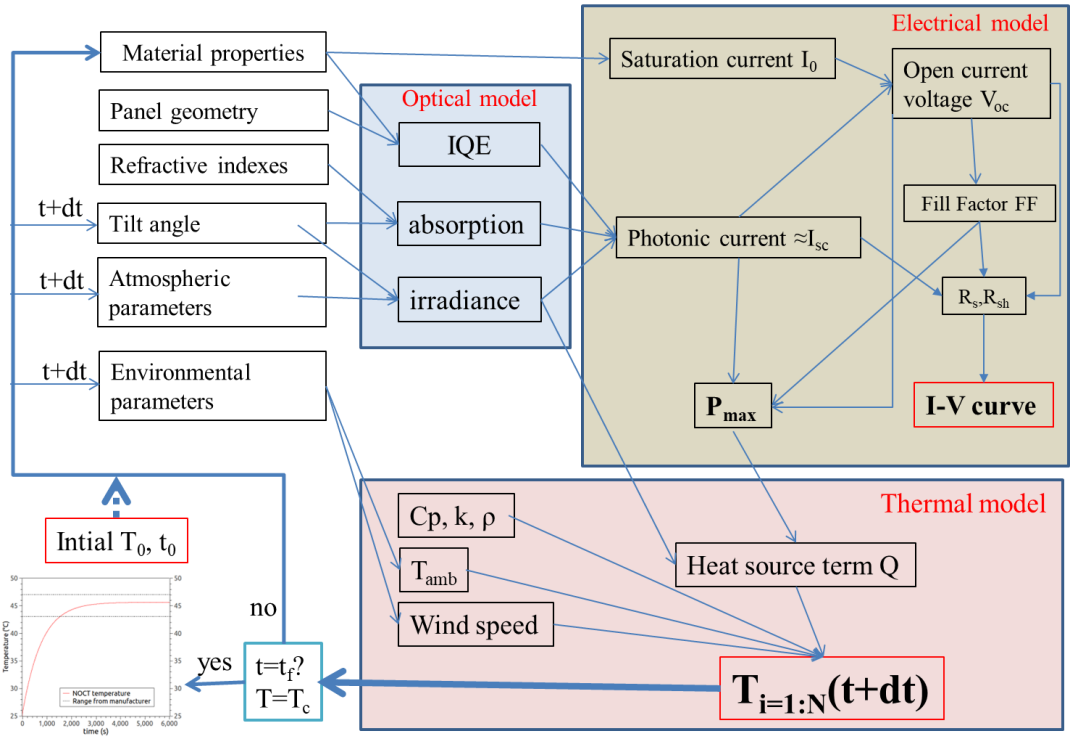

Figure 8 Structure de l'algorithme implémenté sous MATLAB®.

Ces panneaux PV ont été modélisés et étudiés dans des conditions nominales d'utilisation (ou NOCT) : une radiation de 800 W/m², un vent uniforme de 1 m/s et une température ambiante de 20°C et en conditions de circuit ouvert. Les comportements électrique et thermique ont été comparés avec les résultats fournis dans les données du constructeur, et les prévisions numériques des modèles sont en bon accord avec ces données comme montré sur la figure 9.

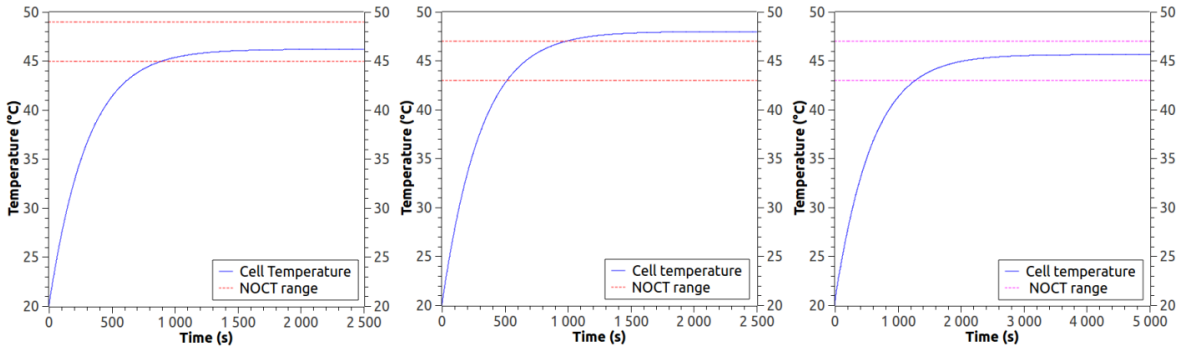

(a) (b) (c)

Figure 9 Evolution de la température de la cellule PV aux conditions NOCT pour les panneaux : BP350 (a), BP585 (b) et VSMS27 (c).

Etude paramétrique de l'effet des radiations solaires :

Le modèle validé a été utilisé pour évaluer la température du panneau à différents coefficients de masse d'air (AM), qui est défini à partir de l'angle que fait le soleil avec le zénith. AM1 correspond à un soleil qui fait 90° avec le zénith, et AM10 correspond à un soleil à 5° de l'horizon.

Les résultats obtenus sont résumés dans le tableau 2.

Tableau 2: Réponse électrique et thermique du panneau pour différentes masses d'air, AM

	AM1	AM1.5	AM4	AM10
Température [°C]	51.6	50.4	46.2	41.2
Puissance électrique [W]	119	114	96	73
Rendement [%]	8.79	8.85	9.04	9.22

Le cas où l'on concentre les radiations à l'aide d'un système de miroirs a aussi été considéré. Les rayons concentrés sont considérés équivalents à des radiations solaires provenant de 2 soleils, 3 soleils et 4 soleils dans les cas étudiés, et les résultats de la simulation sont reportés dans le tableau 3.

Tableau 3: Réponse électrique et thermique des panneaux pour différentes concentration de soleil.

	1 Soleil	2 Soleils	3 Soleils	4 Soleils
Température [°C]	56.6	85.5	113.3	140.1
Puissance électrique [W]	139	242	258	226
Rendement [%]	8.55	6.93	5.28	3.71

On peut voir dans ce cas qu'en passant de 3 à 4 soleils, même si on est en train de donner plus d'énergie solaire, on obtient une puissance électrique plus basse. En plus, la température du panneau atteint 113°C à 3 soleils, ce qui est supérieure de la température de fusion de l'encapsulant (composé en éthylène-acétate de vinyle) qui se situe entre 90° et 120°C selon la composition.

Il est donc conseillé de ne pas dépasser la configuration 2 soleils pour préserver le panneau et les matériaux le composant.

Résultats en temps réel :

Grâce à une collaboration avec « Qatar Environnent and Energy Research Institute (QEERI) » et leur site de production d'énergie PV (Solar Test Facility –STF) localisé à Doha au Qatar, nous avons pu obtenir des mesures en temps réel de la température ainsi que la production d'énergie électrique d'un panneau PV. Le panneau PV considéré sur ce site est le panneau PANASONIC225, qui est un panneau de type biface. Le modèle multi-physique précédemment présenté a été adapté à ce type de panneau PV et ensuite validé sous les conditions nominales d'utilisation (NOCT), présenté dans la figure 10.

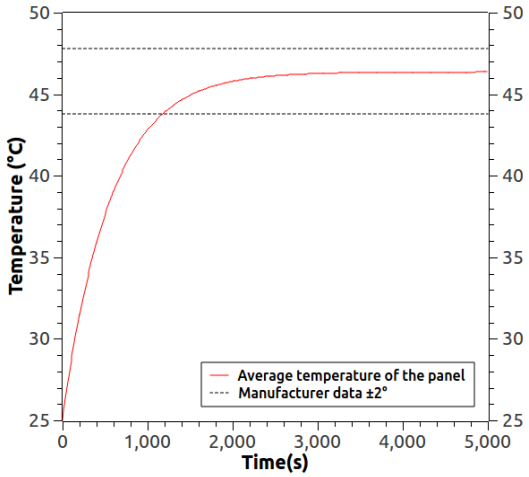

Figure 10 Evolution de la température de la cellule PV aux conditions NOCT pour le panneau Panasonic225.

Connaissant les conditions environnementales (rayonnement solaire, vitesse du vent, inclinaison, …), l'énergie électrique et la température d'un panneau PV biface ont été prévues numériquement pour un fonctionnement durant toute la journée, pour deux types de journées : ensoleillée et nuageuse. Nos prévisions ont été également comparées aux résultats expérimentaux fournis par le site du Qatar. Un bon accord entre prévisions numériques et résultats expérimentaux a été obtenu comme montré dans la figure 11.

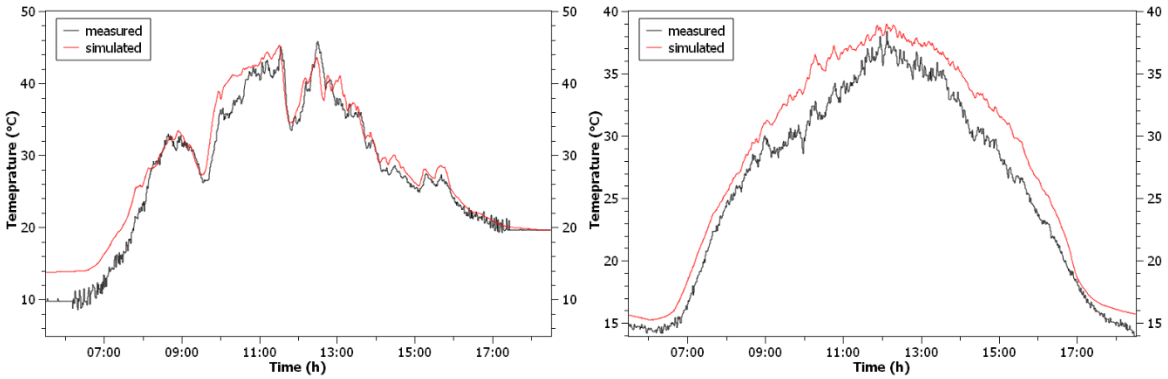

a) b)

Figure 11 Evolution de la température sur toute une journée dans le cas d'un jour: nuageux (a) et clair (b) pour le panneau Panasonic225 à la STF, Doha, Qatar).

Modélisation thermo-mécanique :

Pour compléter le modèle couplé développé dans la partie précédente, nous nous proposons d'étudier le comportement thermomécanique des panneaux photovoltaïques sous différentes conditions de service :

- Conditions nominales d’opération.
- Chargement cyclique décrit dans la figure 12.
-

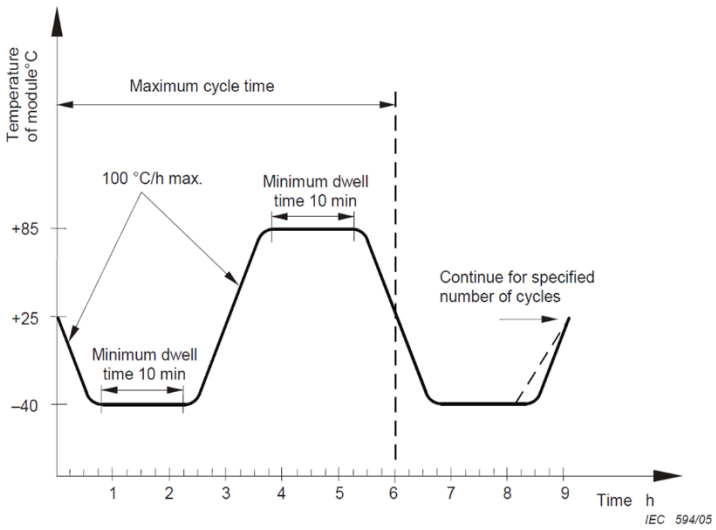

Figure 12 Cycles thermiques dans la norme IEC 61215 standard pour l’accélération accélérée.

Un panneau photovoltaïque monofacial (VSMS275), ainsi qu’un panneau bifacial (Panasonic225) ont été considérés pour ces études.

Les changements de température ainsi que le gradient de température le long de l’épaisseur sont susceptibles de créer des contraintes thermiques dans les différentes couches du panneau PV et au niveau des interfaces.

Pour évaluer ces contraintes, un modèle éléments finis à deux dimensions d’un panneau PV a été développé avec le logiciel commercial de calcul ABAQUS. Les géométries des deux panneaux considérés ainsi que leurs maillages sont représentés dans la figure 13.

Dans ces modèles, le cadre en aluminium a été aussi pris en considération, vu son possible effet sur les échanges thermiques et/ou mécaniques.

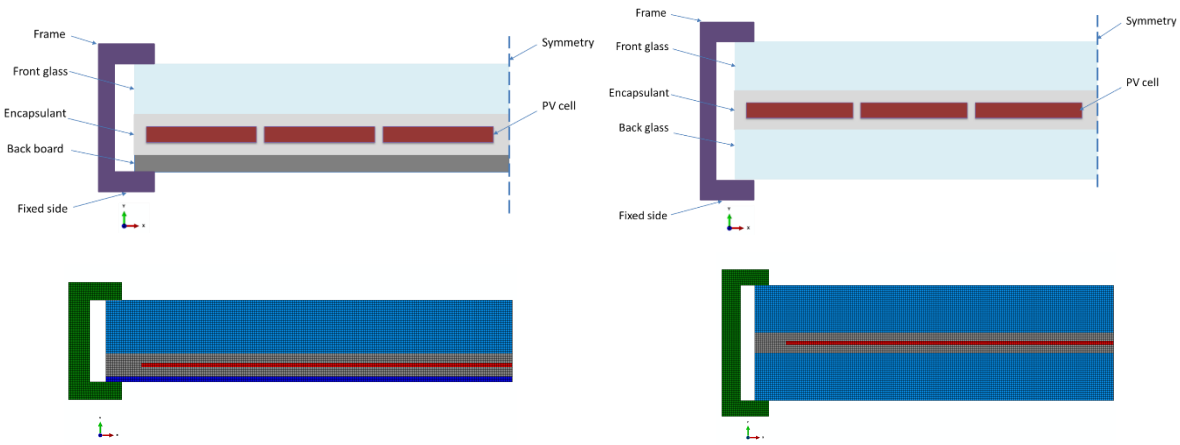

(a) (b)

Figure. 13 Représentation des modèles des deux panneaux : VSMS275 (a) et Panasonic225 (b) ainsi que leurs maillages (échelle non respectée).

Les sources de chaleur prévues par le modèle multi-physique ont été introduites dans les différentes couches du modèle 2D du panneau PV. Le comportement thermique prévu par ABAQUS a été comparé à celui obtenu avec le modèle 1D sous MATLAB dans la figure 14.

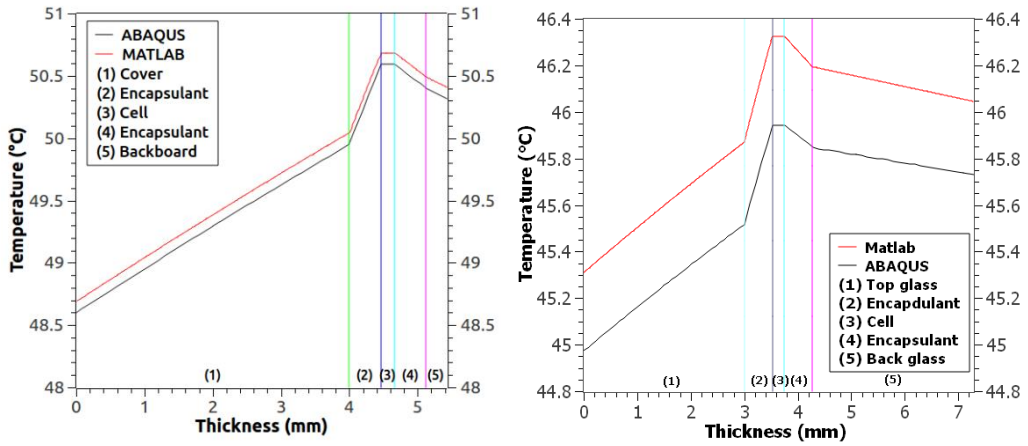

(a) (b)

Figure 14 Comparaison des profils de température obtenues avec Matlab et en 1D et ABAQUS en 2D, en considérant l'épaisseur des panneaux: VSMS275 (a) et Panasonic225 (b).

Simulation en éléments finies en conditions nominales :

Le champ de température obtenu avec ABAQUS a été utilisé pour mener une simulation thermomécanique. La simulation par éléments finis du problème nous permet d'avoir accès aux contraintes thermomécaniques pendant le fonctionnement du panneau en conditions nominales.

Les déformations et les contraintes normales dans la zone entre deux cellules adjacentes sont représentées dans les figures 15 et 16 respectivement.

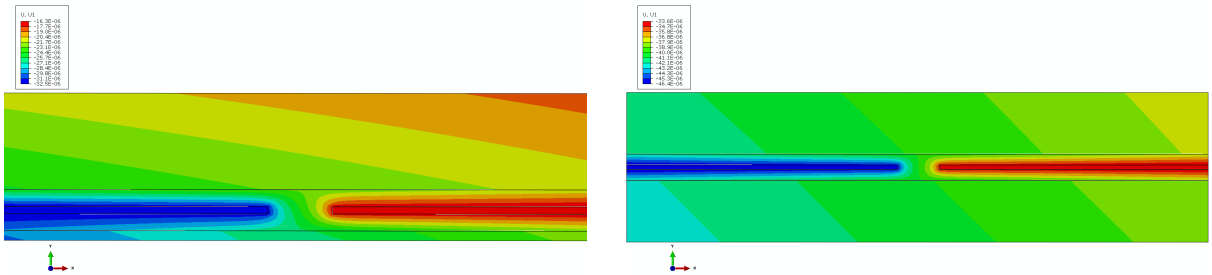

(a) (b)

Figure 15 Déplacement horizontal. Prédictions sous les conditions nominales d'opération pour les panneaux : VSMS275 (a) et Panasonic225 (b).

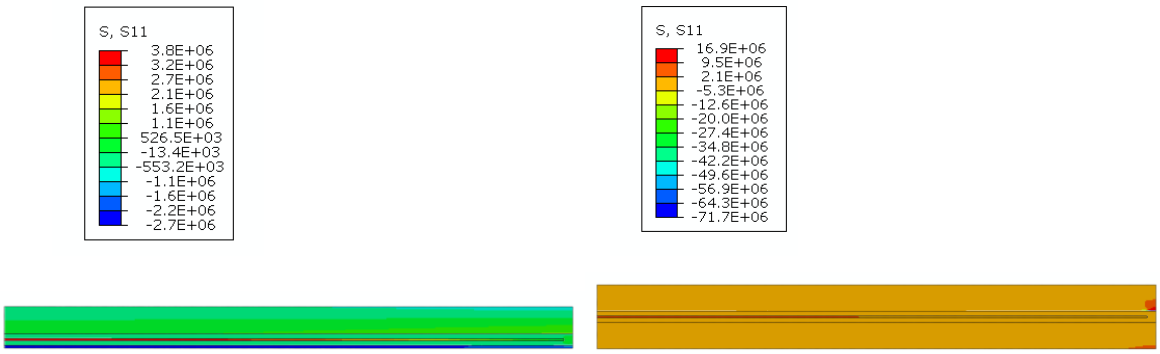

(a) (b)

Figure 16 Distribution de la contrainte normale dans la zone intercellulaire pour les panneaux: VSMS275 (a) et Panasonic225 (b).

Les déformations mesurées entre les cellules atteignent 11.24 et 15.02 µm pour les panneaux Panasonic225 et VSMS275 respectivement, ce qui est en accord avec les résultats expérimentaux reportés.

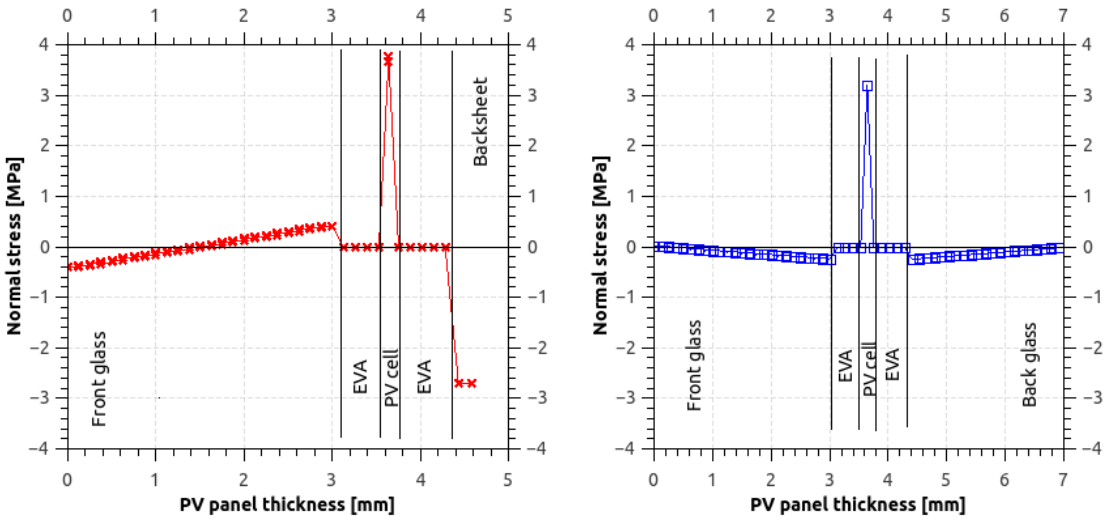

(a) (b)

Figure 17 Distribution de la contrainte normale à travers l'épaisseur en conditions nominales d'opération pour les panneaux : VSMS275 (a) et Panasonic225 (b).

Les contraintes dans la zone entre deux cellules adjacentes sont dues à la différence entre les coefficients d'expansion thermiques entre les différentes couches. Elles sont un peu plus élevées dans le cas du panneau bifacial comparé au panneau monofacial, mais restent faibles. Pour référence, la limite élastique pour le matériau de l'encapsulant est compris entre 100 et 200 MPa.

La distribution de ces contraintes sur l'épaisseur du panneau est représentée dans la figure 17. Elle est plus élevée dans la zone de la cellule pour les deux panneaux, et dans la zone du support « backsheet » dans le cas du panneau monofacial.

Simulations en élément finies du chargement cyclique :

Les étapes décrites dans la figure 12 ont été simulées en éléments finies, et les résultats de la contrainte normale ont été reportés dans les figures 18 et 19 pour les fins des étapes de refroidissement et du chauffage respectivement.

Les contraintes atteintes pendant l'étape de refroidissement sont de 54 MPa et 46 MPa pour les panneaux VSMS 275 et Panasonic225 respectivement. Ces valeurs sont beaucoup plus élevées que les valeurs reportées en conditions nominales d'opération, et peuvent être la cause de développement et propagation de microfissures dans les cellules photovoltaïques.

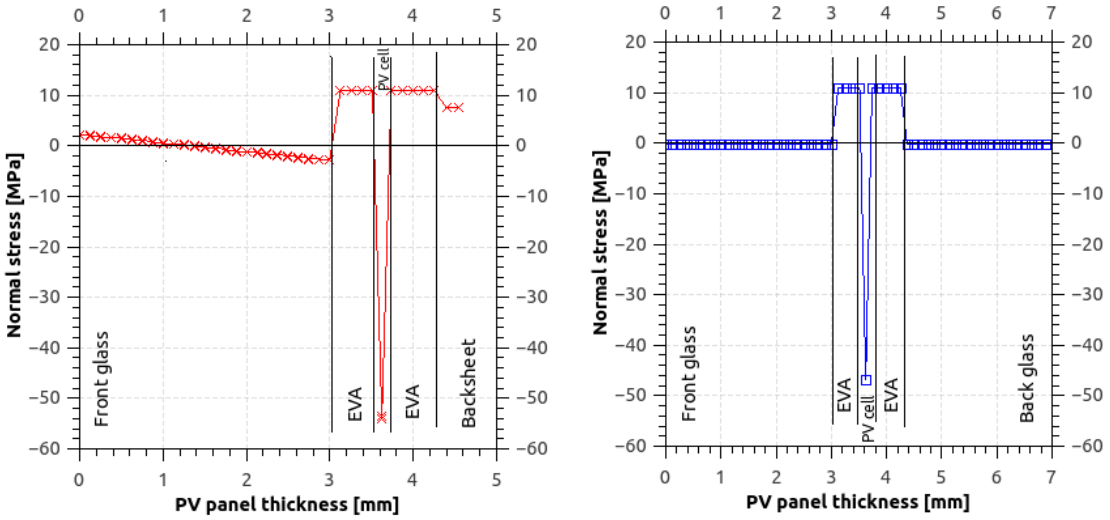

(a) (b)

Figure 18 Distribution de la contrainte normale à travers l'épaisseur après l'étape du refroidissement pour les panneaux : VSMS275 (a) et Panasonic225 (b).

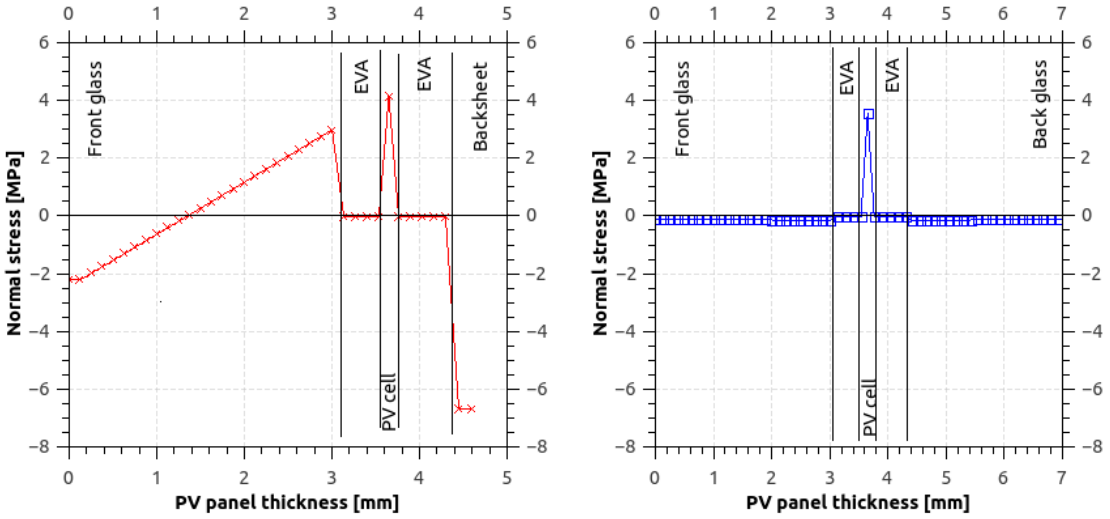

(a) (b)

Figure 19 Distribution de la contrainte normale à travers l'épaisseur après l'étape du chauffage pour les panneaux : VSMS275 (a) et Panasonic225 (b).

Conclusions et perspectives

Un modèle multi-physique qui permet la prédiction du comportement thermique d'un panneau photovoltaïque a été développé, ne se basant que sur les propriétés géométriques et intrinsèques des matériaux qui le composent.

Ce modèle a été développé en utilisant une approche en différences finies pour résoudre l'équation de la chaleur. Les chaines de Markov ont été utilisées pour prédire le comportement optique, et le comportement optique a été déterminé en utilisant une approche probabiliste du comportement des photons selon les chaines de Markov.

Le modèle a été validé sous des conditions nominales d'utilisation en utilisant les températures d'utilisation données par les constructeurs pour trois panneaux différents.

Le modèle a été utilisé pour une étude paramétrique en imposant différents niveaux de radiations solaires sur le panneau. Il a été montré qu'à une concentration solaire équivalente à 4 soleils, on obtient une puissance électrique plus petite que celle obtenue à 3 soleils. De plus, la température atteinte à la concentration de 3 soleils peut être dangereuse pour l'encapsulant car elle s'approche de sa température de fusion.

Ensuite, le modèle a été validé en conditions réelles en comparant les résultats obtenus avec celles mesurées sur un site de tests de panneaux photovoltaïques, pour deux journées différentes : ensoleillée et nuageuse.

Pour étudier le comportement thermomécanique, le modèle a été intégré dans une approche en éléments finies pour déterminer la réponse mécanique dans différents cas : en conditions nominales d'utilisation, et pendant le cycle de vieillissement accélérée.

Le modèle a été validé par rapport aux conditions nominales d'utilisation. Les valeurs des déformations reportées par le modèle sont en accord avec les valeurs expérimentales reportées. Les contraintes sont plus faibles que les limites d'élasticité des composants du panneau. Cependant, elles peuvent être responsable du phénomène du délamination entre les couches.

Le modèle a ensuite été soumis à un cycle de vieillissement accéléré. Les déformations obtenues pour les basses températures ne sont pas en accord avec les résultats expérimentaux, mais ceci peut être justifiés par l'absence des valeurs du module de Young de l'encapsulant pour des températures trop basses (inférieur à -20°C).

Pour aller un peu plus loin, une simulation thermomécanique de la réponse du panneau sous des conditions réelles peut être étudiée pour évaluer les réponses causées par les changements météorologiques, comme le passage des nuages ou le changement de la direction du vent.

Références bibliographiques :

[1] “Solar Power - Here Comes The Sun,” *Below 2C*, 19-Mar-2018. .

[2] S. Armstrong and W. G. Hurley, “A thermal model for photovoltaic panels under varying atmospheric conditions,” *Appl. Therm. Eng.*, vol. 30, no. 11–12, pp. 1488–1495, Aug. 2010.

[3] A. D. Jones and C. P. Underwood, “A thermal model for photovoltaic systems,” *Sol. Energy*, vol. 70, no. 4, pp. 349–359, 2001.

[4] G. Notton, C. Cristofari, M. Mattei, and P. Poggi, “Modelling of a double-glass photovoltaic module using finite differences,” *Appl. Therm. Eng.*, vol. 25, no. 17–18, pp. 2854–2877, Dec. 2005.

[5] R. Vaillon, L. Robin, C. Muresan, and C. Ménézo, “Modeling of coupled spectral radiation, thermal and carrier transport in a silicon photovoltaic cell,” *Int. J. Heat Mass Transf.*, vol. 49, no. 23–24, pp. 4454–4468, Nov. 2006.

[6] H.-L. Tsai, “Complete PV model considering its thermal dynamics,” *J. Chin. Inst. Eng.*, vol. 36, no. 8, pp. 1073–1082, Dec. 2013.

[7] J. C. S. Barroso, J. P. M. Correia, N. Barth, S. Ahzi, and M. A. Khaleel, “A PSO algorithm for the calculation of the series and shunt resistances of the PV panel one-diode model,” in *2014 International Renewable and Sustainable Energy Conference (IRSEC)*, 2014, pp. 1–6.

[8] O. O. Ogbomo, E. H. Amalu, N. N. Ekere, and P. O. Olagbegi, “Effect of operating temperature on degradation of solder joints in crystalline silicon photovoltaic modules for improved reliability in hot climates,” *Sol. Energy*, vol. 170, pp. 682–693, Aug. 2018.

Plan

1. Introduction

1.1. Context

The world energy consumption has noticeably increased in the last fifty years, due to modernization and industrial demand. It was estimated at 18.5 TW in 2015, and is projected to attain 28 TW by 2050.

More than 80% of this energy has always been provided by fossil fuels (i.e. Petroleum, natural gas and coal). Those sources of energy are responsible for the increase of carbon dioxide emissions. Those sources are rapidly depleting and the reserves may not be able to cover the energy demand for the human population in the next decades.

In Europe, the energy makes up 20% of total imports [1], at a cost of more than 1 billion € per day, as the European Union (EU) imports 53% of all the energy it consumes. Specifically, the EU imports:

- 90% of its crude oil
- 66% of its natural gas
- 42% of its coal and other solid fuels
- 40% of its uranium and other nuclear fuels.

Securing supplies of energy and looking for reliable sources of energy at competitive prices is very important for the EU, in order to limit the energy dependency.

Those reasons have motivated the research community to study the possibility of other sources of energy, that must be renewable so that it won't be shorted out, and friendly to the environment.

Those alternative energy sources are finding more and more interest in the scientific community, and the studies of technologies to generate such green energies has been encouraged by many organizations, such as the EU with the goal of attaining 20% renewable energy by 2020. More globally, the United Nations (UN) Climate Change Conferences (COP21 in Paris-France, COP22 in Marrakech-Morocco and COP23 in Bonn-Germany) brought forward the Paris agreement, which aims to reduce the carbon dioxide emissions by 55%, in order to keep the global warming to well below 2°C. These directives will be impossible to achieve without the development and expanding of renewable energy research.

1.2. Renewable energy sources

Renewable energies were not discovered in the last century, they were developed and used even thousands of years ago. The solar power was harvested for heat, the wind and hydraulic energy was used for mills operation. Lately, the efforts have been focused on increasing the yield of these energies, and optimize the mechanisms of transformation of those energies into easily storable and useable energy.

A summary of the renewable energy potential per year, as compared to the remaining reserves of fossil fuel and nuclear energy is presented in Fig. 1. It can be seen that if the consumption keeps on relying on the fossil fuels and nuclear sources, an energy crisis would be reached within a few decades.

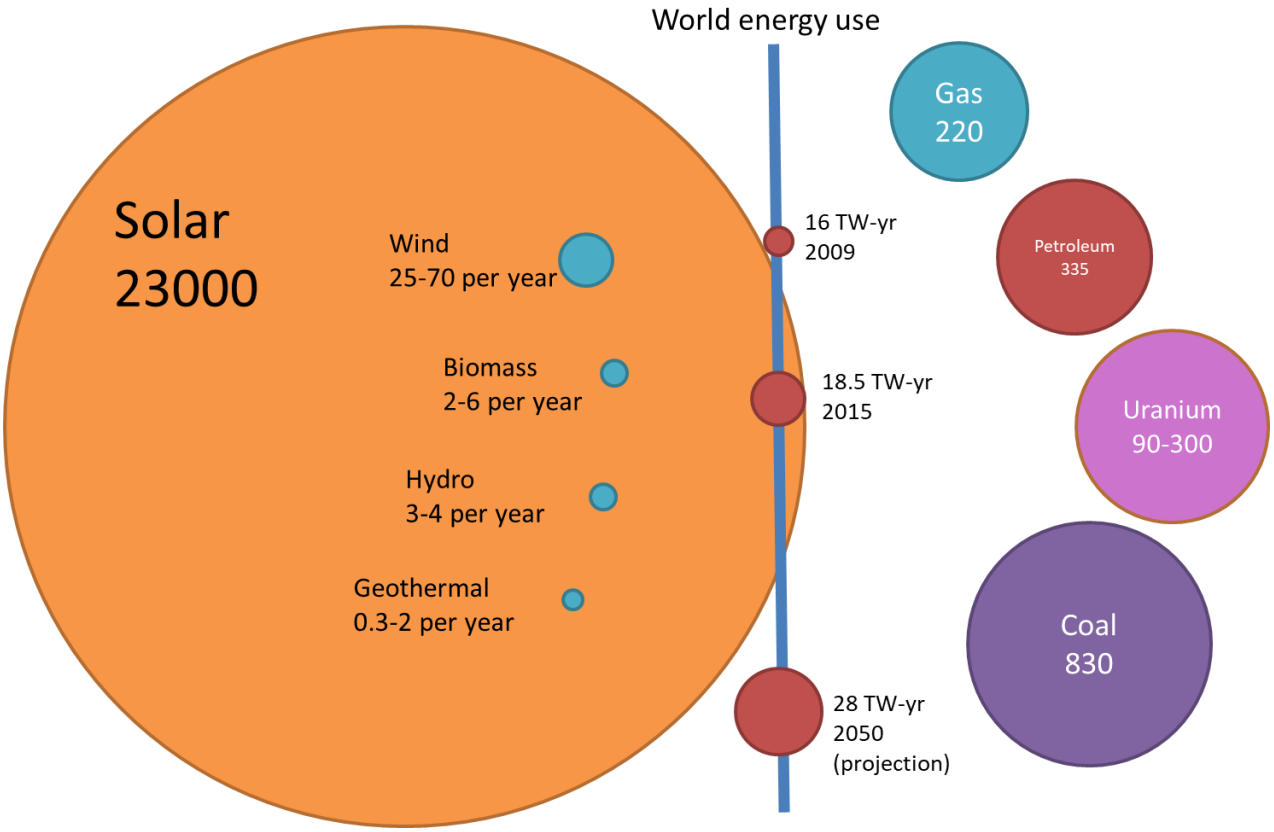

Fig. 20 Comparison of the fossil and nuclear energy sources reserves vs. the potential renewable energy per year (TW/year).

On the other hand, if we consider the renewable energy sources, some of them do not seem to be able to cover the insisting and urgent demand of the energy. Geothermal, hydroelectricity and biomass

and even wind energy can be very interesting in some cases, but for the mass production of energy, solar abundance has a scale of its own. It is estimated that the available solar energy for human is at about 23000 TW-year, which easily covers the human population needs.

1.3. Solar energy

When it comes to harnessing the solar energy, two specific technologies prevail: The Concentrated Solar Power (CSP) and the Photovoltaics (PV) technologies.

1.3.1. Concentrated Solar Power (CSP)

The CSP systems concentrate radiations from the sun onto a small area using mirror or lenses to heat a liquid substance which is then used to drive a heat engine connected to an electric power generator. It can use tracking systems to focus a large area of sunlight, and the systems can attain high concentrations up to 500 suns.

Many technologies exist for the CSP system, mainly based on their optical collection. A summary of the main four technology is presented din the work of Xu [2]. The most known is the parabolic trough, which consists of parabolic reflectors that concentrate light onto a receiver positioned along the focal points of the reflectors.

Most of the installments of this technology exist in Spain and the united states as of 2019, with the biggest plants being the Ivanpah Solar Power facility and the Mojave Solar Project, sitting at 377 and 354 MW production capacity respectively [3], but the interest have been developing in North Africa and the middle east, due to the favorable high temperatures in those regions.

The biggest project in development in the world is in Morocco, called the Noor Solar Project [4]. It is planned to produce 580 MW at peak after the project is finished with its three parts.

The advantages of the CSP technology is that the excess of the thermal energy can be stored and used at times of low to no sunlight, which leads to the continuous production of energy. The technology however demands extremely high direct normal irradiance, and is suitable for specific climates and regions as concluded in the work of [2].

1.3.2. Photovoltaic Systems (PV)

The PV systems differ from CSP in the technology used. Specifically, the sun's irradiance is converted directly into electricity using the photovoltaic effect, which was observed by Alexander Edmond Becquerel in 1839. It was first observed in electrochemical solutions, but recently it is more related to solid state devices, using semi-conductor materials. This effect is fundamental in the operation of the solar cells, and will be explained in the following sections, as the focus of this manuscript is the PV technology.

As the PV systems do not need a high concentration of solar irradiance, it can be mounted individually on the ground or the even the roof for residential use.

The total installed capacity of PV panels attained 500 GW at its peak production in 2018, with China and Europe as the leaders in the growth of those installation [5].

1.4. Solar cells

A solar cell is an electronic device that converts the energy of light directly into electricity. The vast majority of produced solar cells since the emergence of this technology are based on silicon as the major semi-conductor component, due to its abundance (about 28% of earth crust's mass).

A simple explanation of the phenomena is presented in Fig. 2. A photon that has an energy superior to difference between the conduction band and the valence band energies (called the energy gap E_g) upon coming into contact with a silicon atom excites one of the electrons from the valence band, and the transferred energy allows them to reach the conduction band, in which they become mobile. In order to move these mobile electrons and thus creating electricity, an electrical field is created by doping a layer of the semiconductor block negatively (n-type), and doping positively another layer (p-type) and putting them together. The collection of the mobile electrons by a circuit connecting the two layers allows their flow, which creates electricity.

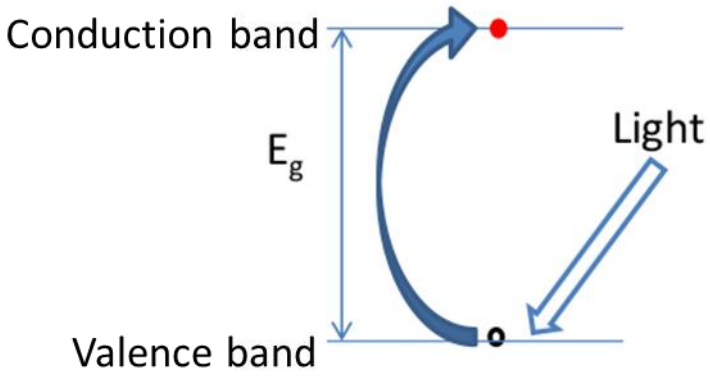

Fig. 21 Photovoltaic effect.

It is noted that this simple mechanism allows the understanding of how the photoelectric effect is used only for simple semi-conductors like silicon, but other mechanisms can be found in novel technologies that won't be discussed in this manuscript.

Silicon itself has different crystalline configurations, depending on the purification process. It is however produced with one of the highest purity possible for metals (99.9999%). It is then doped, usually using phosphorus (n-type) and Boron (p-type).

1.5. Layers of photovoltaic panels

In the case of silicon panels' technology, the panels are composed of many layers of different thicknesses. The cell, which converts the energy of light directly into electricity by the photovoltaic effect, is encapsulated in an ethylene-vinyl acetate (EVA) case. Assemblies of those cells oriented in one plane are covered with glass on the sun facing side, and a backboard on the other side. Thin layer of the encapsulated cells along with the covers is what constitutes a PV module. The module mounted on a frame made of aluminum is a PV panel.

A slice of a typical module is presented in Fig. 3. It is important to note that the thicknesses are not to scale, as the glass layer tends to be very thick (around 3-4 mm) compared to the other layers (in the hundreds of nanometers).

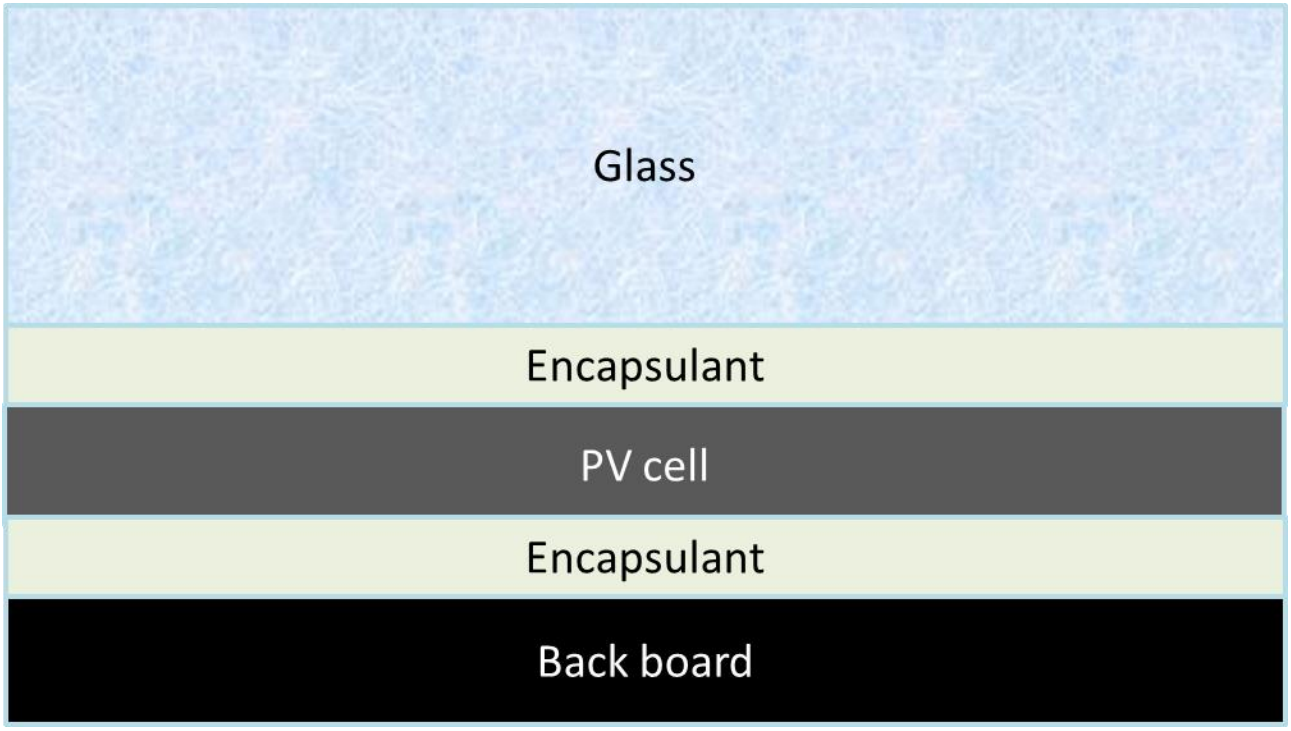

Fig. 22 Slice of a typical PV module.

1.6. Energy yield of photovoltaic panels

The National Renewable Energy Laboratory (NREL) publishes periodically the maximum yields or efficiencies reached by different photovoltaic technologies in laboratory trials [6], as presented in Fig. 4. The efficiency of a photovoltaic panel η_{PV} is defined as:

$$\eta_{PV} = \frac{electrical\ power\ converted}{solar\ power\ recieved} \tag{2}$$

It is noted that there are some technologies that have a higher efficiency than silicon, but they are only laboratory tested, with very specific settings that are not reproducible in real time conditions.

For a single p-n junction solar cell, there is an efficiency limit, called the Schokley-Queisser limit. The losses are caused by many factors, like the black body radiation (~7%), recombination processes (when an electron does not get to leave the semi-conductor to the outer circuit) and also the fact that not all the solar spectrum is absorbed by the semi-conductor. As stated earlier, the photon excites the electron, but it needs an energy E_{ph} that is higher than the energy gap (E_g) between the valence and conduction band.

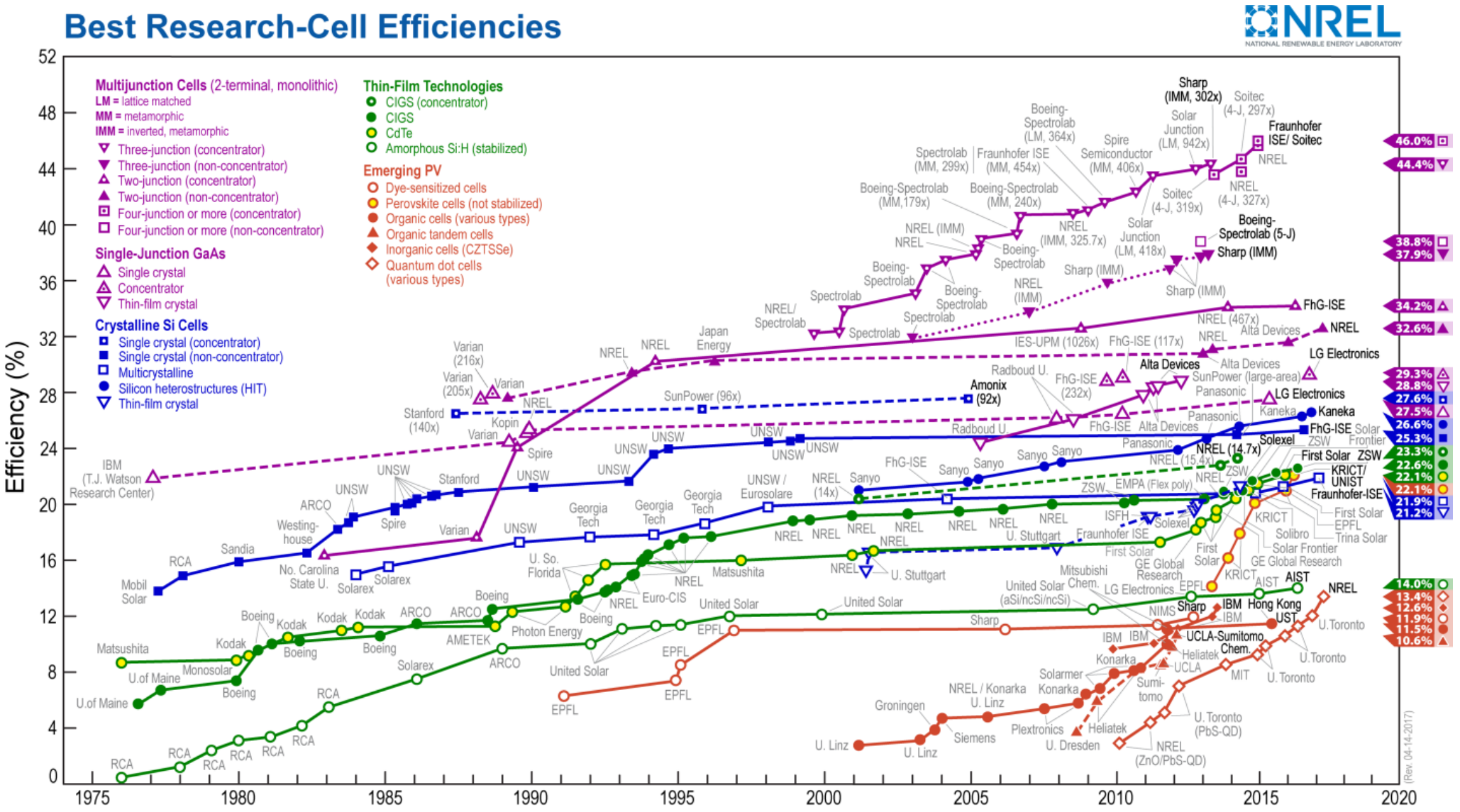

Fig. 23 Maximum cell efficiency chart for different PV cell technologies [6].

The energy of a photon E_{ph} is defined as:

$$E_{ph} = \frac{hc}{\lambda} \tag{3}$$

where $h = 6.626.10^{-34}\ m^2\ kg\ s^{-1}$ is the planck constant, $c = 299\ 792\ 458\ ms^{-1}$ is the speed of light and λ is the photon wavelength.

The sun emits electromagnetic irradiance as a black body at about 5800 K. As it travels through the atmosphere, some of the radiation is absorbed and/or scattered due to the composition of the atmosphere. The irradiance at the top of the atmosphere as well as at the sea level are presented in Fig. 5.

As the sun light is a polychromatic irradiance spectrum, not all the photons are able to excite the electrons, and thus create electricity. All of these losses add up to a theoretical efficiency limit.

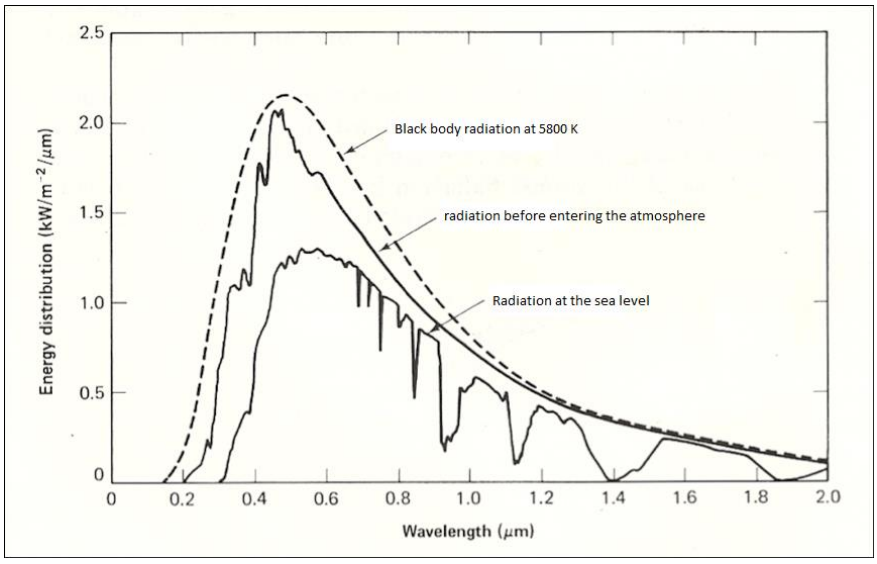

Fig. 24 Solar radiation at the source, the earth's atmosphere and sea level [7].

For an ideal silicon solar cell, that limit is set at 33.7%.

The effective maximum efficiency achieved by a single p-n junction silicon solar cell as declared by the NREL is about 25% (Fig. 4).

1.7. Limitations of the silicon photovoltaic technology

Apart from the theoretical efficiency limit, other factors have an effect on the final product's efficiency. The most important one is the effect of the temperature. It has been observed that the panels will heat up, due to the fact that not all solar irradiance is converted into electricity. The increase of temperature in the panel induces a loss of efficiency, experimentally measuring up to 0.5%/°C.

The ageing of photovoltaic panels is also a big issue. Residential norms imply a 25-year cycle for a panel, and it is observed that the panels' efficiency decays after some years of use [8]. The thermal cycles, as in daily and yearly, must have a certain effect on the ageing of the materials that are being currently used in photovoltaic panels.

1.8. Research statement

The main objective of this research is to develop a model that predicts the thermal and mechanical response of a photovoltaic panel, if all the properties of the materials and the surrounding conditions are known. The link between the thermal and mechanical response cycles, whether they are daily (day and night times) or annually (summer-winter) makes also a part of the motivation of this research.

These objectives may be attained by achieving these sub-goals:

- Modeling the optical interaction between the light and the semi-conductor material, as well as the other layers of the panel.

- Understanding the electrical response of a panel, and how the maximum electrical power can be achieved

- Modeling the distribution of the heat generated inside the panel, and its response in real time.

- Linking the thermal response to a mechanical one, and simulating the different stresses that can affect the photovoltaic panel.

1.9. Layout

This manuscript consists of five chapters. The first one is the present introduction laying the context and the motivation behind the work. In chapter two, a state of the art presentation of the work achieved in the modeling of the photovoltaic cells and panels is presented. In chapter three, a coupled optical, electrical and thermal model is presented, and validated using Standard Test Conditions (STC) and Nominal Operating Temperature Conditions (NOCT) and a parametric study is then simulated and discussed. In chapter four, simulations under real time conditions are performed, and compared to the real response of a PV panel. In chapter five, a thermo-mechanical model is presented using thermal response results from the first model. It is validated under NOCT conditions. Chapter six contains the summary, contributions and recommendations for future works.

2. State of the art

2.1. Commercial panels

Worldwide growth of photovoltaic panel production has been exponential since 2005. It evolved in Europe from a niche market (mostly in Germany) producing 2.17 GW_p (Gigawatt-peak) in 2005 to 94.57 GW_p in 2015. Higher efficiency is achieved, attaining 22.5% for the high end panels, down to 14-16% for the majority of them. This efficiency is measured at Standard Test Conditions (STC) and are included in the datasheets of the commercial panels. Those STC conditions are the following:

- Irradiance=1000 W/m²
- Cell temperature=25°C
- Air mass 1.5 (AM1.5) spectrum.

The panels are mostly identical, some optimization in the electronic parts may be added, but the geometry and the layers' distribution are quite the same.

The market of solar panels is still dominated by silicon solar cells, accounting for more than 90% of the energy produced each year (Fig. 6), due its reliability.

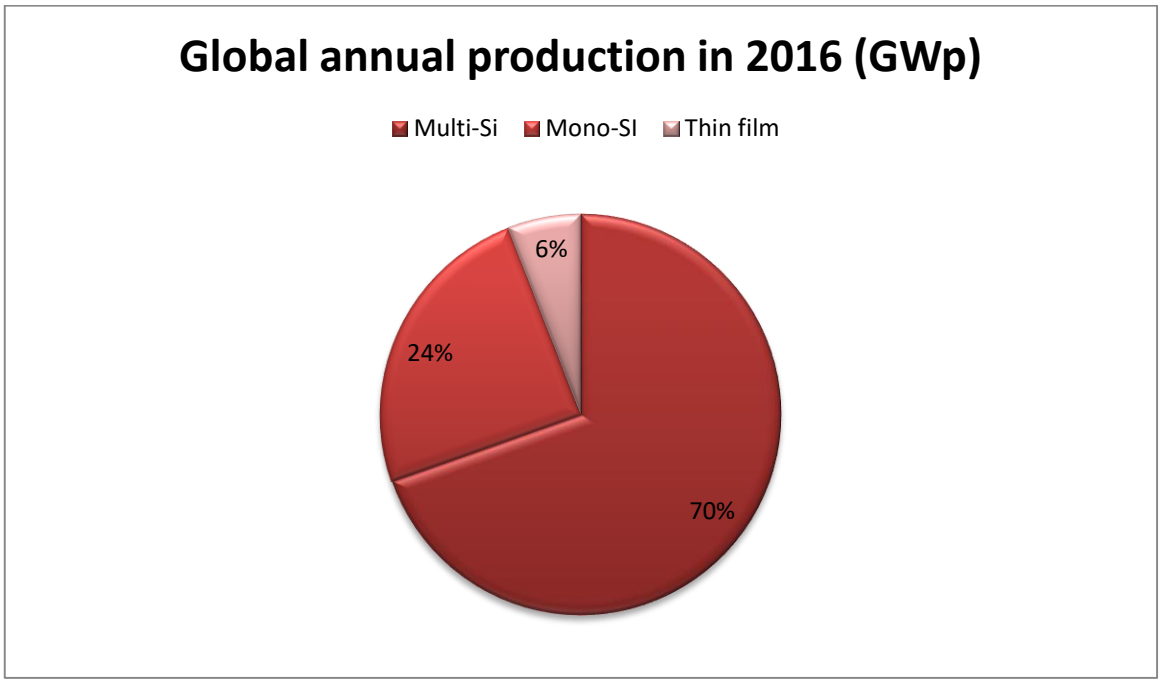

Fig. 25 Percentage of global annual production based on the used technology in 2016.

In the datasheets given by the manufacturer, much information about the panel can be found. Some examples for commercial panels can be found in ANNEX 1. One of the parameters mentioned is the influence of the temperature on the electrical response of the panel. β_{ref} is introduced as the

temperature coefficient. It indicates the loss of efficiency due to the increase in temperature. In order to calculate the efficiency at a certain temperature, the following equation must be applied:

$$\eta_{PV,T_{PV}} = \eta_{PV,Tref}\left[1 - \beta_{ref}\left(T_{PV} - T_{ref}\right)\right] \quad (4)$$

Where T_{ref} the reference temperature at STC, T_{PV} is the temperature of the PV panel, $\eta_{PV,Tref}$ is the reference efficiency measured at T_{ref} and $\eta_{PV,T_{PV}}$ the efficiency at the temperature of the PV panel.

For silicon PV cells, several empirical relations are used to describe the decrease of the electrical efficiency with the increase of the PV cell operating temperature. A review of these relations is presented in Skoplaki et al. [9]. Most of them are close to the linear expression found in the work of Evans et al. [10]. The relations presented in the work of Skoplaki et al. [9] allow to predict the decrease of electrical efficiency (a loss in the electrical output power) when the operating temperature increases due to heating produced by the PV cell.

However, it is observed that these relations are not correct or accurate outside of the standard irradiance conditions of the panel, which is around $1000\ Wm^{-2}$. Since the panel operate outside of these ranges for long periods of the day, it is imperative to find a better relation between the efficiency and the temperature.

Various parameters have an influence on the operating temperature such as: the weather conditions (irradiance level, ambient temperature and wind speed), materials properties (thermal dissipation and absorption properties of the different PV panel layers) and setup conditions of the PV panel.

Moreover, the temperature variations to which the PV cells are subjected lead to cracks and thus deteriorate their electrical performance. A new panel at the beginning of the service may not have the same response as a 5-year-old panel. An extensive study of photovoltaic degradation rates based on experimental measurements from a wide variety of panels in different geographical areas can be found in the work of Jordan et al. [8].

The results for the median degradation rate for panels based on Silicon technology are presented in Table 1. Pre and post refer to installations before and after the year 2000. Furthermore, the losses coming from the module and the losses when the whole panel is taken into account (i.e. the losses coming from the electronic part) are both considered.

Table 4 Summary of median degradation rate prior to and post the year 2000

Technology	Configuration	Median degradation rate (% per year)	
		Pre	Post
Amorphous Silicon	Module	0.96	0.87
	Panel	1.3	0.95
Monocrystalline Silicon	Module	0.47	0.36
	Panel	0.90	0.23
Multicrystalline Silicon	Module	0.61	0.64
	Panel	0.60	0.59

2.2. Modeling overview

Several models were developed to calculate the operating temperature of PV cells / panels taking into account the environmental conditions. The basic methods are built on a simplified energy balance equation with parameters that are empirically determined.

The flow chart (Fig. 7) explains the elements involved in a multi-physics PV panel model. First, the optical response of the panel is presented. It usually involves the sun's irradiance, and the optical properties of the materials of the panel. Then, the electrical response is simulated in order to determine the electrical power generated in the panel. That electrical power is in a direct correlation with the heat source and will be used to determine the new temperature inside the panel.

This output of the model will be used as an input for the next time step, since the temperature has a direct effect on the optical and also electrical response of the panel. This model is fully coupled as it recursively resolves.

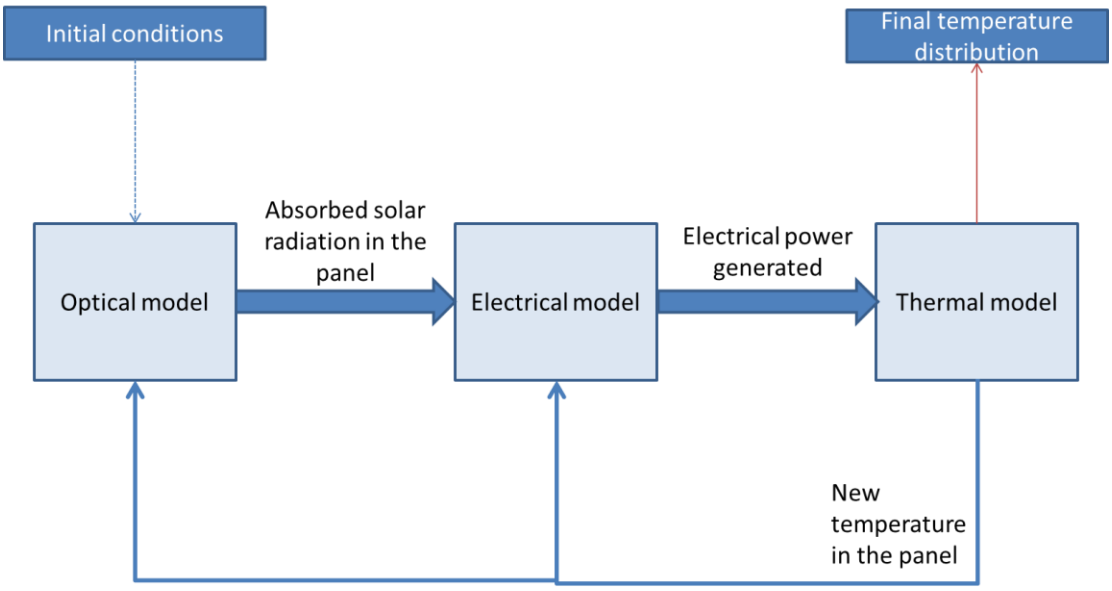

Fig. 26 Coupled multi-physics optical, electrical and thermal model.

2.2.1. Thermal modeling

In order to simulate the panel, one must take into consideration not only the heat generation inside the panel, but also its exchange with the exterior through rigorous definition of the boundary conditions. The PV panel exchanges heat with the outside through convection, and also through radiation towards the sky or the ground.

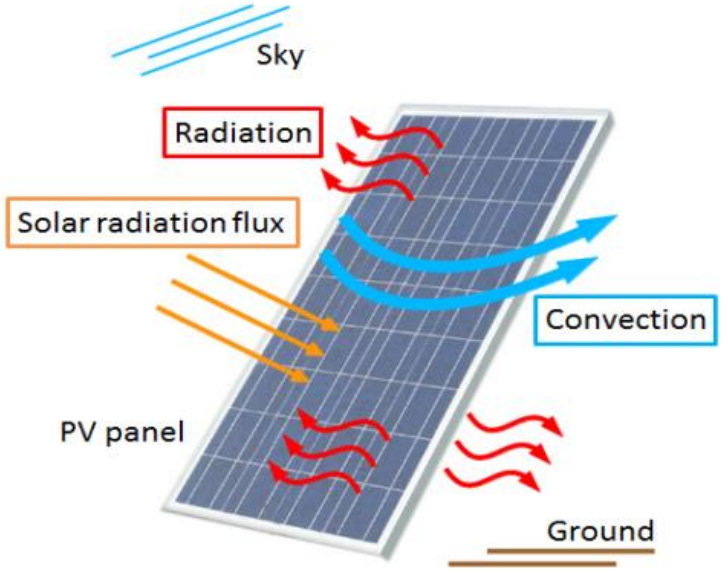

Fig. 27 Representation of the heat exchange with the outside.

The PV panel is subject to convection thorough the wind's effect. Many studies, such as the work of McAdams [11] and the work of Cole et al. [12] interpolate the results from experimental data in order to obtain the convection coefficient as a function of the wind speed.

McAdams [11] proposes that for flat plates exposed to outside winds, the convection coefficient h_{conv} is expressed as

$$h_{conv} = 5.67 + 3.86w \tag{5}$$

Where w is the wind speed, whereas according to Cole et al. [12], the convection coefficient is dependent upon the wind direction and whether the PV panel's surface is on windward or leeward side (Fig. 9). It can be expressed as:

$$h_{conv} = 11.4 + 5.7w \tag{6}$$

for a windward surface, and

$$h_{conv} = 5.7 \tag{7}$$

For a leeward surface.

In order to be able to model the PV panel using these expressions, one must know in advance the direction of the wind, which is fairly hard to simulate, since the direction can change very often during the day in the matter of seconds.

In all of these studies, only the bottom and top surfaces are considered, and the lateral surfaces' convection contribution is neglected.

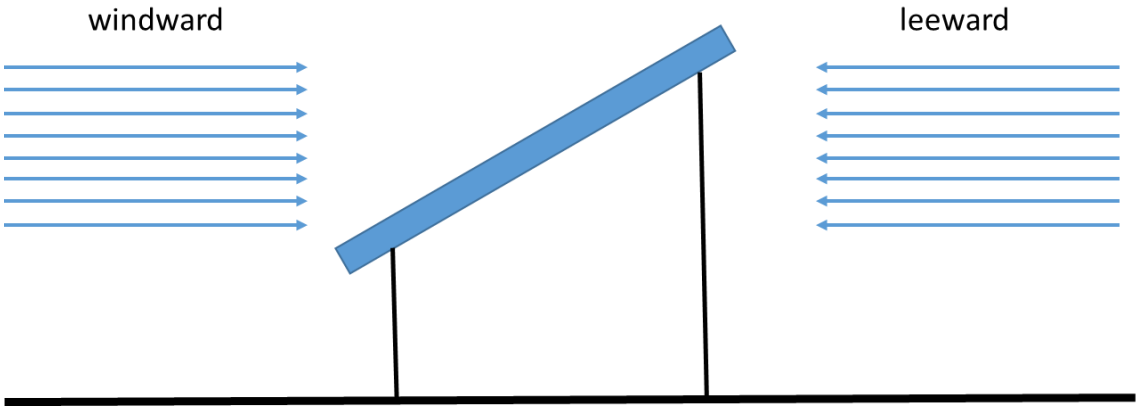

Fig. 28 Representation of the heat exchange with the outside.

Mattei et al. [13] estimated the temperature of a commercial multi-crystalline PV panel considering wind speed and using the convection coefficients proposed in the works of Cole et al. [12]. The exchange coefficient corresponds to the total surface area of the module. The total surface considered is two times the surface area because the heat is lost by the top and the bottom of the PV panel, and the lateral surfaces are neglected, as suggested in the works of McAdams et al. [11] and Cole et al. [12].

However, in the work of Mattei et al. [13], the temperature was considered uniform in the panel and the radiative heat exchanges were neglected. These exchanges are important to take into account, and can influence the overall heat distribution.

The radiative contribution to the heat exchange is the electromagnetic radiation, mainly in the infrared region, emitted by a body that has a temperature higher than absolute 0K. much like the sun, which emits sun light as a part of its thermal radiation, the PV panel radiates heat to the surrounding area. The study of the thermal behavior of the PV panel thus imposes a rigorous definition of its radiative exchange with the surrounding.

In the work of Notton et al. [14], the radiative contribution to the heat exchange is taken into account for the top and bottom surfaces towards the sky and the ground. the radiative conductance between the surface i and the sky $G_{r,i,sky}$, as well as the layer i and the ground $G_{r,i,gr}$ are defined as:

$$\begin{aligned} G_{r,i,sky} &= \varepsilon_{gl} F_{i,sky} \sigma A \left(T_{sky} + T_i\right)\left(T_{sky}^2 + T_i^2\right) \\ G_{r,i,gr} &= \varepsilon_{gl} F_{i,gr} \sigma A (T_{gr} + T_i)(T_{gr}^2 + T_i^2) \end{aligned} \tag{8}$$

where ε_{gl} is the emissivity of the glass, taken as 0.94, $F_{i,sky}$ and $F_{i,gr}$ are the configuration factors between the top or bottom surface and the sky or the ground, σ is the Stephan-Boltzmann's constant, A is the area of the exposed surface, T_{tl} and T_{bl} are respectively the temperature of the top and bottom layer, T_{sky} is the temperature of the sky and T_{gr} is the temperature of the ground.

The configuration factors are defined as a function of the tilt angle of the PV panel κ, and are expressed as:

$$F_{top,sky} = \frac{1}{2}[1 + cos(\kappa)] \tag{9}$$

$$F_{top,gr} = \frac{1}{2}[1 - cos(\kappa)] \tag{10}$$

$$F_{bot,sky} = \frac{1}{2}[1 + cos(\pi - \kappa)] \tag{11}$$

$$F_{bot,gr} = \frac{1}{2}[1 - cos(\pi - \kappa)] \tag{12}$$

The temperature of the sky is defined as the temperature of the atmospheric filter. Several expressions exist in the literature. Some of these expressions are complex, such as the one defined in the work of Berdahl et al. [15] where the temperature of the sky T_{sky} is defined as:

$$T_{sky} = T_{amb}\left[0.8 + \frac{273 \times T_{dp}}{250}\right]^{0.25} \tag{13}$$

where T_{dp} is the dew temperature point, which is rarely available.

Other expressions of the temperature of the sky are more simple, such as the formula used in the work of Schott [16], where the sky temperature for clear sky conditions is defined as:

$$T_{sky} = T_{amb} - 20 \tag{14}$$

And for cloudy sky conditions as:

$$T_{sky} = T_{amb} \tag{15}$$

Another formula that is provided in the work of Swinbank [17] is often used, and is expressed as:

$$T_{sky} = 0.0552 \times T_{amb}^{1.5} \tag{16}$$

In the one dimensional numerical model proposed by Notton et al. [14], the PV panel is divided in three regions (front glass cover, PV cell and back glass cover). For each layer, an energy balance equation was built using an electrical analog model where temperatures, flows, flow sources and imposed temperatures were respectively assimilated to potentials, currents, current generators and voltage generators. The temperature variations in each layer were predicted by the finite difference method. Different thermal conditions taken from literature were investigated, and particularly the influence of convective transfer coefficients.

Armstrong et al. [18] proposed also a thermal model based on an electrical analogy. The thermal properties of the different PV panel layers were correlated with electrical components of a Resistance–Capacitance (RC) circuit.

The thermal resistance Λ_{th} is defined as the index of a material's resistance to heat flow, and is determined as:

$$\Lambda_{th} = \frac{d_l}{kA} \tag{17}$$

where d_l is the thickness of the layer of material, k the thermal conductivity of the material and A is the PV panel surface area.

The thermal capacitance K_{TH} is defined as the ability of a material to absorb and store heat. Thus, K_{TH} is defined as:

$$K_{TH} = \rho C_p A d_l \tag{18}$$

where ρ is the density of the material and C_p is the specific heat capacity. The PV panel considered in the work of Armstrong et al. [18] is the PV panel BP350. It is composed of six layers: glass cover, anti-reflective coating, PV cell, encapsulant, metal back sheet and a back sheet layer. The anti-reflective coating and the metal sheet were not presented in many other studies due to their negligible thickness, and were considered to have no influence on the overall thermal balance of the PV panel.

The modeling proposed by Armstrong et al. [18] was validated by measurements of a PV panel under varying wind speeds. However, the radiative heat losses were neglected.

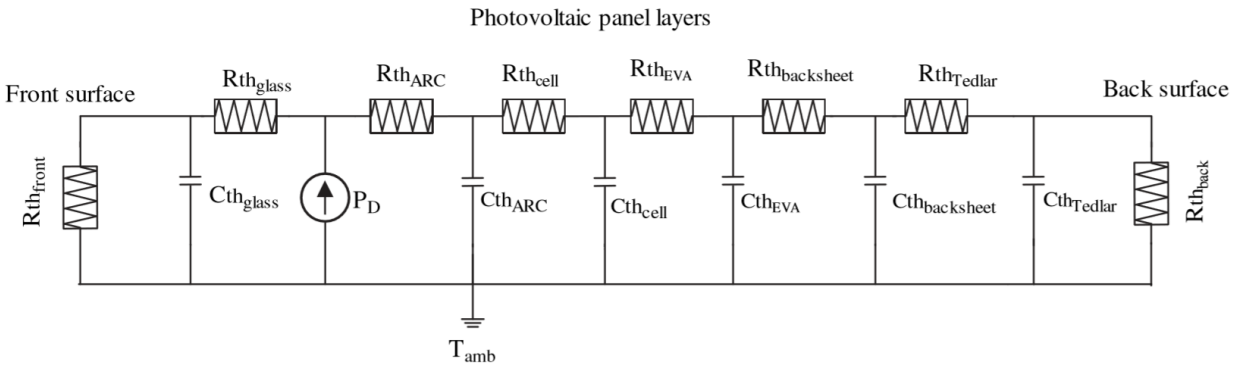

Fig. 29 Photovoltaic thermal resistance network.

A thermal balance equation for a PV panel, where the radiative exchange with the outside was taken into account, was proposed by Jones et al. [19]. In this work, the long wave and short wave radiative contribution are treated separately and the rate of temperature change with time may be expressed as:

$$C_m \frac{dT}{dt} = q_{lw} + q_{sw} + q_{conv} - \frac{P_{out}}{\Delta t} \tag{19}$$

where C_m is the module heat capacity, q_{lw} is the long wave radiation energy, q_{sw} is the short wave radiation energy, q_{conv} is the convective energy exchange and P_{out} is the electrical power generation.

The module heat capacity is defined as the sum of the heat capacities of the different elements of the module, and can be expressed as:

$$C_m = \sum_j A d_j \rho_j C_{p,j} \tag{20}$$

where A is the surface area of the PV panel, j is the the index of the materials, d is thickness of the layer of a certain material, ρ is the density and C_p is the specific heat capacity.

The short wave and long wave radiation heat transfer were calculated separately from each other as detailed in Eq. (18).

For the short wave radiation heat transfer, Jones et al. [19] propose the following expression:

$$q_{sw} = \alpha \Phi A \tag{21}$$

where α is the the absorptivity of the PV panel, taken as 0.7, Φ is the photon flux from the sun and A is the surface area of the PV panel.

The long wave radiation heat transfer is given by the Stephan-Boltzmann law:

$$q_{lw} = \sigma \varepsilon T^4 \tag{22}$$

Which is a more simple expression of the radiative exchange used by Notton et al. [14] in Eq. (7).

For the convection heat transfer, two phenomena were considered; free and forced convection. Free convection is observed during calm days, and on the sheltered rear side of the PV panel, whereas the forced convection is mostly on the front side and is caused by the wind.

Jones et al. [19] considered for a wind speed of 1 $m.s^{-1}$ many values of h_{conv} ranging from 1.2 to 9.6 $W.m^{-2}.K^{-1}$.

For the forced convection, the expression from the work of Holman [20] was considered

$$h_{free} = 1.31 \, (T_m - T_{amb})^{1/3} \tag{23}$$

This model, even though it takes into account all the different heat exchange contribution, is a 0D model. It has been observed that the temperature inside the panel is not uniform, and thus this 0D approach is not enough to adequately represent the evolution of the temperature inside the panel.

A 1D approach was proposed by Barroso et al.[21] using finite differences (FD). The panel was considered in its thickness as a number of equidistanced nodes (Fig. 11). This approach allows the investigation of the temperature evolution inside the layers of the panel.

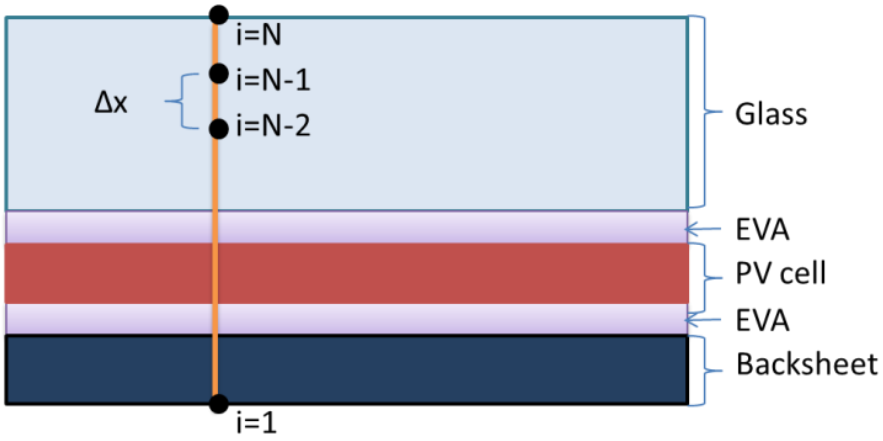

Fig. 30 PV panel layers in 1D approach.

Other models have presented a 2D approach, like the work of Aly et al. [22] and Barth et al. [23], or even a 3D approach, like the work of Siddiqui et al. [24], to the modeling of the PV panel. Although these models present with a fair accuracy the thermal behavior of the panel, it can be noted that the results are comparable to those obtained by 1D simulations under NOCT conditions.

2.2.2. Optical modeling

The optical modeling, which is the first brick of this study, did not get a lot of attention. Mostly, the solar irradiance was treated as a total, rather than a spectrum as it really is (Fig. 5).

The number of photons at each wavelength interval is different, and has a different level of energy. Furthermore, if the photon has a higher energy than the energy gap, the electron will absorb the energy, then quickly thermalize to the bottom of the conduction band (Fig. 12). It can be theorized that any energy that is not used to create the electricity is used to create heat.

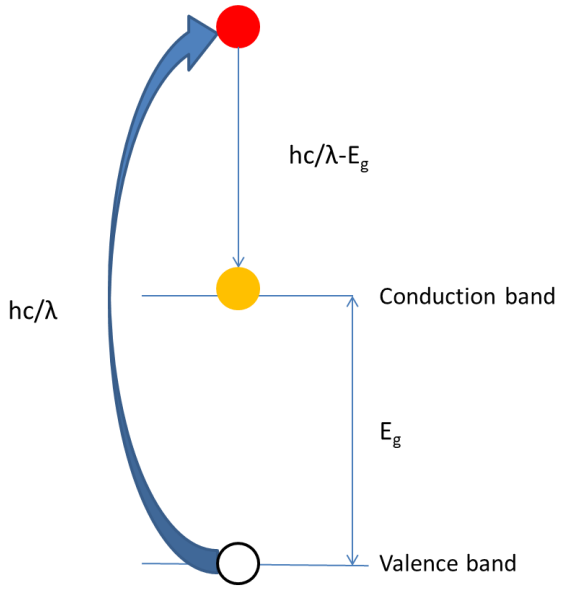

Fig. 31 Instant thermalization of electrons to the bottom of the conduction band in the case of an excitation by a photon with an energy higher than $\boldsymbol{E_g}$.

Jones et al. [19] considered that about 77% of the solar irradiance photons are of the proper energy range to be absorbed by the PV cell, and estimated that 10% of these photons are lost due to the reflective losses, which leads to the absorptivity coefficient $\alpha = 0.7$ defined in Eq. (20) when defining the heat created by short wave radiation. Jones et al. [19] also theorizes that this absorptivity coefficient is considered during the central day time, and that a 20-30% reduction should be considered for lower irradiances, i.e. in the sunrise or sunset time.

Notton et al. [14] considered the absorption at the level of the PV cell, but also the absorption of the glass, and an absorptivity coefficient for the glass $\alpha_{gl} = 0.05$ was assigned.

These approaches might allow the thermal calculation and modeling of the PV panel, but it does not give many information about how much of the irradiance turns into electricity, as well as not giving accurate measurements of the absorptivity of the different layers. The encapsulant was not even considered, even though it surely absorbs some of the irradiance, which will be converted into heat.

A detailed multi-physics and numerical modeling investigating the optical behavior of the panel is proposed by Vaillon et al. [25] to predict the photoelectric conversion of silicon made cells.

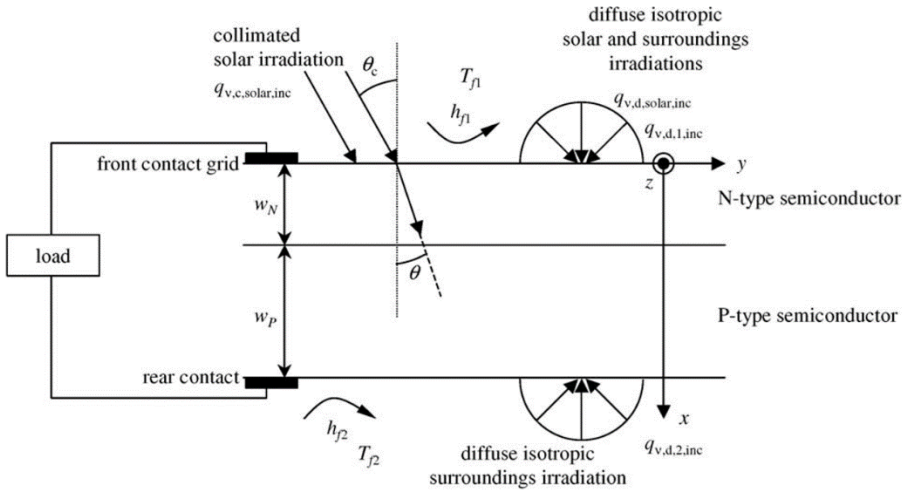

Fig. 32 Schematic description of the PV panel from the work of Vaillon et al. [25].

The modeling proposed in the work of Vaillon et al. [25] accounts for collimated solar irradiance, which is the direct solar irradiance on the panel, as well as diffuse irradiance. It can also be used as a design tool, which is one of the goals of this work. However, the encapsulation of the PV cell was not considered in the work of Vaillon et al. [25].

Following the framework of the work of Vaillon et al., Weiss et al. [26] proposed a bi-dimensional modeling where the different physical phenomena (optical, electrical and thermal) are coupled. The work of Weiss et al. [26] was mainly focused on radiation heat transfer in a PV panel. The temperature predictions were performed with a commercial finite element code. They are in fair agreement with the experimental value measured during one day.

2.2.3. Electrical modeling

The electrical modeling is usually coupled to the thermal modeling, as the electrical properties of the materials are heavily influenced by the temperature [27]. The panel can be modelled as an electrical circuit, called the one-diode model circuit (Fig. 14).

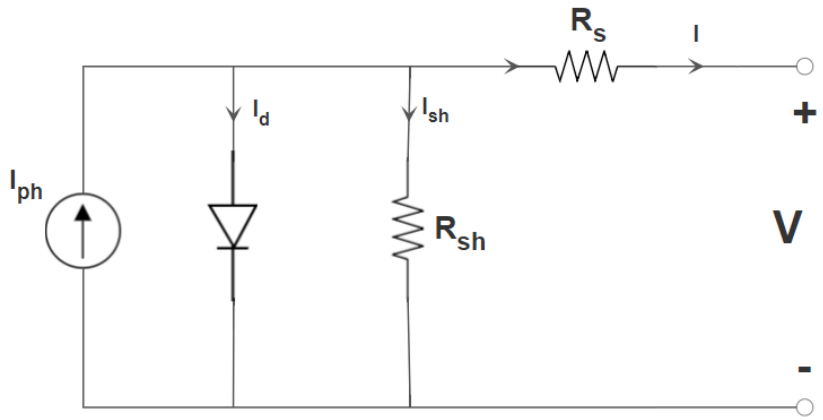

Fig. 33 One diode model equivalent electrical circuit.

where I_{ph} is the photonic light generated current in the cell, I_d is the voltage dependent current lost due to recombination inside the cell, I_{sh} is the current lost due to shunt resistances, R_{sh} is the shunt resistance and R_s is the series resistance and I and V the resulting current and voltage respectively.

The governing equation for this equivalent circuit is formulated using Kirchhoff's current law for current I as:

$$I = I_{ph} - I_d - I_{sh} \tag{24}$$

The current lost to recombination I_{re} can be expressed using the Shockley equation for an ideal diode as:

$$I_{re} = I_0 \left(exp\left(\frac{e(V + IR_s)}{k_b XT} \right) - 1 \right) \tag{25}$$

where I_0 is the saturation current, k_b is the Boltzmann constant, e is the elementary charge and X is the diode ideality factor.

The shunt current I_{sh} is expressed using Kirchhoff's mesh law as:

$$I_{sh} = \frac{V + IR_s}{R_{sh}} \tag{26}$$

Which leads to the development of Eq. (23) to:

$$I = I_{ph} - I_0\left(exp\left(\frac{e(V + IR_s)}{k_B XT}\right) - 1\right) - \frac{V + IR_s}{R_{sh}} \quad (27)$$

The electrical behavior of the PV panel is then described by plotting the current I as a function of the voltage V, which is called the $I - V$ curve. In order to do that, the electrical parameters found in Eq. (26) must be determined, which are I_{ph}, I_0, X, R_s and R_{sh}.

Using a series of experimental voltage-intensity curves, under different irradiances and temperatures, it is possible to use analytical methods to extract these parameters, like the one developed in the work of Blas et al. [28]. In the work of Petreus et al. [29], two empirical models are proposed and used to determine the $I - V$ curve of the PV panel without calculating all the parameters.

The photonic current I_{ph} can be determined using the relation found in the work of Zhao and Green [30]:

$$I_{ph} = eA \int \Phi(\lambda) \times \alpha(\lambda) \times IQE(\lambda) d\lambda \quad (28)$$

where IQE is the internal quantum efficiency at the determined wavelength, which is defined as ratio of the number of charge carriers collected by the cell to the number of photons with higher energy than the energy gap E_g and are absorbed by the cell

$$IQE = \frac{number\ of\ electrons\ collected}{number\ of\ absorbed\ photons\ with\ energy\ higher\ than\ E_g} \quad (29)$$

Some commercially available software, like PC1D which is a solar cell modeling graphical program [31]. The interface is presented in Fig. 15.

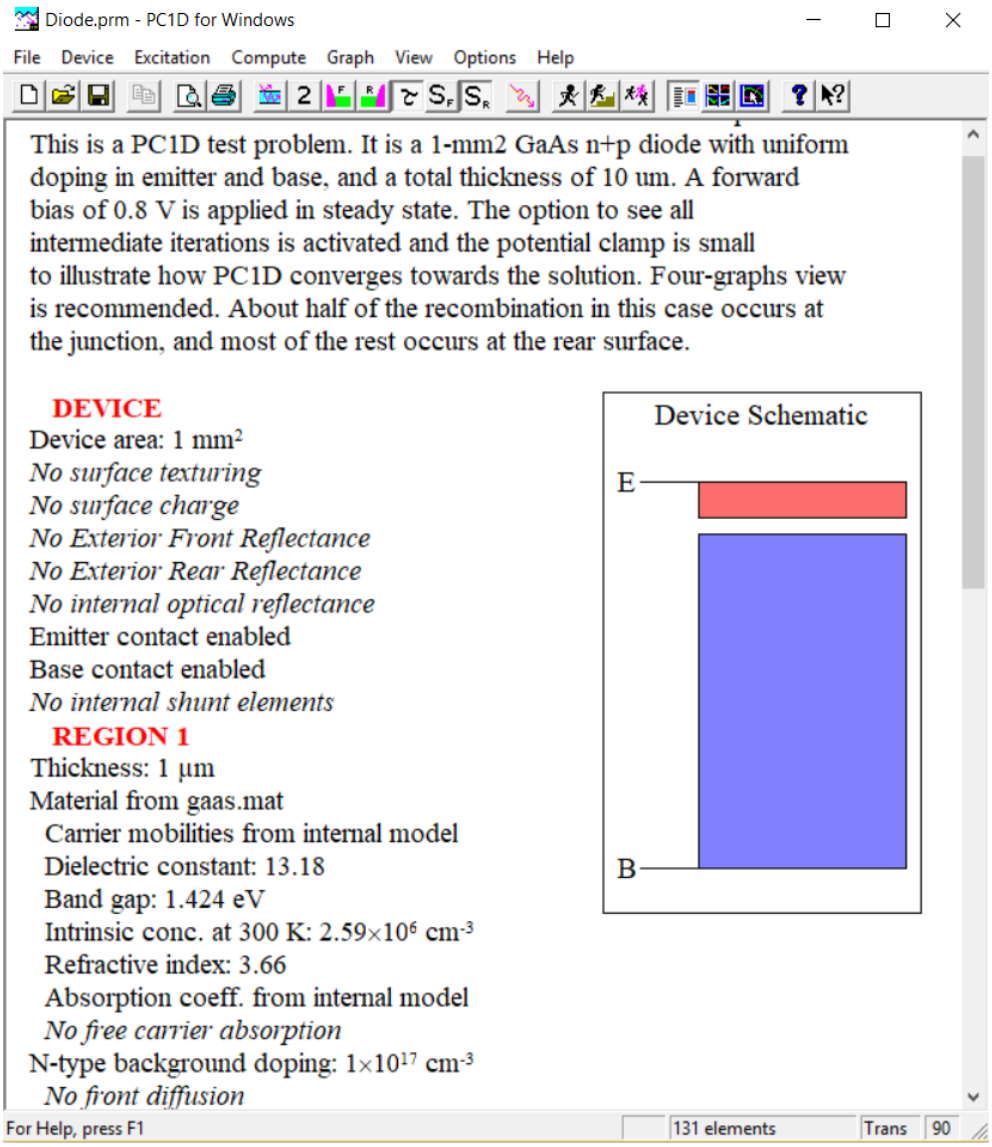

Fig. 34 Interface of PC1D for windows.

If given the geometrical and electrical properties of the PV cell, the internal quantum efficiency, as well as many electrical responses of the PV panel, can be calculated as shown in Fig. 16.

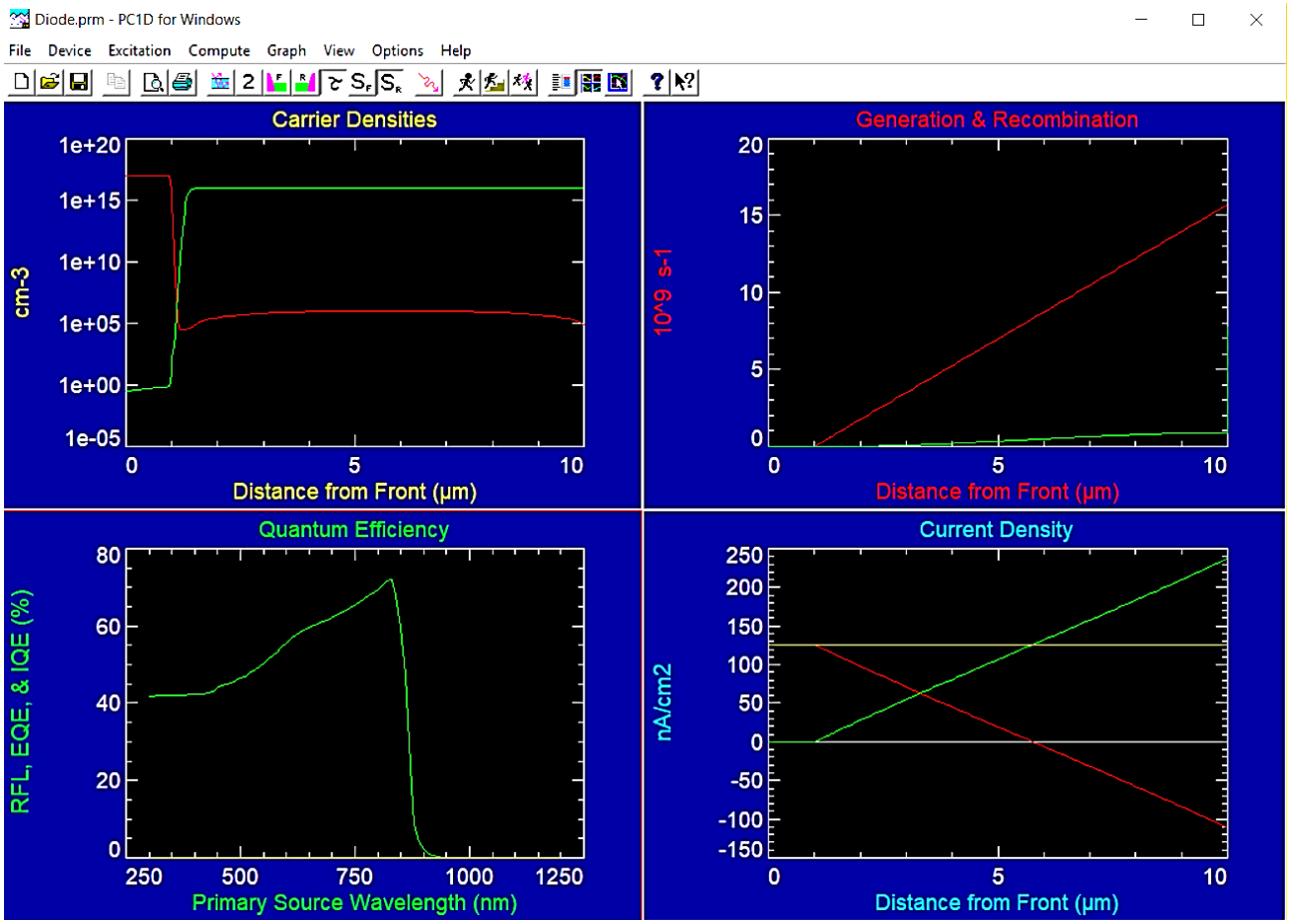

Fig. 35 Electrical properties calculated for a test cell.

Even though this software can present valuable information about the electrical response of the PV panel, its graphic version is a black box. As the electrical properties depend on the temperature, the integration of its results in an independent coupled thermal electrical model proves to be difficult.

The work of Yang et al. [32] presents the relations required to calculate the internal Quantum efficiency of Silicon PV cells. It can be calculated and integrated in a coupled model if needed.

The diode ideality factor X depends on the PV cell technology, and on the used semi-conductor material. The difference in semi-conductors implies a different energy gap between the Valence and conduction bands.

In the literature, many of these ideality factors as listed, such as in the works of Fraas et al. [33], Hua et al. [34] and De Soto et al. [35]. These values are presented in Table 2.

Table 5: Diode ideality factor and energy gap of different PV cells technologies

Technology	Ideality factor X	Energy gap E_g (eV)
Mono-Si	1.026	1.12
Poly-Si	1.025	1.14
Amorphous Si:H	1.8	1.65
Amorphous Si: H tandem	3.3	2.9
Amorphous Si:H triple	3.09	1.6
CdTe	1.5	1.48
CIS	1.5	1
AsGa	1.3	1.43

A method to determine the shunt and series resistances is proposed in the work of Tsai et al. [36] using an optimization algorithm. Another method developed in the work of Barroso et al. [37] using the Particle Swarm Optimization (PSO) method.

Other models, such as the work of Barth et al. [38], propose a two diode model, which takes into account other physical phenomena that happen inside the PV cell, which is the recombination at the junction, by introducing another diode in parallel as presented in Fig. 17.

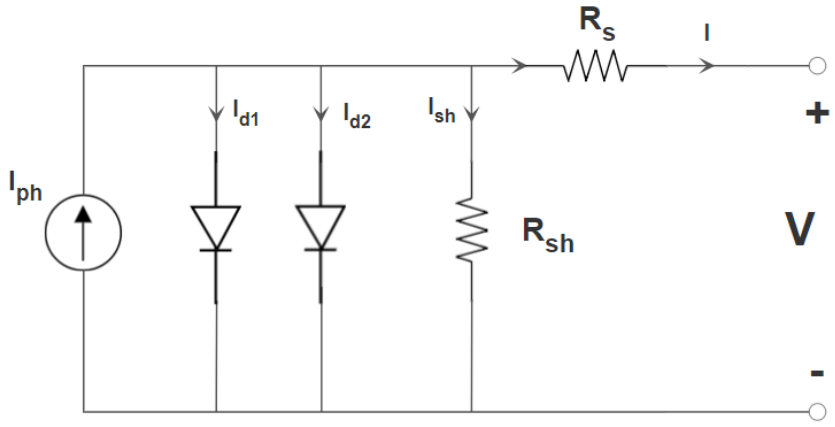

Fig. 36 two diode model equivalent electrical circuit.

Determining the 5 parameters would allow to plot the $I-V$ curve by sweeping the values of the voltage. Usually, the experimental $I-V$ curves of PV modules are given by the manufacturer (See APENDIX A-D). the electrical response is measured for different fixed temperatures and irradiance conditions [39]. Conventionally, the Standard Test Conditions (STC) are used.

Sometimes, the manufacturer provides additional $I-V$ curves for different temperatures at the same STC irradiance (1000 W.m^{-2}), as seen for the BP 585 PV panel in Fig. 18, or for different Irradiances at the same STC temperature (25°C), as seen in Fig. 19.

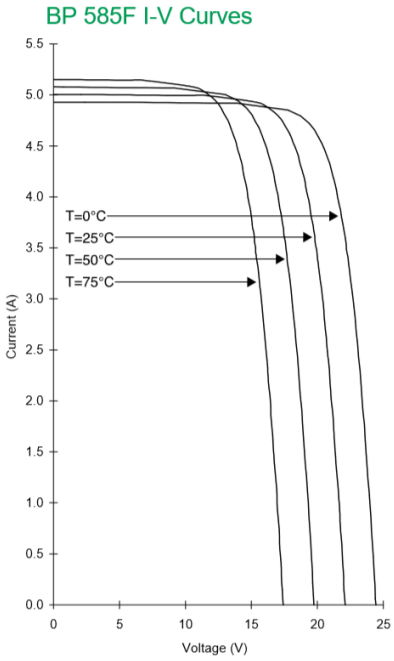

Fig. 37 $\boldsymbol{I-V}$ curves for temperatures from 0°C to 75°C and 1000 W.m^{-2} for the BP585 PV panel.

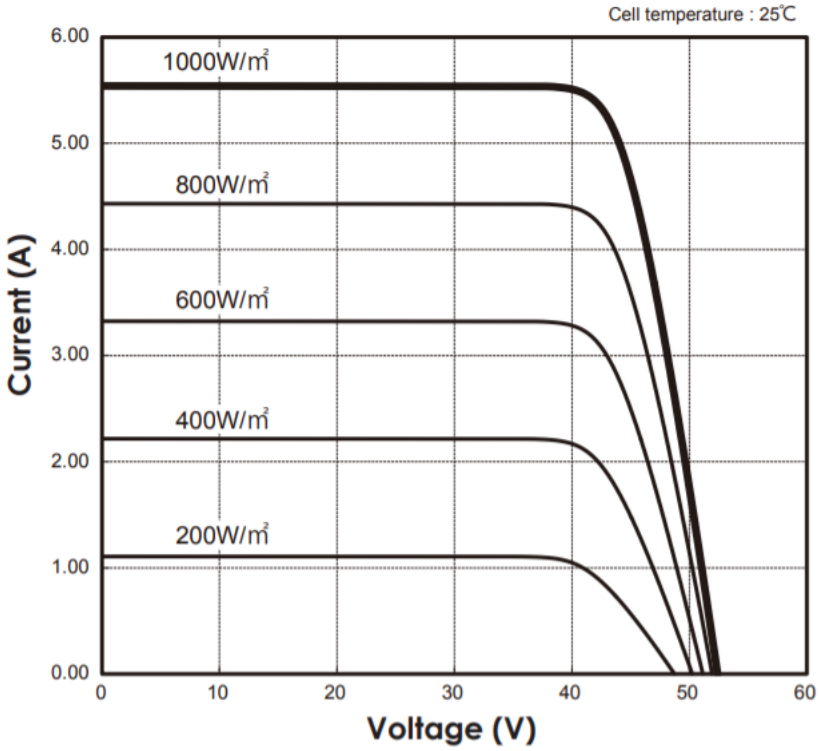

Fig. 38 $\boldsymbol{I-V}$ curves for irradiances from 200 W.m^{-2} to 1000 W.m^{-2} and 25°C for the Panasonic225 PV panel.

As the electrical power is defined as the product of the voltage by the electrical current,

$$P = I \times V \tag{30}$$

It is important that the values of the voltage and the current are optimal, in order to obtain the maximum electric power available. For that reason, many optimization algorithms were developed in order to continuously adjust the impedance to keep the PV system operating at the peak power point. They are called Maximum Power Point Tracking (MPPT) algorithms and are developed using many methods.

In the work of Liu et al. [40], the perturbation and observation (P&O) method is used to develop their algorithm. Incremental conductance with a direct control method is used in the work of Safari et al. [41]. Another MPPT algorithm based on fractional open circuit voltage is used in the work of Ahmad [42].

From the $I - V$ curve of a PV module, one can define performance parameters for the cell:

- Short Circuit current I_{sc}, which corresponds to the short circuit condition when the impedance is low and thus the voltage is equal to 0

- Open Circuit voltage V_{oc}, which occurs when there is no current passing through the cell, thus the current is equal to 0.

- Maximum Power P_{max}, which corresponding to the maximum power current I_{MP} and voltage V_{MP}. At the I_{sc} and V_{oc} points, the power will be 0, and the maximum value for the electrical power occurs between the two. It is important find the values of I_{MP} and V_{MP} in order to obtain the maximum electric power available.

- Fill Factor FF, which is calculated as a ratio between the maximum power P_{max} and the theoretical power that would be output at both the open circuit voltage and short circuit current together

Just like the $I-V$ curve, it is possible to draw the $P-V$, which presents the power as a function of the voltage. It allows an easier visual tracking of the maximum power point in Fig. 20 where the peak of the power curve is visible.

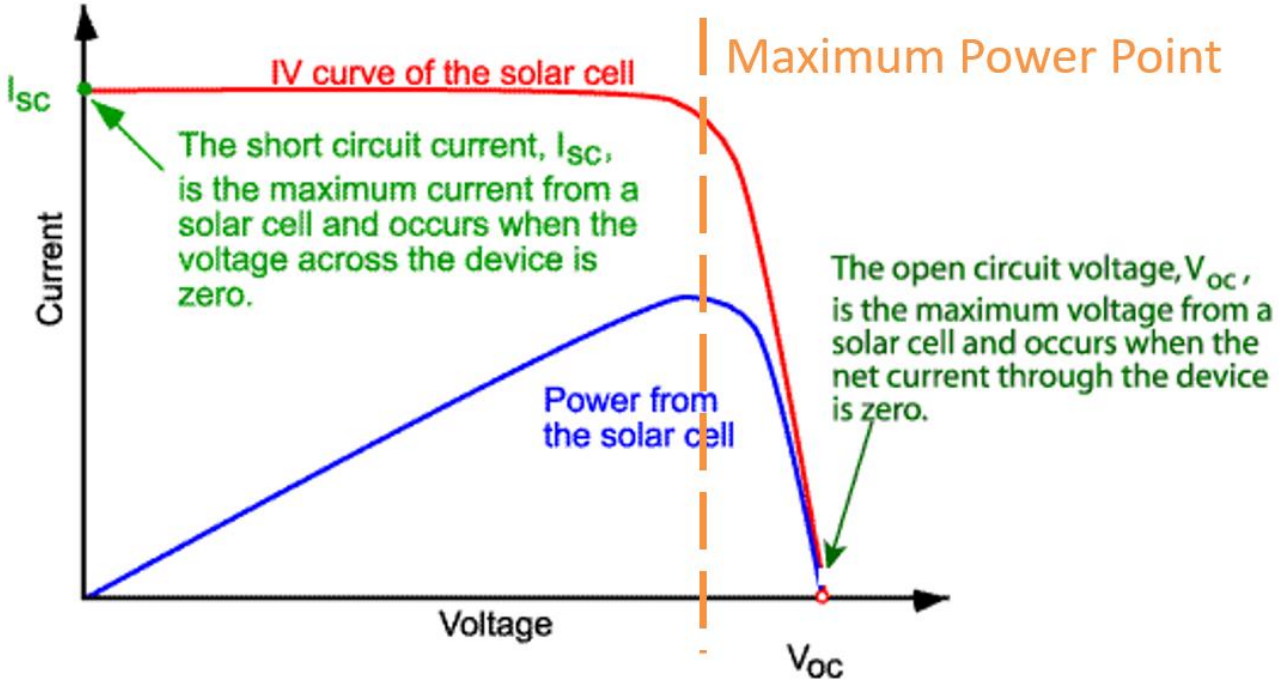

Fig. 39 Representation of superimposed $I-V$ and $P-V$ curves.

The fill factor can thus be defined as:

$$FF = \frac{P_{max}}{I_{sc} \times V_{oc}} \tag{31}$$

As stipulated in the section above, MPPT algorithms are used to keep the PV module operating at the maximum power, which leads to:

$$P_{elec} = P_{max} \tag{32}$$

Where P_{elec} is the electrical power produced by the PV module. It can also be expressed as:

$$P_{elec} = FF \times I_{sc} \times V_{oc} \tag{33}$$

2.2.4. Thermo-mechanical modeling

Like in the electrical and optical modeling, the mechanical properties and responses of the PV panel are affected by the changing temperature. The PV panel is exposed to the two cycles of thermal loading during its life:

- The daily cycle, where the panels heats during the day, and then cools off during the night

- The annual cycle, related to the ambient temperature being different in the summer/winter cycle.

The mechanical response of the panel to the thermal load that is imposed on it was studied by Dietrich et al. [43]. The different expansion differences between the materials is considered to be the cause of the interaction between the layers.

The work of Dietrich et al. [43] concentrated only on the lamination process, where all the components are heated up to 150°C, which is considered to be the initial strain-free temperature. The deflection of the glass and the deflection of the cell gap, which is the distance between two adjacent cells, are studied.

A parametric study of the cell thickness and polymer thickness influence on the change of the cell gap was also performed as shown in Fig. 21 and Fig. 22 respectively.

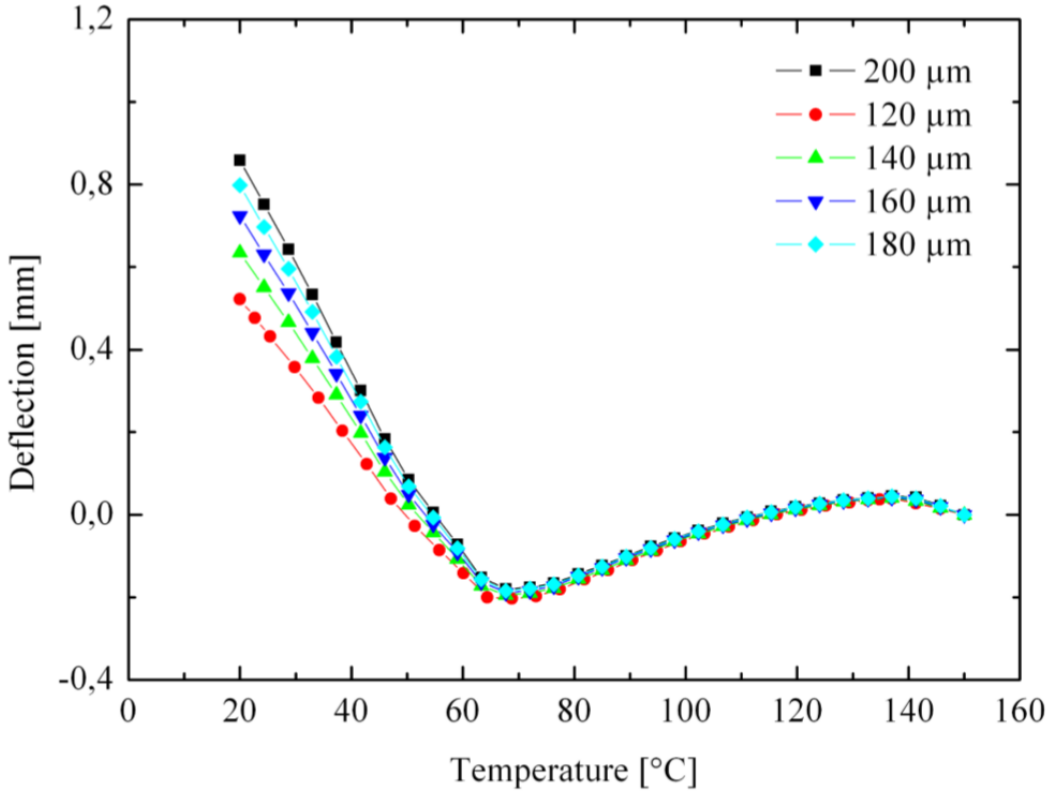

Fig. 40 Parameter study of the cell thickness regarding laminate deflection after lamination.

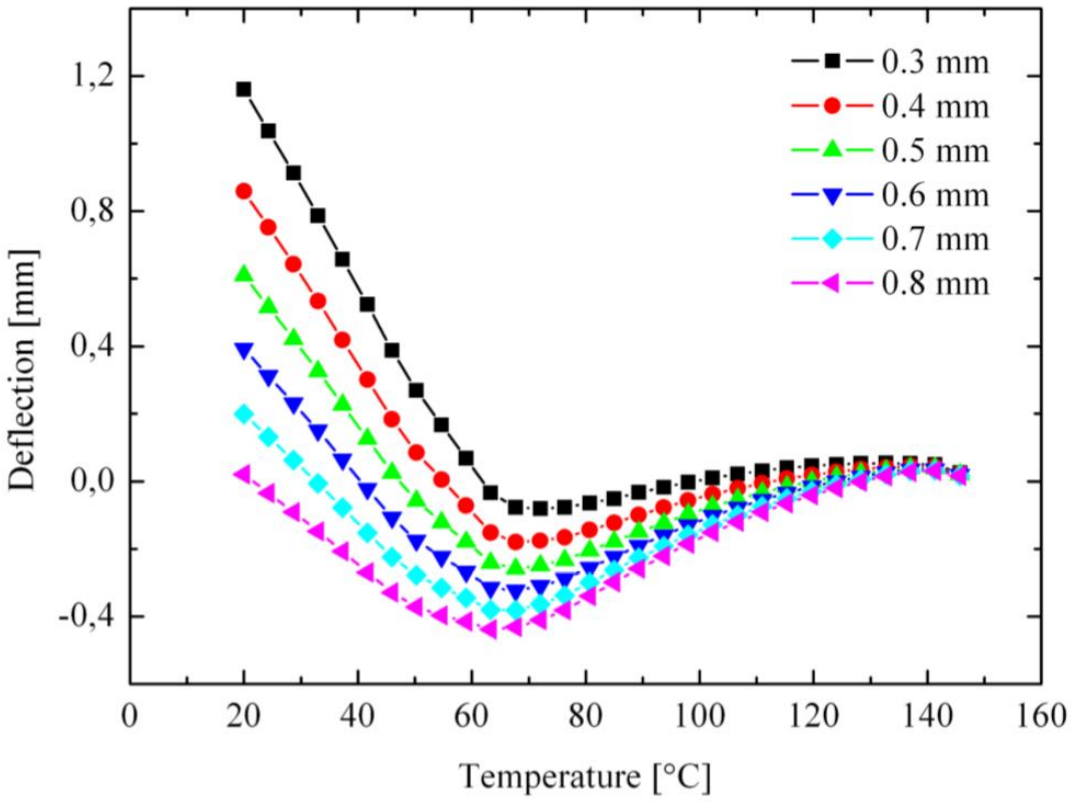

Fig. 41 Parameter study of the polymer thickness regarding laminate deflection after lamination.

The thermo-cycle test was then studied, where the strain free temperature of 20°C was considered. 200 cycles of cycles between -40°C and 85°C are considered following the IEC 61215 standard accelerated test. A hysteresis cycle was observed in Fig. 23.

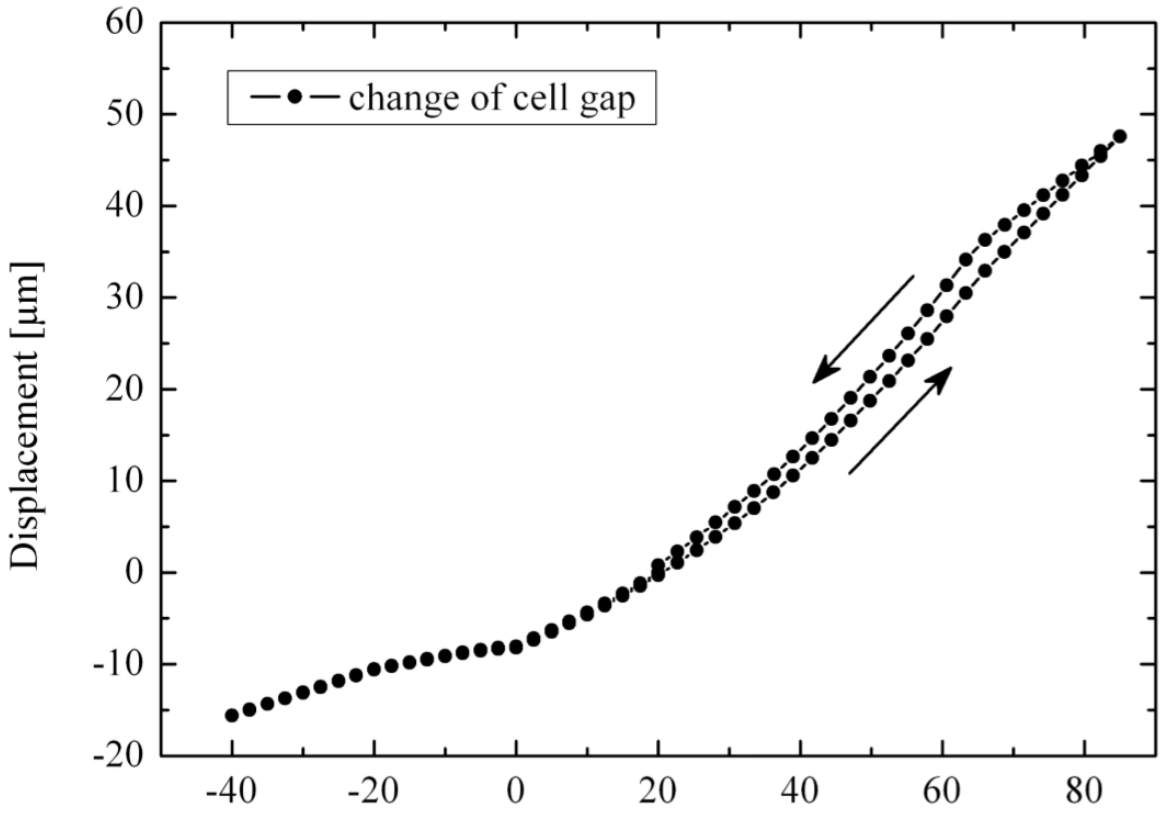

Fig. 42 Parameter study of the polymer thickness regarding laminate deflection after lamination.

The work of Paggi et al. [44], [45] focused on thermo-elastic analysis of the PV panels, or parts of it, considering the cells and the junction of encapsulant between them. The model based on the multilayered beam theory was developed, but while imposing fixed temperatures on the model.

The elastic modulus of EVA depends strongly on the temperature. In the work of Paggi et al. [44], isothermal tensile relaxation tests were performed for different relaxation times ranging from 1s to 2h. The results were then used to plot the elastic modulus as a function of the temperature as seen in Fig 24.

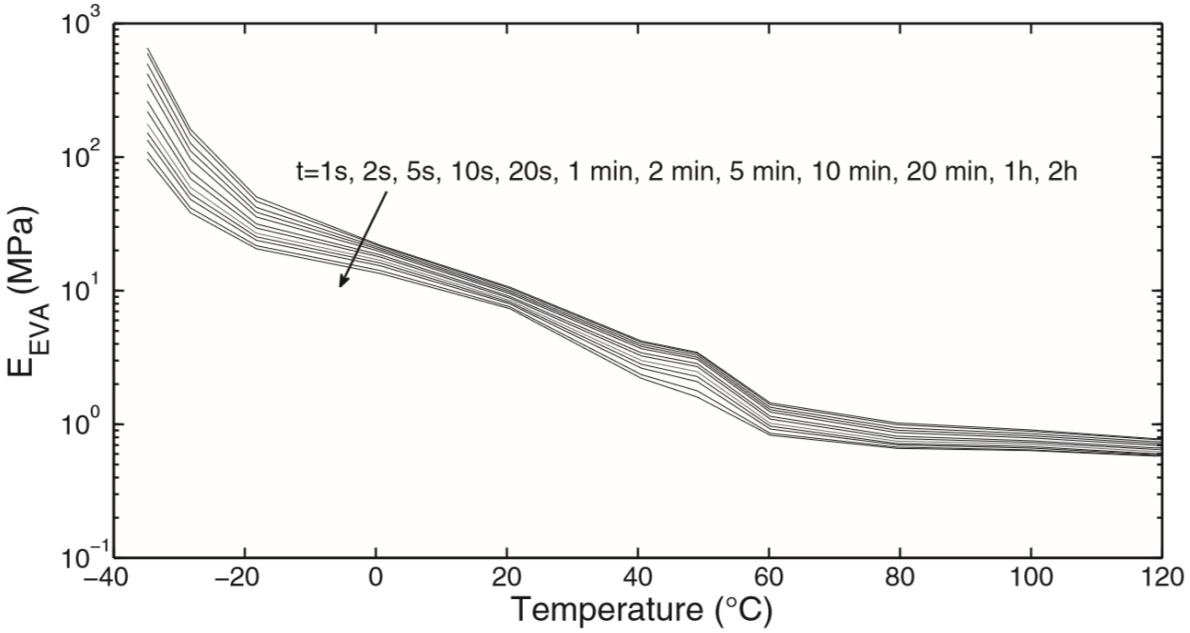

Fig. 43 Young modulus of EVA as a function of the temperature and for different relaxation times.

A one-dimensional (1D) analysis is considered, since the deformation is assumed to be shear free. The influence of the other layers on the glass was considered to be negligible. It was considered mainly as a boundary condition to the rest of the layers.

In the work of Ogbomo et al. [46], PV degradation is investigated, especially for hot climates. It is postulated that hot climates can cause a difference of 40-50°C between the ambient temperature and the PV temperature, especially in the absence of wind convection as seen in the work of Kurnik et al. [47], which can lead to higher than 80°C temperatures in the PV module.

The influence of the ambient temperature on the accumulated max strain energy density was linked to the mean fatigue life of the PV panel. It was observed that an increase from 25°C to 45°C of the ambient temperature yields a decrease in life from 9.6 years to 4.3 years as shown in table 3.

Table 6: Mean fatigue life change as a function of the ambient temperature

Ambient temperature (°C)	Mean fatigue life (years)
25	9.6
30	7.5
35	6.1
40	5.1
45	4.3

This fatigue can be explained due to the mismatch of the material's thermal expansion coefficient values combined with the no uniform distribution of the temperature through the PV panel thickness and width. The resulting stresses can lead to defects such as micro cracks in the PV cells [48], solder bond failure and/or delamination at the PV cell-encapsulant interface as it can be seen in the work Chianese et al. [49] where delamination of the backsheet causes water penetration as seen in Fig.25

Fig. 44 Water penetration in a 21-year-old PV panel caused by backsheet detachment.

In the work of Sanchez-Friera et al. [50], the delamination happens in the EVA-cell interface and in proximity to the interconnection ribbons. Consequently, they could reduce the produced electrical power and deteriorate the electrical efficiency of the PV panel. .

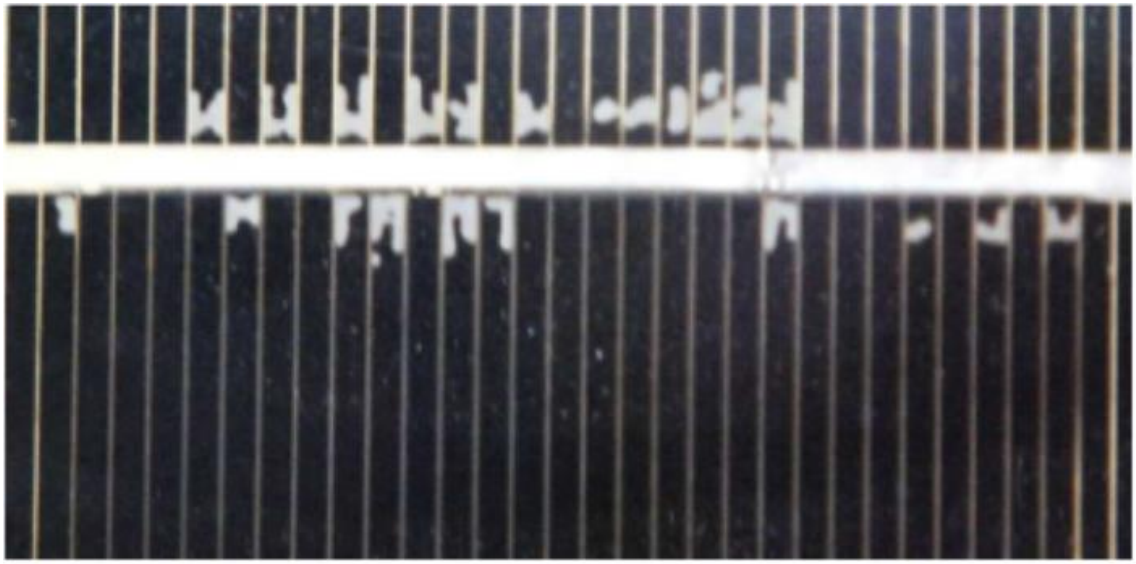

Fig. 45 Delamination at the cell-EVA interface in the proximity of the interconnection ribbons.

2.3. Conclusion

The state of the art shows that there are multiple models of PV panels with almost the same approach of coupling the optical, thermal and electrical parts of the panel. However, some of these models lack an accurate optical consideration of the absorption of the sun's irradiance at all the layers leading to the PV cell. Others omit the fact that the different intrinsic properties of the materials composing the panel make a 0D approach inaccurate.

The mechanical modeling is also done for tests under certain norms, and does not take into consideration the distribution of the temperature inside the PV panel. Also, the simulations are mostly done for cells considered inside the panel, but no information is available for the cells that are on the edge, right next to the aluminum frame of the model.

3. Coupled thermal, electrical and optical modeling and validation under nominal condition

3.1. Introduction

One way to improve the performance of the PV panels is to minimize/control its temperature increase or variation. To achieve this goal, it is necessary to characterize its thermo-electrical behavior when it is subjected to changing meteorological conditions.

Different approaches were developed to determine the thermal response of a PV panel. In all approaches, a thermal model was coupled with some others models that provide all the necessary inputs (or boundary conditions) but also estimate the electrical performance of the PV panel.

The present work is focused on the PV panels composed of silicon made cells. Different technological configurations were adopted by PV manufacturers. However, a PV panel can be viewed as a stack of different layers if the metallic frame and the copper ribbons that interconnect PV cells are neglected. Consequently, the proposed modeling can be applied to different commercial PV panels.

The multi-physics model presented hereinafter allows us to study the thermal response and the electrical performance of a commercial PV panel while it works under different conditions such as standard test conditions (STC), nominal operating cell temperature (NOCT) or continuously changing environmental conditions (irradiance, wind velocity, outdoor temperature, ...). The complete description of the multi-physics modeling implemented in this work is given in the following subsections.

Firstly, the optical model is presented since it is necessary to determine the solar irradiance that contributes to electricity production and the part that is dissipated into heat. Next, the thermal model is presented. It allows to estimate the heat interactions with the surroundings and the temperature throughout PV panel thickness. Finally, an electrical model that calculates the electrical output power is presented.

3.2. Model derivation

3.2.1. Optical modeling

As it was said before, a PV panel can be considered as a stack of layers composed by different materials. The front layer of a PV panel is generally a glass sheet. The PV-cells are next embedded between two insulation layers (in most cases Ethylene-Vinyl Acetate also called EVA). The rear layer of the PV panel is a back sheet that ensures electrical insulation (composed in Tedlar for instance).

The solar light that hits the PV panel is not fully converted into electricity. A small amount of the photons is absorbed by the first layers of the PV panel (glass and EVA layers) and generates heat. The majority of photons are next absorbed by the PV cells and converted into electricity. The light not absorbed by the PV cells generates heat inside and under the PV cell, in the insulation layers.

To estimate the heat sources in the stack of layers that makes up the PV panel correctly, Aljoaba et al. [51] proposed a mathematical model that uses a Markov process. In Aljoaba's work [51], the light absorption coefficients, $a_i(\lambda)$, are equivalent to the percentage of photons (at a specific wavelength value) that are assumed to be absorbed in each layer.

This model is adopted here and is briefly described below. Since the anti-reflective coating that covers the upper side of the PV-cell is a very thin layer, it was not considered as a layer but accounted for in the refraction index between the PV-cell and the insulating layer located above. It should be noted that the scattering from the structured PV-cell surface is not considered in the present work.

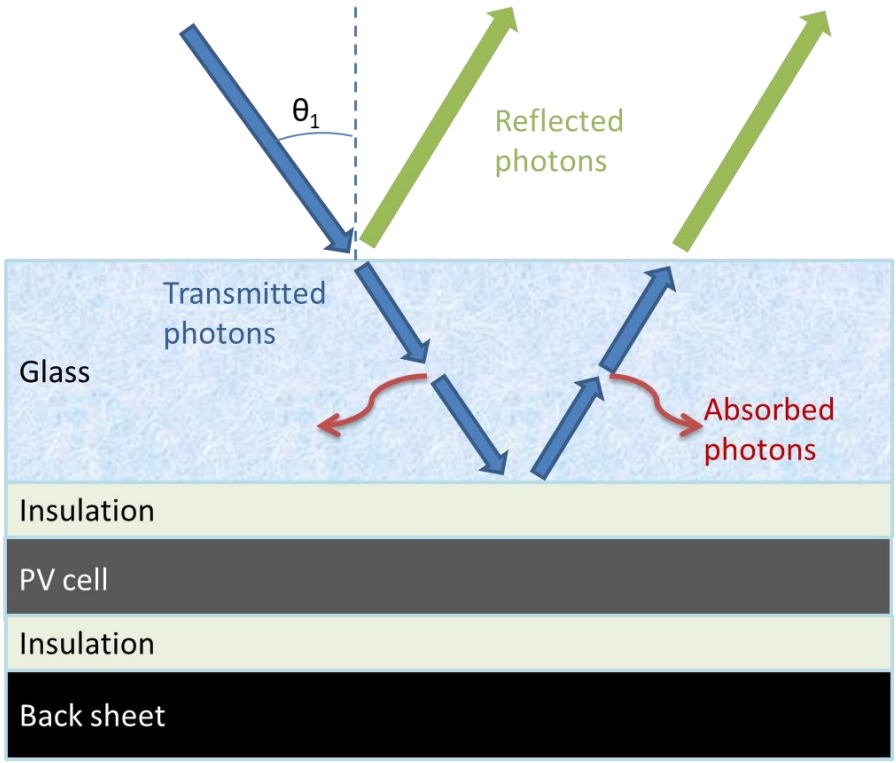

Fig. 46 Diagram of light propagation through the thickness of the glass layer of the PV panel.

Following the framework proposed in Aljoaba's work [51], the light (or photons) is assumed to propagate only throughout the PV panel thickness, thus along one direction. However, the incident angle of light, θ_1 is considered via the average value of refraction index of anti-reflective coating.

The probable positions of photons through the PV panel thickness are called states. The propagation of solar light (or photon flux) throughout the first layer (glass) of the PV panel is also presented in Fig. 27.

In accordance with Aljoaba's work [51], photons traveling inside a layer of the PV panel can be absorbed, reflected or transmitted as seen in Fig. 27. Thus, five different states were used to specify the probable positions of a photon in a layer j inside the PV panel. The five different states are: top going down (further inside the layer, abbreviated as TD), top going up (outwards, TU), bottom going down (BD), bottom going up (BU) or absorbed into the layer (AB).

These different states are schematically shown in Fig. 28 along with the states that relate to them directly in the surrounding layers $j-1$ and $j+1$.

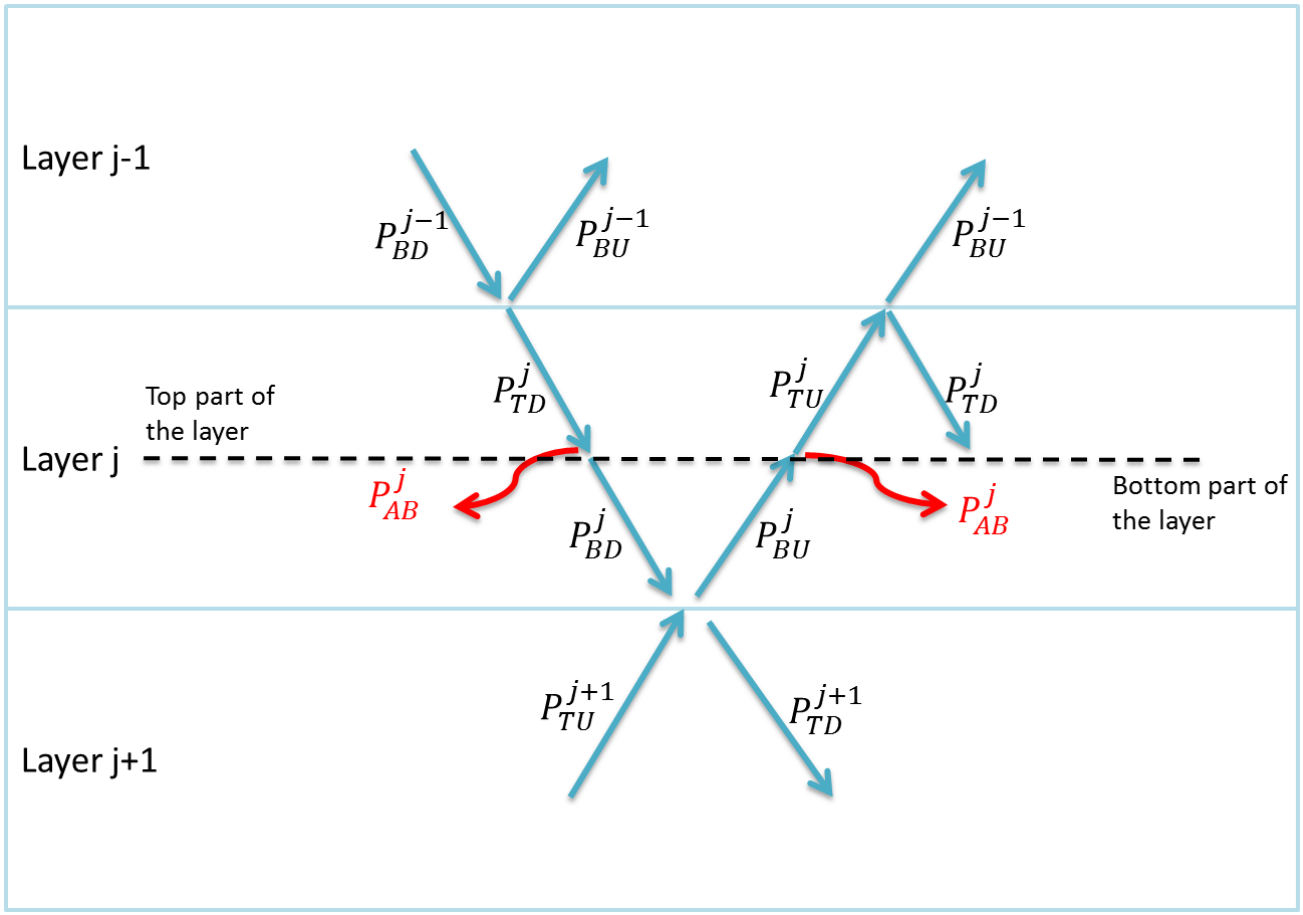

Fig. 47 Different states of photons inside a layer j, along with their relations with surrounding layers j-1 and j+1.

The probability of finding a photon (or probable position of a photon) is related to its position (in the layer and inside of it), state and time. Afterwards, it will be denoted as $P_s^j(i)$ where P refers to the probability, the subscript s the state, the superscript j the layer and i the time increment. For example, the probability of finding a photon in the layer j at a time increment i in the state top going down (i.e. TD) is denoted $P_{TD}^j(i)$. It was assumed that the probabilities of the photons at a time increment $i+1$ only depend on the probabilities at the current increment i.

From Fig. 28, at time increment i, a photon arriving at the interface between the two layers $j-1$ and j is in the state $P_{BD}^{j-1}(i)$. At time increment $i+1$, it can be either transmitted to the next layer (corresponding to the state $P_{TD}^{j}(i+1)$) or reflected (corresponding to the state $P_{BU}^{j-1}(i+1)$), as seen in Fig. 28.

Moreover, at time increment i, a photon traveling inside the top part of layer j and in the "going up" direction is in the state $P_{TU}^{j}(i)$. At time increment $i+1$, it can be either reflected to the top part of the same layer ($P_{TD}^{j}(i+1)$) or transmitted to the next layer ($P_{TU}^{j-1}(i+1)$).

Consequently, at time increment $i+1$, the photons in state $P_{TD}^{j}(i+1)$ were at increment i in the states $P_{TU}^{j}(i)$ and $P_{BD}^{j-1}(i)$. Mathematically, it can be written as:

$$P_{TD}^{j}(i+1) = R_j P_{TU}^{j}(i) + (1-R_j) P_{BD}^{j-1}(i) \tag{34}$$

where $R_j$is the surface reflection coefficient between the layers $j-1$and j.

In the same way, all the probabilities or states at a time increment $i+1$ are determined using the probabilities at a time increment i. For the layer j, these are given by:

$$\begin{aligned}
P_{TD}^{j}(i+1) &= R_j P_{TU}^{j}(i) + (1-R_j) P_{BD}^{j-1}(i) \\
P_{TU}^{j}(i+1) &= (1-A_j) P_{BU}^{j}(i) \\
P_{AB}^{j}(i+1) &= P_{AB}^{j}(i) + A_j P_{TD}^{j}(i) + A_j P_{BU}^{j}(i) \\
P_{BD}^{j}(i+1) &= (1-A_j) P_{TD}^{j}(i) \\
P_{BU}^{j}(i+1) &= R_{j+1} P_{BD}^{j}(i) + (1-R_{j+1}) P_{TU}^{j+1}(i)
\end{aligned} \tag{35}$$

where A_j is the absorption coefficient of the layer j.

It should be noted that Eqs. (33) and (34) are valid for layers inside the PV panel. However, for front and back sides of the PV panel, boundary conditions are necessary to complete the optical model. The boundary conditions that were used are presented in Fig. 29.

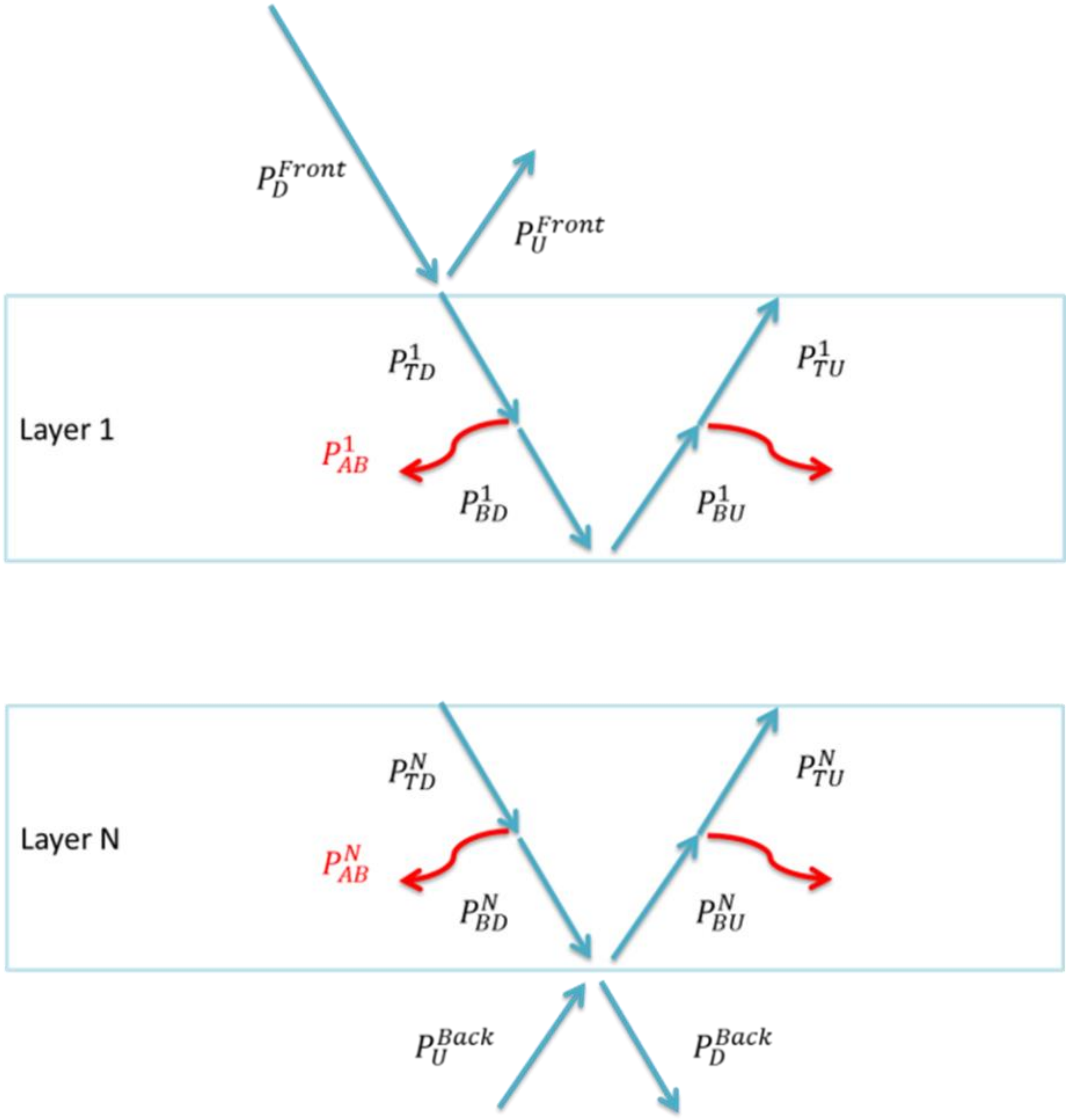

Fig. 48 Boundary conditions at the front side (in our case the glass layer) and the back side (back sheet) of the panel.

In the air layer above the first PV panel layer ($j = 1$, which corresponds to the glass layer), the probabilities of finding photons at a step time $i + 1$ can be expressed as:

$$\begin{aligned} P_D^{Front}(i+1) &= 0 \\ P_U^{Front}(i+1) &= P_U^{Front}(i) + R_1 P_D^{Front}(i) + (1 - R_1) P_{TU}^1(i), \end{aligned} \tag{36}$$

while in the air layer below the last PV panel layer ($j = N$, which generally corresponds to the back sheet), the probabilities can be expressed as:

$$P_D^{Back}(i+1) = P_D^{Back}(i) + R_{N+1}P_U^{Back}(i) + (1 - R_{N+1})P_{BD}^{N}(i)$$
$$P_U^{Back}(i+1) = 0 \tag{37}$$

In Eq. (35), $P_D^{Front}(i+1)$ denotes the probability of finding a photon in the air layer above (or in front of) the PV panel at a time increment $i+1$ with the direction going down (i.e. through the thickness, which corresponds to the subscript D, as in down), and $P_U^{Front}(i+1)$ denotes the probability of finding a photon in the air layer above the PV panel at a time increment i + 1 in the direction going up (i.e. outward in the air which corresponds to the subscript U, as in up).

In the same way, the probability of finding a photon in the air layer below the PV panel at a time increment i + 1 are denoted $P_D^{Back}(i+1)$ and $P_U^{Back}(i+1)$.

All the states of photons at a time increment i can be arranged in a vector form denoted by $P(i)$. The relation between $P(i)$ and $P(i+1)$ can be expressed mathematically in the following matrix-vector form:

$$P(i+1) = [M] \times P(i) \tag{38}$$

where $[M]$ is called the transition matrix, and its terms are expressed by writing the relations from Eq. (34) for each layer of the PV panel and using the boundary conditions defined in Eqs. (35-36).

Thus, the elements of the matrix $[M]$ include the optical properties of the PV panel (the reflectance coefficients R_j between the adjacent layers and the absorption coefficients A_j of each material layer).

It should be noted that the optical properties A_j and R_j are wavelength dependent. The calculations of optical properties A_j and R_j are presented below. Consequently, the transition matrix $[M]$ has to be expressed for each wavelength value of solar irradiance. In the case of a PV panel made with 5 layers, knowing that there are 5 states in each layer, plus the 2 states above the PV panel and 2 states below it, the probability vector P amounts to 29 elements. Therefore, the transition matrix $[M]$ is a square matrix and has 29×29 elements.

The calculation of the optical properties A_j and R_j is detailed below.

For any layer j, light coming through will either be absorbed, reflected or transmitted. Conservation of energy requires that:

$$A_j + R_j + T_j = 1 \tag{39}$$

where A_j, R_j and T_j are the absolute absorption, reflectance and transmission of the layer respectively as presented in Fig. 30.

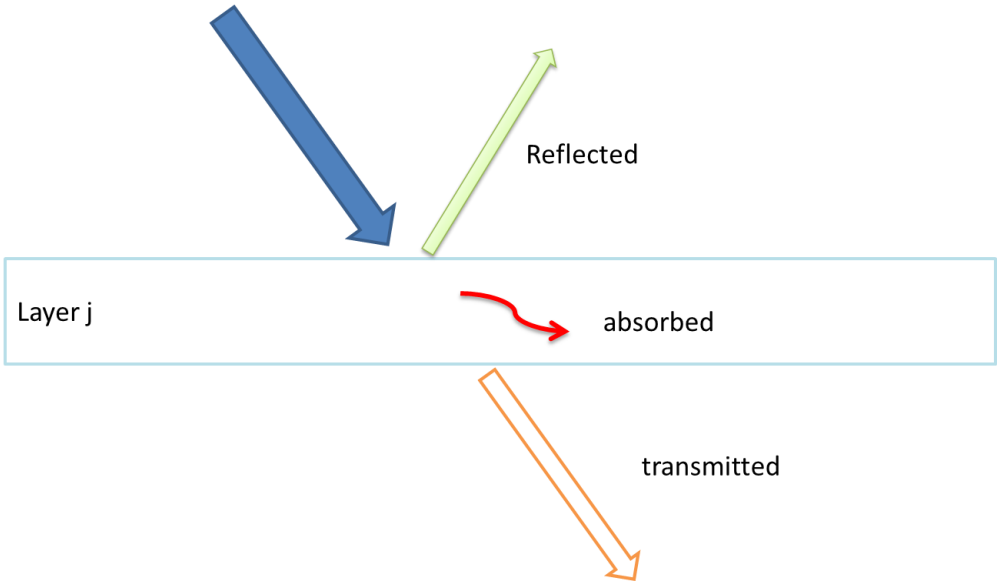

Fig. 49 Scheme of the distribution of incident light in a layer ***j***.

If both surfaces of the material have the same reflection, which is the case of the encapsulant and the glass, the light transmission can be represented as:

$$T_j = \left(1 - R_j\right)^2 \sum_{i=0}^{\infty} R_j^{2i} \tag{40}$$

which is a geometric series with a ratio $R_j^2 < 1$. It can then be expressed as:

$$T_j = \frac{1 - R_j}{1 + R_j} \tag{41}$$

The reflectance coefficient is then expressed as:

$$R_j = \frac{1 - T_j}{1 + T_j} \tag{42}$$

The material's light transmission for the glass and the encapsulant are measured as a function of wavelength as mentioned in the work of Aljoaba [51], and from those measures, one can deduce A_j and R_j in the case of the encapsulant and the glass from Eqs. (38) and (41).

For the PV cell, the surfaces do not have the same reflection coefficient. On the front, an anti-reflective coating is added to maximize the transmission into the cell, and a reflective coating is added on the back to maximize the optical path of the light inside the PV cell (Fig. 31). Those coatings are very thin, and are considered to not absorb any of the light going through them.

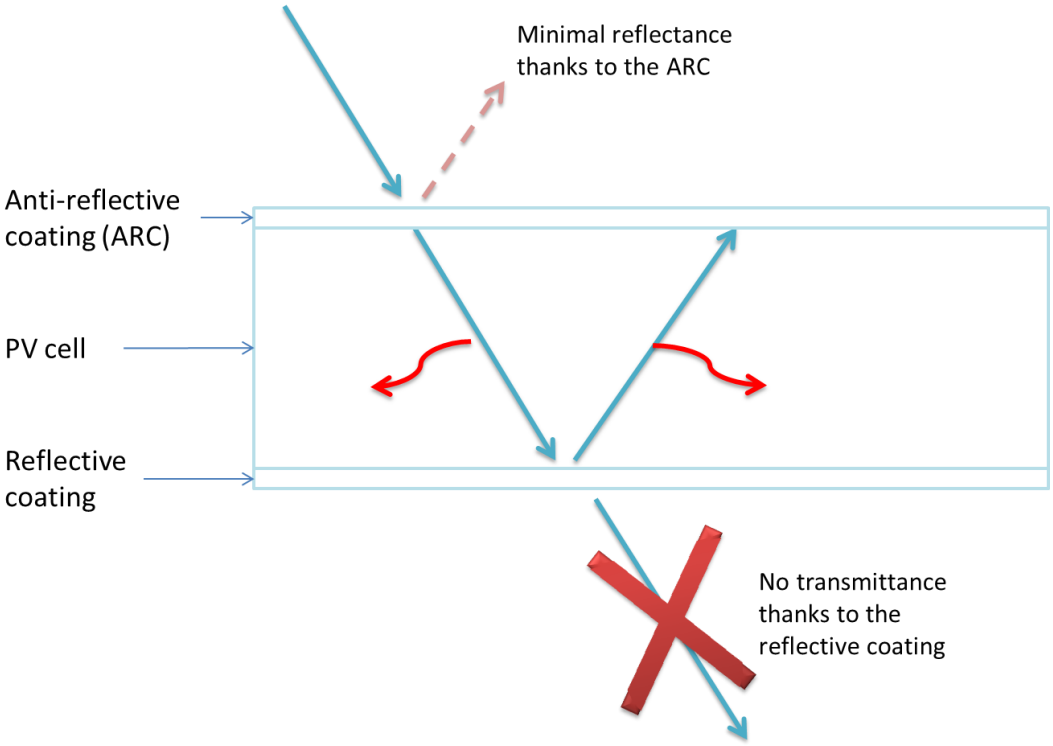

Fig. 50 Light path inside the PV cell.

The anti-reflective coating's reflectance is calculated using the method explained in [52], which in turn is considered to be the reflectance of the cell layer R_{cell}. The transmittance T_{cell} is considered to be negligible thanks to the reflective coating on the back of the cell, which means that the absorption of the cell can be expressed as:

$$A_{cell} = 1 - R_{cell} \tag{43}$$

These absolute reflectance R_j and absorption A_j are calculated as a function of the wavelength for all the materials of the panel, and used in the Markov chains scheme.

At the step time $i = 0$, photons are hitting the panel at its top surface (on the glass). Thus, the initial state vector is a vector composed with 1 at the first line and 0 in all the others. It can be written as:

$$P(0) = [1,0,\ldots,0,\ldots,0]^t \tag{44}$$

Using Eq. (34), the state vector $P(i)$ can be expressed as function of $P(0)$:

$$P(i) = M^i * P(0) \tag{45}$$

At a certain point of calculation, when the time increment tends to a large number ($i \to \infty$), the values of the state vector $P(\infty)$ stops changing and achieves a steady-state. The distribution of the photons in their respective states is final. In the end, photons can be reflected from the PV panel, absorbed in one of the layers or transmitted through the PV panel thickness.

An example of predicted result obtained for a commercial PV panel made with five layers is presented in Fig. 32.

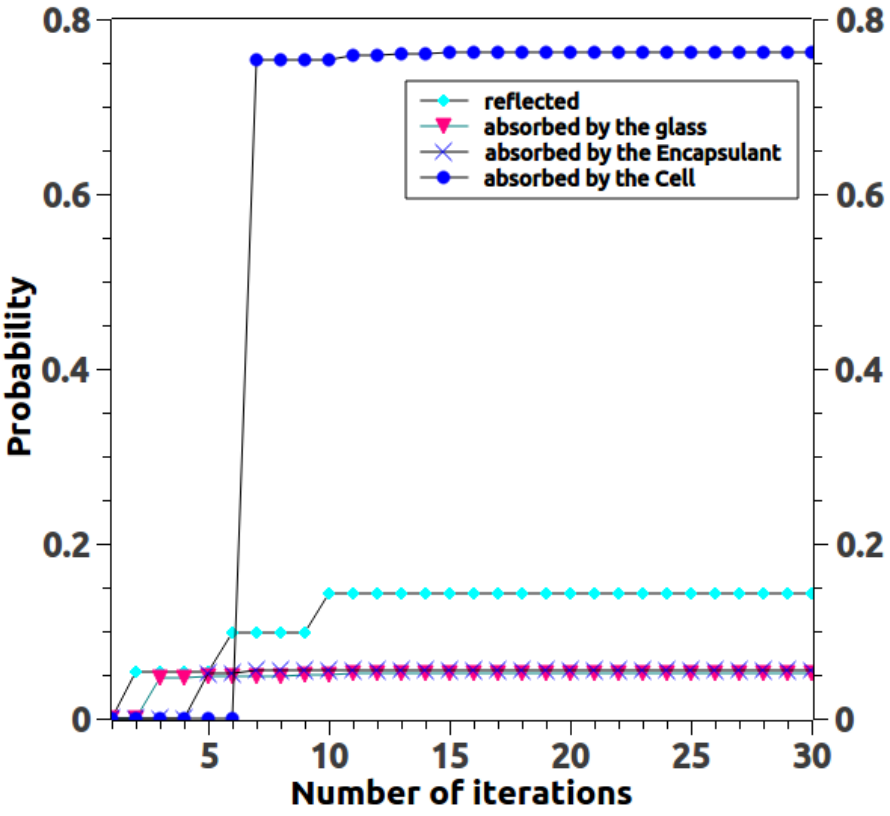

Fig. 51 Example of results obtained with the proposed optical modeling: Probabilities of photons in the layers of a PV panel (predictions for wavelength value of 600 nm).

The state vector $P(i)$ that contains the photons probabilities was calculated for an angle of incidence of 45 degrees and a wavelength equals to 600 nm. This wavelength value corresponds roughly to the middle of useful wavelength range of silicon PV cells. In Fig. 32, after almost 10 time increments, the state vector reaches a steady state ($i = 10$), and all the future vectors will have the same value.

As expected and in agreement with the numerical results of Aljoaba [51], most of the elements of the state vector $P(i \geq 10)$ are equal to zero, except four of them: the probabilities of photons being reflected at the top surface of the PV panel, and being absorbed by layers corresponding to glass, insulation (EVA) and PV-cell. The evolution of only these probabilities is plotted in Fig. 32, as the other probabilities will decay to zero after 5 time increments.

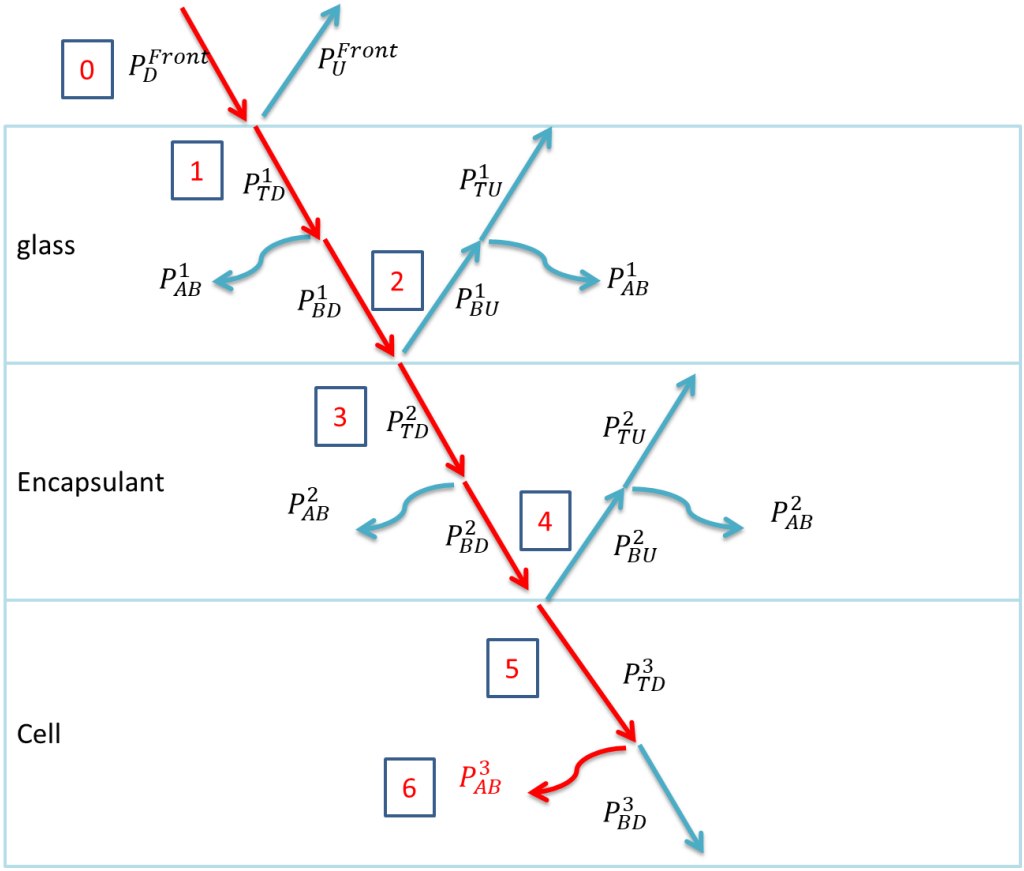

Fig. 52 Schematic representation of the first steps of the light propagation through the PV panel thickness.

To further explain what happens to the photons entering the panel, Fig. 33 describes the steps that a photon goes through before being probably absorbed by the PV-cell itself. The number in the squares denote the time step i. In the initial step $i = 0$, all the photons are in the state P_D^{Front}.

At the step $i = 1$, the photons are either reflected from the surface and are in the state P_U^{Front}, (which means they did not make it into the panel) or they are transmitted through the upper part of the glass layer and are in the state P_{TD}^1. The vector $P(1)$ has only two non-zero states.

At the step $i = 2$, the photons can either be absorbed by the glass (corresponding to the state P_{AB}^1) or transmitted through the lower part of the glass layer (corresponding to the state P_{BD}^1), where they would come to contact with the next layer. The $P(2)$ vector then has three non-zero states (i.e. P_{AB}^1, P_{BD}^1 and P_U^{Front}).

In Figs. 32 and 33, it is noted that only starting time increment $i = 6$ that the photons may be absorbed by the PV-cell, and that's when the P_{AB}^3 takes a non-null value in the state vector $P(i)$.

It is worth remembering that the surface reflection and absorption coefficients of the material layers are dependent on the wavelength of the photon, λ. The global vector of probabilities P must thus be calculated for the whole spectrum of the solar irradiance.

The probability of photons being absorbed in the layer j (i.e. P_{AB}^j) computed for a wavelength λ is equal to the value of relative light absorption coefficient of the layer, $a_j(\lambda)$. Knowing the relative absorption coefficients as a function of the wavelength for every layer of the PV panel, they will allow to calculate the different internal heat sources and also the photonic current produced by the PV-cell with the help of the electrical modeling.

3.2.2. Thermal model

3.2.2.1. Heat equation and boundary conditions

The thermal model used in this work is based on the one proposed by Barroso et al. [21]. The three main heat transfer modes (radiation, conduction and convection) are taken into account in the model. Ohmic heating was not considered in the model, since it has a negligible effect on the thermal behavior of the PV panel as stipulated in the work of Lee et al. [53]. The governing equation of the thermal model is the classical heat transfer equation for a solid domain that can be written as:

$$\rho C_p \frac{\partial T(x,y,z,t)}{\partial t} = \nabla \vec{q} + Q \tag{46}$$

where ρ is the density, C_p the specific heat capacity, t the time, $T(x,y,z,t)$ the temperature at a given coordinate and time, $\vec{q}$ the heat transferred by conduction and Q an internal heat source.

The heat transferred by conduction needs to be defined at the boundaries, which are the front and the rear of the PV panel. It is defined at the boundaries as:

$$-\vec{n} \cdot \vec{q} = h(T_{amb} - T_s) \tag{47}$$

Where $\vec{n}$ is the vector normal to the considered surface, h is the heat exchange coefficient, accounting for both the convection and the radiation at the boundaries, T_{amb} is the ambient temperature and T_s the surface temperature.

The heat transfer inside the panel itself is defined for every layer as:

$$\vec{q} = k\nabla T(x,y,z,t) \tag{48}$$

Where k is the thermal conductivity of the considered material.

In accordance with the work of Barroso et al. [21], we assumed that thermal exchanges from the sides of the PV panel are negligible since the PV panel is thin. Consequently, the domain was considered one-dimensional, along the thickness of the panel. Thus, for each layer of the panel, the heat transfer equation can be written as:

$$\rho C_p \frac{\partial T(x,t)}{\partial t} = k \frac{\partial^2 T(x,t)}{\partial x^2} + Q \tag{49}$$

where $T(x,t)$ the temperature now only dependent on the time and the coordinate alongside the thickness of the panel. The material constants ρ, C_p and k must be determined for each layer of the PV panel.

Following the work of Barroso et al. [21], the heat transfer equation, Eq. (48) is solved numerically with a finite difference approach (first-order central finite difference scheme combined with implicit time integration rule). The discretization of the heat equation is presented in details in the next section.

To complete thermal modeling, boundary conditions must be added to the model. The heat exchange at the boundaries is also determined. In our case, it incorporates two different phenomena: convection and radiation.

Although the convection is considered for both surfaces, the radiation is only considered at the front as we assume that the radiation from the back is negligible.

The convection heat loss q_{conv} is expressed by:

$$q_{conv} = h_{conv}\left(T_{front} - T_{amb}\right) \tag{50}$$

Where h_{conv} is the convective heat transfer coefficient, T_{front} the temperature of the front surface of the PV panel and T_{amb} the ambient temperature.

The convective heat transfer coefficient h_{conv} is divided into two parts: a forced convection coefficient h_{forced} due to the wind, and a free convection coefficient h_{free}. Their expressions are given below:

$$h_{forced} = 5.67 + 3.86w \tag{51}$$

where w is the wind speed, and

$$h_{free} = 1.31 \times \left(T_{front} - T_{amb}\right)^{1/3} \tag{52}$$

The expressions of the convective heat transfer coefficient in Eq. (50) and (51) are taken from the work of McAdams [11].

The radiation heat exchange is accounted for in the thermal model. The expression to calculate the radiation heat loss is defined by:

$$q_{rad} = \varepsilon \times \sigma\left[\left(T_{sky}^4 - T_{front}^4\right) + \left(T_{ground}^4 - T_{front}^4\right)\right] \tag{53}$$

where ε is the emissivity of the glass taken as $\varepsilon = 0.9$ and $\sigma = 5.67 \times 10^{-8} Wm^{-2}K^{-4}$ is the Stefan-Boltzmann constant. The sky and ground temperatures (i.e. T_{sky} and T_{ground}) must be estimated since they are required in Eq. (52).

In the present work, the sky temperature is defined with the equation given by the work of Swinbank [17] for clear sky conditions:

$$T_{sky} = 0.0552 \times T_{amb}^{1.5} \tag{54}$$

In agreement with several thermal models of the literature [19], [21], [24], the ground temperature was simply assumed equal to the ambient temperature in this work:

$$T_{ground} = T_{amb} \tag{55}$$

Finally, the internal heat sources appearing in Eq. (48) must be estimated for the different layers of the PV panel. For the glass and the insulation (EVA) layers, the internal heat source is defined as:

$$Q = \int_{\lambda_1}^{\lambda_2} a(\lambda) I_{rr}(\lambda)\, d\lambda \tag{56}$$

where λ is the wavelength of the photons, $a(\lambda)$ is the value of absorption coefficient of the considered layer at a certain wavelength λ, $I_{rr}(\lambda)$ the global solar irradiance that depends on a set of environmental conditions (such as the location, time and weather) and λ_1- λ_2 the useful range of wavelengths of solar spectrum.

The starting value λ_1 of the useful range of wavelengths is taken equal to 300 nm, whereas the ending value λ_2 is defined with respect to the band gap energy value of silicon (which is a function of temperature).

In Eq. (55), the absorption coefficient values $a(\lambda)$ are evaluated with the optical model defined in the previous section. The global solar irradiance $I_{rr}(\lambda)$ can either be measured or estimated with a solar spectral model (for instance, Bird [54]).

For the layer corresponding to the PV-cell, in the work of Barroso et al. [21], the estimation of the internal heat source Q was computed from solar radiation flux and from an empirical relation of electrical efficiency.

However, the approach used in the work of Barroso et al. [21] cannot be used as a generalized reliable predictive tool for designing new PV panels. The internal heat source Q in Eq. (48) comes from the solar radiation not converted to electrical energy by the PV-cell.

Thus, in this work, it is defined as:

$$Q = t(P_{sol} - P_{elec}) \tag{57}$$

where t is the time, P_{sol} is the solar power received by the PV cell through its front surface and P_{elec} the electrical power produced by the PV cell. The solar power is expressed as:

$$P_{sol} = A \int_{\lambda_1}^{\lambda_2} I_{rr}(\lambda) d\lambda \tag{58}$$

Knowing that PV cells are always working to provide the maximum electrical power, the output electrical power in Eq. (56) P_{elec} can be written as:

$$P_{elec} = FF \times I_{sc} \times V_{oc} \tag{59}$$

where, FF is the fill factor, I_{sc} the short circuit current and V_{oc} the open circuit voltage. Thus, to compute the output electrical power for different temperature and irradiation conditions, an appropriate electrical model needs to be defined.

It should be noted that the current and the voltage produced by a PV-cell, or PV panel in general, are strongly dependent on operating temperature and environmental conditions. Knowing all the equations necessary to build the thermal model, one can proceed to its numerical implementation.

3.2.2.2. Discretization

A finite difference method is used to solve numerically the heat transfer problem defined by the equation presented in the subsection above (Eq. (48)). The spatial domain (in our case the PV panel thickness) is thus subdivided into *N* equally spaced points, also called nodes. These points or nodes constitute a grid, as seen in Fig. 34.

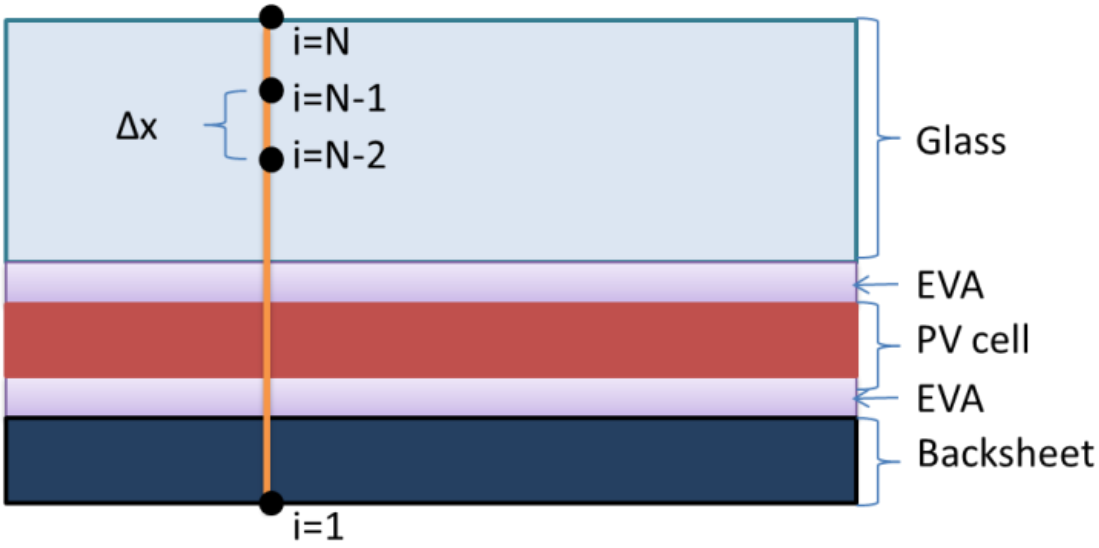

Fig. 53 Spatial discretization of the problem.

The position of a node is defined by its coordinate:

$$x_i = i\Delta x, 1 \leq i \leq N \tag{60}$$

where Δx is the thickness increment which is defined as the ratio between the PV panel thickness and the number of nodes *N*. The first node of the model ($i = 1$) is located at the rear side of the PV panel (or bottom surface corresponding to $x = 0$), while the last node ($i = N$) is located at the front side of the PV panel (or top surface corresponding to $x = d_{panel}$).

It should be noted that the distance between the nodes is constant through all PV panel thickness. Furthermore, as in the optical modeling, anti-reflective coating (ARC) and rear contact layers (that carry the electric current) are not accounted for in the thermal modeling since their

thicknesses are too small compared to the other layers (such as glass, PV-cell or insulation). This last assumption allows to keep a reasonable number of nodes in the domain.

Taking into account the discretization of the problem presented in Fig. 34, the spatial derivatives are approximated by second-order central finite differences:

$$\frac{\partial^2 T(x,t)}{\partial x^2} \approx \frac{T_{i+1} - 2T_i + T_{i-1}}{\Delta x^2} \tag{61}$$

where the subscript i indicates the node related to the thickness coordinate x. The Euler implicit scheme approximation was used in this work for the time derivative. Its expression is given by:

$$\frac{\partial T(x,t)}{\partial t} \approx \frac{T(x,t+\Delta t) - T(x,t)}{\Delta t} = \frac{T_i^{n+1} - T_i^n}{\Delta t} \tag{62}$$

Where Δt is the time step and the subscript n indicates the time increment.

The implicit time scheme was chosen as it gives numerical stability and takes less computational time if large time steps are used.

Using Eqs. (60) and (61), the one-dimensional heat equation expression given in Eq. (48) is discretized as follows:

$$\rho_i C_{p,i} \frac{T_i^{n+1} - T_i^n}{\Delta t} = \frac{1}{\Delta x}\left[k_{i+1/2}\left(\frac{T_{i+1}^{n+1} - T_i^{n+1}}{\Delta x}\right) - k_{i-1/2}\left(\frac{T_i^{n+1} - T_{i-1}^{n+1}}{\Delta x}\right)\right] + Q_i \tag{63}$$

Where the nodes $i + 1/2$ and $i - 1/2$ indicate the mean value between nodes.

It is noticed that Eq. (62) is only valid for the internal nodes of the domain (i.e. $i = [2 \dots N-1]$). For the nodes at the boundaries ($i = 1$ and $i = N$) the heat exchanges by convection and by radiation have to be added. The different expressions of heat exchange coefficient h are presented in the previous subsections.

The discretized heat transfer equations for the nodes located at the boundaries of the domain are obtained from an energy balance of half of the volume formed between the boundary node and the node adjacent to it. The equation of the energy balance for the rear surface of the PV panel (i.e. $i = 1$) is:

$$\rho_1 A \frac{\Delta x}{2} C_{p,1} \frac{T_1^{n+1} - T_1^n}{\Delta t} = kA \left(\frac{T_2^{n+1} - T_1^{n+1}}{\Delta x} \right) + hA\left(T_{amb}^{n+1} - T_1^{n+1}\right) + Q_1 A \frac{\Delta x}{2} \tag{64}$$

while the equation of the energy balance for the front surface of the PV panel (i.e. $i = N$) is:

$$\rho_N A \frac{\Delta x}{2} C_{p,N} \frac{T_N^{n+1} - T_N^n}{\Delta t} = kA \left(\frac{T_{N-1}^{n+1} - T_N^{n+1}}{\Delta x} \right) + hA(T_{amb}^{n+1} - T_N^{n+1}) + Q_N A \frac{\Delta x}{2} \tag{65}$$

Rearranging Eqs. (63) and (64) yields:

$$\rho_1 C_{p,1} \frac{T_1^{n+1} - T_1^n}{2\Delta t} = k \left(\frac{T_2^{n+1} - T_1^{n+1}}{\Delta x^2} \right) + h \left(\frac{T_{amb}^{n+1} - T_1^{n+1}}{\Delta x} \right) + \frac{Q_1}{2} \tag{66}$$

$$\rho_N C_{p,N} \frac{T_N^{n+1} - T_N^n}{2\Delta t} = k \left(\frac{T_{N-1}^{n+1} - T_N^{n+1}}{\Delta x^2} \right) + h \left(\frac{T_{amb}^{n+1} - T_N^{n+1}}{\Delta x} \right) + \frac{Q_N}{2} \tag{67}$$

Eqs. (62), (65) and (66) in their current form can be arranged into a system of N linear equations that can be converted into a matrix form such as $[A] \times [T] = [b]$ as:

$$\begin{bmatrix} A_{1,1} & A_{1,2} & \cdots & A_{1,N} \\ A_{2,1} & A_{2,2} & \cdots & A_{2,N} \\ \vdots & \vdots & \ddots & \vdots \\ A_{N,1} & A_{N,2} & \cdots & A_{N,N} \end{bmatrix} \begin{bmatrix} T_1^{n+1} \\ T_2^{n+1} \\ \vdots \\ T_N^{n+1} \end{bmatrix} = \begin{bmatrix} b_1 \\ b_2 \\ \vdots \\ b_N \end{bmatrix} \tag{68}$$

The matrix $[A]$ is a square tridiagonal matrix, as the linear equations of the temperature at a node are only written with the unknown temperatures on that node, the one before it and the one after it (i.e. i, $i-1$ and $i+1$).

In Eq. (67), the unknown temperatures are stored in the vector or matrix column $[T]$, and all the known parameters in the vector or matrix column $[b]$.

The coefficients of the matrix $[A]$ are expressed as:

$$\begin{cases} A_{1,1} = \dfrac{\rho_1 C_{p,1}}{2\Delta t} + \dfrac{k_1}{\Delta x^2} + \dfrac{h_{rear}}{\Delta x} \\ A_{i,i-1} = \dfrac{-k_{i-1/2}}{\Delta x^2} \\ A_{i,i} = \dfrac{\rho_i C_{p,i}}{\Delta t} + \dfrac{k_{i+1/2}}{\Delta x^2} + \dfrac{k_{i-1/2}}{\Delta x^2} \\ A_{i,i+1} = \dfrac{-k_{i+1/2}}{\Delta x^2} \\ A_{N,N} = \dfrac{\rho_N C_{p,N}}{2\Delta t} + \dfrac{k_N}{\Delta x^2} + \dfrac{h_{front}}{\Delta x} \end{cases} \tag{69}$$

and the coefficients of the vector $[b]$ are:

$$b_1 = \rho_1 C_{p,1} \frac{T_1^n}{2\Delta t} + h_{rear} \frac{T_{amb}}{\Delta x} + \frac{Q_1}{2} \tag{70}$$

$$b_i = \rho_i C_{p,i} \frac{T_i^n}{\Delta t} + Q_i$$

$$b_N = \rho_N C_{p,N} \frac{T_N^n}{2\Delta t} + h_{front} \frac{T_{amb}}{\Delta x} + \frac{Q_N}{2}$$

The vector with the unknown temperatures in the domain are obtained by solving the system of equations given in Eq. (67).

There are several algorithms for solving a system of linear equations. In the present work, the system is solved in the MATLAB ® environment with the operator "\" (i.e. $[T] = [A] \backslash b$), which opts for the appropriate solver according to the characteristics of the matrix $[A]$. The system of equations is solved for each time step and each time the temperatures of the previous step are updated with the ones obtained in the current step.

3.2.3. Electrical model

The electrical behavior of a PV panel or cell is given by its current-voltage curve (i.e. $I - V$ curve). The $I - V$ curve depends on solar radiation and on temperature of the device. It can be represented by a mathematical equation that is linked to an equivalent electrical circuit. The classical one-diode equivalent circuit is used in this work. It consists of a current source connected in parallel with a diode and shunt resistance and also connected to a series resistance as presented in Fig 35.

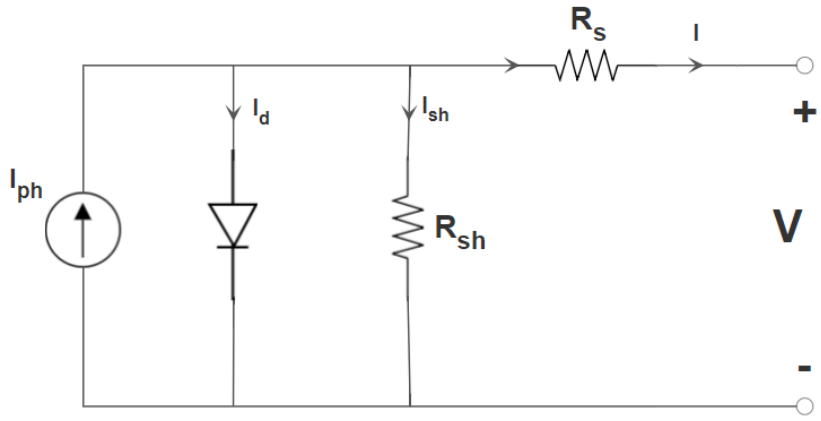

Fig. 54 One diode model equivalent electrical circuit.

In accordance with the work of Siddiqui et al. [24], the current and voltage relationship can be defined as:

$$I = I_{ph} - I_0\left(\exp\left(\frac{\mathrm{e}(V + IR_s)}{k_B X T}\right) - 1\right) - \frac{V + IR_s}{R_{sh}} \tag{71}$$

where I_{ph} represents the current source (also known as photo-current), I_0 is the diode reverse saturation current, R_{sh} and R_s are respectively the shunt and the series resistances, X the diode ideality factor taken as $X = 1.5$, T the temperature of the PV cell, e the elementary electron charge and k_B the Boltzmann constant.

The different electrical parameters in Eq. (70) can be identified using the $I - V$ curves provided by the manufacturers (generally under standard test conditions, i.e. STC). In this work, the series and shunt resistances are calculated with the optimization method proposed in Tsai's work [36]. It should be noted that other optimization techniques can be used for both one-diode as well as two-diode models (for instance the works of Barroso et al. [21] and Barth et al. [38]).

In order to plot $I - V$ curves, it is necessary to first define the expression of the diode reverse saturation current and after that of the photo-current. The diode reverse saturation current I_0 in Eq.

(70) is calculated from the material properties. In the case of silicon cells, this dark saturation current can be defined from the work of Schubert [55] as:

$$I_0 = \frac{qAD_e n_i^2}{L_e N_A} + \frac{qAD_h n_i^2}{L_h N_D} \tag{72}$$

where A is the cell area, D_e and D_h are respectively the electrons and holes diffusion coefficient, n_i the intrinsic charge carrier concentration, L_e and L_h the electron and hole diffusion length and N_A and N_D are acceptor and donor concentrations, respectively.

The acceptor and donor concentrations are taken from the work of Vaillon [25] and are $N_a = 1.5 \times 10^{15} cm^{-3}$ and $N_d = 5 \times 10^{19} cm^{-3}$.

The intrinsic charge carrier concentration n_i is temperature dependant. In the range between the temperatures of 275K and 375K is calculated using the empirical formula proposed by Sproul et al. [56]

$$n_i = 9.38 \times 10^{25} \left(\frac{T}{300}\right)^2 e^{\frac{-6884}{T}} \tag{73}$$

The diffusion coefficient of electrons (subscript e) and holes (subscript h) are defined from the Einstein relation as:

$$\begin{aligned} D_e &= \frac{\mu_e k_b T}{e} \\ D_h &= \frac{\mu_h k_b T}{e} \end{aligned} \tag{74}$$

where μ_e is the mobility of electrons and μ_h is the mobility of holes. They are expressed following the work of Arora et al. [57] as:

$$\mu_e = 88{T_n}^{-0.57} + \frac{7.4 \times 10^8 \, {T_n}^{-2.33}}{1 + \left(\frac{N_a}{1.26 \times 10^{17} {T_n}^{2.4}}\right) 0.88 \, {T_n}^{-0.146}}$$

$$\mu_h = 54.3 \, {T_n}^{-0.57} + \frac{1.36 \times 10^8 \, {T_n}^{-2.33}}{1 + \left(\frac{N_d}{2.35 \times 10^{17} {T_n}^{2.4}}\right) 0.88 \, {T_n}^{-0.146}} \tag{75}$$

where T_n is defined as the normalized temperature, and is expressed as:

$$T_n = \frac{T}{300} \tag{76}$$

The diffusion length of electrons (subscript e) and holes (subscript h) are defined as:

$$L_e = \sqrt{D_n \tau_e}$$

$$L_h = \sqrt{D_p \tau_h} \tag{77}$$

Where τ_e and τ_h are the lifetime of minority carriers of electrons and holes respectively. Following the work of Hull [27], they can be expressed as:

$$\tau_e = \frac{1}{3.45 \times 10^{-12} N_a + 9.5 \times 10^{-32} N_a^2}$$

$$\tau_h = \frac{1}{7.8 \times 10^{-13} N_d + 9.5 \times 10^{-31} N_d^2} \tag{78}$$

To complete the electrical model, the definition of photo-current I_{ph} is needed. It was taken from the work of Zhao and Green [30]. In their work, the photo-current (or photodiode) is written as:

$$I_{ph} = qA \int_{\lambda_1}^{\lambda_2} \phi_{rr}(\lambda) \times a(\lambda) \times IQE(\lambda) d\lambda \tag{79}$$

where $\phi_{rr}(\lambda)$ is the photonic flux (that is computed from the solar irradiance $I_{rr}(\lambda)$), $\alpha(\lambda)$ is the light absorption coefficient of the PV-cell, and $IQE(\lambda)$ is the internal quantum efficiency.

The photonic flux $\phi_{rr}(\lambda)$ is defined as the number of photons in the solar irradiance $I_{rr}(\lambda)$. It is expressed as:

$$\phi_{rr}(\lambda) = \frac{I_{rr}(\lambda)}{E_{ph}(\lambda)} \tag{80}$$

Where $E_{ph}(\lambda)$ is the energy carried by a single photon, and defined as:

$$E_{ph}(\lambda) = \frac{h \times c}{\lambda} \tag{81}$$

The absorption coefficient $a(\lambda)$ is estimated for the PV-cell layer with the optical modeling that is presented in the previous subsection.

The Internal Quantum Efficiency $IQE(\lambda)$ is computed with the equations proposed in the work of Yang et al. [32].

Basically, The IQE for a homo-junction silicon solar cell is sum of the contribution of the three parts of the PV-cell: the base, the emitter and the depletion region between them, as shown in Fig. 36.

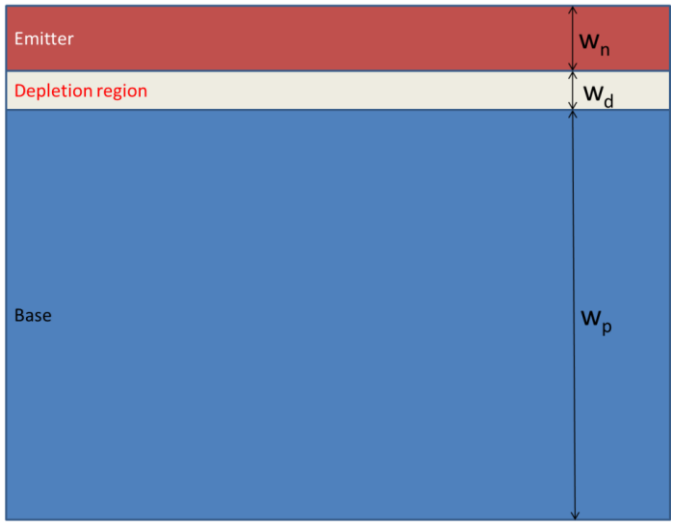

Fig. 55 Schematic view of P-N homo-junction solar cell.

In the work of Yang et al. [32], the equations governing these parts are the following:

$$IQE_p = \frac{\alpha . L_p}{(\alpha - L_p)^2 - 1} \times e^{-\alpha.(w_n + w_d)} \times \left[\alpha L_p - \frac{s_p . cosh\frac{w_p}{L_p} + sinh\frac{w_p}{L_p} + (\alpha L_p - s_p)e^{-\alpha w_p}}{s_p . sinh\frac{w_p}{L_p} + cosh\frac{w_p}{L_p}} \right] \quad (82)$$

$$IQE_n = \frac{\alpha . L_n}{(\alpha - L_n)^2 - 1} \times \left[\frac{s_n + \alpha . L_n - (s_n cosh\frac{w_n}{L_n} + sinh\frac{w_n}{L_n} + e^{-\alpha w_n})}{s_n . sinh\frac{w_n}{L_n} + cosh\frac{w_n}{L_n}} - \alpha . L_n e^{-\alpha w_n} \right] \quad (83)$$

$$IQE_d = e^{-\alpha w_n}(1 - e^{-\alpha w_d}) \quad (84)$$

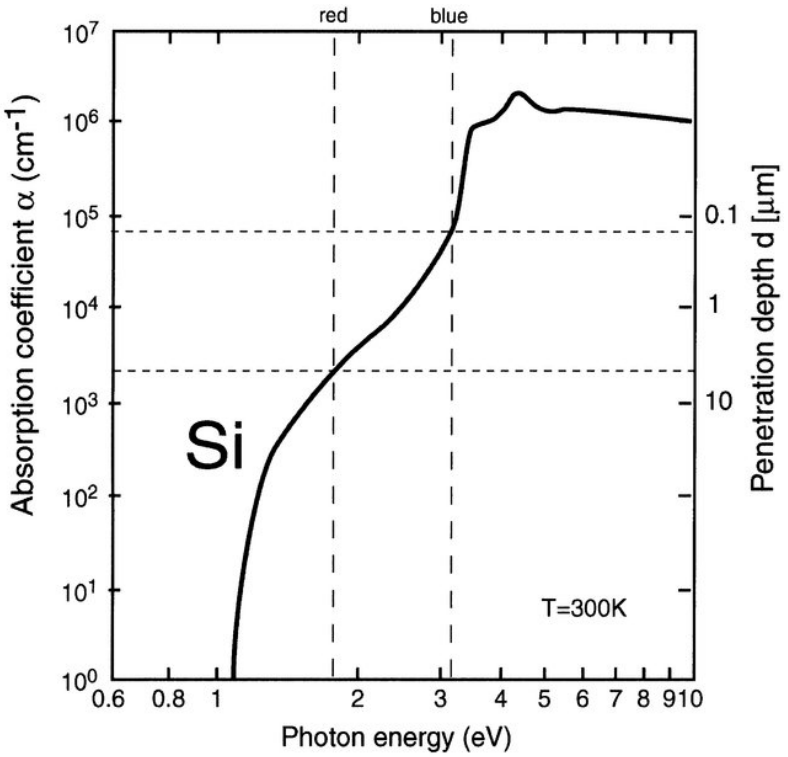

Fig. 56 Absorption coefficient and penetration depth of light in Silicon.

where α is the light penetration depth, which is a function of the wavelength. Its value for every wavelength (i.e. every energy photon level) is taken from the work of De Graaf et. al [58]. s_n and s_p are respectively the surface recombination velocity in the base and the emitter, and considered to be equal to 10 and 1 m/s respectively from the work of Vaillon et al. [25].

In agreement with the work of Yang et al. [32], the total IQE is the sum of the contributions of these parts:

$$IQE = IQE_p + IQE_n + IQE_d \tag{85}$$

Knowing all the factors in Eq. (78), the photo-current I_{ph} is estimated numerically by the midpoint rule.

As we are mainly interested by estimating the maximum electrical power, some additional assumptions ca be made. In silicon PV cells, it can be considered that the shunt resistance R_{sh}

reaches high values. Thus, the current and voltage relationship in Eq. (70) can be simplified and it can be defined as:

$$I = I_{ph} - I_0 \left(\exp\left(\frac{q_e (V + IR_s)}{k_B A T} \right) - 1 \right) \tag{86}$$

Now, with the relation defined in Eq. (85), the two particular operating points (corresponding to the maximum current and voltage produced) can be calculated more easily. The maximum current produced by a PV cell is called the short-circuit current (denoted I_{sc}) and it is obtained when the voltage is equal to zero (i.e. $V = 0$).

From Eq. (85), it can be assumed that the short-circuit current is close to the photo-current, $I_{sc} \approx I_{ph}$. The maximum voltage produced by a PV cell is called the open-circuit voltage (denoted V_{oc}) and it is obtained when the current is equal to zero (i.e. $I = 0$).

When the current is taken equal to zero, the current and voltage relationship in Eq. (85) leads to the following expression:

$$V_{oc} = \frac{k_B A T}{q} \ln\left(\frac{I_{ph}}{I_0} + 1 \right) \tag{87}$$

Next, the fill factor appearing in the expression of maximum electrical output power, Eq. (58) must be defined. A commonly used and accepted expression for the fill factor in the case of silicon solar cells is the one proposed in the work of Green [59] and is expressed by:

$$FF = \frac{V_n - \ln(V_n + 072)}{V_n + 1} \tag{88}$$

where V_n is the normalized voltage and it is defined by:

$$V_n = V_{oc} \frac{q}{k_B A T} \tag{89}$$

3.2.4. Implementation in MATLAB

In the present work, the different models were linked following a loosely coupled approach. This approach gives accurate results with a reasonable computational time. In a loosely coupled approach, the different physical aspects of the simulation are treated as independent problems. The optical, electrical and thermal models explained in the subsections above were solved using a script written in the commercial software MATLAB®. The simulation algorithm of the PV panel behavior is schematically presented in Fig. 38. The three main parts of the script structure (optical, electrical and thermal) can be viewed in Fig. 38.

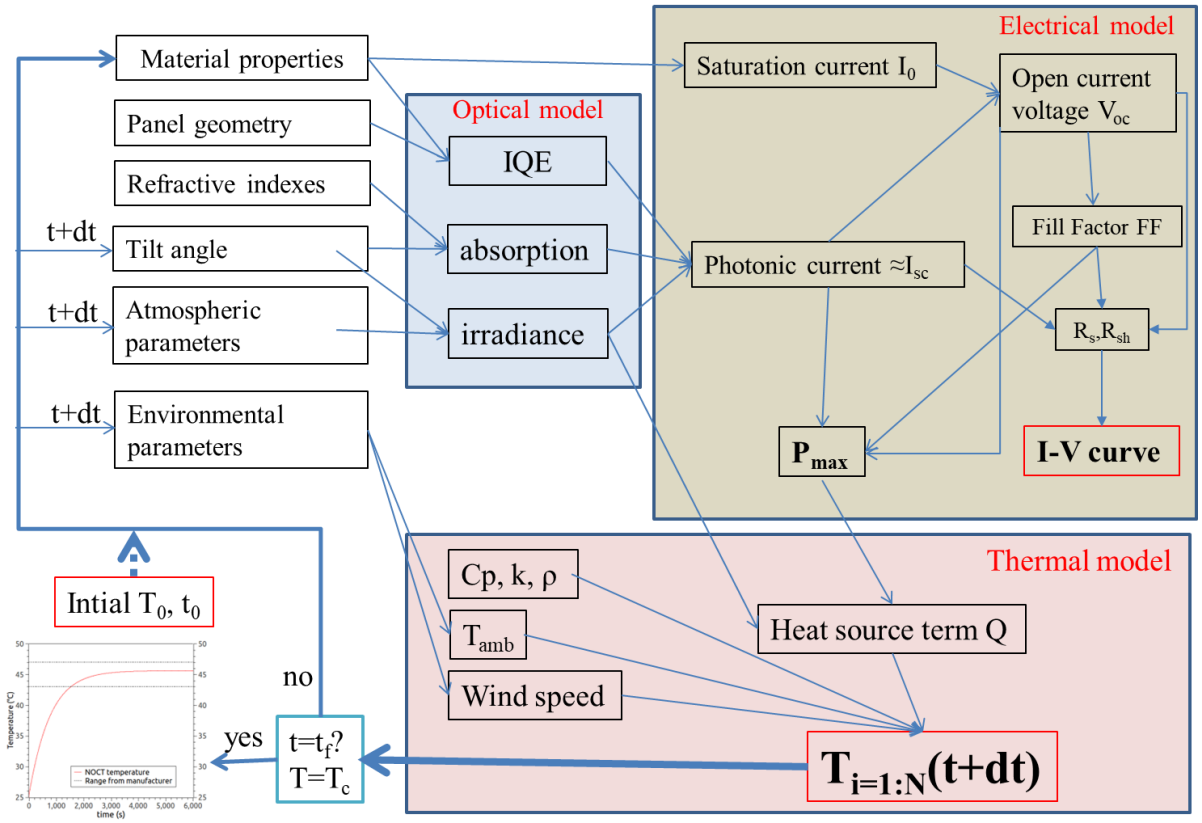

Fig. 57 Structure of the algorithm implementation in MATLAB® software.

The input data are the PV panel geometry (number of the layers and their thicknesses), materials' properties, the tilt angle and environmental parameters (such as ambient temperature, wind velocity, etc.).

At each step of time increment, the solar irradiance on the panel is first imported from an input file (in-field data) or determined using the model proposed by Bird [54]. Then, the absorption coefficients of each layer of the PV panel are computed with the optical model. Afterwards, the internal quantum efficiency IQE, the saturation current I_0, the photo-current I_{ph}, the open current voltage V_{oc} and the fill factor FF are predicted using the electrical modeling. The maximum electrical power is next determined. It should be mentioned that in this work the electrical output power is assumed to be equal to the maximum electrical power.

In the thermal analysis, the heat source terms inside each layer are first estimated. Next the heat equation is solved and the temperature distribution inside the PV panel is updated. At the next time increment, the updated temperatures from the thermal model are used to calculate the new values of materials' properties. This process is repeated in an iterative manner until the final time step is achieved.

3.3. Results and discussion

3.3.1. Preliminary results / Models Validation (under STC and NOCT conditions)

3.3.1.1. Geometries and material properties

In order to validate the different physical models discussed above and the proposed coupling method, preliminary simulations were made in standard test conditions (STC) and in nominal operative cell temperature condition (NOCT). These conditions were chosen since they are used by manufacturers to test their PV panels. The characteristics are provided in the data sheet edited by PV panel manufacturers.

Three commercial silicon-based PV panels were considered in this work. These are the monocrystalline VSMS275 [60] produced by VOLTEC Solar and the polycrystalline BP350 [61] and the monocrystalline BP585 [62] both produced by BP Solar. The thickness and the material properties (such as density, thermal conductivity and specific heat capacity) of each layer of the studied PV panel are listed in Table 4 for BP350, Table 5 for BP585 and in Table 6 for VSMS275.

The data listed in Tables 4-6 are taken from the data sheet provided by the manufacturers or from existing works in the literature. In order to decrease computational costs, the material properties of the different PV panel layers (Tables 4-6) are assumed to be isotropic and temperature independent.

Table 7: Layer characteristics of BP350 PV panel (taken from Armstrong et al. **[18]**)

Layer	Thickness [mm]	Density [kg/m^3]	Thermal conductivity [W/m/K]	Specific heat capacity [J/kg/K]
Front glass	3	3000	1.8	500
PV-cell	0.225	2330	148	677
EVA	0.5	960	0.35	2090
Tedlar	0.1	1200	0.2	1250

Table 8: Layer characteristics of BP585 PV panel (taken from Aljoaba et al. **[51]**)

Layer	Thickness [mm]	Density [kg/m^3]	Thermal conductivity [W/m/K]	Specific heat capacity [J/kg/K]
Front glass	3	3000	1.8	500
PV-cell	0.3	2330	148	677
PES/Tedlar	0.5	1200	0.35	1250

Table 9: Layer characteristics of VSMS275 PV panel (taken from Weiss et al. **[26]**)

Layer	Thickness [mm]	Density [kg/m^3]	Thermal conductivity [W/m/K]	Specific heat capacity [J/kg/K]
Front glass	4	3000	1.8	500
EVA	0.46	960	0.35	2090
PV-cell	0.2	2330	148	677
EVA	0.46	960	0.35	2090
Tedlar	0.3	1200	0.2	1250

3.3.1.2. Optical model predictions

The first task in the implementation of the multi-physics modeling is to predict the absorption probabilities, $a_j(\lambda)$ in Eq. (55), in the different layers of the studied PV panel. In the proposed optical modeling which is based on a Markov chain process, the transition matrix elements are functions of the optical properties of the different layers of the studied PV panel. The optical properties (surface reflectance R_j and absorption coefficients A_j) have to be defined as a function of the wavelength and the temperature.

The percentages of photons absorbed in each PV panel layer are presented in Fig. 39a for the BP panels and in Fig. 39b for VSMS275 PV panel. Since both panels produced by BP solar have the same number of layers and are composed with the same materials, the predicted percentages of photons absorbed in each layer are the same.

As expected, the PV-cell absorbed the major part of the photons that hit the PV panel. The glass and insulation layers absorbed each roughly 5% of the photons hitting the PV panel. In Fig. 39, the absorption in the cell is interrupted when the wavelength reaches the value λ_2 corresponding to the lowest energy absorbed by the cell (which is equal to the band gap energy E_g of silicon).

The band gap energy of silicon depends on the temperature, so that the absorption profile will change for every calculated PV-cell temperature with the thermal model.

From Fig. 39, the absorption coefficient of each layer $a_j(\lambda)$ is determined for all the range of useful wavelengths $(\lambda_1 - \lambda_2)$.

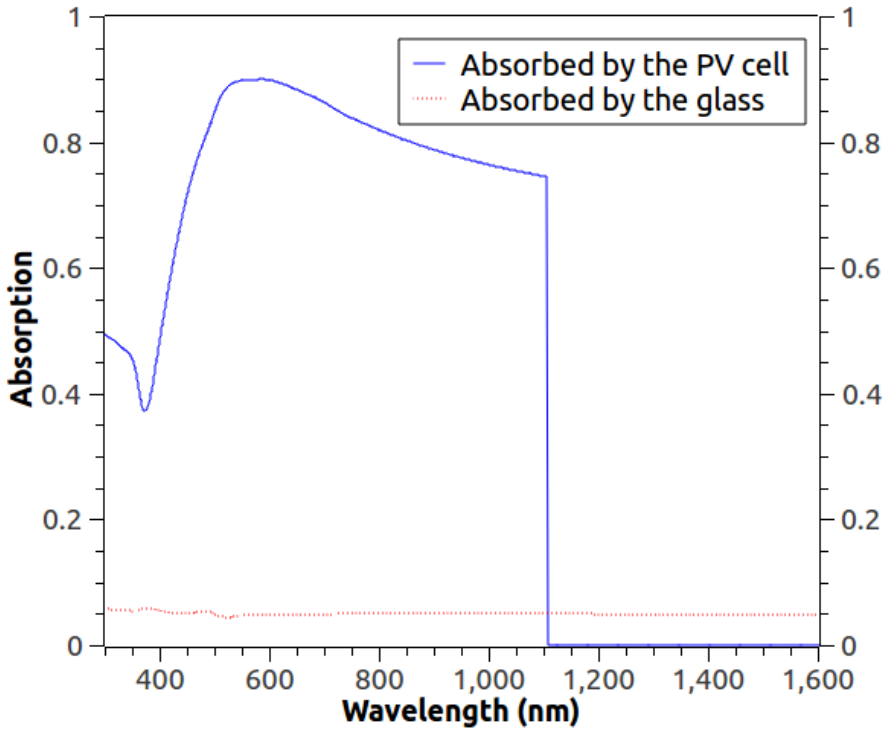

(a)

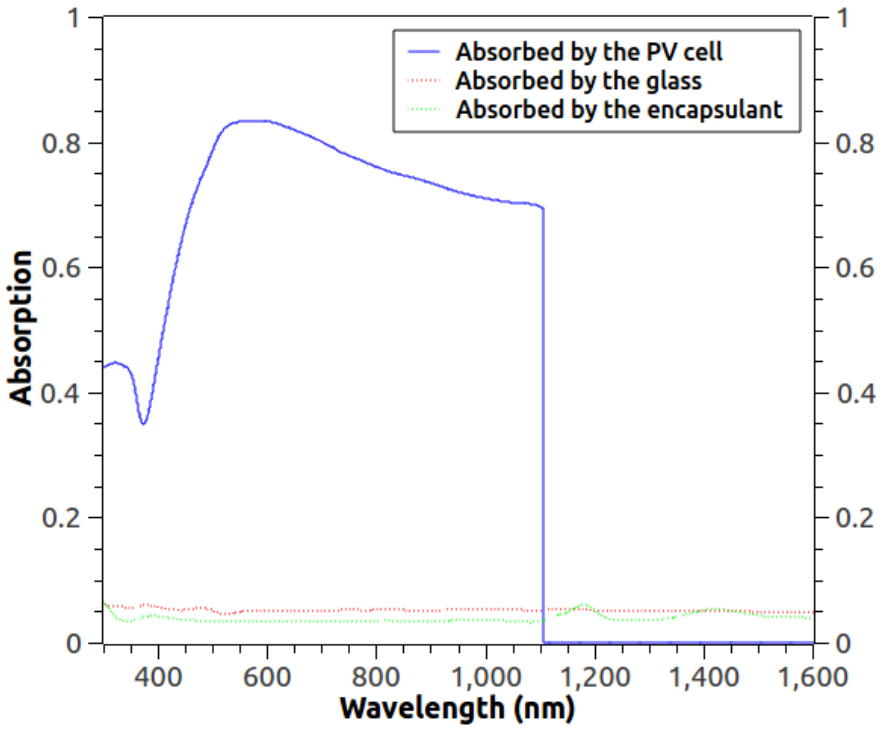

(b)

Fig. 58 Percentages of photons absorbed by the layers of the PV panel as a function of the wavelength for BP350 and BP585 panels (a) and VSMS275 panel (b).

3.3.1.3. Electrical model predictions

The electrical behavior of a PV panel is known by its manufacturer. To inform the customers, the manufacturer provides basically the $I-V$ curves and some tables with the range of current and voltage available for the load connected to the PV panel at any given moment.

These data are usually provided in the data sheet at some reference conditions, typically at STC. Thus, the electrical model has to be calibrated on the operating points found in the data sheets. The calibration process starts by identifying the total internal quantum efficiency IQE defined in the Eq. (84), and next the electrical parameters, like the series and shunt resistances R_s and R_{sh} respectively, defined in Eq. (85).

As mentioned before, the total internal quantum efficiency $IQE(\lambda)$ was calculated with the approach proposed in the work of Yang et al. [32]. Since the thickness of the PV cell layer is

different for each studied PV panel, the total internal quantum efficiency was computed separately for the three PV panels. The IQE curves as a function of the wavelength are plotted for each commercial PV panel in Fig. 40 for a temperature of 25°C. it can be seen that the differences caused by the thickness differences are negligible.

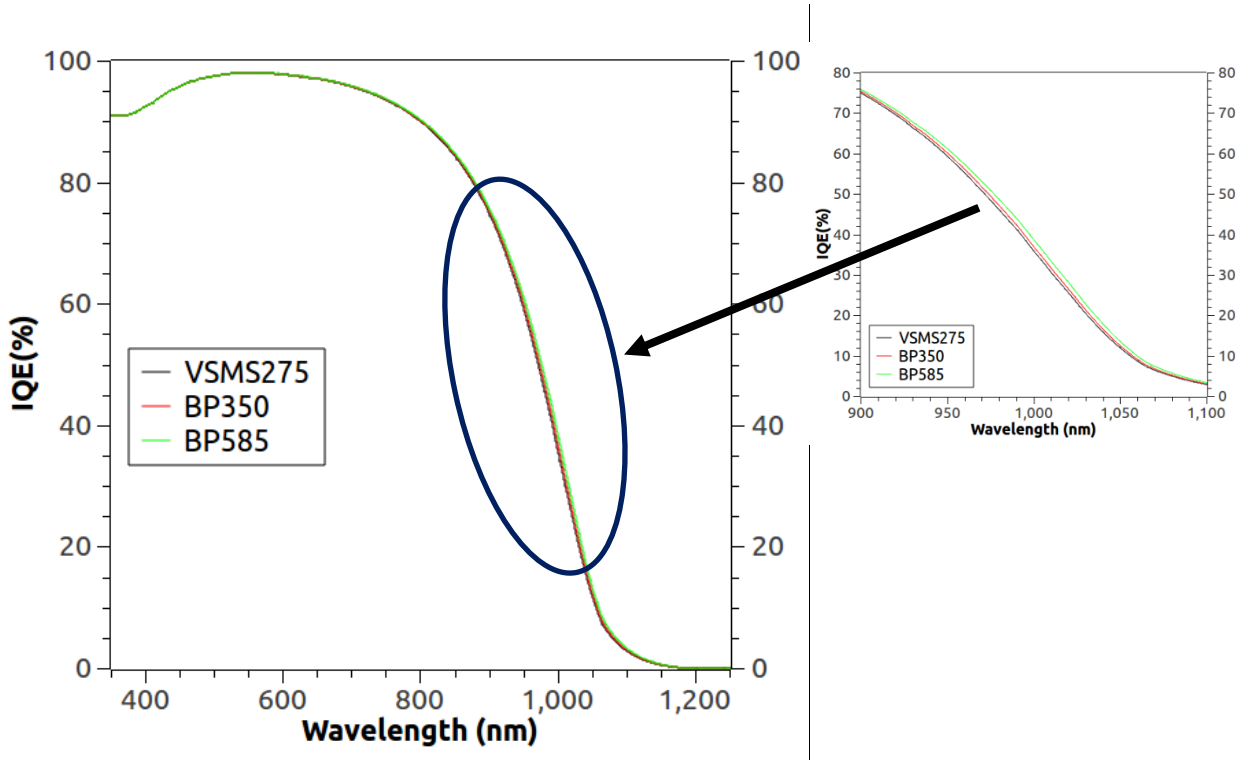

Fig. 59 Total internal quantum efficiency predicted for the three commercial PV panels: BP350, BP 585 and VSMS275.

Since the $IQE(\lambda)$ curves are quite similar for the three commercial PV panels, only the $IQE(\lambda)$ curves calculated for VSMS275 PV panel are presented thereafter. For validation purposes, the $IQE(\lambda)$ was also calculated using the PC1D software [31]. The $IQE(\lambda)$ curve predicted by PC1D software [31] is plotted in Fig. 41 as well as the curve predicted with Eq. (84) taken from the work of Yang et al. [32] .

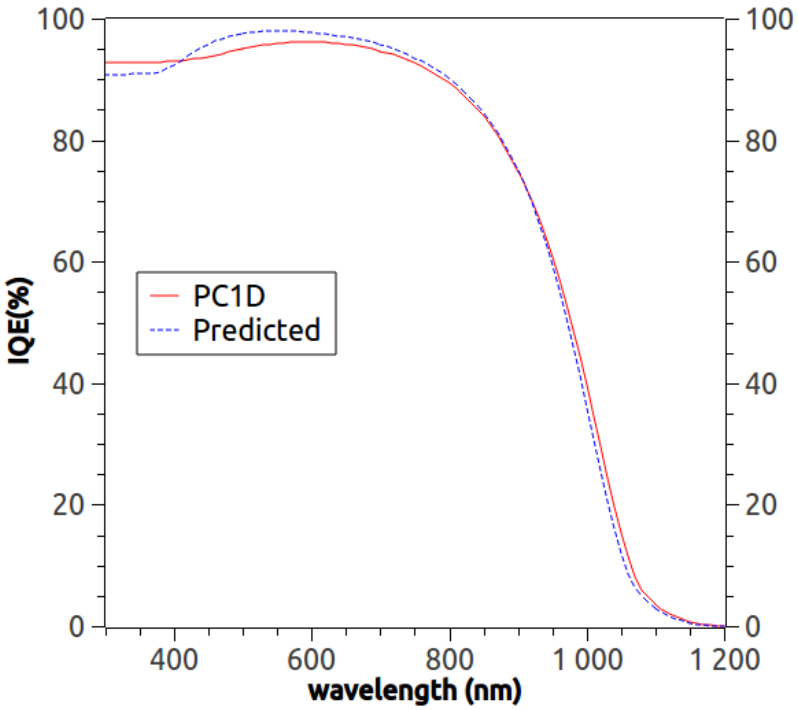

Fig. 60 Total internal quantum efficiency predicted for the VSMS275 PV panel at 25°C as a function of the wavelength.

The influence of temperature on the total internal quantum efficiency $IQE(\lambda)$ was investigated. Three temperature values were chosen to cover the range of working temperatures. These values are: $0°C$ (corresponding to a cold climate), $25°C$ (corresponding to Standard Test conditions, i.e. STC) and $50°C$ (corresponding to a hot climate).

The $IQE(\lambda)$ curves for three temperatures values are plotted in Fig. 42 for VSMS275 PV panel. It can be concluded that the usual temperatures that are observed for the PV panels during the day does not influence significantly the values of $IQE(\lambda)$. The same trend was predicted for both BP350 and BP585 PV panels.

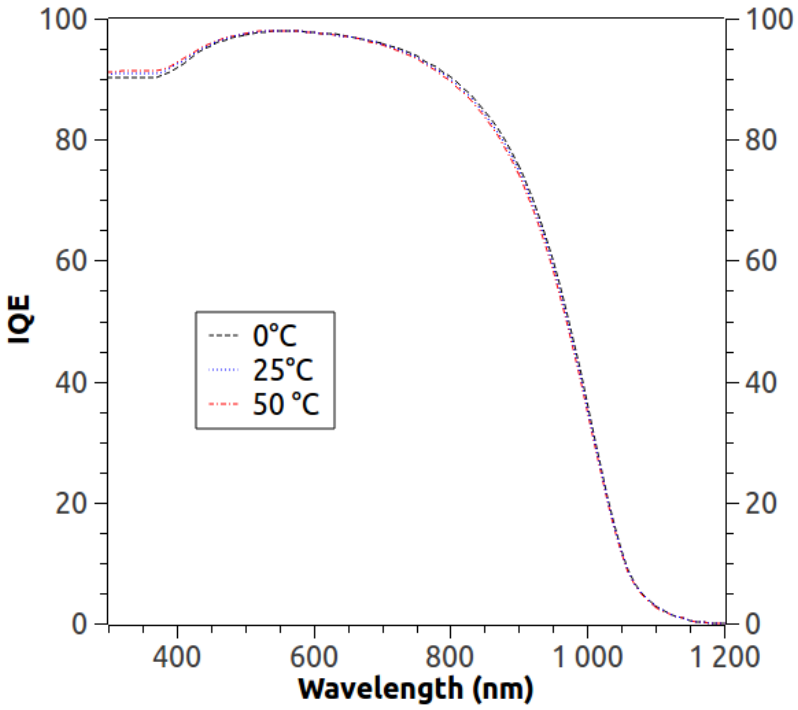

Fig. 61 Influence of the temperature on the internal quantum efficiency of the cell.

The electrical series and shunt resistances, R_s and R_{sh} respectively, defined in Eq. (70) can be computed using an optimization method like the one proposed in the work of Sanchez-Barroso et al. [21]. But, in this work, they were identified with the method proposed in the work of Tsai [36]. Taking their $I - V$ curves at STC (i.e. $25°C$) from their respective data sheets, series and shunt resistances were identified for each PV panel.

The values found for the series R_s and shunt R_{sh} resistances which are used in the electrical model (Eqs. (85-87)) are listed in Table 7 for the three studied panels. It should be noted that the PV cells in the BP350 panel are arranged in two parallel rows of 36 cells, whereas the BP585 panel and the VSMS275 panel have respectively 32 and 60 cells in series.

Table 10: Resistances values obtained for the studied PV panels

Panel	R_s(ohm)	R_{sh}(ohm)
BP350	0.0293	10.8816
BP585	0.0076	46.2223
VSMS275	0.0054	3.9014

Knowing the total internal quantum efficiency IQE as a function of the wavelength, the values of the series and shunt resistances and the absorption coefficient of the PV-cell $a_{cell}(\lambda)$ from the optical modeling, the $I-V$ curves for the three commercial PV panels can be plotted using Eq. (85). For each studied PV panel, the $I-V$ curves are plotted in Fig. 43 are computed for constant solar irradiance of 1000 W/m² and for different temperatures.

When they are available, some points extracted from the data sheets provided by the manufacturers of the panels are added in Fig. 43. As expected, the predicted $I-V$ curves are close to the points taken from the data sheets edited the PV panels manufacturers; and this is also true for the different operating temperatures tested.

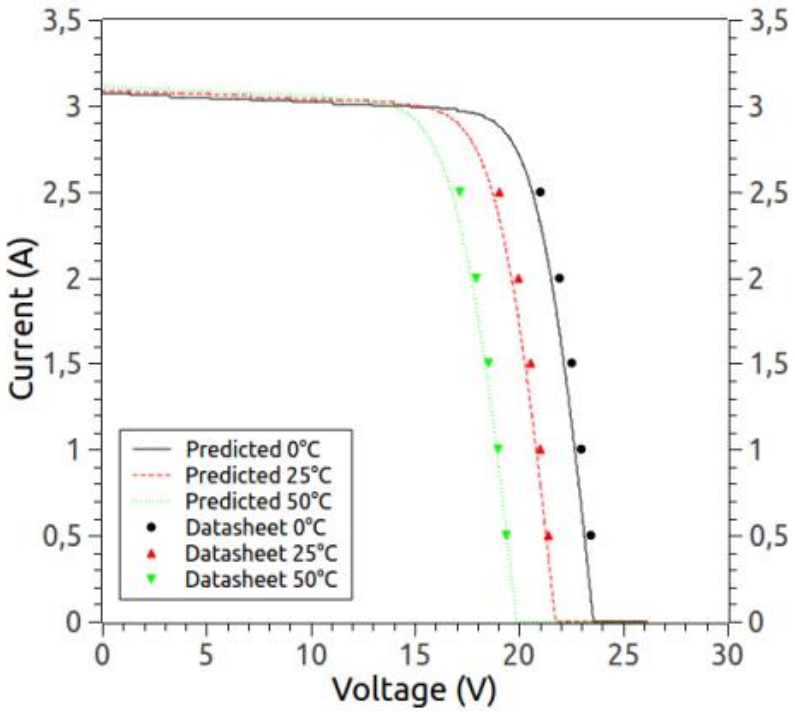

(a)

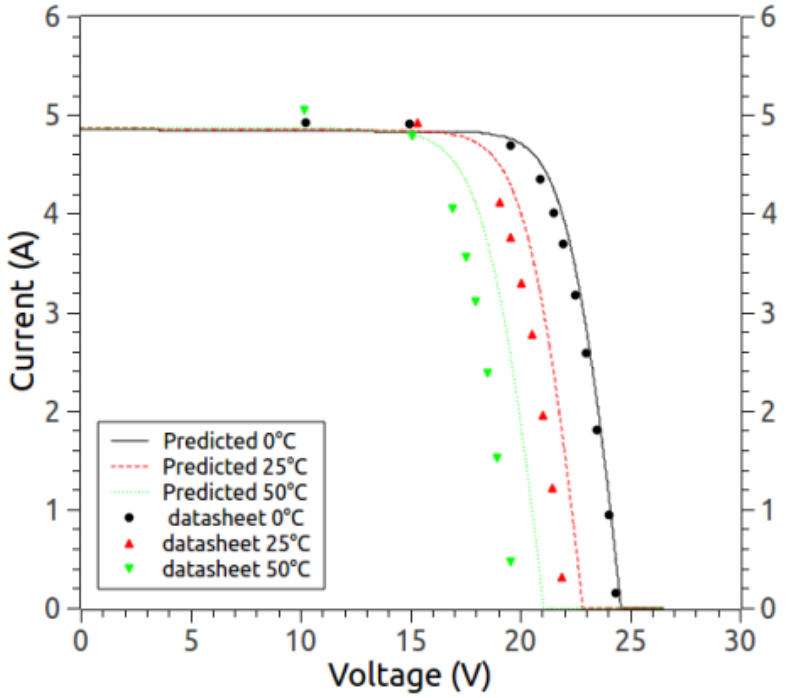

(b)

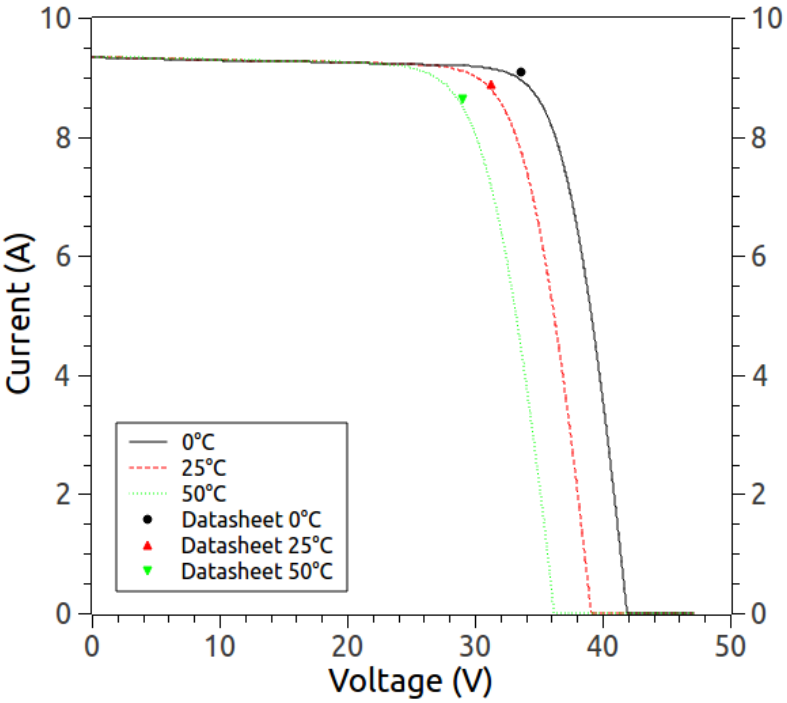

(c)

Fig. 62 $\boldsymbol{I-V}$ curves predicted at different operating temperatures for: BP350 panel (a), BP585 panel (b) and VSMS275 panel (c). Results from panels' data sheets are also reported for comparison.

The electrical performance of the PV panel can also be described basically by the power versus voltage curve (i.e. $P-V$ curve). Moreover, the maximum power point can be clearly distinguished in the $P-V$ curve. For each studied panel, the $P-V$ curves are plotted in Fig. 44.

The $P-V$ curves shown in Fig. 44 were computed at a constant solar irradiance (1000 W/m²) and for different temperatures. The maximum power points taken from the data sheet provided by the manufacturers are also added in Fig. 44. The predicted values of maximum electrical power were reported in Table 8, along with the values taken from the data sheets provided by the manufacturers.

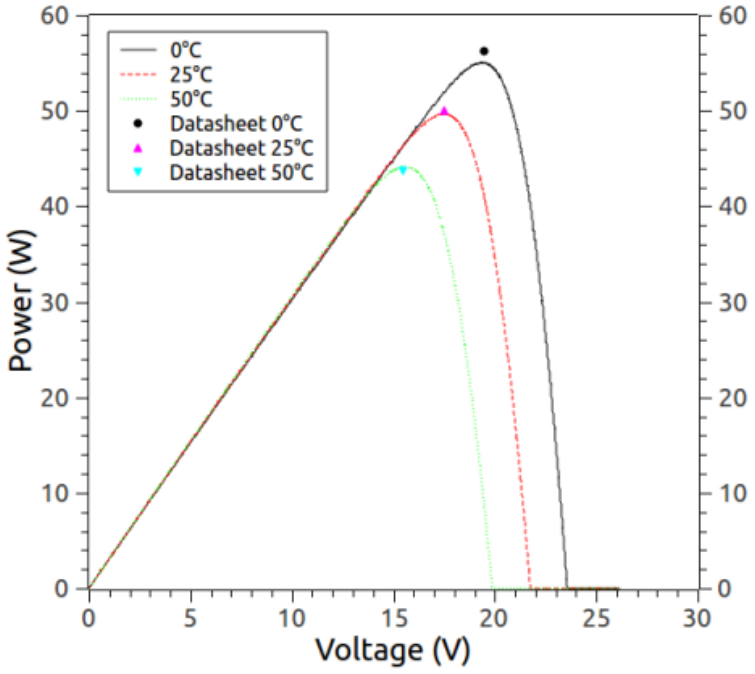

(a)

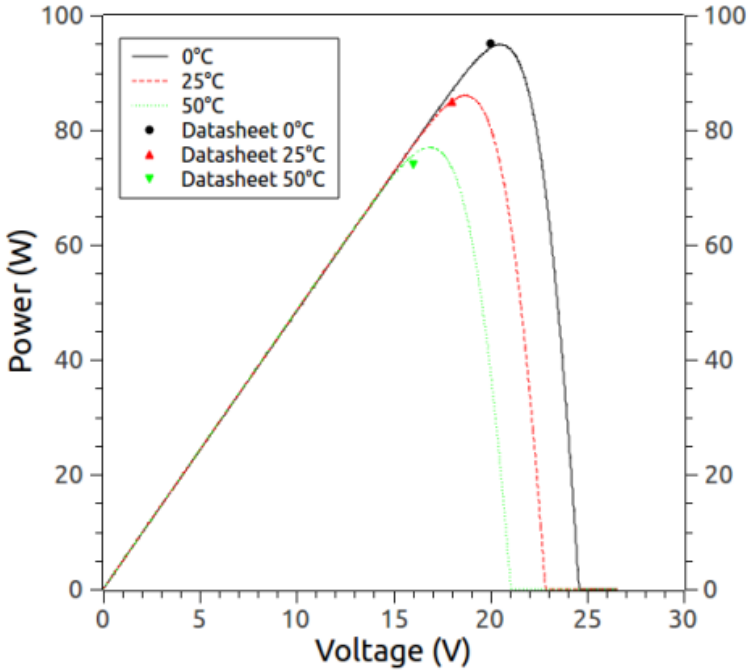

(b)

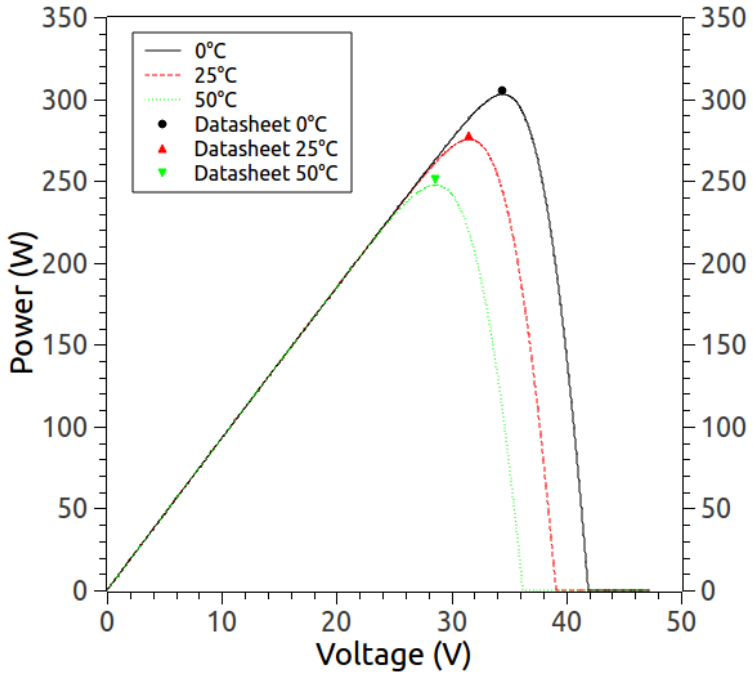

(c)

Fig. 63 P-V curves predicted at different operating temperatures for : BP350 panel (a), BP585 panel (b) and VSMS275 panel (c). The maximum power given by the panels' data sheets are also shown.

From Fig. 44 and Table 8, it can be said that the numerical predictions of the proposed electrical model are in close agreement with the data provided by the manufacturers. Therefore, it can be concluded that the proposed electrical model captures with a fair agreement the electrical behavior of the three studied commercial PV panels and also that the electrical modeling is well implemented.

Table 11: Maximum power point values obtained for the different PV panels

	Panel	**Data sheet**	**Predicted**
P_{max} **(W)**	BP350	50	49
	BP585	80	82
	VSMS	203	185

3.3.1.4. Thermal model predictions

One of the objectives of the work is to predict the temperature distribution through all the panel thickness, taking into account the environment conditions in time. In this work, it as chosen to validate the proposed thermal modeling by comparing the predicted Nominal Operating Cell Temperature (NOCT) with the one provided by the PV panel manufacturers. The PV panel manufacturers determine the NOCT in field conditions or measure it in controlled laboratory conditions.

In accordance with the IEC 61215, the NOCT is defined as the temperature reached under the conditions defined below:

- Irradiance=800 W/m²,
- Ambient temperature=20°C,
- Wind speed=1m/s,
- Open circuit conditions.

The terrestrial solar spectrum at NOCT irradiance is given by the standard ASTM G173-03. Those conditions are kept constant during the entire test simulations. With the help of optical and electrical models, the heat generation terms Q in the heat equation (Eq. (48)) were estimated for each layer of the PV panels. In the thermal model, the wind velocity was kept constant and equal to 1 m/s on the front side of the panel.

At t=0, the temperatures on the front and rear sides of the PV panel were assumed equal to the ambient temperature (20°C). The heat equation (Eq. (48)) was solved numerically with the finite difference (FD) approach presented in the sections above.

For the three studied PV panels, the FD simulations were carried out with an FD mesh equally spaced through the PV panel thickness ($\Delta x = 25\mu m$). The number of nodes varies between panels as they have different total thicknesses. the time increment was kept constant for all of them ($\Delta t = 1s$). It was defined that the NOCT is achieved when the panel reaches an equilibrium temperature (or a steady state temperature).

The PV cell temperature was plotted in Fig. 45 for each one of the three commercial PV panels. For all studied panels, the temperature increases until it achieves constant value. After a transient period of 25 minutes for the BP350 and BP585, and 50 minutes for the VSMS275, it can be assumed that the NOCT was achieved. The NOCT range found in the data sheets given by the manufacturers was also added in Fig. 45 (red dashed lines).

The predicted values of temperature when the system reaches its steady state are close to the NOCT values found in those data sheets. It can be thus concluded that the proposed thermal model is validated since NOCT conditions offer a general overview of the multi-physics behavior.

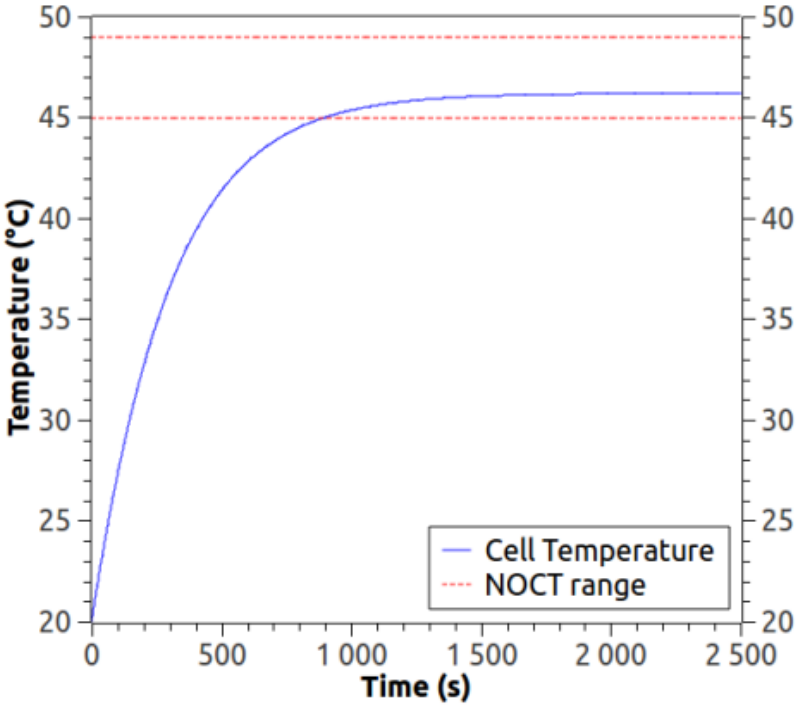
Temperature (°C)
Time (s)
Cell Temperature
NOCT range

(a)

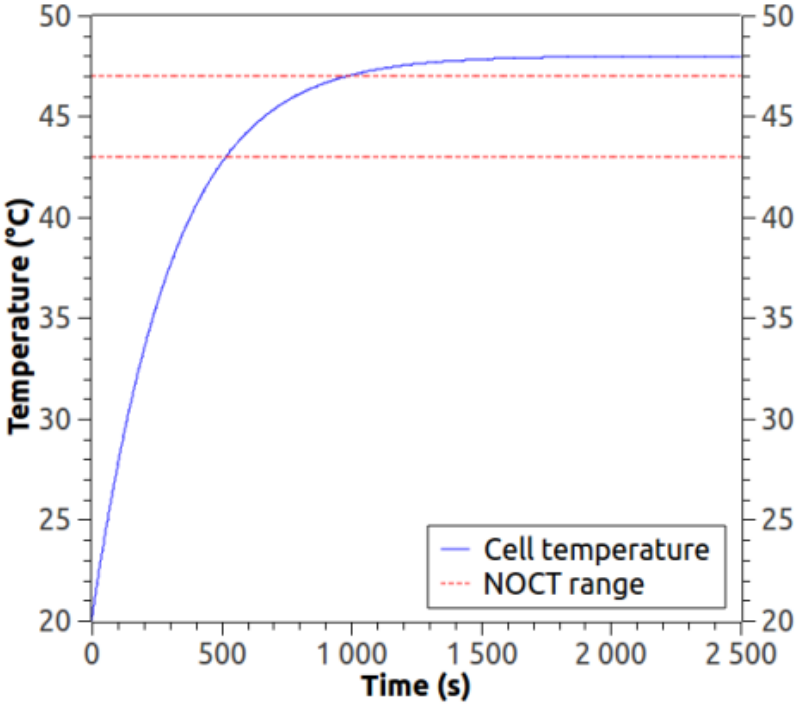
Temperature (°C)
Time (s)
Cell temperature
NOCT range

(b)

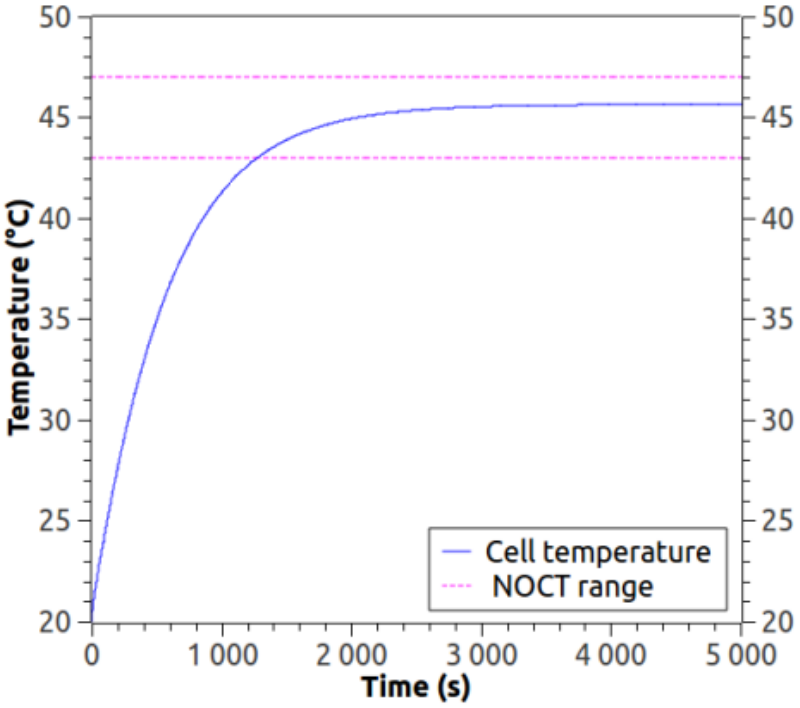

(c)

Fig. 64 Evolution of PV cell temperature at NOCT conditions for: BP350 panel (a),BP585 panel (b) and VSMS275 panel (c).

With the proposed thermal model, the temperature distribution throughout the thickness PV panel can also be predicted. The temperature profiles were plotted in Fig. 46 at the end of the simulation for each one of the three commercial PV panels.

As expected, the highest value of temperature is reached in the PV-cell layer for all the studied PV panels. In all the cases plotted in Fig. 46, the predicted temperature on the front side of the PV panel achieves a lower value than the one on the rear side. This can be explained since, in the FD simulations, the front side of the PV panels is subjected to forced convection while the rear side is subjected to free convection.

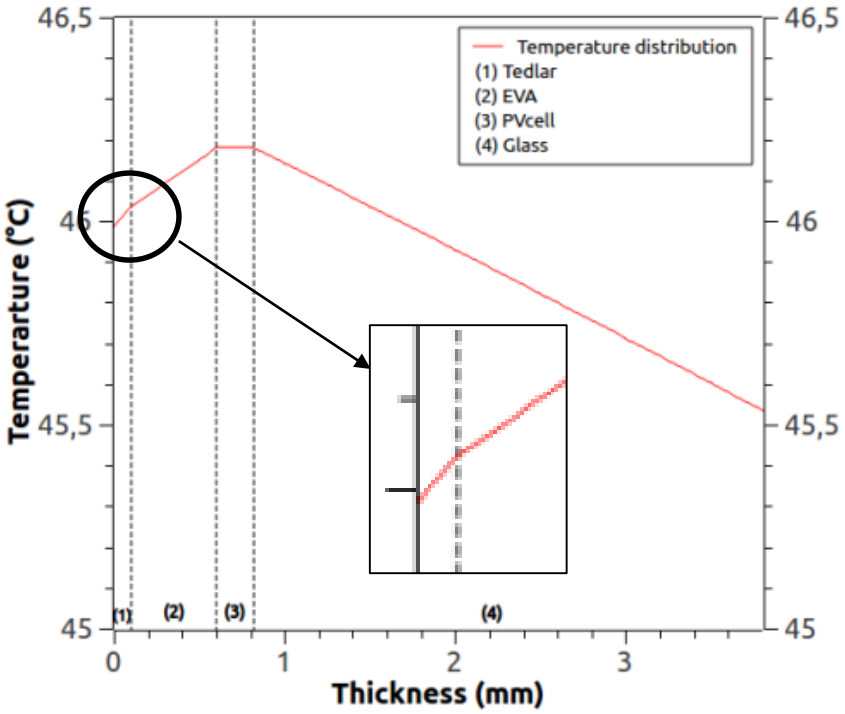
Temperature distribution
(1) Tedlar
(2) EVA
(3) PVcell
(4) Glass
Temperature (°C)
Thickness (mm)
46,5
46
45,5
45
0
1
2
3
(1)
(2)
(3)
(4)

(a)

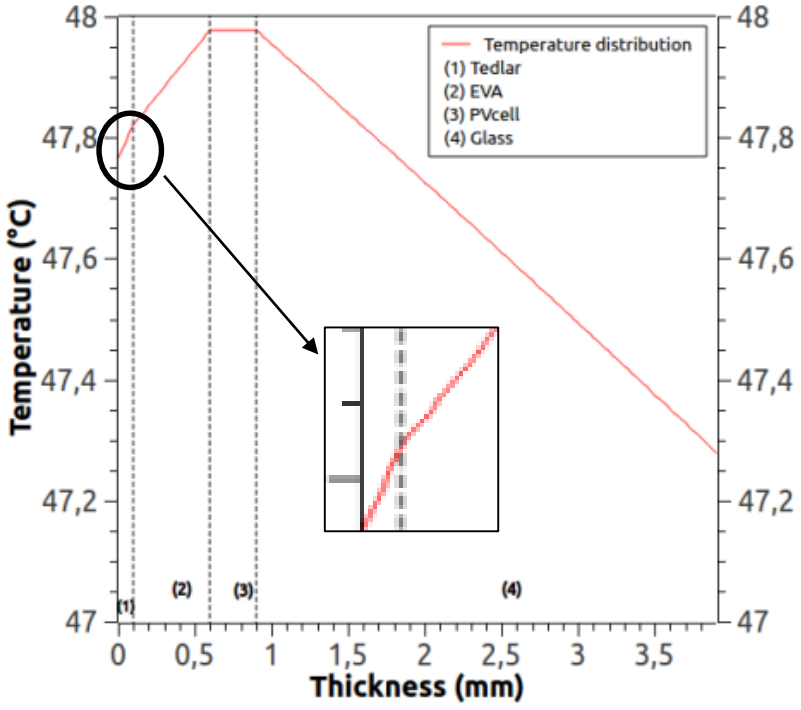
Temperature distribution
(1) Tedlar
(2) EVA
(3) PVcell
(4) Glass
Temperature (°C)
Thickness (mm)
48
47,8
47,6
47,4
47,2
47
0
0,5
1
1,5
2
2,5
3
3,5
(1)
(2)
(3)
(4)

(b)

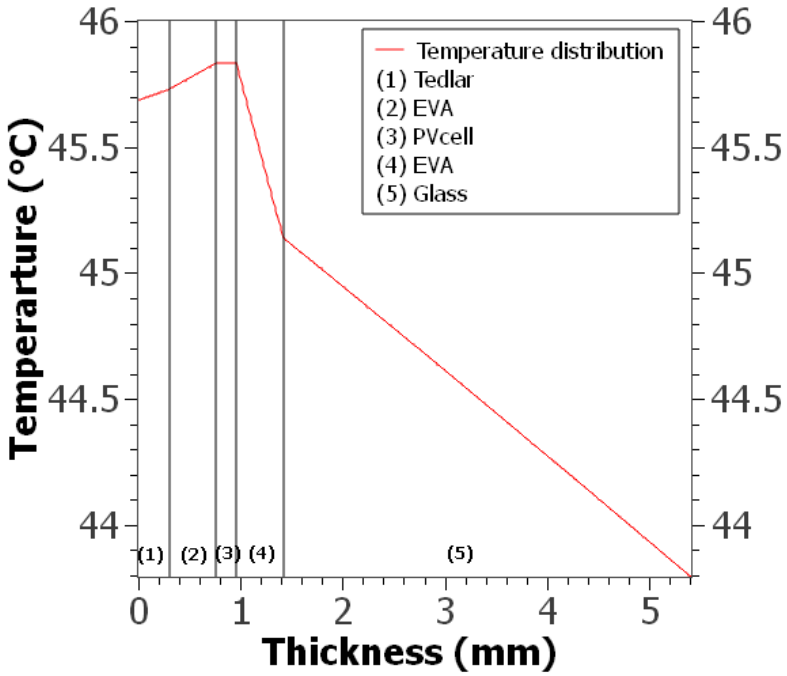

(c)

Fig. 65 Temperature profile at NOCT for: BP350 panel (a),BP585 panel (b) and VSMS275 panel (c).

From the subsections hereinabove, the proposed multi-physics modeling and its implementation in the MATLAB® environment allows us to predict the electrical and thermal behavior of three different commercial PV panels under laboratory test conditions. Finally, it can be concluded that the validation procedure was achieved successfully.

3.3.2. Parametric study: effects of solar irradiance

The proposed multi-physics model was validated by comparison with NOCT values provided by the manufacturers. However, the NOCT laboratory tests do not correspond to real conditions undergone by PV panels. As it is well known, the incident solar irradiance highly modifies the PV panel and cells temperature and also their electrical performance. Thus, the PV panel's temperature needs to be predicted at different levels of incident solar irradiance.

Since the modeling accounts for wavelength effects on the electrical performance of the PV panel, the influence of Air Mass coefficient (i.e. AM) and of the utilization of Sun light concentrators are investigated. For this parametric study, only the PV panel VSMS275 manufactured by VOLTEC SOLAR was considered.

3.3.2.1. Effects of Air mass coefficient

Assuming clear sky conditions, the effects of AM coefficient are first evaluated by taking four different values: 1, 1.5, 4 and 10. The AM coefficient is defined as the path length which light takes through the Earth's atmosphere normalized to the zenith path length (i.e. normal to the Earth's surface) at sea level. The AM coefficient is linked to the Sun elevation angle. Then, AM1 is when the Sun is high in the sky (a Sun elevation angle of 90°) and AM10 is when the Sun is low in the sky (a Sun elevation angle of 5°).

For all values of AM coefficient, the global solar irradiances were estimated with the solar spectral model proposed by Bird [54]. The chosen location is Strasbourg (France) and the date is the 15th of May 2015 (corresponding to a clear sky day. The predicted solar spectral irradiances are presented in Fig. 47.

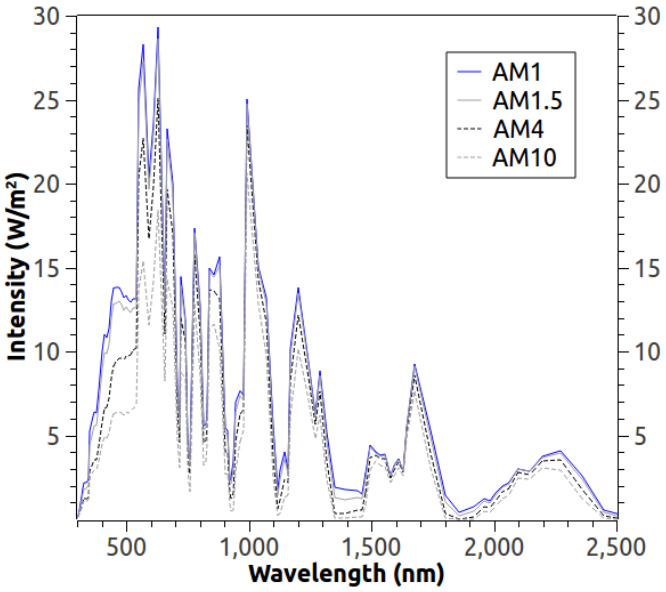

Fig. 66 Solar spectral irradiance for different values of AM coefficient (for Strasbourg, France, on May 15th, 2015).

The other boundary conditions for the thermal model are the same as in NOCT simulations. Thus, the wind speed was kept constant and equal to 1 m/s and the temperatures on the front and rear sides of the panel were taken equal to the ambient temperature (20°C) at t=0.

The numerical simulations were stopped when the thermal behavior of the PV panel reached its steady state. The temperature distributions through the PV panel thickness predicted for the different values of AM coefficients are presented in Fig. 48.

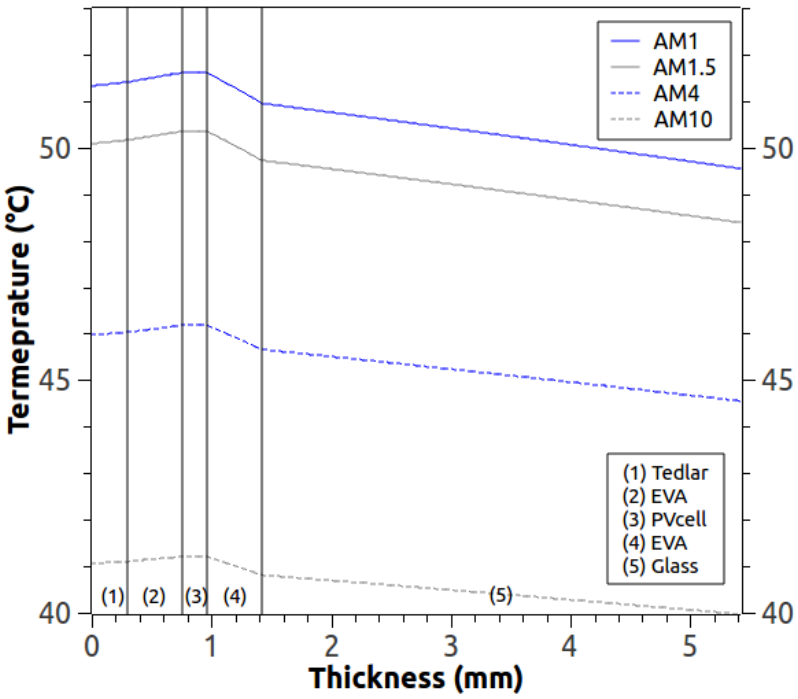

Fig. 67 Temperature profiles predicted for different AM coefficients.

As the Sun moves down toward the horizon, the AM coefficient increases and consequently, the solar irradiance level decreases. As it was expected, the temperature of the PV panel decreases as the AM coefficient increases as it can be seen in Fig. 49. The predicted values of output electrical power and of efficiency reached when the PV panel achieves its steady state are reported in Table 9.

Table 12: Electrical and thermal response of the panel with different air mass values

	AM1	AM1.5	AM4	AM10
PV cell temperature [°C]	51.6	50.4	46.2	41.2
Output power [W]	119	114	96	73
Efficiency [%]	8.79	8.85	9.04	9.22

The PV-cell temperature decrease implies an increase of its efficiency (see Table 9). However, even if the PV-cell efficiency slightly increases, the electrical output power sharply decreases when the AM coefficient increases. Consequently, in Table 9, the maximum value of output electrical power is obtained for AM1 as it was expected for silicon solar cells.

3.3.2.2. Effects of concentrated solar irradiances

One can think that it is possible to improve PV-cell efficiency by using mirrors that concentrate solar light to PV-cells. That is the reason why simulations were performed for different light intensities also called the number of suns.

In this work, the simulations were performed for four values: 1 Sun, 2 Suns, 3 Suns and 4 Suns. Higher values of Suns number were not simulated since the temperature reached for the material of the insulation layer would exceed its melting temperature. The value of 1 Sun corresponds to the standard solar irradiance at AM1.5. The parameters for the solar spectral model of Bird [54] were kept constant.

The irradiances computed for different Suns values are not presented since the wavelength distribution is not affected by increasing the light intensity. The predicted temperature of the PV-cell is plotted in Fig. 49 for the different values of Suns number. As expected, the PV-cell temperature increases as the Suns number increases. In Fig. 49, the evolution of PV-cell temperature reaches a constant value for time values higher than $1500s$. That means that the PV panel reaches a steady state. The numerical simulations were stopped when the thermal behavior of the VSMS275 PV panel reached its steady state.

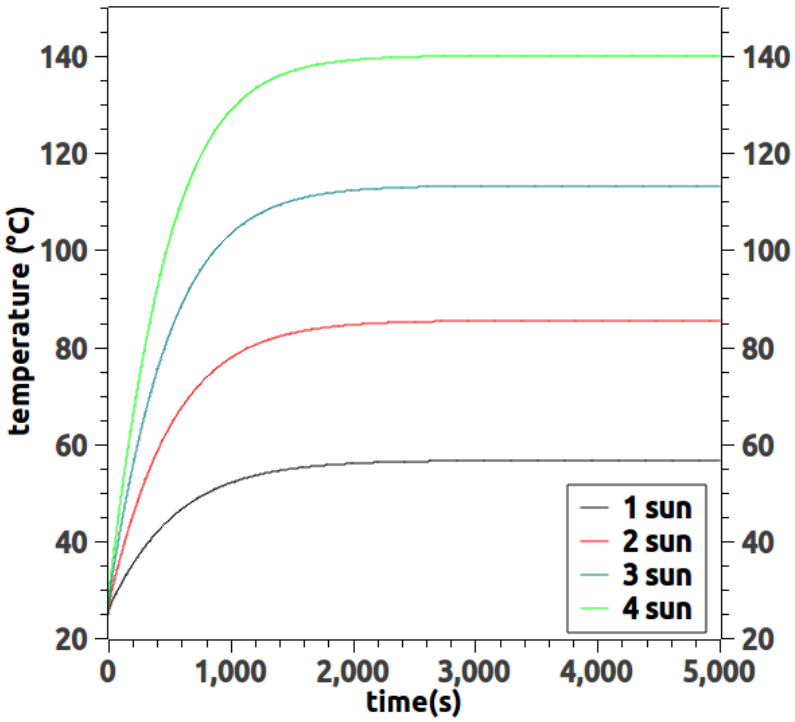

Fig. 68 Evolution of PV cell temperature under NOCT conditions.

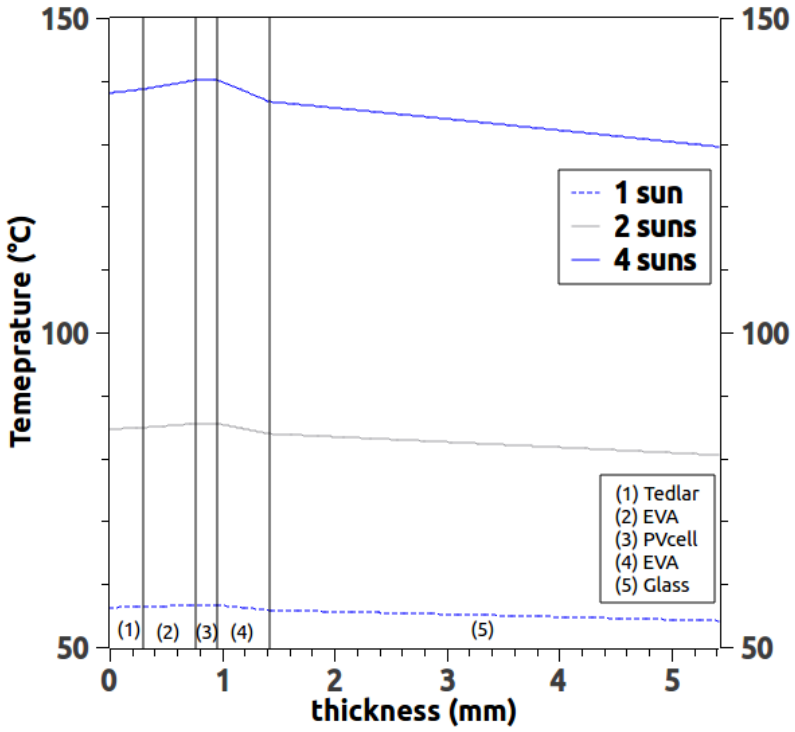

Fig. 69 Temperature profiles predicted for different light intensities.

Afterwards, the temperature distributions through the PV panel thickness predicted for the different light intensities are presented in Fig. 50. As expected, the predicted temperature inside the PV panel sharply increases when the number of Suns increases.

It should be noted that the melting temperature of EVA (material of insulation layer) is close to $120°C$. Consequently, from Fig. 49, Suns values higher than 2 Suns can lead to damage in the insulation layers.

The electrical behavior of the PV panel was also investigated. The time-related evolution of electrical power and of efficiency are plotted for the different values of light intensity in Figs. 51 and 52. As for the PV-cell temperature in Fig. 49, the electrical output power and the efficiency reach constant values for time values higher than $1500s$.

From Figs. 51 and 52, the electrical output power seems to increase when Suns value increases as long as Suns value stays below 3 suns. However, the efficiency of the studied PV panel sharply decreases as Suns value increases. To summarize the predictions of the multi-physics model, different parameters such as PV-cell temperature, fill factor FF computed with Eq. (87), electrical output power and PV-cell efficiency are reported in Table 10.

Table 13: electrical and thermal response of the panel with different sun concentrations

	1 Sun	2 Suns	3 Suns	4 Suns
PV cell temperature [°C]	56.6	85.5	113.3	140.1
Filling Factor FF	0.75	0.72	0.66	0.60
Output power [W]	139	242	258	226
Efficiency [%]	8.55	6.93	5.28	3.71

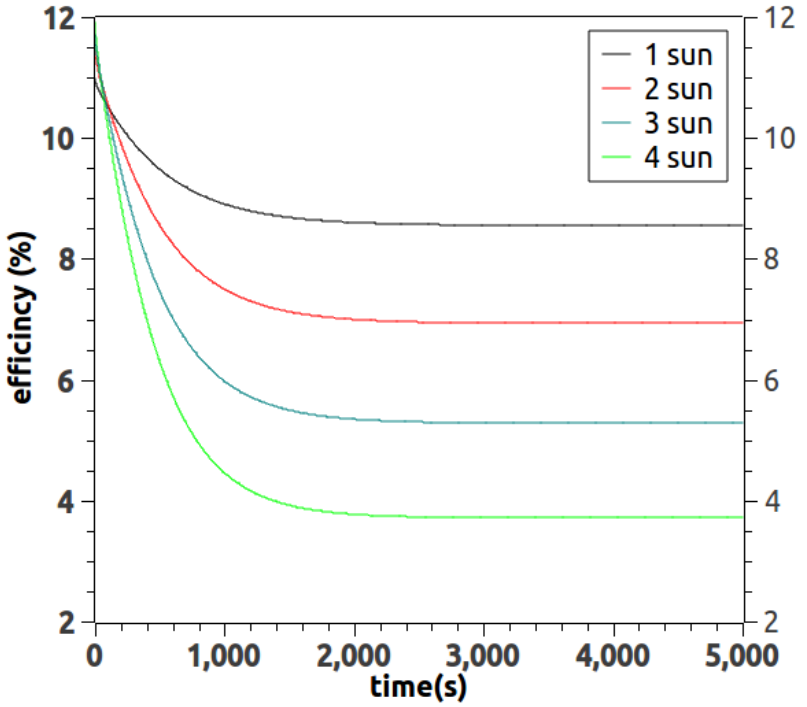

Fig. 70 Evolution of PV efficiency under NOCT conditions.

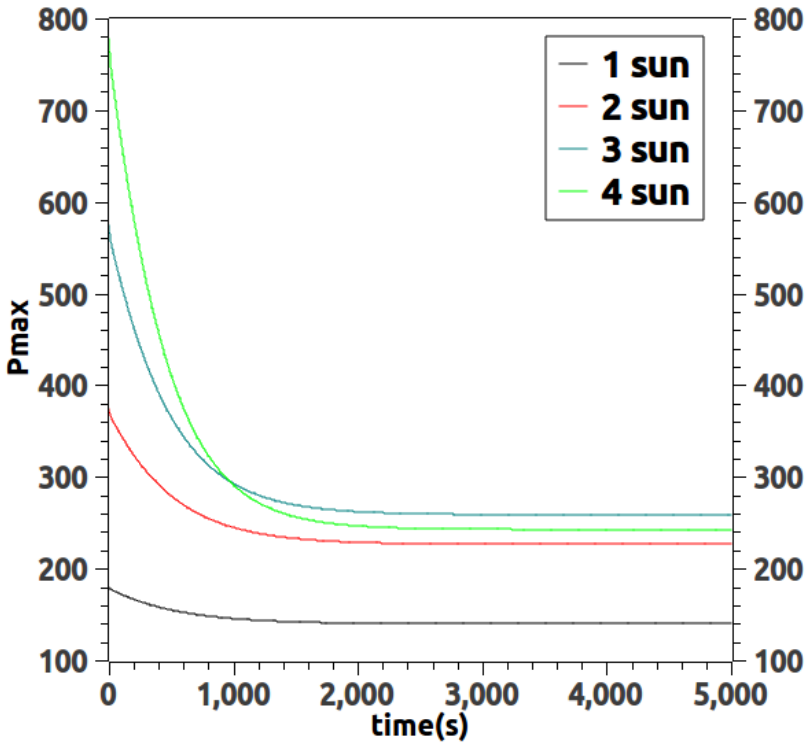

Fig. 71 Evolution of the maximum electrical power under NOCT conditions.

In Fig. 49-52 and Table 10, it is noticeable that the PV panel attains temperature values that are dangerous for some of its components because the insulation layer made of EVA melts at a temperature value near 120°C. Then, a temperature of 140°C is not advisable in these conditions (such as light intensity of 4 Suns). The output electrical power is also noticeably lower for four Suns than for 2 or 3 suns. Even the final output power at the steady state gain between 2 and 3 Suns is very small, and since the three Suns conditions brings the panel to a temperature close to the melting point of the EVA, it is advisable to stay at two Suns.

3.4. Conclusion

In this chapter, a detailed multi-physics modeling is presented for silicon PV panels. It combines an optical, electrical and thermal models.

The optical model was used to determine the total light absorption coefficients of the different layers that composes the PV panel. These coefficients are function of the wavelength and account for optical properties of the materials. The electrical model is based on the equivalent one-diode circuit. It computes the maximum electrical power that can be extracted from the PV panel. The thermal model is based on the classical heat equation and was solved using 1D finite differences approach. These different models were sequentially coupled and implemented in the commercial software MATLAB®.

It should be highlighted that the heat generated in the PV cell layer was evaluated without the use of an empirical efficiency relation. Consequently, the performance of the PV panel is an output and not an input as some works found in the literature. The multi-physics model was next used to predict at a constant temperature the $I-V$ curves and the $P-V$ curves for three commercial PV panels. The predicted values of maximum electrical output power and the predicted $I-V$ curves are in fair agreement with the data sheet values provided by the manufacturers.

Afterwards, it was used to predict the thermal behavior in NOCT conditions. The predicted NOCT values are in the range of the ones given in the data sheets. From the electrical and thermal behavior predicted, it can be concluded that the proposed multi-physics model is validated.

A parametric study was also conducted to investigate the effects of AM coefficient (different Sun elevation angles) and of Sun light intensity on the PV panel behavior. From the predictions, the maximum electrical output power can be reached when Sun light intensity is close to 2 Suns, without approaching melting temperature for the insulation material.

Finally, the model will be used in the next chapter to determine the behavior of PV panels in real meteorological conditions (varying wind speed, temperature and irradiance...).

4. Application of multi-physics modeling: Study of a bifacial panel under real time conditions

4.1. Introduction

From the literature review presented in section 2.2.1, it can be concluded that 1D thermal models are able to predict correctly the behavior of a commercial PV panel under dynamic boundary conditions corresponding to varying field conditions that it experiences (see for instance the works of Armstrong et al. [18] or more recently Sanchez-Barroso et al. [37]).

After preliminary verification of the proposed model under the norms used in PV panels industry, the next step is to validate it under real time conditions, and study how the model fares with changes that could happen every day to the PV panel (like for example the passing of clouds, the drops in temperature, high ambient temperatures, etc.).

In order to study the PV panel behavior under service conditions, it is necessary to provide to the developed multi-physics modeling external time-related inputs such as: incident solar irradiation, wind velocity and ambient temperature.

The Qatar Environment and Energy Research Institute (QEERI) is based in Doha, Qatar. One of the field of investigation is solar energy and its integration within the broader global energy system. The Institute owns outdoor and indoor testing capabilities. The outdoor solar test facility is composed by 35,000-square meter of PV panels and it is located at Qatar Science and Technology Park [63].

Thanks to Professor Ahzi's collaboration, the Institute provided the outdoor input data that were used for the simulations, and also the output of the PV panels (produced electrical power and PV-cells temperature) that were compared to the predicted output of the proposed model in order to validate it.

The present chapter is structured as follows. First, one of the PV panels that is used by QEERI solar test facility is modeled, and its response to NOCT and STC conditions are simulated and compared to the data provided by the manufacturer. Second, the panel was simulated under real time conditions, and the temperature of the panel as well as the output power obtained from the

simulation during one day are compared to the actual temperature and electrical power measured onsite in the test facility.

4.2. PV panel description (materials properties and geometry)

The PV panel considered in this chapter is the VBHN225DJ06 manufactured by Panasonic (henceforth referred to as Panasonic225). It is a bi-facial module, where the back sheet is replaced by a glass layer, to allow the light reflected from the back to be absorbed by the PV panel. For the rest of the components, it is considered to be the same as any usual PV panel. A front cover layer made of glass, and the PV cells surrounded by the insulation layers made of EVA.

Bi-facial PV panels offer the advantage that photo-current can be produced from both sides of the panel. Consequently, total electrical generated power is increased in comparison with a classical mono-facial PV panel. A schematic cross-section view of PV panel that allows us to make out the different layers is presented in Fig. 53. Moreover, to complete the PV panel description, the different useful material properties and layer thicknesses are given in Table 11.

Table 14: Layer characteristics of Panasonic225 PV panel

Layer	Thickness [mm]	Density [kg/m^3]	Thermal conductivity [W/m/K]	Specific heat capacity [J/kg/K]
glass	3	3000	1.8	500
PV cell	0.225	2330	148	677
EVA	0.525	960	0.35	2090

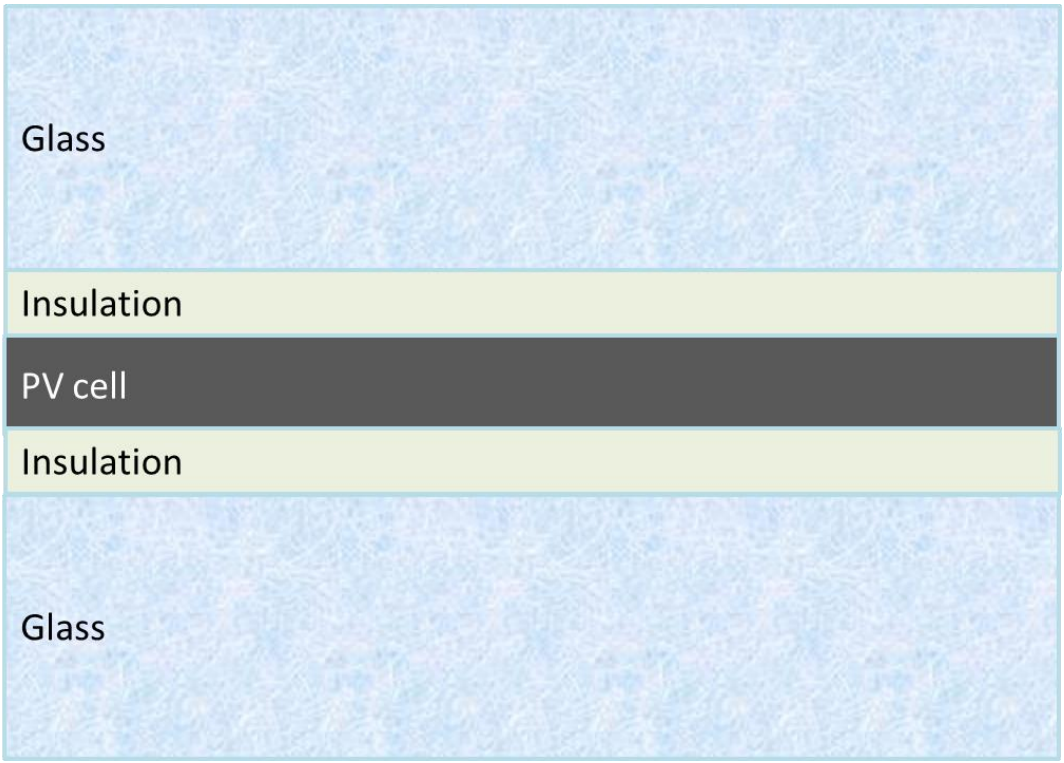

Fig. 72 Schematic cutting view through the thickness of the Panasonic PV panel.

It should be highlighted that the PV-cells inside the Panasonic225 PV panel are a proprietary technology developed by the Panasonic company. They are hybrids of single crystalline silicon surrounded by ultra-thin amorphous silicon layers. The manufacturer claims in the data sheet that their bi-facial panel produce up to 30% more power in outdoor conditions than in STC conditions (ANNEX E).

4.3. Multi-physics model of the bi-facial PV panel

4.3.1. Optical model modifications

The optical model presented in the previous chapter is used to estimate the light absorption in each layer of the PV panel. It was developed in the case of mono-facial PV panels. Thus, the model has to be adapted with minor modifications to predict the optical behavior of bi-facial ones.

It can be recalled that it is based on Markov chains process. As the bi-facial PV panel possesses the same number of layers than the mono-facial ones studied before (i.e. 5 layers), the Markov transitional matrix $[M]$ (defined in Eq. (37) of the previous chapter) keeps the same number of elements (i.e. 29×29 elements). The transition matrix elements are linked to the optical properties of each material layer, which are a function of the wavelength as discussed in the previous chapter.

The expression of the Markov transitional matrix $[M]$ defined for the Panasonic225 PV panel can be found in ANNEX A. We have to remember that the elements of the matrix $[M]$ are wavelength dependent. Therefore, the transition matrix $[M]$ have to be expressed for each wavelength value of solar irradiance.

The main modification concerns the state vector at time step $i = 0$, $P(0)$, initially defined in Eq. (43) of the previous chapter. In the case of Panasonic225 PV panel, the initial state of photons can be considered as photons hitting the top surface of the PV panel, and also a fraction of them that hits the bottom surface. The light absorbed from the bottom surface is mostly reflected from the ground, and can be estimated from the surface albedo, a.

The surface albedo is the ratio of irradiance reflected to the irradiance received by the surface under the PV panel. Thus, the surface albedo's value is ranged between 0 and 1. The element vector corresponding to the photons hitting the bottom surface is taken equal to the surface albedo, $\bar{a}$. In the case of a bi-facial panel, $P(0)$ is a vector composed with 1 at the first line, $\bar{a}$ (the surface albedo) at the line before last, and 0 in all the others. Thus, the initial state vector is a vector composed as:

$$P(0) = [1,0,\dots,0,..,a,0]^t \tag{90}$$

In the vector defined in Eq. (89), the contribution of the irradiance under the panel is taken into account. The surface albedo, $\bar{a}$, can take different values that depend on the surface conditions as seen in Fig. 54 taken from the work of Coakley [64].

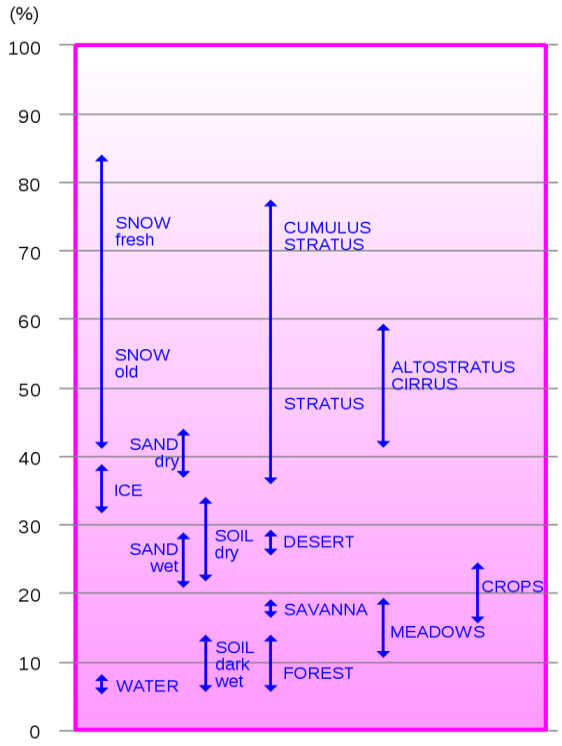

Fig. 73 Percentage of diffusely reflected sunlight (or surface albedo $\bar{a}$) relative to various surface conditions.

The initial state vector expressed in Eq. (89) is next introduced in Eq. (44) of the previous chapter. The framework of the optical model remains unchanged; the probabilities of finding a photon in the different layers of the PV panel are obtained by successive multiplication until a steady state is achieved.

4.3.2. Thermal model modifications

The framework of the thermal modeling remains globally unchanged. The FD approach developed in the previous section need a mesh grid through the spatial domain. The Panasonic225 PV panel thickness is thus subdivided into 1456 equally spaced points leading to a thickness increment $\Delta x = 5\ \mu m$.

The main modifications concern the number of heat sources to estimate at each time increment. In the case of mono-facial PV panels, the heat sources were located in the front glass, the insulation

layer above the PV-cell and in the silicon layer (corresponding to the PV-cell). Whereas in the case of bi-facial PV-panels, the layers below the PV-cells can also absorb photons and thus generate heat. Consequently, the heat sources have to be estimated for all the five layers constituting the Panasonic225 PV panel.

The spectral irradiance of the Sun is first estimated with the model proposed by Bird [54]. Using the absorption coefficients derived from the optical model, the heat sources in the layers above and below the PV-cell are next estimated with Eq. (55) while in the silicon layer with Eqs. (56-58).

It should be noted that it was assumed that the absorbed sunlight in all the layers excepted the PV-cell one is completely converted into heat. To compute the heat generated in the silicon made layer, the electrical behavior of the PV panel has to be defined.

Finally, the boundary conditions (convection and radiation heat losses defined with Eqs. (50-52) in the previous chapter) are defined in the same way than in the previous chapter. The heat exchange coefficients related to the boundary conditions on top and rear surfaces of the studied PV panel are summarized in Table 12 as proposed in the work of Aly et al.[22].

In the present work, we chose to refer to the formula from the work of Swinbank [17] where the sky temperature is represented to be:

$$T_{sky} = 0.0552 \times T_{amb}^{1.5} \tag{91}$$

where T_{amb} is the ambient temperature measured in field on QEERI solar test facility.

Table 15: Relations used to define the heat exchange coefficients related to the boundary conditions on top and rear surfaces of the studied PV panel

Heat exchange coefficient	Formula
Effective front coefficient	$h_{front} = h_{forced(wind)} + h_{free,front} + h_{rad,front}$
Effective rear coefficient	$h_{rear} = h_{free,rear} + h_{rad,rear}$
Forced convection (wind velocity)	$h_{forced} = 5.67 + 3.86w$
Free convection on front side	$h_{free,front} = 1.31 \times \left(T_{front} - T_{amb}\right)^{1/3}$
Free convection on rear side	$h_{free,rear} = 1.31 \times \left(T_{rear} - T_{amb}\right)^{1/3}$
Radiative heat exchange on front side	$h_{rad,front} = \frac{\sigma\left[(T_{sky}^2 + T_{front}^2)(T_{sky} + T_{front})\right]}{\frac{1-\varepsilon_{front}}{\varepsilon_{front}} + \frac{1}{F_{front,sky}}} + \frac{\sigma\left[(T_{ground}^2 + T_{front}^2)(T_{ground} + T_{front})\right]}{\frac{1-\varepsilon_{front}}{\varepsilon_{front}} + \frac{1}{F_{front,ground}}}$
Radiative heat exchange on rear side	$h_{rad,rear} = \frac{\sigma\left[(T_{sky}^2 + T_{rear}^2)(T_{sky} + T_{rear})\right]}{\frac{1-\varepsilon_{rear}}{\varepsilon_{rear}} + \frac{1}{F_{rear,sky}}} + \frac{\sigma\left[(T_{ground}^2 + T_{rear}^2)(T_{ground} + T_{rear})\right]}{\frac{1-\varepsilon_{rear}}{\varepsilon_{rear}} + \frac{1}{F_{rear,ground}}}$

Both temperatures appearing in Eq. (90) are expressed in Kelvin. The expression of sky temperature written in Eq. (90) was also used in the work of Aly et al. [22] in their thermal modeling of PV panels subjected to the same conditions as the one studied herein.

In agreement with the work of Aly et al. [22], the sky temperature estimation mainly affects the thermal response of the PV panel under outdoor conditions.

4.3.3. Electrical model modifications

The electrical model is used without any modifications. However, the parameters have to be identified on the $I-V$ curves and/or on the tables provided in the datasheet edited by the manufacturer. Following the method proposed in the work of Tsai [36], the series and shunt resistances were identified from the PV manufacturer data sheet.

The series and shunt resistances are respectively equal to $R_s = 0.0073\Omega$ and $R_s = 4.3541\Omega$. Nevertheless, as the PV-cells that compose the PV panel are in silicon, the values of the other electrical parameters are taken equal to the ones presented in the previous chapter. Their values are recalled in Table 13 presented below.

Table 16: Electrical parameters values of the Panasonic225 PV panel

Material electrical parameter	Value
Base thickness $[m]$	198.5×10^{-6}
Emitter thickness $[m]$	0.5×10^{-6}
Depletion region thickness $[m]$	1×10^{-6}
Acceptor concentration $[m^{-3}]$	1.5×10^{15}
Donor concentration $[m^{-3}]$	5×10^{18}
Surface recombination velocity (base) $[m/s]$	10
Surface recombination velocity (emitter) $[m/s]$	1

4.4. Results and discussion

4.4.1. Validation of the multi-physics model

4.4.1.1. Optical model predictions

Before starting to predict the thermo-electrical behavior of the PV panel in outdoor conditions, we need first to check if the different parameters of the models were correctly identified. For this purpose, the absorption probabilities were first computed in the different layers of the studied PV panel, coefficients $a_j(\lambda)$ in Eq. (55) in the previous chapter.

The percentages of photons absorbed in each PV panel layer are presented in Fig. 55 for different albedo values. As expected, the percentage of photons absorbed in the silicon layer (i.e. PV-cell) increases when the albedo value increases.

The same happens with the percentage of photons absorbed in the layers below the PV-cell (glass and EVA layers). However, the percentage of photons absorbed in the layers composed with glass and EVA remains at very low values. Knowing the absorption coefficient of the silicon made layer (PV-cell layer), the electrical behavior of the PV-cell can be predicted.

At higher albedo values, the values of the absorption probabilities obtained are higher than 1, but it is only because it's based on the total percentage of photons from the top and the bottom side of the PV panel. For instance, in the case of an albedo value of 0.3, the real total "percentage" value of photons is actually 1.3, and not 1 like what was observed in the case of a monofacial panel, which explains the absorption values higher than 1 in some cases.

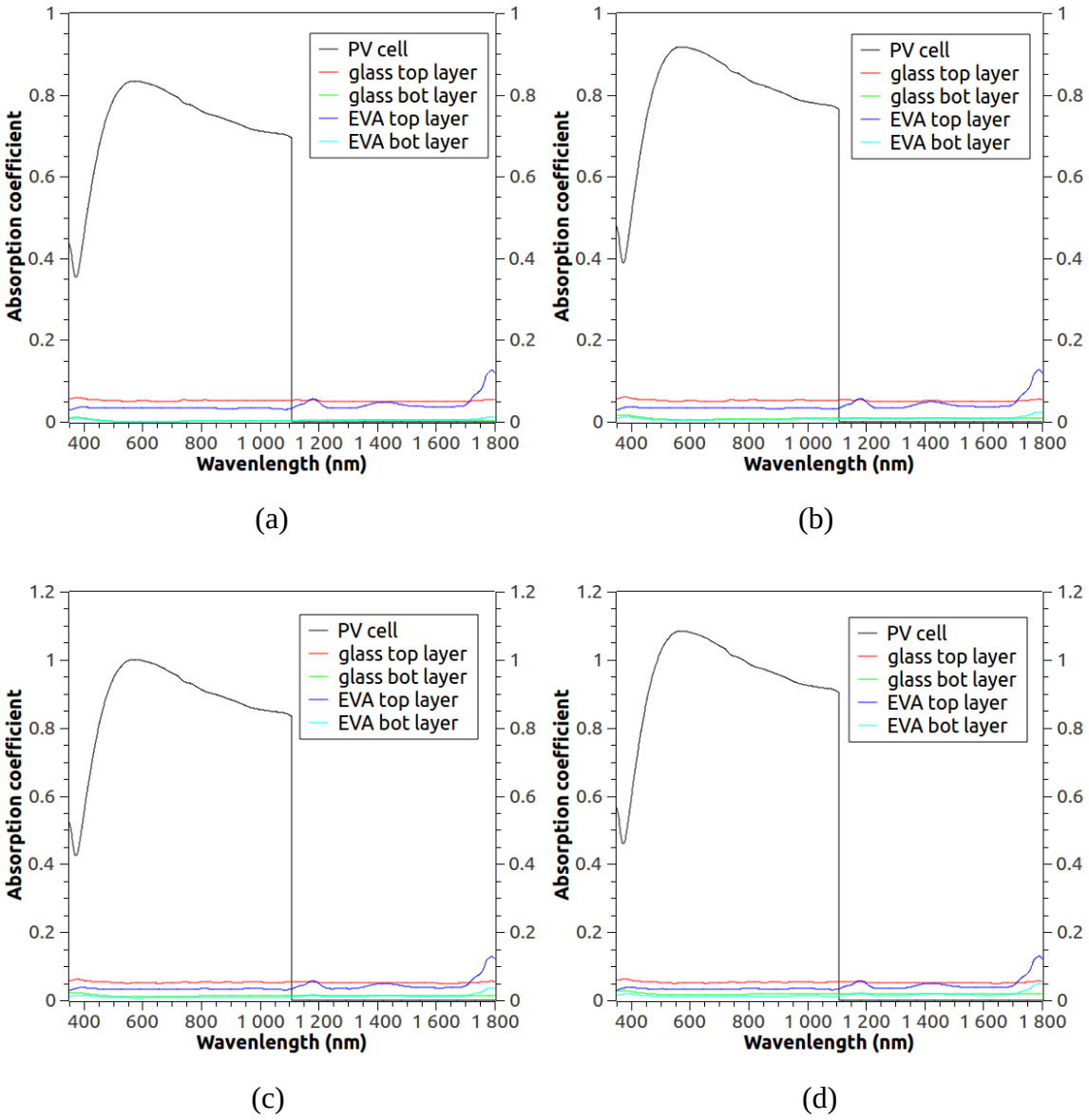

Fig. 74 Percentages of photons absorbed by the layers of the PV panel as a function of the wavelength and for different albedo values: 0% (a), 10% (b), 20% (c) and 30% (d).

4.4.1.2. Electrical model predictions

As aforementioned, the total internal quantum efficiency curve $IQE(\lambda)$ and the other material parameters used to compute the diode reverse saturation current I_0 are taken equal to the ones defined for the other commercial PV panels in the previous chapter. We postulate this assumption since all the studied PV panels are composed with silicon PV-cells.

The values of the series and shunt resistances R_s and R_{sh} were identified with the help of the method proposed in the work of Tsai [36]. The response of the PV panel was firstly analyzed under STC conditions. The light spectra used to reproduce STC conditions is presented in Fig. 56.

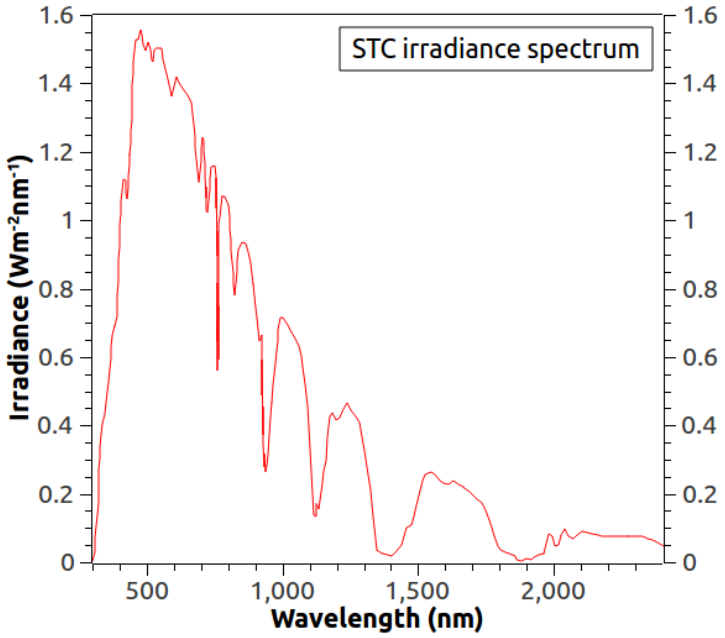

Fig. 75 Light spectrum used to simulate the behavior of Panasonic225 PV panel under STC conditions.

To evaluate the electrical output power of its PV panel, the manufacturer provides in the data sheet the $I-V$ curves measured in STC. In the standard industry of PV, STC specifies that the

measures were performed at a constant PV-cell temperature of $25°C$, an irradiance of $1000\ W/m^2$ and with an air mass of 1.5 (AM1.5).

Moreover, the manufacturer provides $I-V$ curves measured at different constant values of global irradiance but, for a constant PV-cell temperature at $25°C$. The electrical modeling of the studied PV panel was first verified by plotting the $I-V$ curves. The corresponding predicted $I-V$ curves are plotted in Fig. 57.

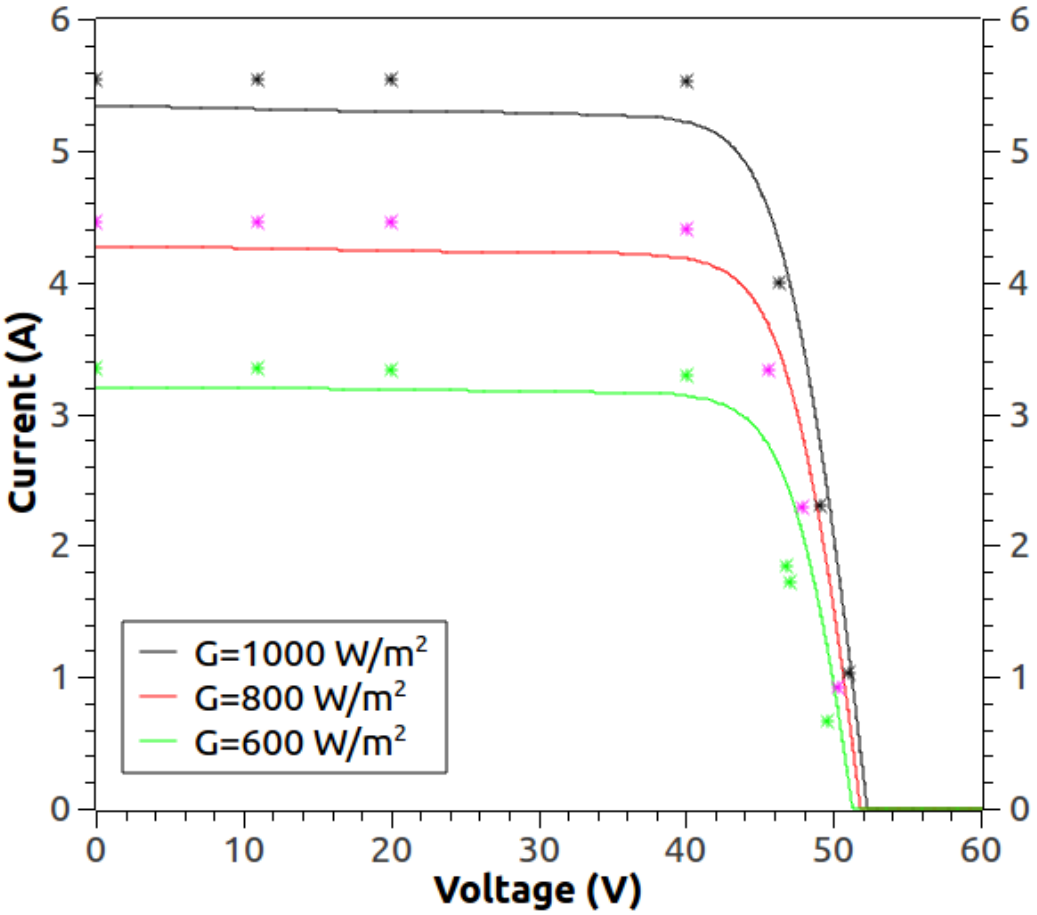

Fig. 76 Predicted $I-V$ curves of the Panasonic225 PV panel computed for different values of global irradiance and at a constant temperature of $25°C$.

Several points extracted from the data sheet edited by the manufacturer are added in Fig. 57. As expected, the predicted $I-V$ curves are near to the experimental points taken from the data sheets. This is also true for the different global irradiance values tested. The manufacturer provided also data about the performance of the PV panel under STC conditions with different surface albedo values (ranged between 0 and 0.3). In these conditions, the back of the PV panel contributes to the irradiance received by the PV panel. The output electrical power predicted under STC conditions with different surface albedo values are reported in Table 14.

Table 17: Electrical Comparison of the maximum electrical power predicted by simulations and provided by the manufacturer under STC and with different backside additional contributions

Surface albedo value	Pmax (W) (Prediction)	Pmax (W) (datasheet)
0%	222	225
5%	234	236
10%	246	247
15%	258	259
20%	270	269
25%	282	280
30%	294	291

From Table 14, the predicted results are close to the values declared by the manufacturer. It is important to note that for the predicted values, the output power reported is the one obtained while maintaining the system at the ambient temperature (i.e. a constant temperature of $25°C$). In our simulations, as the PV panel's temperature increases, the electrical output power will drop till it reaches a certain equilibrium coinciding with the equilibrium temperature, just like the NOCT simulations (see subsection below). In Fig. 57 and Table 14, it can be concluded that electrical behavior is well predicted by the proposed modeling.

4.4.1.3. Thermal model predictions

To validate the thermal modeling proposed, the response of the PV panel was analyzed under NOCT conditions. For the NOCT conditions simulations, the manufacturer states in the data sheet that there is no contribution by the back of the panel. Consequently, the surface albedo value is taken as $\bar{\alpha}_{noct} = 0$. The environmental conditions to obtain the NOCT of the studied PV panel are recalled below:

- Irradiance = 800 W/m^2,
- Ambient temperature = 20°C,
- Wind speed = 1m/s,
- Open circuit conditions.

The global irradiance of 800 W/m^2 is computed with the terrestrial solar spectrum given by the standard ASTM G173-03. The light spectrum used to reproduce NOCT conditions is presented in Fig. 58.

The conditions listed above are kept constant during the entire test simulations. The thermal response of the PV panel is presented in Fig. 59. The temperature of the PV panel, initially at the ambient temperature, increases until reaching an equilibrium temperature.

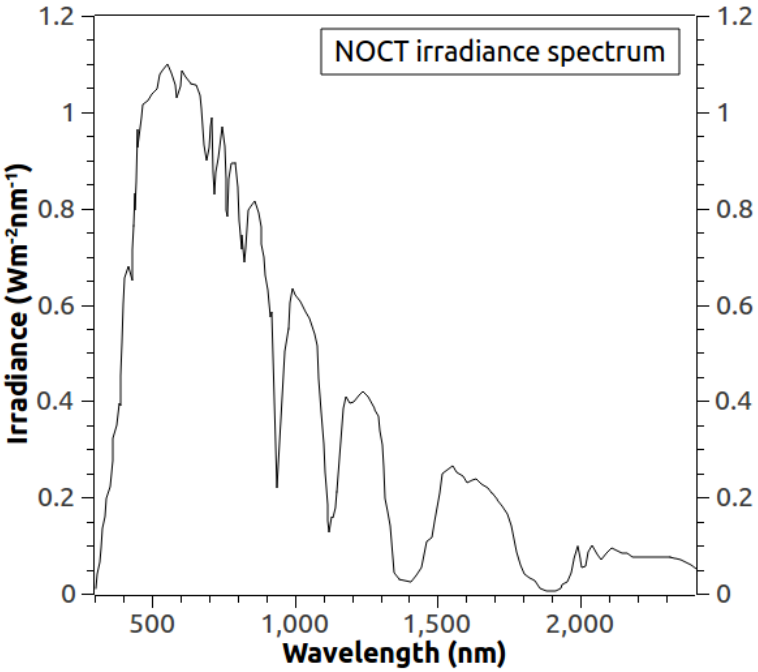

Fig. 77 Light spectrum used to simulate the behavior of Panasonic225 PV panel under NOCT conditions.

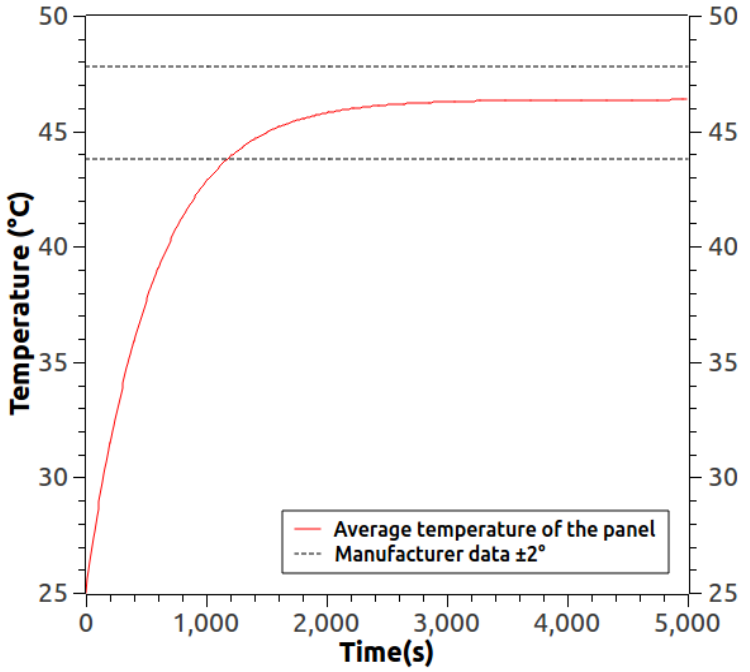

Fig. 78 Time-related evolution of PV-cell temperature at NOCT conditions for the commercial bi-facial PV panel Panasonic225.

The predicted temperature is compared to the one given by the manufacturer in Fig. 59. It is noted that the thermal response predicted with our multi-physics model agrees with the margin of error data provided by the manufacturer.

The maximum electrical power supplied by the studied PV panel was also predicted and it is plotted in Fig. 60. The output power reaches an equilibrium after a while, just like the temperature, at about $148\ W$.

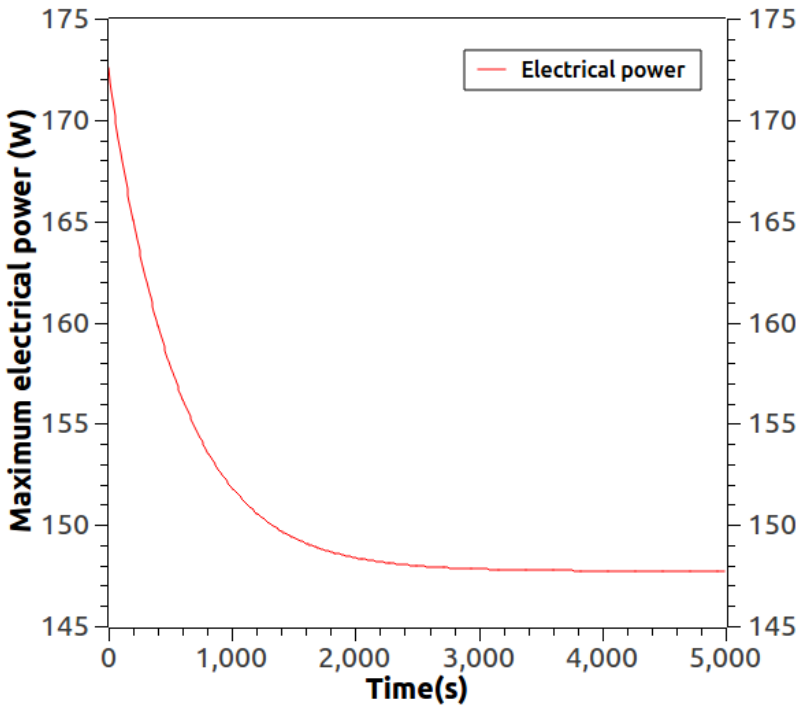

Fig. 79 Time-related evolution of the maximum electrical power at NOCT conditions for the Panasonic225 bi-facial panel.

In Fig. 60, the predicted electrical output power is equal to $173\ W$ when the PV-cell temperature is still equal to the ambient temperature $25°C$, which is close to the one declared by the manufacturer in the data sheet ($169.9\ W$). However, it is not the power predicted at the end of the test, when the NOCT is reached. We obtained the same results in our simulations in STC.

Consequently, it seems that the manufacturer provides its data when the PV-cell temperature is still equal to the ambient temperature $25°C$. Nevertheless, we can consider that the different

models (optical, electrical and thermal) are validated to predict the response of the commercial bi-facial PV panel produced by Panasonic.

4.4.2. Outdoor and real-time simulations

The simulations performed under NOCT conditions allows us to have an overview of the behavior of our multi-physics model. Running the multi-physics model under real meteorological data is required to validate it in a more general context. The environmental input data necessary to the proposed modeling are: ambient temperature, wind velocity and irradiance. The QEERI solar test facility provided us with all the required data measured in the Solar Test Facility (STF) located in Doha, Qatar.

The real-time measurements were performed during two whole days (19/01/2017 and 30/01/2017) from 5:30 to 18:30, which was the sunny portion of the day. One of the days corresponds to a sunny day and the second one to a sunny day with clouds.

The wind speed, ambient temperature and irradiance are recorded once every minute, so the time step was adjusted to meet this frequency of measurements. The time-related evolution of the ambient temperature and wind speed during the sunny day with clouds are presented respectively in Figs. 61a and 61b, while the sunny day are presented respectively in Figs. 61a and 61b.

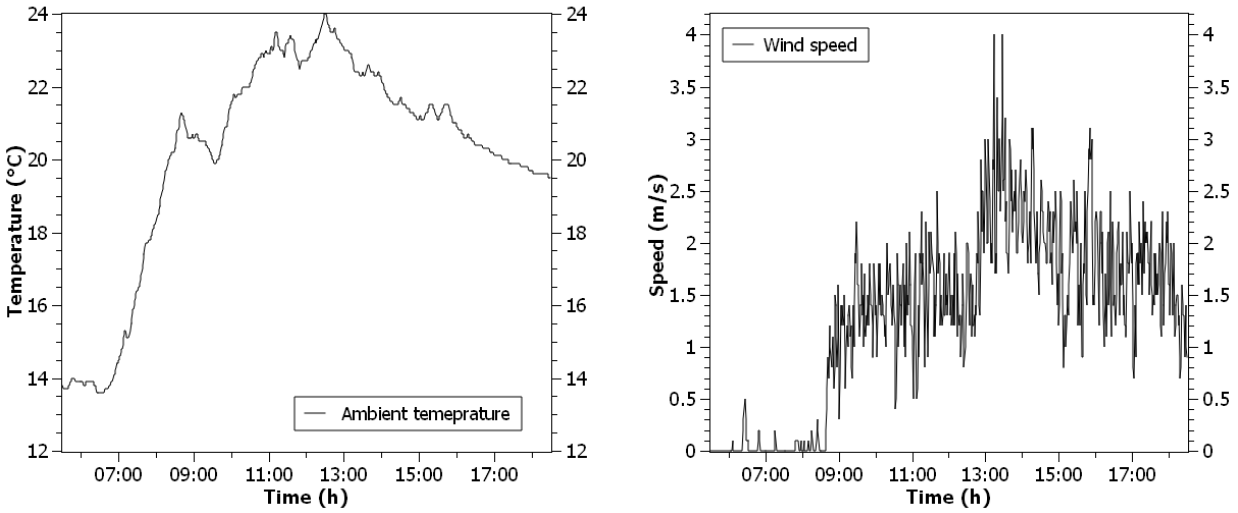

(a) (b)

Fig. 80 Ambient temperature (a) and wind velocity (b) variations during the whole day of 19/01/2017 in Doha, Qatar.

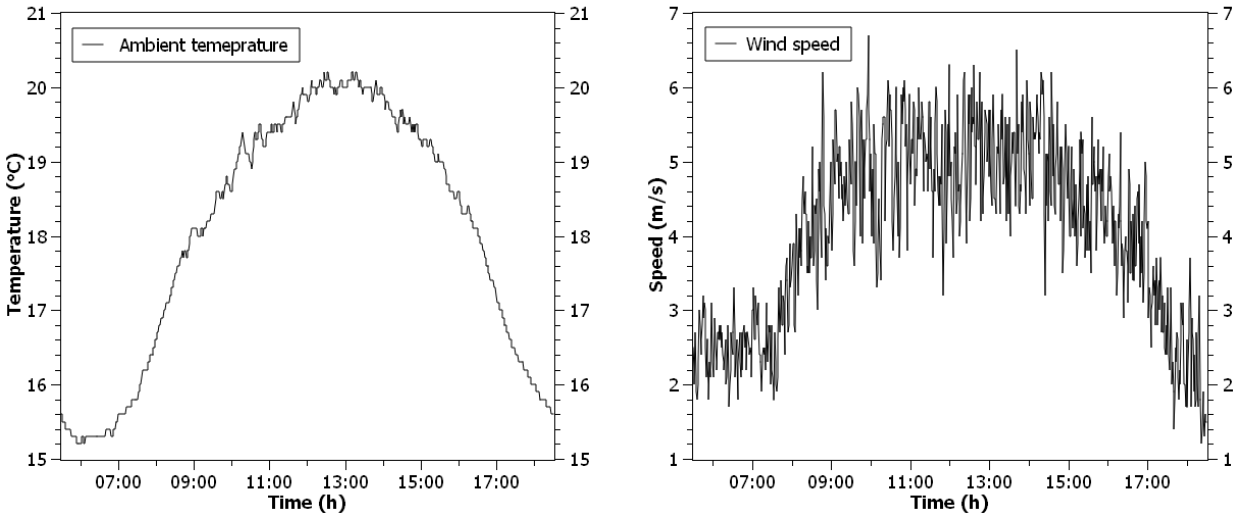

(a) (b)

Fig. 81 Ambient temperature (a) and wind velocity (b) variations during the whole day of 30/01/2017 in Doha, Qatar.

Since the proposed optical model accounts for the wavelength effects, the spectral irradiance from the Sun as a function of the wavelength has to be measured. This was performed using a spectroradiometer (MS-700N) in the STF.

The spectral irradiance is plotted at noon (19/01/2017) in Fig. 63a. The global irradiance can be computed by integrating the spectral irradiance in relation to wavelength. The global irradiance recorded during whole day is presented in Fig. 63b for the sunny day with clouds and in Fig.64 for the sunny day. Furthermore, for comparison purposes, the STF staff recorded the evolution of the temperature at the back of the panel, and also the electrical power output.

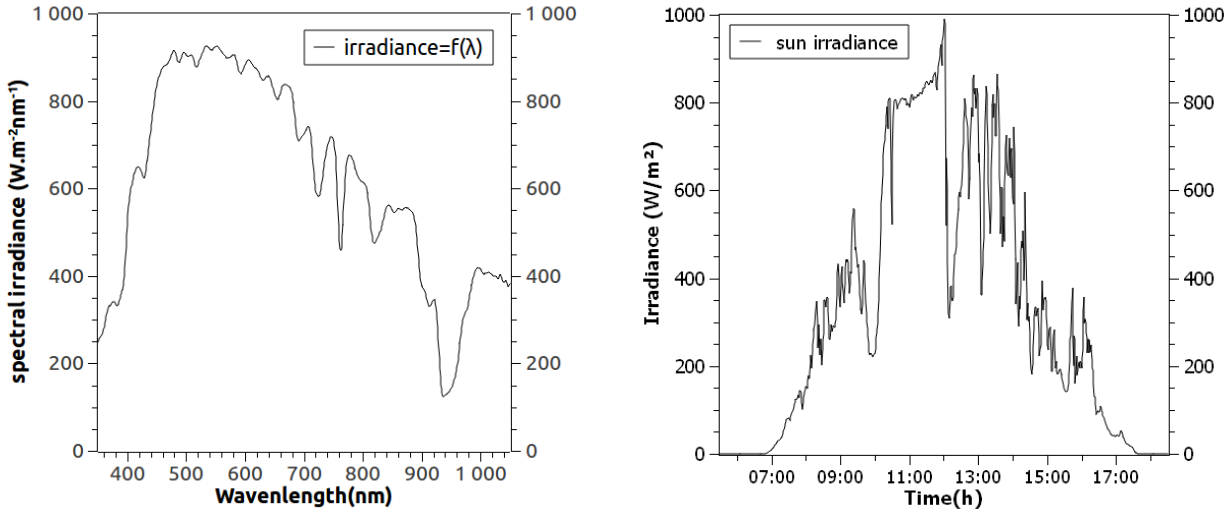

(a) (b)

Fig. 82 The spectral irradiance at noon (a) and global irradiance variation (b) during the whole day of 19/01/2017 at Doha, Qatar.

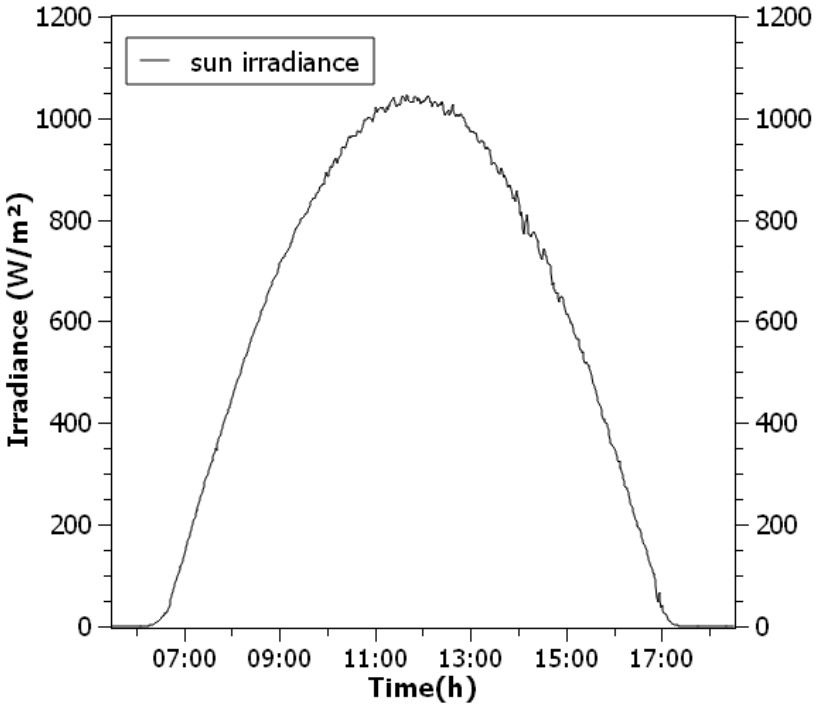

Fig. 83 The global irradiance variation during the whole day of 30/01/2017 at Doha, Qatar.

Moreover, the real time simulations were performed with a surface albedo of 0.4, which means an additional 40% contribution from the ground, as specified by the Solar Test Facility (STF) in Doha, Qatar. This value seems to be consistent with the literature, as seen in the comparative of the percentage of diffusely reflected sunlight relative to various surface conditions (Fig. 54). For a dry sand area, which is the surface mostly found in Middle East, the surface albedo is closer to 40%.

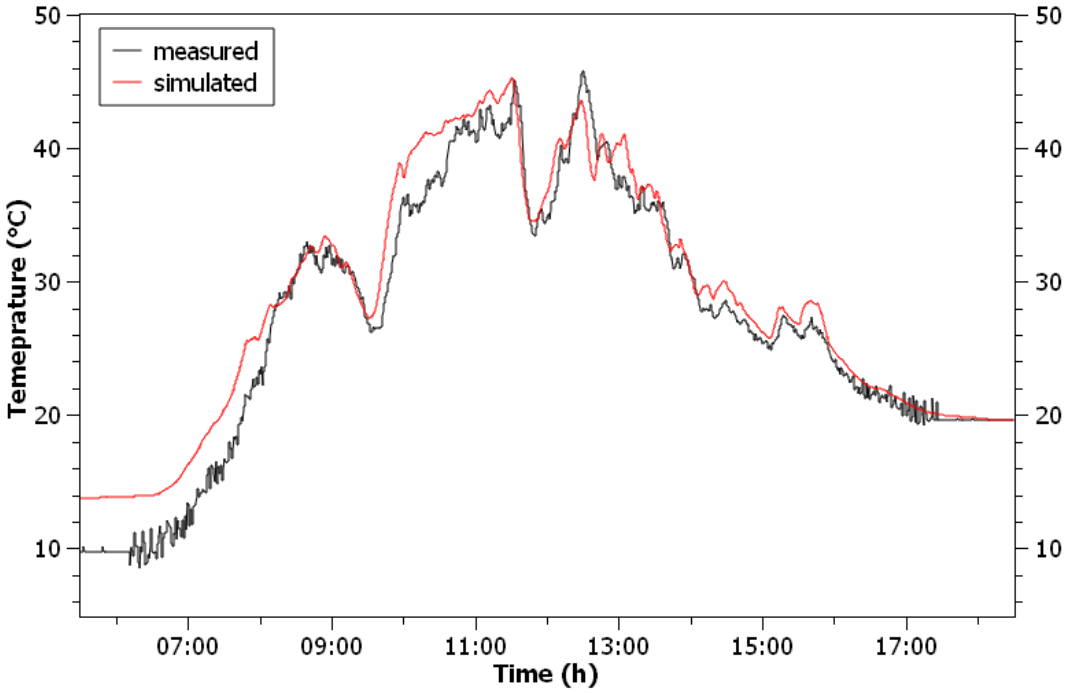

Fig. 84 Time-related evolution of the measured and predicted temperature of the Panasonic 225 bi-facial PV panel (19/01/2017 at the STF, Doha, Qatar).

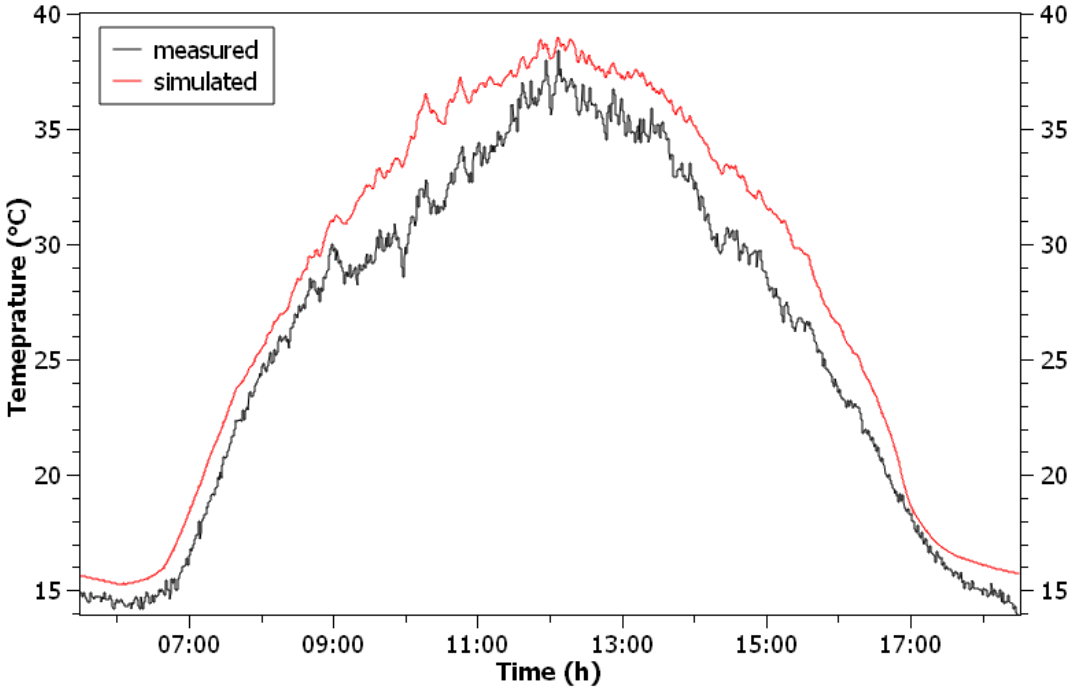

Fig. 85 Time-related evolution of the measured and predicted temperature of the Panasonic 225 bi-facial PV panel (30/01/2017 at the STF, Doha, Qatar).

It should be noted that the outdoor real-time data collected by the STF staff correspond to a sunny portion of the day. The temperature measured is plotted as a function of time, as well as the predicted temperature with a surface albedo value of 40% (Figs. 65 and 66). The experimental time-related evolution of the temperature reported in Figs. 65 and 66 corresponds to the one recorded at the back of the PV panel.

The simulations were made using the ambient temperature from the meteorological station, and a separate sensor was used to measure the temperature of the PV panel installed directly on it. Initially, it is noticeable that the temperature values recorded and the one predicted are not the same during the first 2-3 hours of the studied daytime (Figs. 65 and 66). This can be explained by the different positions of the temperature sensors.

However, after the first 2-3 hours of time range of measurement, the predicted temperature evolution is in accordance with the experimental one (recorded at the back of the PV panel). Furthermore, there were some clouds passing by during the day, which explains the sudden changes of irradiance at certain points (Fig. 63b).

For both studied day, the predicted temperature values seem to follow the recorded temperature values even at those periods, which validates our multi-physics model for the thermal response.

Our multi-physics model allows to predict the maximum electrical output power supplied by the PV panel. The predicted evolution of maximum electrical output power is plotted in Figs. 67 and 68 as well as the values recorded on-site.

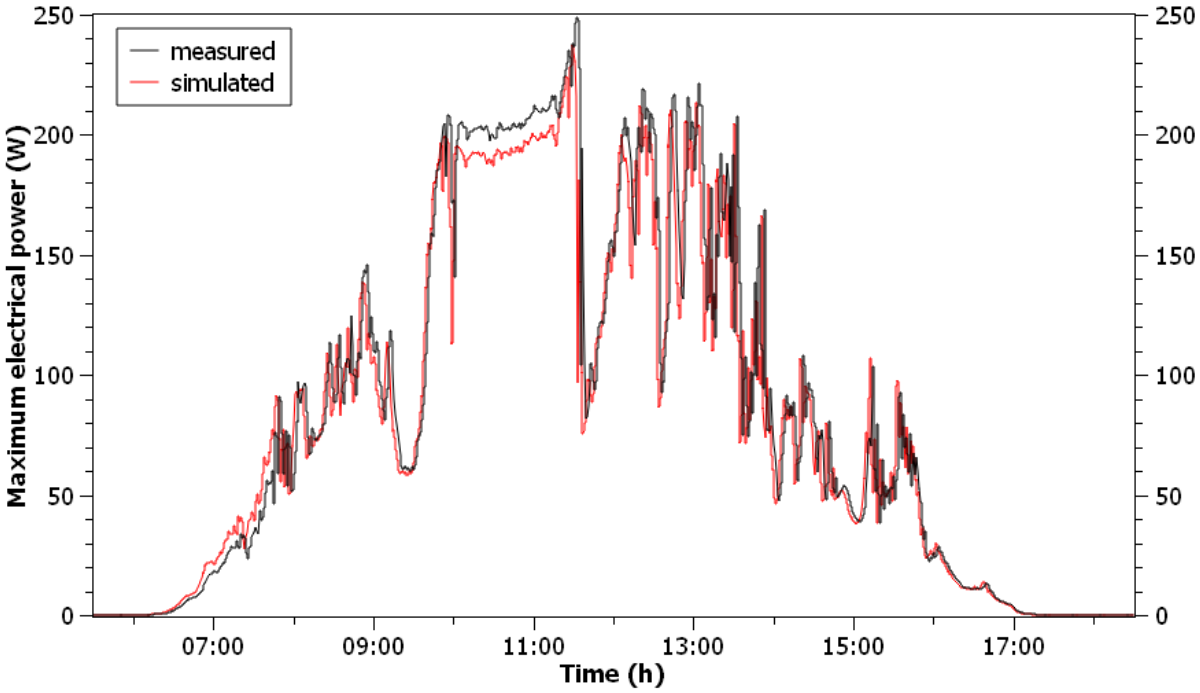

Fig. 86 Time-related evolution of the measured and predicted electrical output power of the Panasonic 225 bi-facial PV panel (19/01/2017 at the STF, Doha, Qatar).

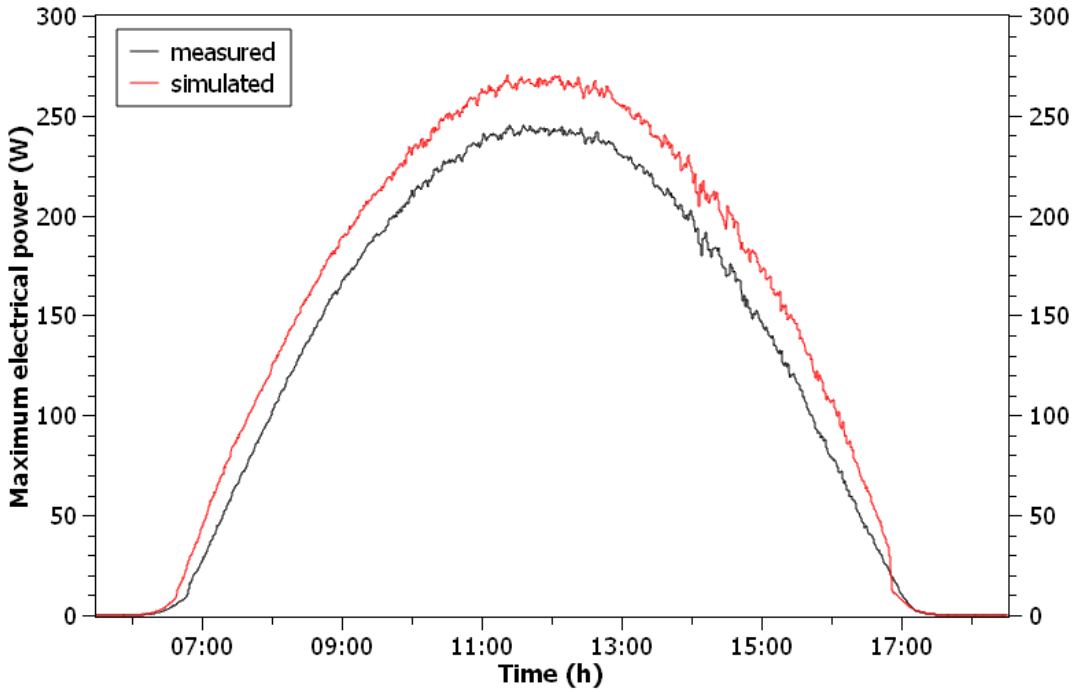

Fig. 87 Time-related evolution of the measured and predicted electrical output power of the Panasonic 225 bi-facial PV panel (30/01/2017 at the STF, Doha, Qatar).

For both studied day, the predicted results seem to be in accordance with the maximum electrical power measured. However, the weak discrepancy between the predictions and the experimental results can be explained by the spectroradiometer that is used to measure the spectral irradiance on-site. The spectroradiometer that was used at the STF does not cover the whole range of the solar spectral irradiance.

4.5. Conclusion

The multi-physics modeling proposed in the previous chapter was adapted to a commercial bi-facial PV panel. It was next successfully validated in STC and NOCT conditions with the information given in the data sheet edited by the manufacturer. The last step is to test the capabilities of our multi-physics modeling to capture the transient electrical and thermal behavior of a PV panel under time-varying field conditions.

To carry out this last step, it is needed to know the external loads to which is subjected the PV panel such as: the solar irradiation, wind speed and ambient temperature. This essential information is provided by QEERI which is based in Doha, Qatar. Two different data sets were chosen: a sunny day with passing clouds and a sunny day. The solar irradiation evolves uniformly in the case of the sunny day, while it can change abruptly in the case of cloudy sky. This last data set allow to test the reactivity of our modeling in real test conditions.

Even if a weak discrepancy between the numerical predictions and the experimental results can be observed, we can consider that the proposed multi-physics modeling capture sufficiently the transient electrical and thermal behavior of a PV panel under time-varying field conditions.

5. Thermomechanical investigation of PV panels behavior under various conditions

5.1. Introduction

In the previous chapters, we have focused your attention on the prediction of the thermal response of PV panels. The PV panel temperature is indeed one of the factors that heavily affects the electrical efficiency of PV panels.

However, the PV panel temperature is also one of the factors that affects its durability. From our numerical predictions, it can be concluded that the temperature distribution throughout the PV panel thickness is never uniform in the different testing conditions studied: STC, NOCT and also in field conditions. Furthermore, the values of thermal expansion coefficient for the different materials of the layers are significantly different, as stated in the work of Knausz et al. [65]; and this even if their thermo-mechanical properties are chosen carefully to guarantee a sufficient service lifetime.

The non-uniform temperature distribution combined with the mismatch of thermal expansion coefficient values induce internal thermal stresses inside the structure of PV panels. Theses stresses can lead to defects such as micro-cracks in the PV-cells [48], solder bond failure and/or delamination at the interfaces between PV-cell and insulation layers [49], [50]. Consequently, they could reduce the produced electrical power and thus deteriorate the electrical efficiency of the PV panel.

Delamination results from the loss of adhesion between two different layers of the PV panel (generally at the interface between insulation layer generally made in EVA and PV-cell or glass layer). It is well known that delamination occurs more frequently and is more severe in hot and humid climates. Delamination is one of the investigation fields for PV panels because it allows air and moisture to creep inside which will lead to corrosion and next will adversely affect its electrical characteristics [66].

The delamination phenomenon is not only driven by internal stress state but also by chemical processes such as auto-oxidation of EVA, [67]. Nevertheless, the present work will be focused on

the thermal stresses effects on the delamination phenomenon between the PV-cell and the insulation layers made in EVA.

The internal stresses are difficult to measure since a PV panel is a complex structure. Numerical simulations with finite element (FE) codes can be helpful to estimate the internal stress states inside the PV panel layers.

Firstly, in this work, thermal FE simulations were performed with the commercial code ABAQUS/CAE under nominal operating conditions as well as under accelerated weathering conditions. In the FE simulations, the thermal boundary conditions were mainly imported from the numerical predictions of our multi-physics modeling.

Then, mechanical FE simulations were performed with the same commercial code taking into account the thermal response of the PV panel. Temperature variations and local stresses are estimated everywhere inside the PV panel.

Finally, the PV panel is modeled in its entirety, and the differences between the different positions of the cells is studied. The numerical results of this work should give a better understanding of the thermo-mechanical behavior of a PV panel under various operating conditions.

5.2. Preliminary FE modeling and simulations (thermal analysis)

5.2.1. Geometry and mesh

Before estimating or predicting the stress/strain states across a PV panel section, the first task to do is to check the temperature values predicted by the FE analysis. Due to the geometrical symmetries of PV panels, a representative portion of the PV panel was considered. This portion corresponds approximately to one quarter of the PV panel cross section geometry and takes into account the structural continuity of the insulation material.

Consequently, a two dimensional (2D) FE model was built to predict the temperature distribution along the thickness and the width of the studied PV panel. In order to simplify the FE model, the Anti-Reflective Coating (ARC) as well as the copper ribbon wires were neglected in this study.

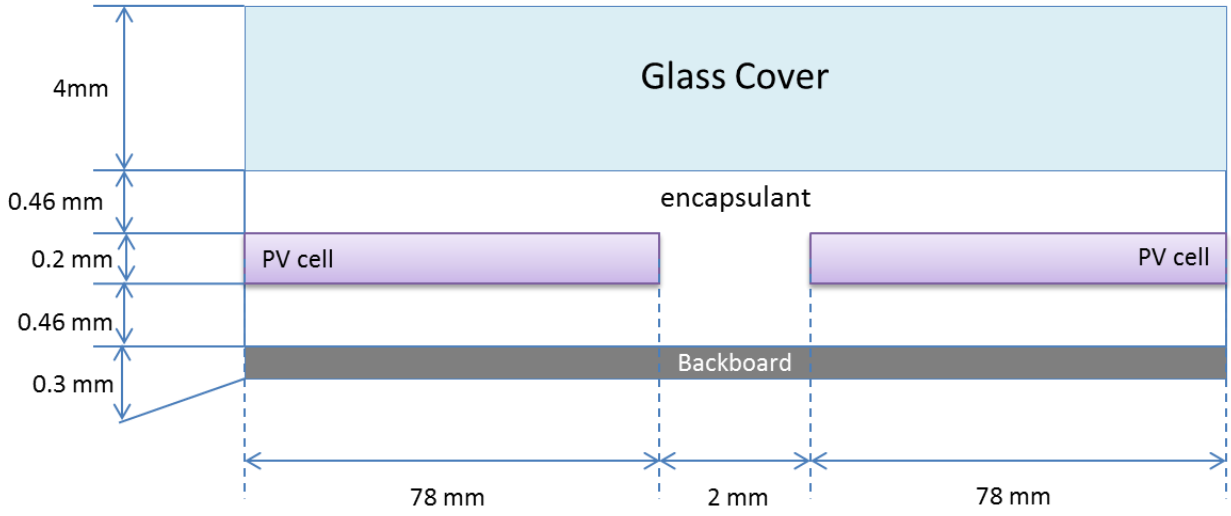

(a)

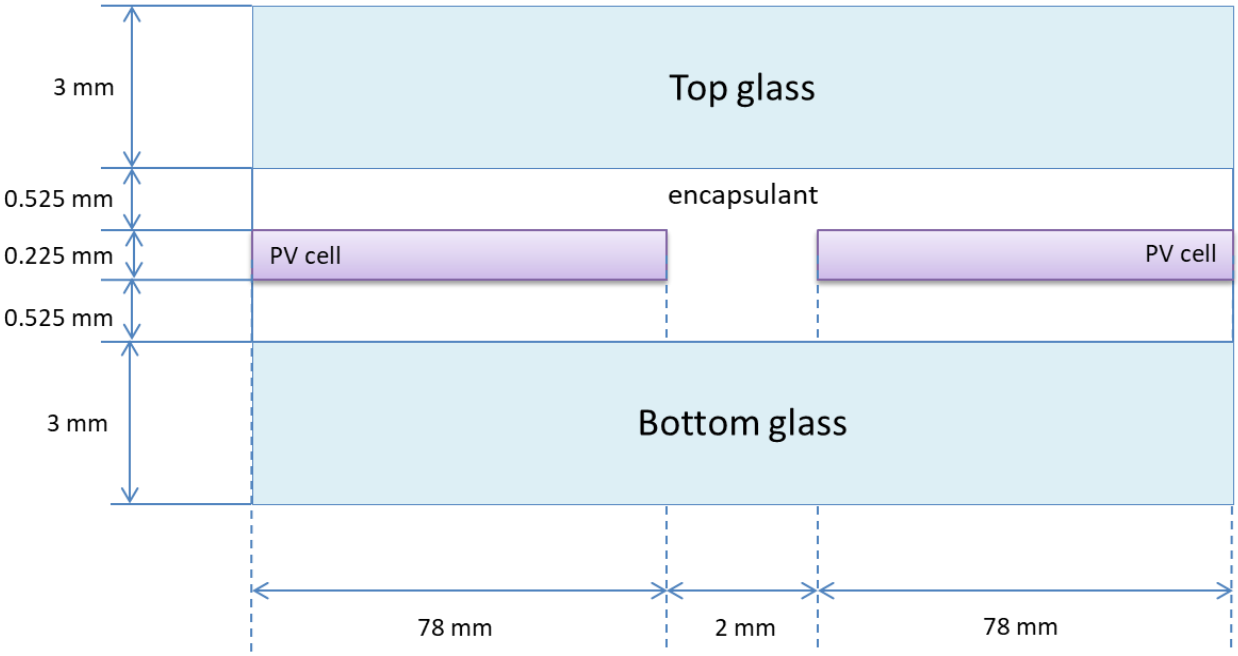

(b)

Fig. 88 Not-to-scale representative sketch of the PV panels cross sections: VSMS275 (a) and Panasonic225 (b).

As in the previous chapter, two different PV panels with different technologies were considered: the mono-facial VSMS275 and the bi-facial panel Panasonic225, as they are the most common ones. The cross section of both studied PV panels with the thickness and width values of the layers are presented in Fig. 69. Two halves of two different silicon cells, and the 2mm gap between them filled with EVA are considered.

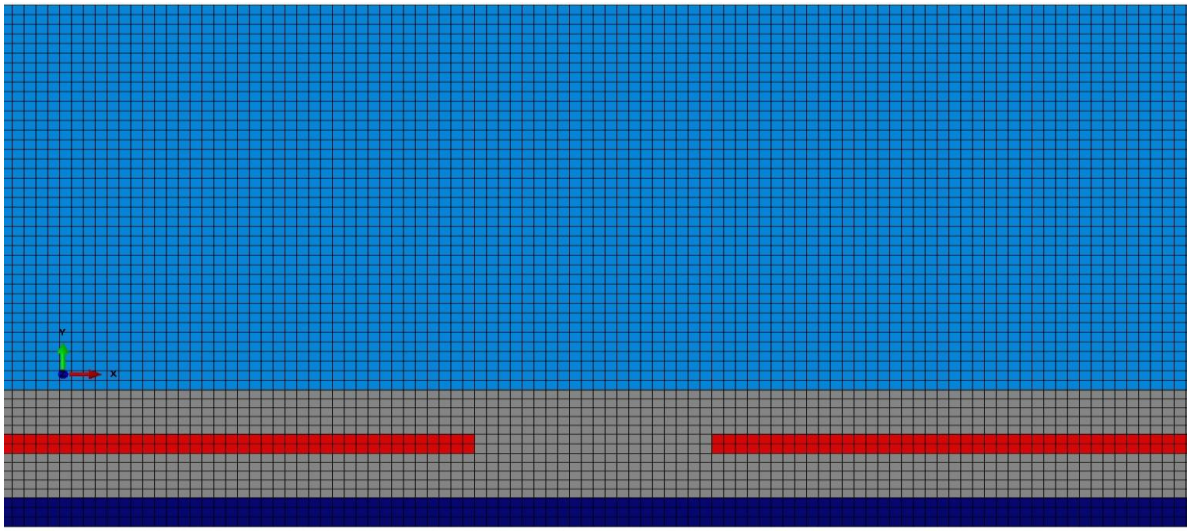

(a)

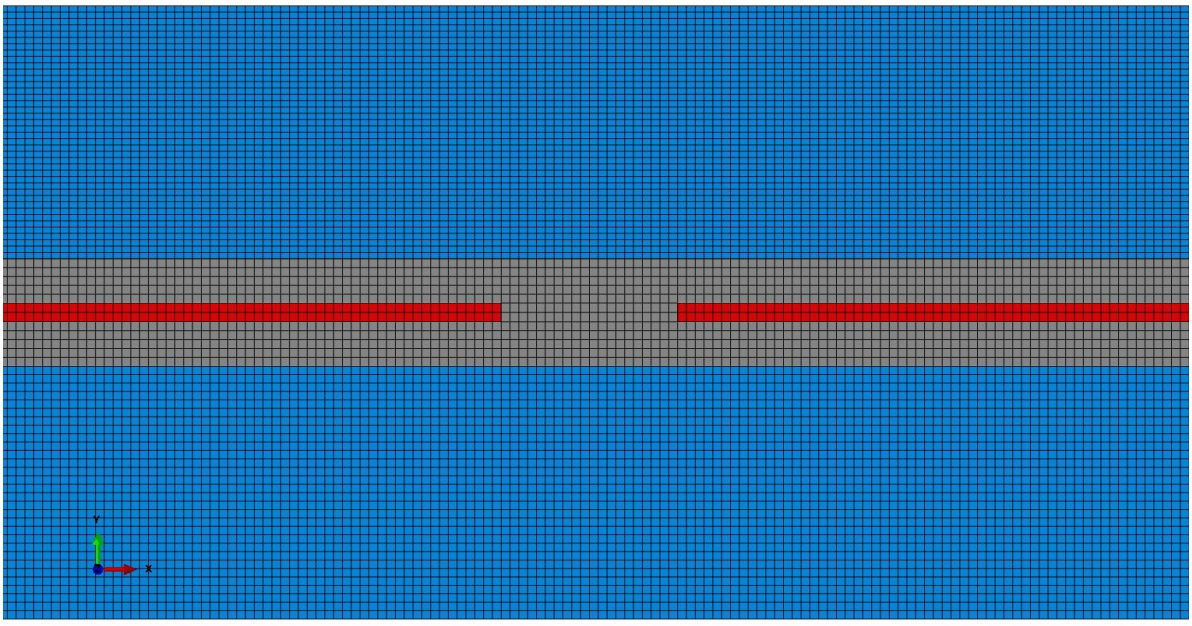

(b)

Fig. 89 Meshes of the PV panels cross sections: VSMS275 (a) and Panasonic225 (b).

The different layers of the PV panels were meshed with 4-node linear heat transfer elements, called DC2D4 in ABAQUS documentation [68]. The nodes at the interfaces between different layers are constrained with the "tie" option, leading to a perfect conduction between the different layers' surfaces. The meshes used in the FE heat transfer analysis are presented in Fig. 70. The mesh of VSMS275 PV panel is composed with 86,900 elements leading to 94,824 nodes, whereas the mesh of Panasonic225 PV panel is built with 129,560 elements leading to 137,511 nodes.

In Fig. 70, the x-direction is considered as the direction along the PV panel's width, whereas the y-direction is taken along its thickness. For both meshes presented in Fig. 70, the glass layer was colored in light blue, the insulation layer in gray, PV cells in red and the backboard (only in the case of the VSMS 275 panel) in dark blue.

5.2.2. Material properties

The properties of the materials have to be defined in ABAQUS/CAE. The thermal properties of the materials composing the layers of the VSMS275 PV panel are recalled in Table 15. These physical properties were already used in the multi-physics modeling presented in chapter 3.

The thermal properties of the materials composing the layers of the Panasonic225 PV panel are recalled in table 16. The physical properties reported in table 16 were already used in chapter 4.

Table 18 Thermal characteristics of the materials used in VSMS275 PV panel

Layer	Density [kg/m^3]	Thermal conductivity [W/m/K]	Specific heat capacity [J/kg/K]
Front glass	3000	1.8	500
EVA	960	0.35	2090
PV-cell	2330	148	677
Tedlar	1200	0.2	1250

Table 19 Thermal characteristics of the materials used in the Panasonic225 PV panel

Layer	Density [kg/m^3]	Thermal conductivity [W/m/K]	Specific heat capacity [J/kg/K]
Glass	3000	1.8	500
EVA	960	0.35	2090
PV-cell	2330	148	677

Two important assumptions were used in our FE modeling:

- The thermal properties of the materials listed in Tables 15 and 16 do not vary with the temperature
- The thermal behavior of the different materials was assumed to be isotropic.

5.2.3. Thermal loading conditions

The next step is to define the boundary conditions of the FE models. In order to validate the FE thermal modelling, FE analysis for both studied PV panels were performed under nominal operating conditions (i.e. NOCT). In agreement with the standards used in the field of photovoltaics, the nominal operating conditions are defined as:

- Irradiance = 800 W/m^2,
- Ambient temperature = 20°C,
- Wind speed = 1m/s,
- Open circuit conditions.

In the FE simulations, it was hypothesized that the solar irradiance absorbed by the glass and insulation layers is entirely converted into heat; whereas the solar irradiance absorbed by the PV-cells that was not converted into electricity is dissipated as heat.

The different heat sources were estimated beforehand inside each layer of the PV panel with the multi-physics modelling proposed in Chapter 3. Thus, they were directly imported from the MATLAB simulations as input data into ABAQUS/CAE.

Since the heat exchange to the sides of the entire PV panel is considered negligible, the heat exchanges are assumed to happen at the top and bottom layers of the PV panel. A convective heat flux caused by the wind on the top surface, as well as a radiative heat flux on the top and bottom surfaces has to be defined.

The heat exchange between the front or bottom surfaces of the PV panels due to convection are defined in ABAQUS/CAE by creating a surface film condition interaction. The film coefficients for top and bottom sides were defined with Eqs. (50) and (51) from section 3.2.2, and the sink temperature was taken equal to the ambient temperature.

The heat exchange between the outside plane surfaces of the PV panel and the surrounding ambient environment due to radiation are defined in ABAQUS/CAE by creating a surface radiation interaction. Following the work of Armstrong et al. [18], the emissivity value of the backsheet surface of the VSMS275 PV panel was taken equal to 0.85, whereas the value for the emissivity from the glass surfaces of both PV panels (VSMS275 and Panasonic225) is taken as 0.91 following the work of Notton et al. [14].

Adiabatic boundaries (the default condition in ABAQUS/CAE) are imposed on both lateral sides of studied portion of the PV panels. Finally, an initial temperature has to be set to whole the PV panel, and it was taken as the initial ambient temperature, 20°C.

5.2.4. Thermal predictions

Since both PV panels are subjected to constant thermal loads defined by the nominal operating conditions, steady-state thermal FE analysis were performed to predict temperatures and thermal gradients inside the studied PV panels. The steady-state thermal FE analysis are non-linear because they include radiation effects and also temperature dependent convection coefficients.

The predicted nodal temperatures (denoted NT11 in ABAQUS/CAE) are plotted on the meshes of both studied PV panels in Fig. 71. The 2D simulations performed with ABAQUS/CAE allow

to determine the field temperature distribution and thus give more information than the 1D multi-physics modelling implemented in the commercial code MATLAB with a Finite Difference scheme.

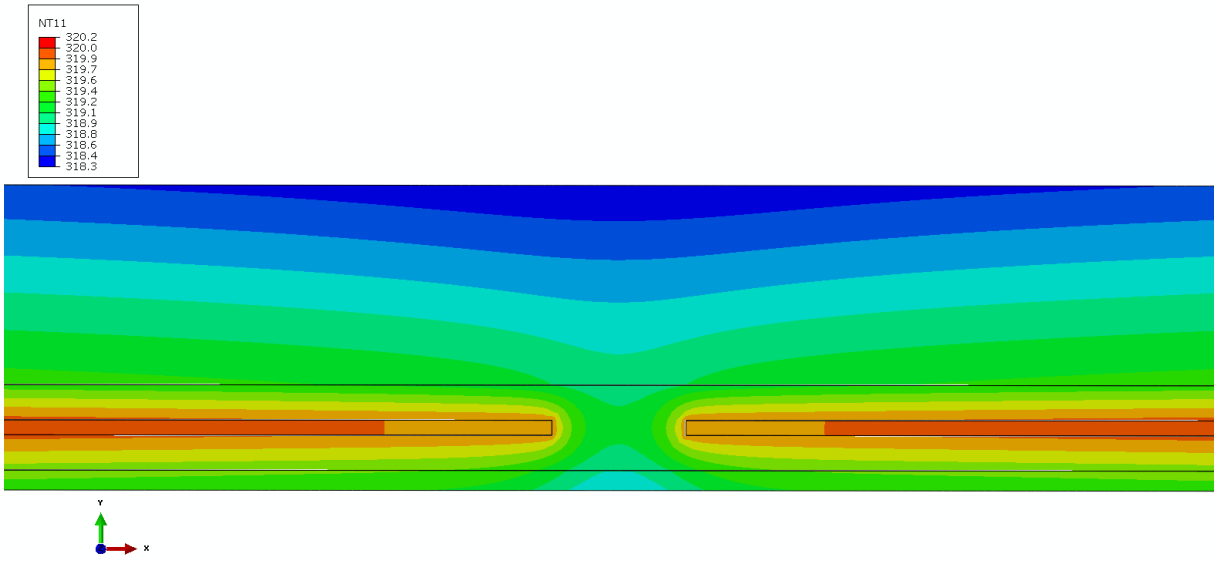

(a)

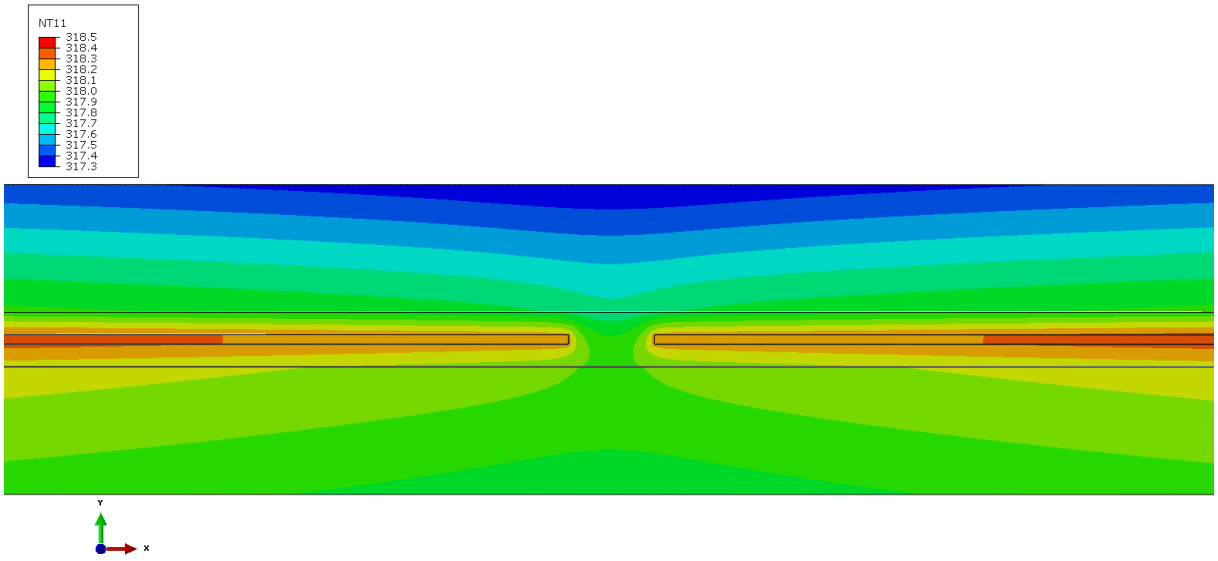

(b)

Fig. 90 Nodal temperature field (denoted NT11 and expressed in Kelvin) inside the PV panels: VSMS275 (a) and Panasaonic225 (b).

A vertical path of nodes (along y-direction in Fig. 70) that crosses the PV-cell layer was created in ABAQUS/CAE. The nodal temperature values of the nodes on the path were recorded and are plotted in Fig. 72 for both studied PV panels. For validation purposes, the temperature profiles obtained with the 1D multi-physics modelling, and presented in the previous chapters, are also plotted in Fig. 72.

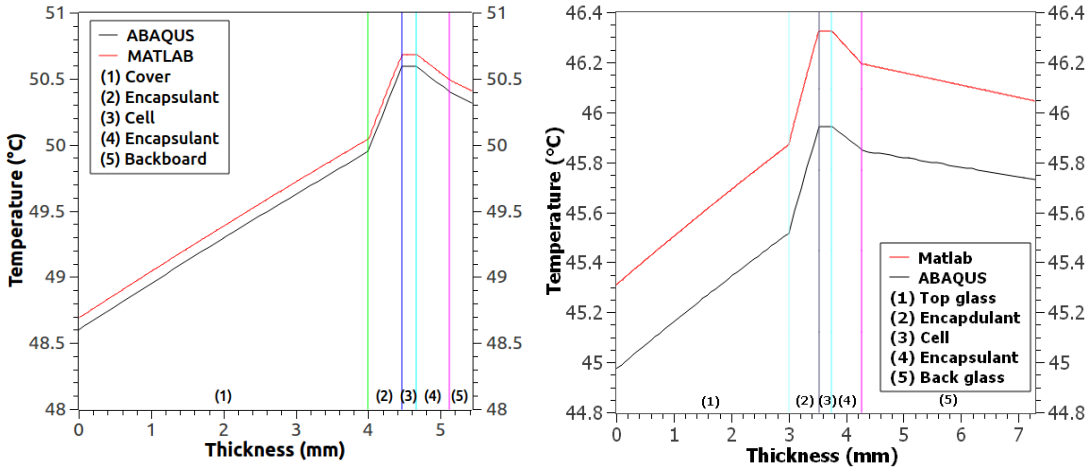

(b) (b)

Fig. 91 Comparison of the temperature profiles predicted with the in-house FD code in MATLAB and the FE code ABAQUS/CAE: throughout the thickness of the VSMS275 PV panel (a) and the Panasonic225 PV panel (b).

As expected, the PV-cell layer presents the highest value of temperature, for both PV panels. The numerical results obtained by both models (the 1D Finite Difference (FD) model implemented in MATLAB and the 2D model developed with the commercial FE code ABAQUS/CAE) are quite similar. The difference between the temperature values predicted under NOCT conditions with our in-house code developed with MATLAB and the commercial code ABAQUS/CAE are less than 0.5°C, which is less than the error value given by the manufacturers in their data sheets (±2°C). From Fig. 72, it can be concluded that the thermal boundary conditions are well defined in the FE models developed with ABAQUS/CAE.

Several longitudinal paths of nodes (along x-direction in Fig. 70) were created in ABAQUS/CAE. The path of nodes located in PV cell layer crosses also the insulation material

since it separates two adjacent PV cells as seen in Fig. 69. The nodal temperature values for each path of the nodes were recorded and are plotted in Fig. 73 for both studied PV panels.

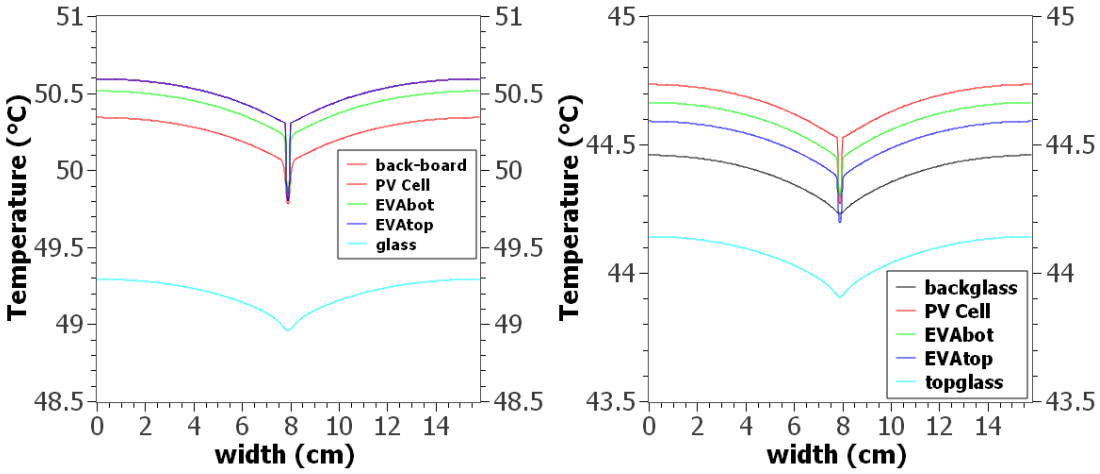

(a) (b)

Fig. 92 Temperature profiles predicted with the commercial FE code ABAQUS/CAE: for different thickness levels inside the VSMS275 PV panel (a) and the Panasonic225 PV panel (b).

The temperature field plotted in Fig. 73 is non-uniform especially at the junction between the PV cells. This result cannot be assessed with our in-house 1D Finite Difference (FD) model implemented in MATLAB. The temperature distributions along the PV panel width plotted in Fig. 73 show that the highest values of temperature are obtained in the middle of the PV cells. In the junction zone between two adjacent PV-cells, the temperature values decrease for both studied PV panels.

These numerical predictions are in agreement with the numerical work of Zhou et al. [69]. One can think that it is possible that the gap between two adjacent PV cells changes and leads to mechanical stress concentrations. That is the reason why thermo-mechanical FE simulations were performed for both studied PV panels.

5.3. Thermo-mechanical FE modeling and simulations

In the previous section, thermal FE analysis were performed on two commercial PV panels made with silicon PV cells. From our previous FE predictions, one found that the temperature field inside a PV panel is not homogeneous and particularly at the junction between two adjacent PV cells. It is known that the volume of a body varies when it is subjected to a temperature change: it will expand if it is heated or contract if cooled. If the body is free to expand or contract, its volume will change without any stresses.

However, the temperature change induces stresses if the body is partially or fully constrained. The heterogeneous temperature field in the neighboring of two adjacent PV cells combined with the mismatch of the material's thermal expansion coefficient values in the assembly could induced compression or tensile stresses. Consequently, thermo-mechanical FE simulations are performed to investigate the internal stress states in the different layers that compose commercial PV panels. Two different thermal loading conditions are considered: first in NOCT and next in thermal cycling test according to the IEC 61215 standard for accelerated aging [70].

5.3.1. Geometry and mesh

To estimate the internal stress states induced by the temperature field inside both studied PV panels, 2D plane stress FE models were created using the commercial FE code ABAQUS/CAE. The FE models correspond to a cross-section of a studied PV panel in its plane of bending (i.e. along the width of the PV panels). To reduce the computational time requirements, we took advantage of the geometrical symmetries of the studied PV panels. Thus, one half of the PV panels was only modeled.

The left side of both studied PV panels incorporates the metallic frame. The design of the metallic frames can be taken from the sketches of the PV panel provided by the manufacturers. In

order to minimize the problem size (or nodes number), a simplistic form of the frame was then added to the FE models.

The two PV panels considered in this section are the mono-facial VSMS275 and the bi-facial Panasonic225. The cross-sectional sketches of the models are presented in Fig. 74. The effects of residual stresses due to the lamination process are neglected in the present numerical work. Moreover, the Anti-Reflective Coating (ARC) as well as the copper ribbon wires were neglected in the FE modeling. The dimensions for each layer are summarized in Table 17 for the VSMS275 PV panel and in Table 18 for the Panasonic225 PV panel.

In the present problem, fully coupled thermal-stress analyses were conducted for different thermal loading conditions. In these FE analyses, the heat transfer problem and mechanical one are solved simultaneously. The solver used to obtain the thermal and mechanical solutions is ABAQUS/Standard.

In ABAQUS/Standard solver, the temperatures are integrated using a backward-difference scheme, and the nonlinear coupled system is solved using Newton's method. For each FE model developed under ABAQUS/CAE, the different parts (or layers) were meshed using standard 4-node coupled temperature-displacement plane stress elements.

The elements are denoted by CPS4RT in ABAQUS library [68] (4-node bilinear displacement and temperature with reduced integration and hourglass control). The meshes used in the different FE analyses are presented in Fig. 7. The mesh of VSMS275 PV panel is composed with 86,900 elements leading to 94,824 nodes, whereas the mesh of Panasonic225 PV panel is built with 129,560 elements leading to 137,511 nodes.

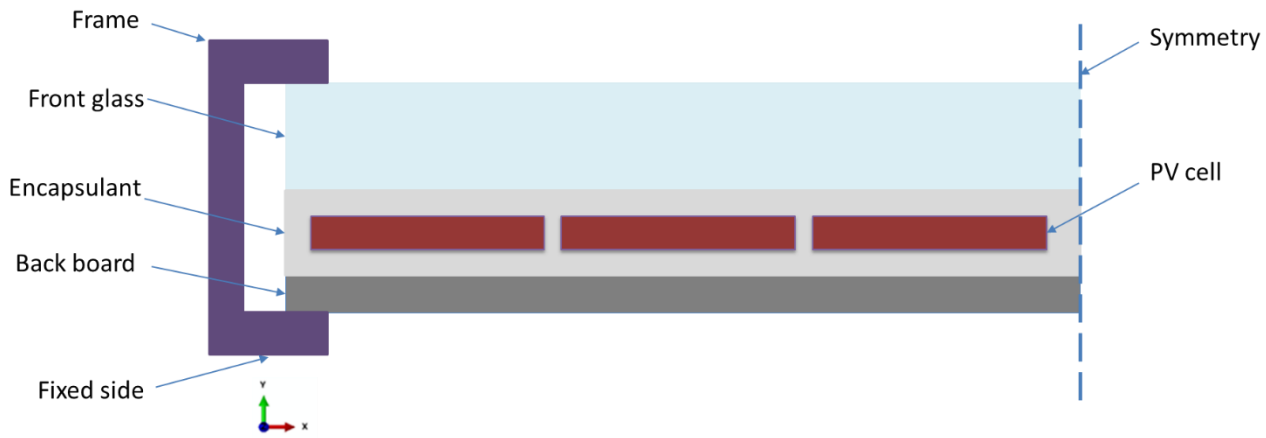

(a)

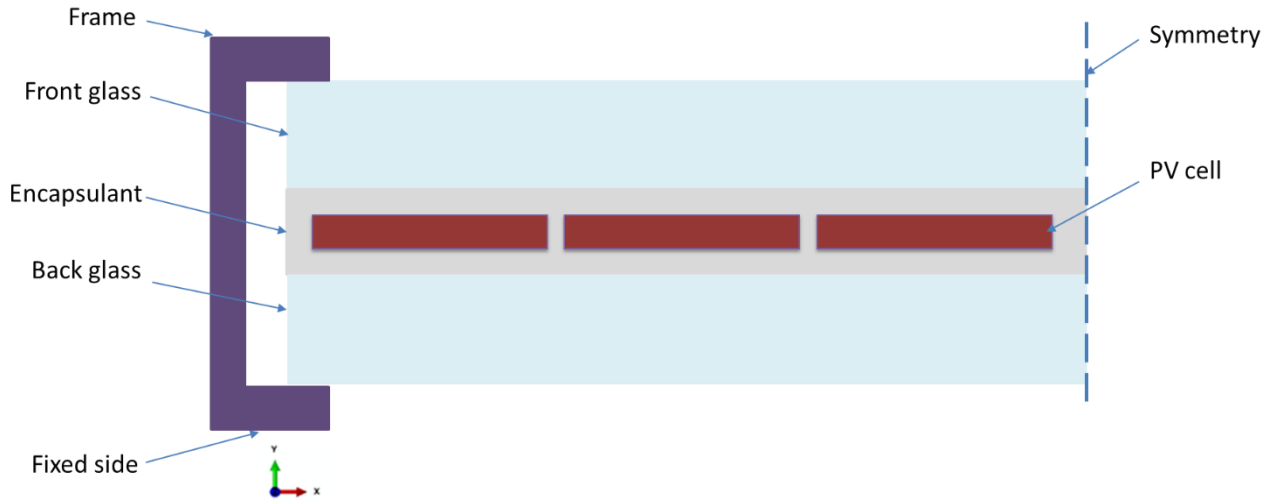

(b)

Fig. 93 Not-to-scale representative cross-sectional sketches
for the FE models of VSMS275 PV panel (a) and Panasonic225 one (b).

In Fig. 75, the x-direction is considered as the direction along the PV panel's width, whereas the y-direction is taken along its thickness. For both meshes presented in Fig. 75, the glass layer was displayed in light blue, the insulation layer in gray, PV cells in red and the backboard layer in dark blue (Fig. 75a).

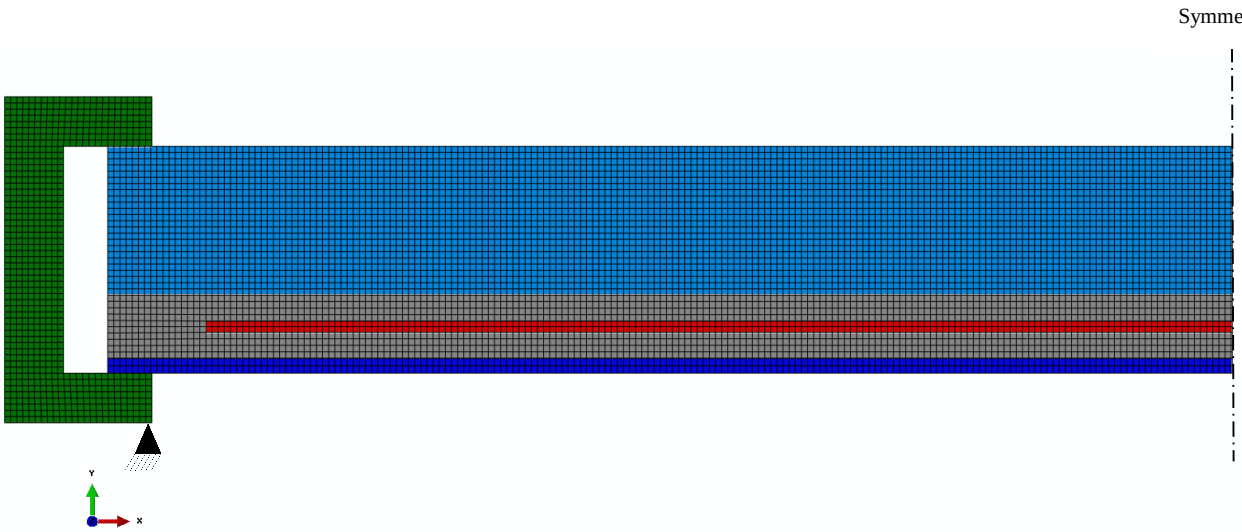

(a)

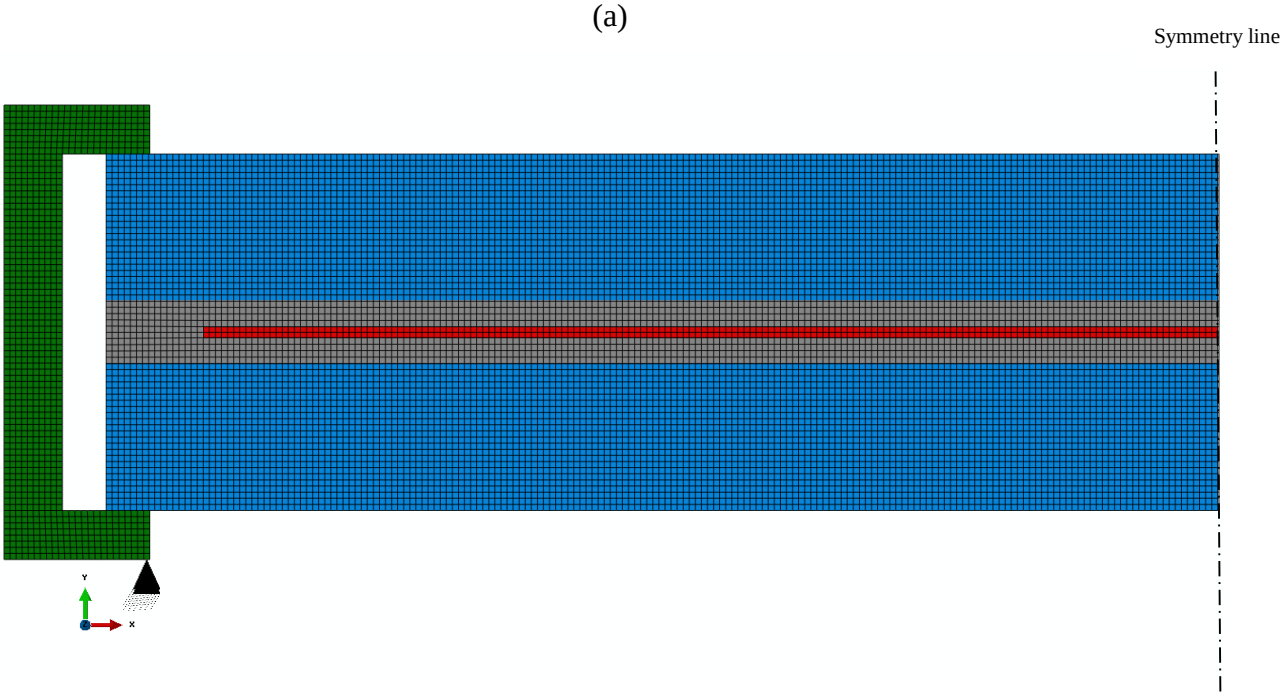

(b)

Fig. 94 Not-to-scale Meshes (on the frame side) used in both FE analyses for the different PV panels cross-sections: VSMS275 (a) and Panasonic225 (b).

Mechanically, some boundary conditions are imposed. The right side of the model is taken as symmetry condition. The bottom and top boundaries of the PV panel were left free. One point on the aluminum frame was taken as an anchor point for the model to pin it, at the bottom left. The choice of the position of the anchor point can be justified by the mechanical properties of the aluminum. It is expected that the aluminum frame is not highly affected mechanically by the temperature, due to its low thermal expansion coefficient.

Since the considered problem is 2D, one may use either plane strain or plane stress assumption. However, the plane strain assumption cannot be taken since the PV panel can extend freely in the out-of-plane direction. The loading is in the plane of symmetry of the PV panel (like the loading that can be seen in the case of a bending test), therefore the plane stress assumption is more appropriate to simplify the FE modelling. To check the difference between these two assumptions, a simple thermo-mechanical model was run with ABAQUS in both cases, and the only difference between both predictions lies in the level of stresses achieved.

5.3.2. Material properties

To perform thermal-stress analyses of the PV panels subjected to different thermal loading conditions, it is necessary to define the thermal and mechanical behavior of the materials that build the layers of these PV panels. The thermal properties of the materials have already been defined in the previous section (Tables 15 and 16).

The magnitude of the stresses induced by thermal loading conditions are proportional to the material’s thermal expansion coefficient value and also to the material's Young's modulus value. Some additional assumptions were made since there is a lack of information about the materials in the data sheets provided by the PV panel manufacturers.

The thermal expansion or contraction is assumed to be isotropic and temperature independent as well as the linear elastic behavior of the different materials, except EVA. Consequently, the properties to provide for the mechanical analyses are: the thermal expansion coefficient, Young’s

modulus and Poisson's ratio. The mechanical properties of the materials composing the PV panels are listed in Table 17 for the VSMS275 PV panel and in Table 18 for the Panasonic225 PV panel. All of these physical properties are introduced in ABAQUS/CAE for the FE simulations.

Table 20: Mechanical properties of the materials composing the layers of the VSMS275 PV panel

Layer	Length [mm]	Thickness [mm]	Thermal expansion coefficient [10^{-6}/K]	Young's modulus [MPa]	Poisson's ratio [-]
Front glass	382	4.00	8.0	73.0	0.23
EVA	382	0.46	270.0	thermoelastic	0.33
PV cell	125	0.20	2.5	130.0	0.22
Tedlar	382	0.30	50.4	2.8	0.33

Table 21: Mechanical properties of the materials composing the layers of the Panasaonic225 PV panel

Layer	Length [mm]	Thickness [mm]	Thermal expansion coefficient [10^{-6}/K]	Young's modulus [GPa]	Poisson's ratio [-]
Front glass	382	4.00	8.0	73	0.23
EVA	382	0.46	270.0	thermoelastic	0.33
PV cell	125	0.20	2.5	130	0.22

The elastomeric polymer EVA exhibit a complex thermoelastic behavior that is strain rate and temperature dependent; that is the reason why the Young's modulus value of EVA is not given in Tables 17 and 18. The thermoelastic behavior of EVA was experimentally studied in several works. To illustrate the specific behavior of EVA, the Young's modulus vs temperature curves are

plotted in Fig. 76. These curves were taken from the experimental work presented in Paggi et al. [44].

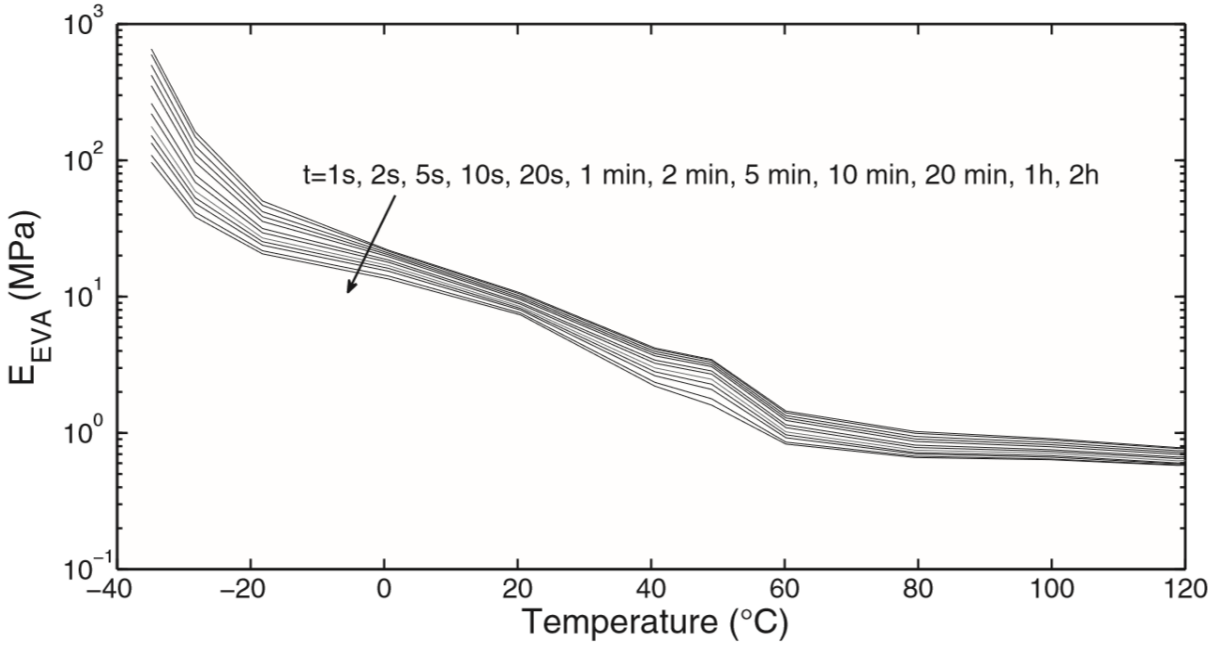

Fig. 95 Young's modulus vs temperature curves of EVA for different relaxation times (taken from the work of Paggi et al. [44]).

In Fig. 76, the Young's modulus of EVA increases slowly until the temperature decreases to -20°C. After this temperature value, the Young's modulus of EVA increases sharply to achieve values close to 1 GPa (depending on time relaxation value). The glass transition region (with the glass transition temperature, T_g) can be defined from the curves plotted in Fig. 76.

The glass transition region corresponds to the strong increase of Young's modulus values when the temperature falls below 0°C. Through the glass transition, the mechanical properties of EVA change without a phase transition. From Fig. 76, the glass transition region begins at -40°C and ends at about 0°C depending on time relaxation value.

In the glass transition region, the mechanical behavior is quasi brittle (glassy state) while after the mechanical behavior is close to the one of a rubber (rubbery state). For temperature values higher than 60°C, the Young's modulus of EVA is quite constant and equal to 1MPa.

In all the FE simulations performed, we assume that the temperature changes are very slow. So the time relaxation (or strain rate) influence on the mechanical behavior of EVA was not taken into account in our simulations. Consequently, the long term response of EVA plotted in Fig. 76 was considered and introduced in ABAQUS/CAE. With this assumption, the behavior of the encapsulant is considered as thermoelastic.

Moreover, the thermal and mechanical properties of the metallic frame surrounding the PV panels have to be defined since the frame is taken into account in our FE models. Since we do not have material data on the frames of both PV panels, we assumed that the frame is always made of aluminum and its physical properties are temperature independent. The material properties of the frames are reported in Table 19.

Finally, it should be mentioned that all the mechanical properties listed in Tables 17-19 are taken at 25°C.

Table 22: Thermal and mechanical properties of the aluminum frame used in both studied PV panels

Frame	Thermal conductivity [W/m/K]	Specific heat capacity [J/kg/K]	Thermal expansion coefficient [10^{-6}/K]	Young's modulus [GPa]	Poisson's ratio [-]
Aluminum	237	898.7	23.1	68.9	0.33

5.3.3. Loading conditions

The thermal response of the PV panel influences the stress state inside the PV panel. Two different sets of thermal boundary conditions were considered in the present study. The first set of

thermal boundary conditions corresponds to the NOCT test, because this test is close to the working field conditions. The boundary conditions used to simulate the NOCT test have been already defined in the previous section.

The second set of thermal boundary conditions corresponds to the IEC 61215 standard for accelerated aging [70]. In the cycling test defined in the IEC 61215 standard, the PV panels are successively cooled to -40°C and next heated to 85°C. The time-related evolution of temperature defined IEC 61215 standard is plotted in Fig. 77.

Some mechanical boundary conditions have to be added in the coupled FE models. Symmetry boundary conditions are introduced on the right side of the PV panels (symmetry line). On the opposite edge of the PV panels (corresponding to the left side), the bottom side of the frame is simply supported in the direction orthogonal to the longitudinal axis (y-axis in Fig. 74).

Furthermore, the frame is on contact with the top and bottom side of the PV panels. Since we have any information concerning the contact conditions between the PV panels and their frames, we assumed that these contacts can be modeled with the “tie constraint” option of ABAQUS/CAE FE code.

The “tie constraint” can be used in coupled temperature-displacement FE analyses. With this contact option, all the motions and temperature values are passed through the contact surface. It should be noted that the different layers of the studied PV panels are assumed to be rigidly joined together (“tie constraint” option in ABAQUS/CAE FE code).

Consequently, the expansion or contraction of the different layers will be affected by the movement of the others due to the mismatch of coefficient thermal expansion values of the materials inside the PV panels.

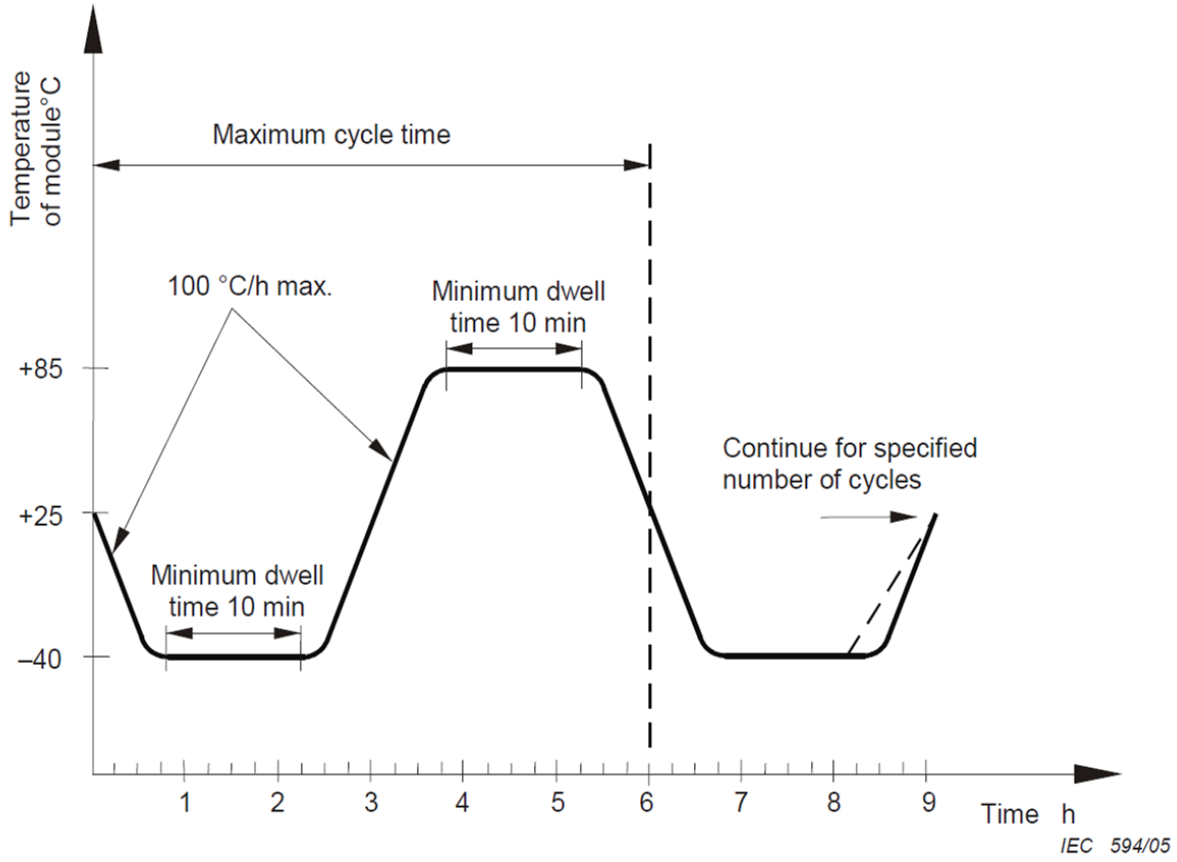

Fig. 96 Thermal cycling test according to the IEC 61215 standard for accelerated aging [70].

5.3.4. Thermo-mechanical FE predictions and discussion

5.3.4.1. FE predictions under NOCT

The horizontal component of displacement vector at nodes (denoted by U1 in ABAQUS/CAE) is first presented in the zone of two adjacent PV cells. It is plotted for both PV panels in Fig. 78, and the values of nodal displacements are presented in meters (m).

The initial value of the gap between two adjacent PV cells is the same for both PV panels and is defined equal to 2 mm. It should be mentioned that the different figures plotted herein are obtained with a scale deformation factor taken equal to 1.

Because of the increase of temperature, the PV panels expand freely towards the left side (opposite to the x-direction) since the right side of both PV panels is constrained with symmetry boundary condition (constrained in the x-direction).

Consequently, the gap between two adjacent PV cells increases and achieves values equal to 2.01502 mm for the VSMS275 PV panel and 2.01124 mm for the Panasonic225. The final gap between two adjacent PV cells is then equal to 15.02 µm for the VSMS275 PV panel and 11.24 µm for the Panasonic225.

These values can be compared with the change in gap width between two adjacent PV cells, measured with digital image correlation technique by Eitner et al. [71].

For non-interconnected PV cells, Eitner et al. [71] found a gap width change ranged between 8 to 16 µm when the PV cells temperature reached roughly a value of 44°C (which is close to the predicted value of NOCT).

Thus, the numerical predictions are in agreement with the experimental results of Eitner et al. [71].

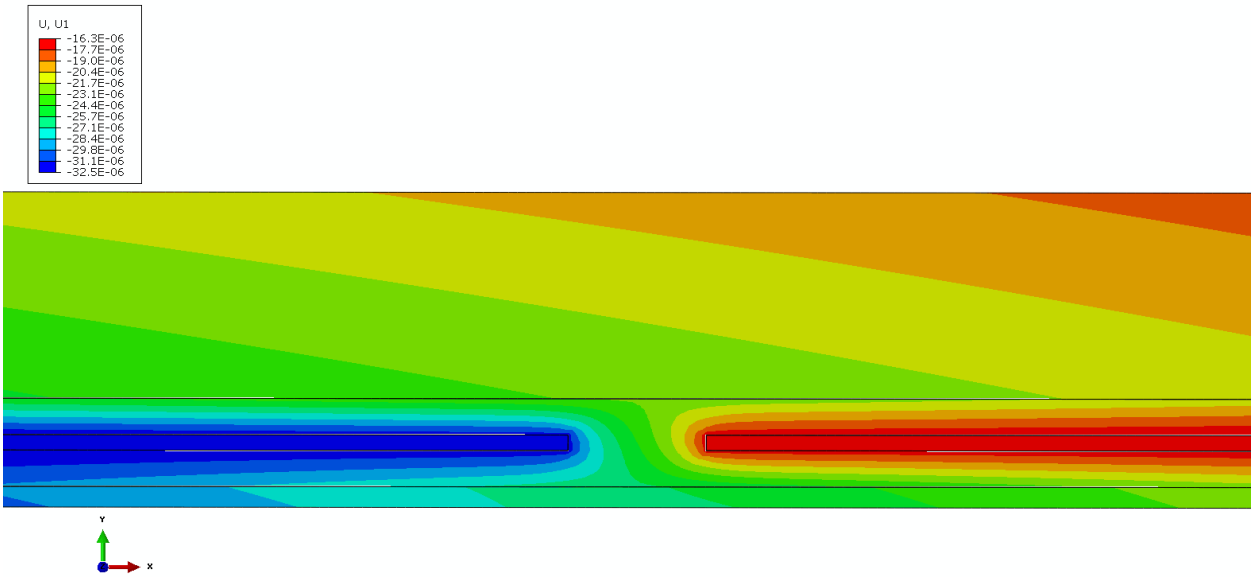

(a)

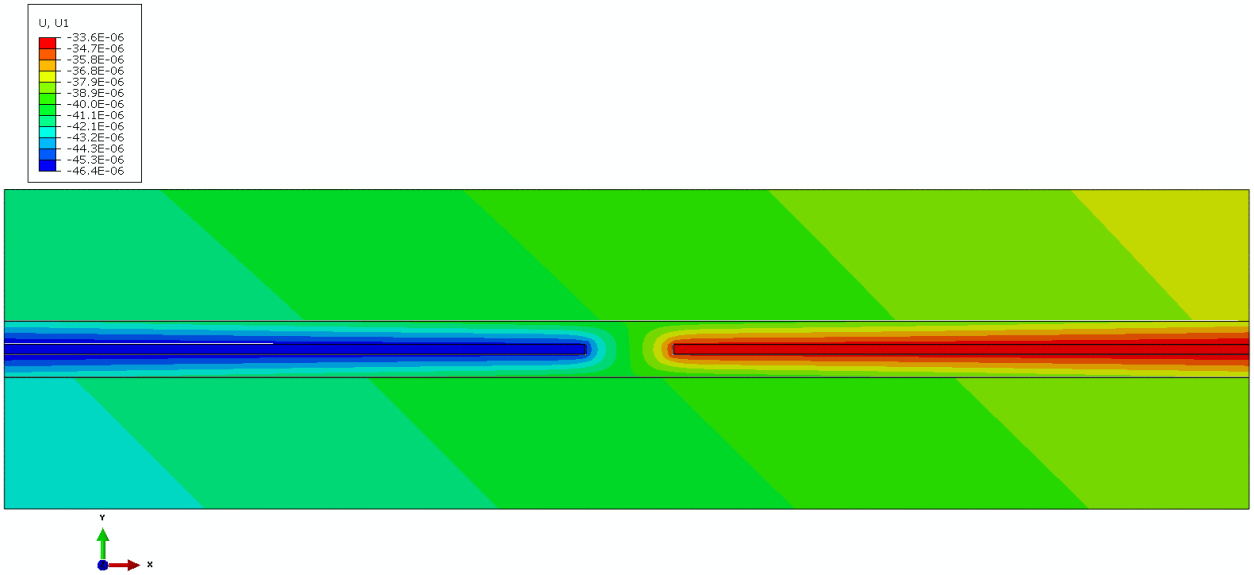

(b)

Fig. 97 Horizontal displacement at nodes (plotted in [m]) predicted under NOCT for VSMS275 (a) and Panasonic225 (b) PV panels.

The vertical component of displacement vector at nodes (denoted by U2 in ABAQUS/CAE and also called deflection) is next presented in the zone close to the symmetry boundary condition (*i.e.* close to the middle of the PV panels).

The deflection is presented for both PV panels in Fig. 79, and its value is also plotted in meters. As expected, for both PV panels, the different layers expand but by different amounts. Consequently, both PV panels bend and their vertical displacement reach their maximum value on the symmetry line (middle of the PV panels). The left side of both PV panels is constrained in the vertical direction during the FE simulations.

In Fig. 79, the vertical displacement achieves maximal values equal to -603.9 µm for the VSMS275 PV panel and -59.5 µm for the Panasonic225. The vertical displacement has a higher value when the bottom layer of the PV panel is in Tedlar; indeed, the layer made with Tedlar has a greater coefficient of thermal expansion (CTE) in comparison with the glass layer (Table 17). Thus, the Panasonic 225 PV panel seems to be stiffer than the VSMS275.

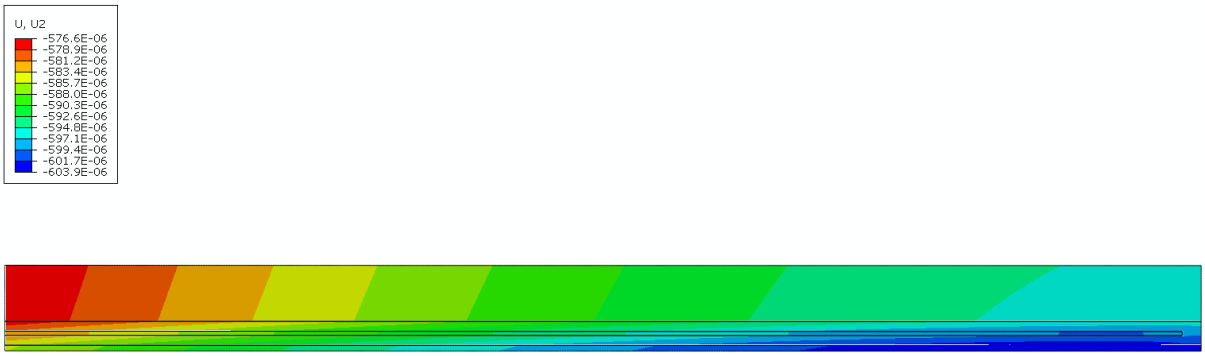

(a)

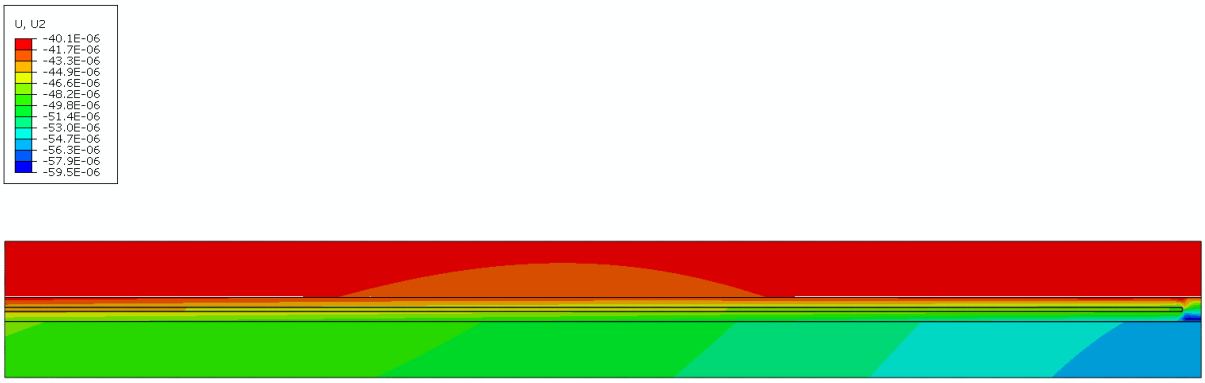

(b)

Fig. 98 Vertical displacement at nodes (or deflection, plotted in [m]) predicted under NOCT for VSMS275 (a) and Panasonic225 (b) PV panels.

The Cauchy stress tensor $\sigma(M)$ is defined as:

$$\sigma(M) = \begin{pmatrix} \sigma_{11} & \sigma_{12} & 0 \\ \sigma_{21} & \sigma_{22} & 0 \\ 0 & 0 & 0 \end{pmatrix} \tag{92}$$

where σ_{11} denotes the normal stress along the x-direction, σ_{22} the normal stress along the y-direction, $\sigma_{12} = \sigma_{21}$ the shear stresses (since the Cauchy stress tensor is symmetric). All the other terms of the Cauchy stress tensor $\sigma(M)$ are equal to zero because the model is in plane stress conditions (2D). The stress state presented in Eq. (91) is illustrated below in Fig. 80.

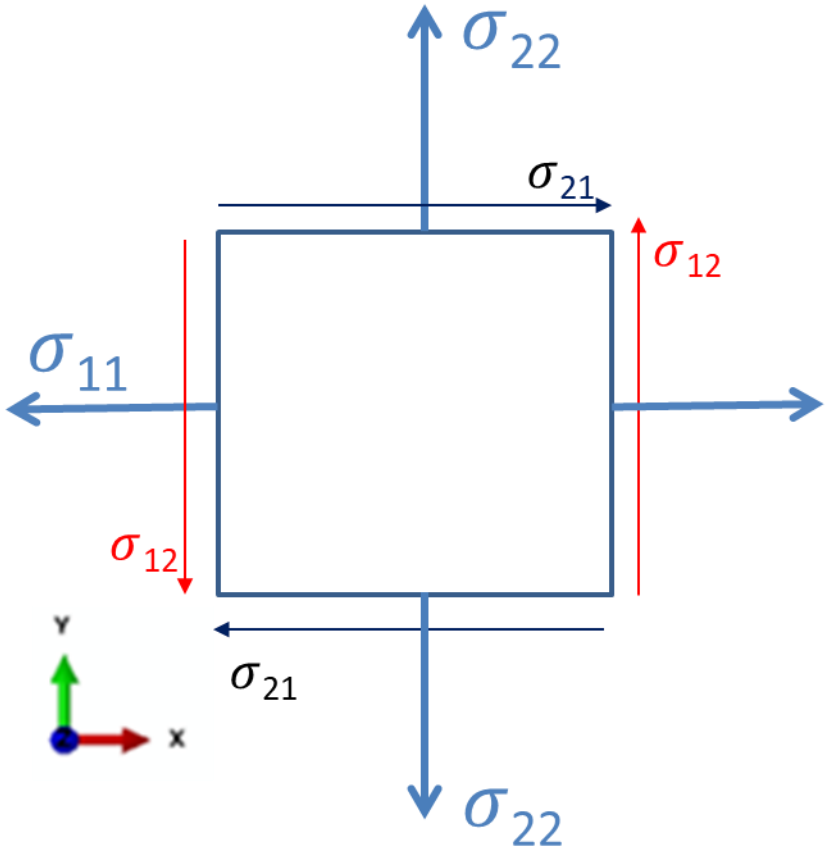

Fig. 99 Illustration of plane stress state in xy-plane corresponding with Eq. (91).

Since the PV panels bend as seen in Fig. 79, the normal stress along the x-direction σ_{11} was investigated.

The normal stress σ_{11} is plotted at the spot of interest, which is the zone near the symmetry line in Fig. 81. The distribution of normal stresses presented in Fig. 81 are due to the difference between CTE values of the materials making up of the PV panels and the temperature gradient. In Fig. 81, the values of normal stress σ_{11} predicted in NOCT are weak for both PV panels. In comparison, the elastic limit of silicon or EVA is ranged between 100 to 200 MPa for instance.

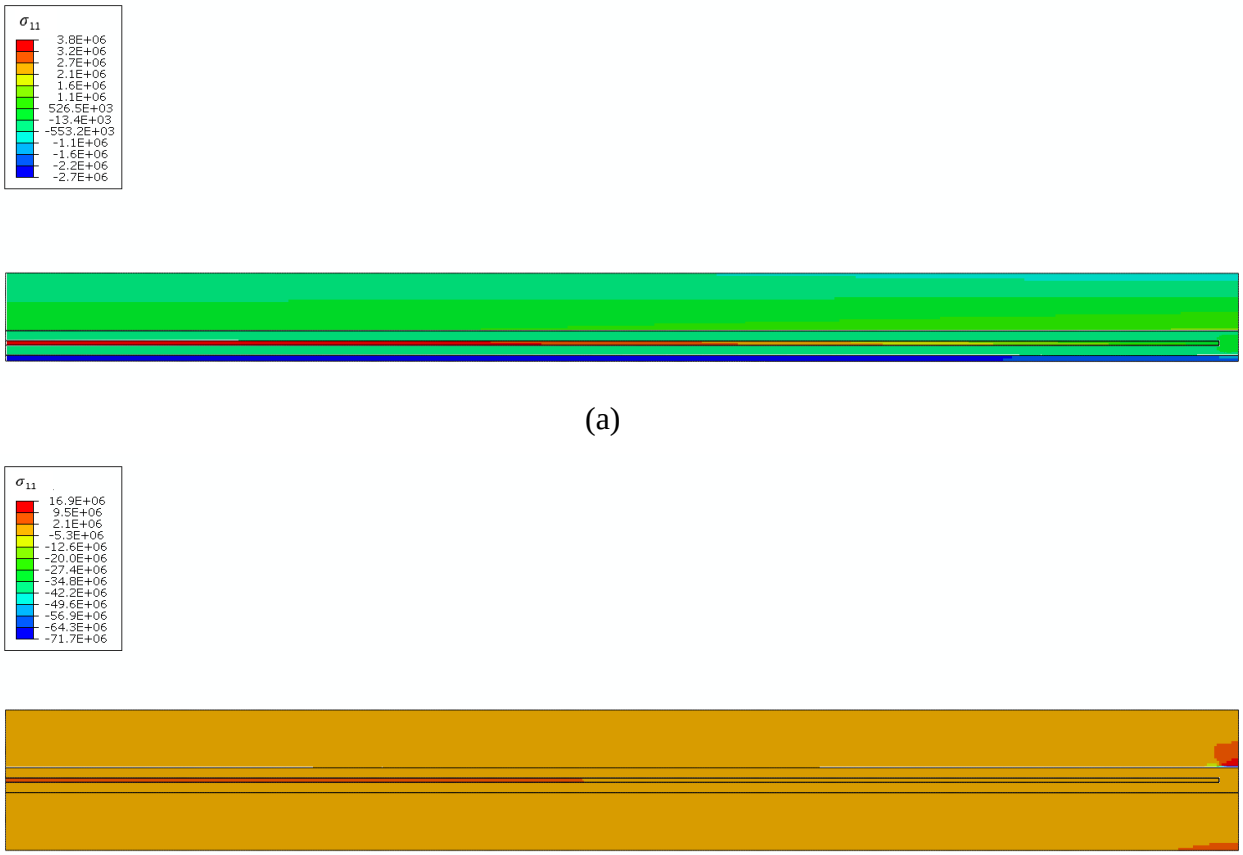

Fig. 100 Distribution of the normal stress (σ_{11} in [Pa]) close to the symmetry line in the case of VSMS275 (a) and Panasonic225 (b) PV panels.

The normal stress σ_{11} is next presented in the area of two adjacent PV cells in Fig. 82. In this area of the PV panels, the values of stresses reach values of the same order than in the area close to the symmetry line.

Even if the stress values are small (in the order of a few MPa), the distributions of the normal stress σ_{11} are clearly different between the two zones for the same PV panel when comparing Figs. 81 and 82. The normal stress predictions along y-direction, denoted by σ_{22} in ABAQUS/CAE, are not presented since the values are always close to zero in all the FE predictions in NOCT. For the same reason, the shear stress predictions (denoted by σ_{12}) are not presented.

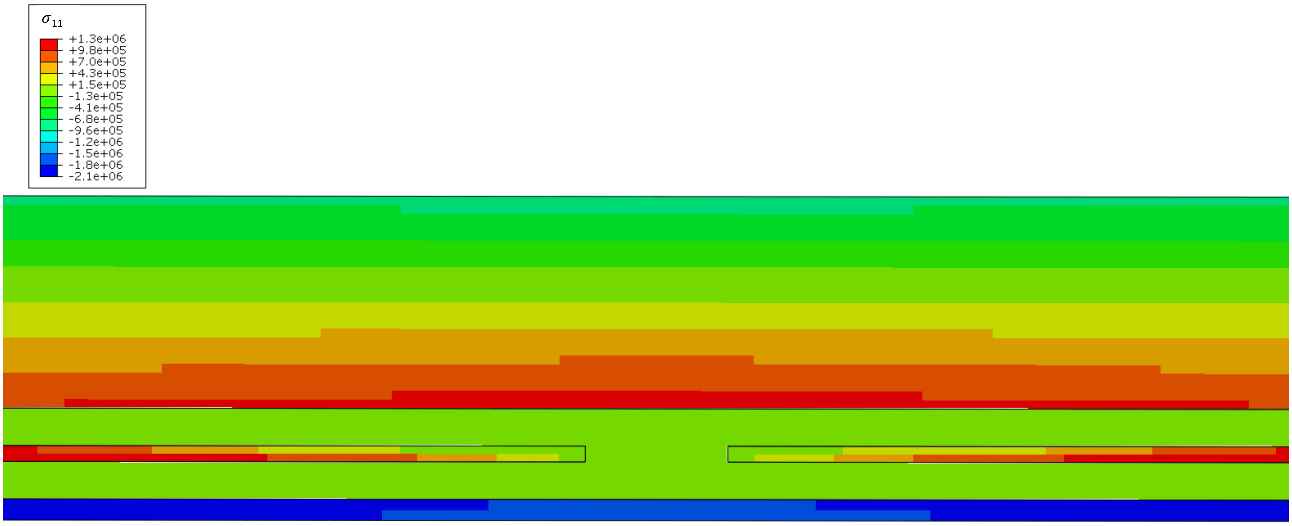

(a)

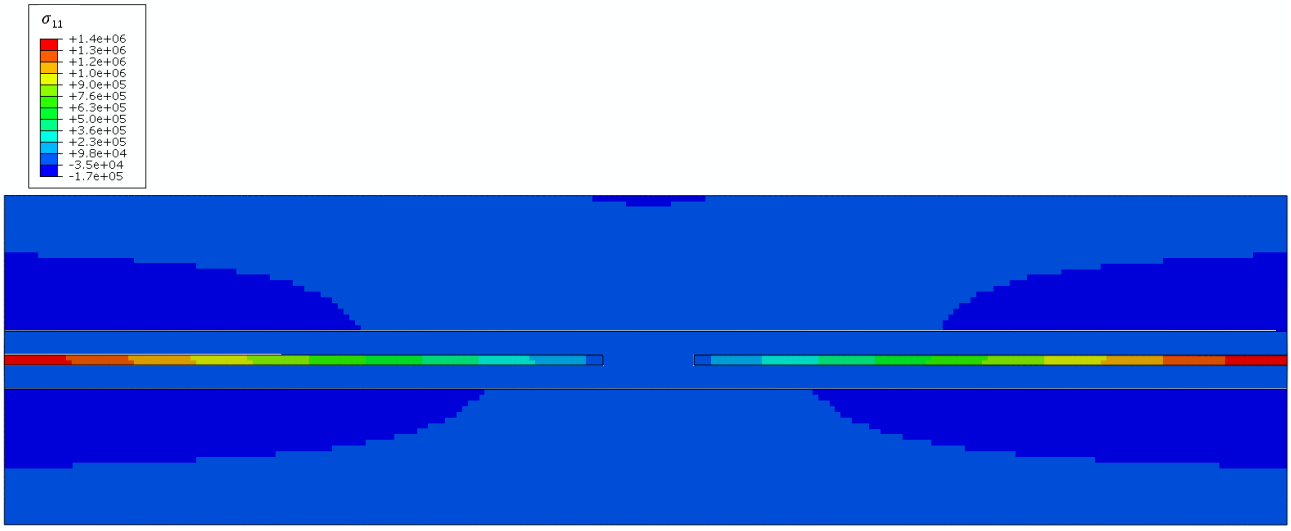

(b)

Fig. 101 Distribution of the normal stress (σ_{11} in [Pa]) between two adjacent PV cells in the case of VSMS275 (a) and Panasonic225 (b) PV panels.

The normal stress σ_{11} distribution through the PV panel thickness was investigated for both studied PV panels. In Fig. 83, the normal stress σ_{11} for each PV panel was plotted for a path of nodes located at the middle of the PV cell. For both PV panels, the middle part of PV cell layer is in tension (reaching roughly 3.7 MPa, the highest stress value), whereas the insulation layer (in EVA) is almost in a free stress state. In the case of VSMS275 PV panel, the backsheet layer is in compression (reaching roughly 3.7 MPa, the highest stress value) as seen in Fig. 83a.

For the VSMS275 PV panel, the front surface of the glass layer is in tension, whereas the inner surface of the glass layer is in compression as seen in Fig. 83a.

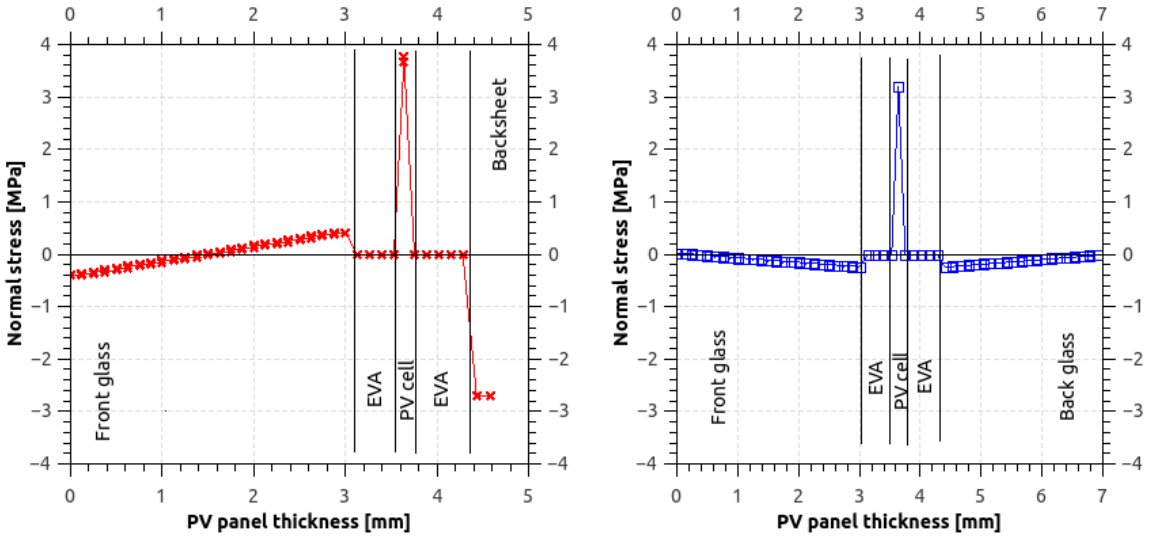

(a) (b)

Fig. 102 Distribution of the normal stress (σ_{11} in [Pa]) through the PV panel thickness in the case of VSMS275 (a) and Panasonic225 (b) PV panels.

5.3.4.2. FE predictions under thermal cycling test (i.e. TCT)

The temperature history defined in Fig. 77 was introduced as a boundary condition in the FE thermo-mechanical simulations performed with ABAQUS/CAE. The first step of the simulations consists of a cooling stage at -40°C. At the end of this step, all the nodes of both studied PV panels possess a temperature value equal to -40°C. Therefore, the nodal temperature distributions predicted for both studied PV panels are not presented.

Due to the mismatch of CTE values between the different layers, both studied PV panels bend. The vertical deflection is higher on the symmetry line and is equal to zero on the frame side (where the vertical displacement is constrained by a boundary condition). The maximum predicted value of vertical deflection is equal to 2.863 mm in the case of VSMS275 PV panel; whereas it is roughly equal to zero (5.719 µm more precisely) in the case of Panasonic225. As expected, the vertical component of nodal displacement has a higher value when the bottom layer of the PV panel is in Tedlar, then in the case of VSMS275 PV panel.

In Fig. 84, the horizontal component of nodal displacement (denoted U1 in ABAQUS/CAE) is presented in the region around two adjacent PV cells. The nodal displacement values are plotted in meters [m] in Fig. 84. With the temperature decrease, the PV panels shrink freely towards the right side (opposite to the x-direction) since the left side of both PV panels is only constrained in the y-direction. Consequently, the gap between two adjacent PV cells decreases and achieves values equal to 1.99023 mm for the VSMS275 PV panel and 1.99413 mm for the Panasonic225.

The final gap between two adjacent PV cells is then equal to -9.77 µm for the VSMS275 PV panel and -5.85 µm for the Panasonic225. These values can be compared with the experimental values of change in gap width between two adjacent PV cells obtained by Eitner et al. [71].

For non-interconnected PV cell$_s$, Eitner et al. [71] found a gap width change roughly equal to -20 µm when the PV cells temperature reached a value of -20°C. Thus, the numerical predictions underestimate the gap change in comparison with the experimental results of Eitner et al. [71].

This can be explained by the fact that the Young modulus as a function of the temperature in the case of the EVA (presented in Fig. 76) does not provide the Young modulus at -40°C.

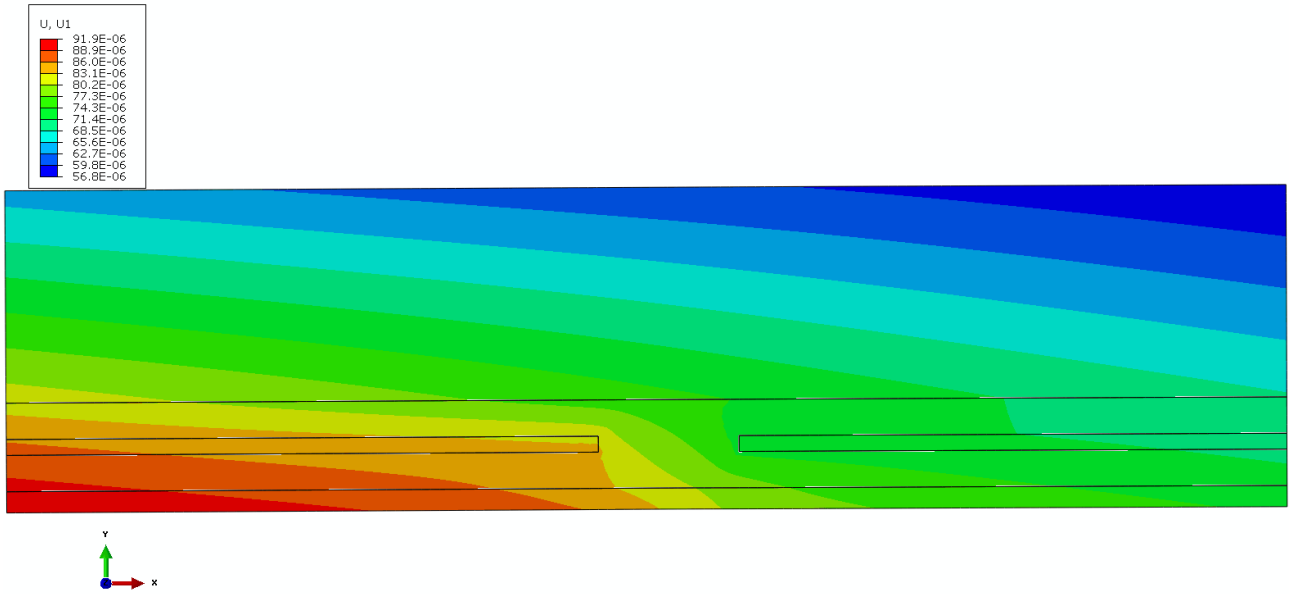

(a)

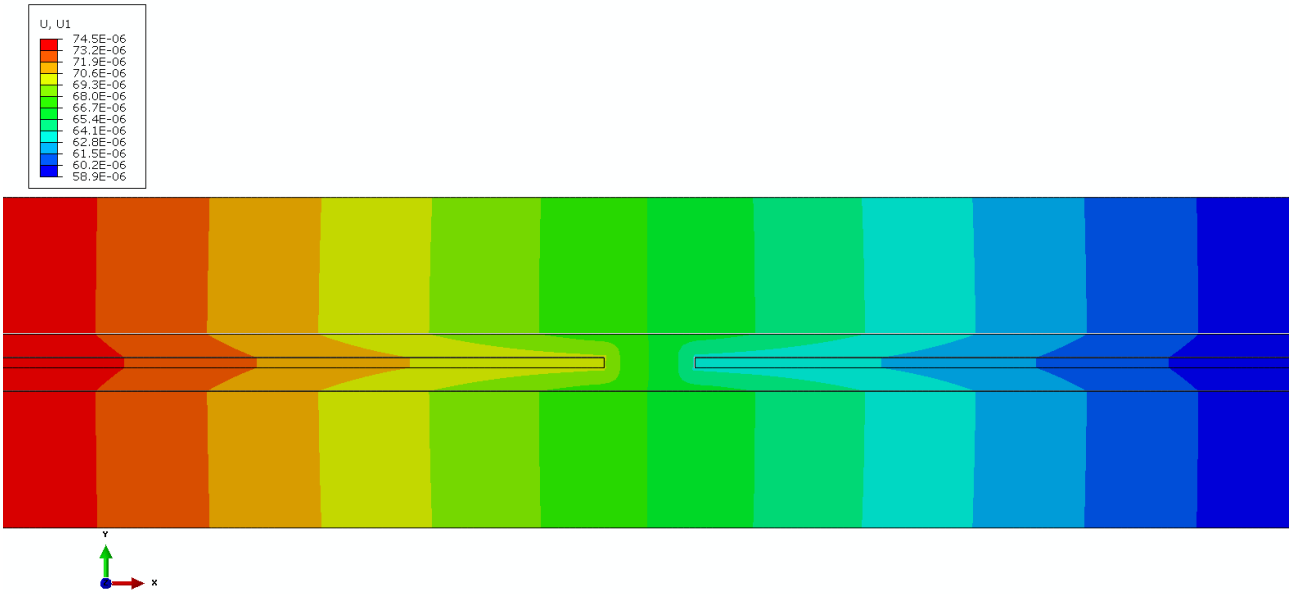

(b)

Fig. 103 Horizontal component of nodal displacement (plotted in [m]) predicted by FE simulations for: VSMS275 PV panel (a) and Panasonic225 PV panel (b).

Since the PV panels shrink as seen in Fig. 84, the normal stress along the x-direction (denoted by σ_{11} in ABAQUS/CAE) was next investigated. The normal stress σ_{11} is plotted at the spot of interest, which is the region around two adjacent PV cells, in Fig. 85.

The values of the stress component σ_{11} are plotted in Pascal [Pa] in Fig. 85. In both FE simulations, when the PV panel reaches a temperature of -40°C, the PV cells undergo high levels of compression stresses. These stresses are maximum in the center part of PV cells. The normal stress distribution was plotted along a vertical path of nodes passing through the different layers in Fig. 86. The path location was chosen near the center of the PV cells because the stress values are highest in this area.

In Fig. 86, the normal stress distribution across the thickness was plotted at the end of the cooling stage and for both PV panel. It should be noted that the stress values plotted in Fig. 86 are in MPa.

The maximum value of normal stress is approximately equal to 54 MPa for VSMS275 PV panel and 46 MPa for Panasonic225. These values are predicted for the layer corresponding to the PV cell in both PV panels (mono-facial and bi-facial). The stress values achieved during cooling are larger than the ones experienced in NOCT. These stress levels could cause some damages to the PV cells over time.

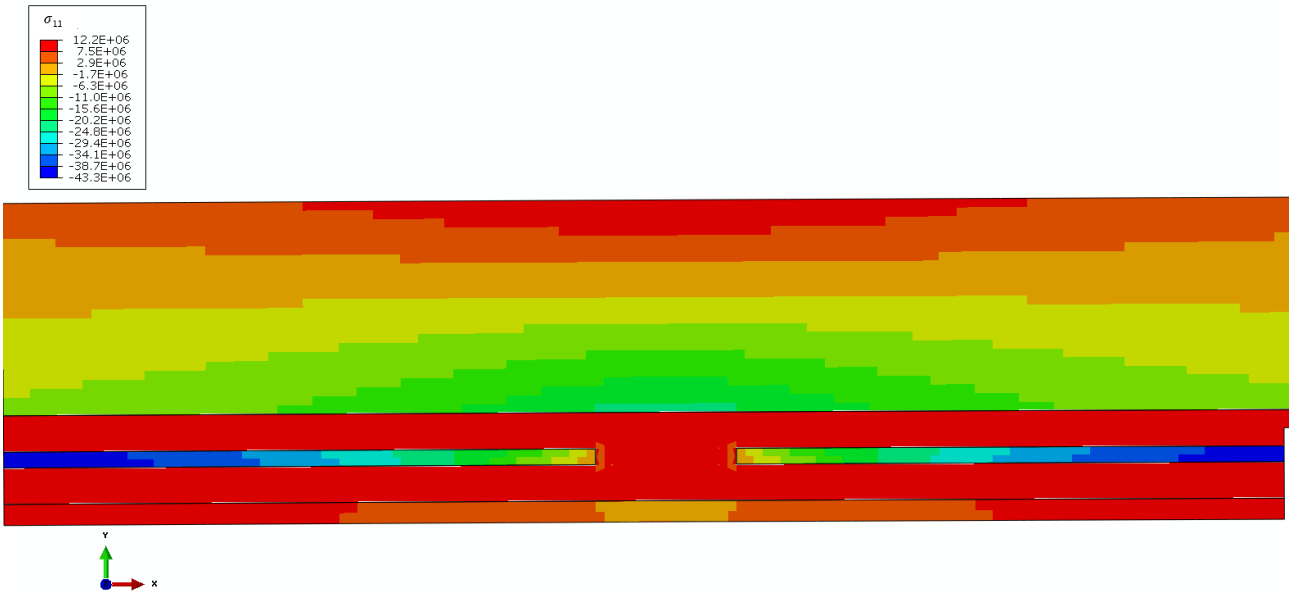

(a)

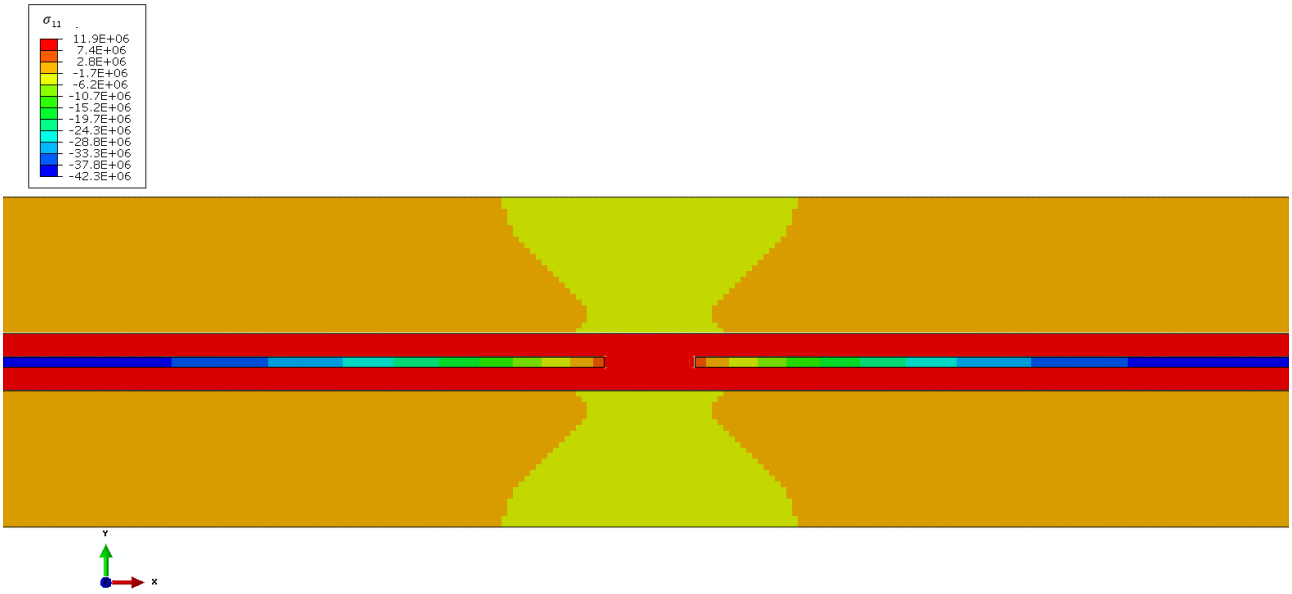

(b)

Fig. 104 Normal component σ_{11} of Cauchy stress tensor (plotted in [Pa]) predicted by FE simulations for the VSMS275 PV panel (a) and the Panasonic225 PV panel (b).

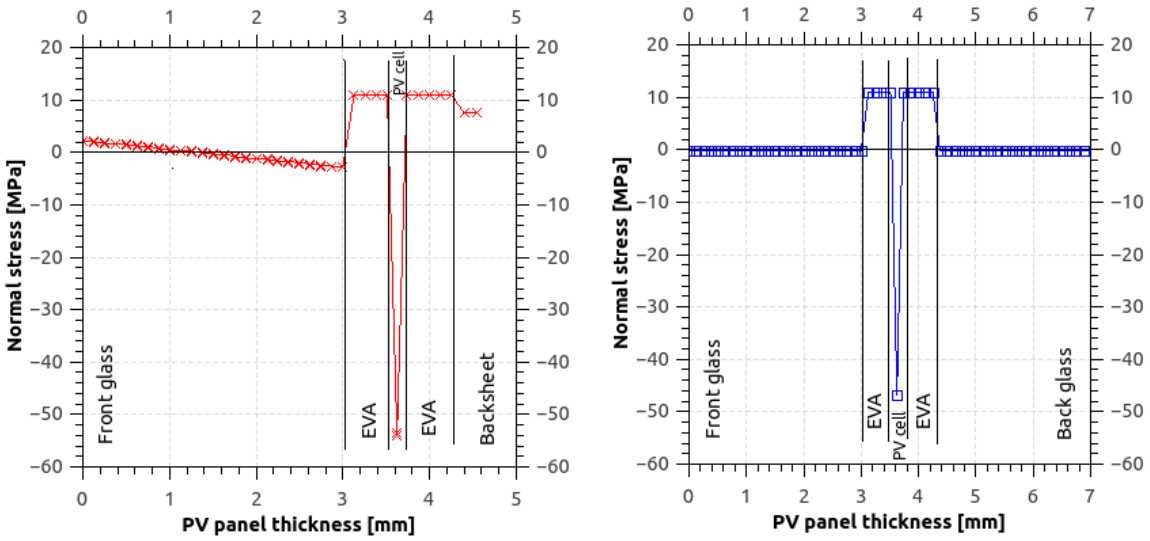

(a) (b)

Fig. 105 Distribution of the normal stress (σ_{11} in [MPa]) through the PV panel thickness after the cooling stage in the case of the VSMS275 PV panel (a) and the Panasonic225 PV panel (b).

In the cooling stage, the EVA layers of the two PV panels are subjected to tensile stresses of the order of 12 MPa; whereas the PV cells layer is in compression. The increase of stress levels in the insulation layer are mainly due to the drastic increase in Young's modulus value of EVA when temperatures drop below 0°C as seen in Fig. 76.

Moreover, the difference between the stress states found between the PV cell and insulation (EVA) layers may lead over time to plastic deformations in the metallic interconnections (such as ribbons and wires) or contribute to delamination between the layers. The FE predictions presented above are in agreement overall with the numerical predictions presented in the work of Owen-Bellini et al. [72].

Even if the normal stress σ_{11} reaches high values, the other components of Cauchy stress tensor remain close to zero. The effective stress defined in the sense of von Mises is plotted in Fig. 87 for the two studied PV panels. One can see that the von Mises stress values are almost equal to the ones of normal stress σ_{11} presented in Fig. 85.

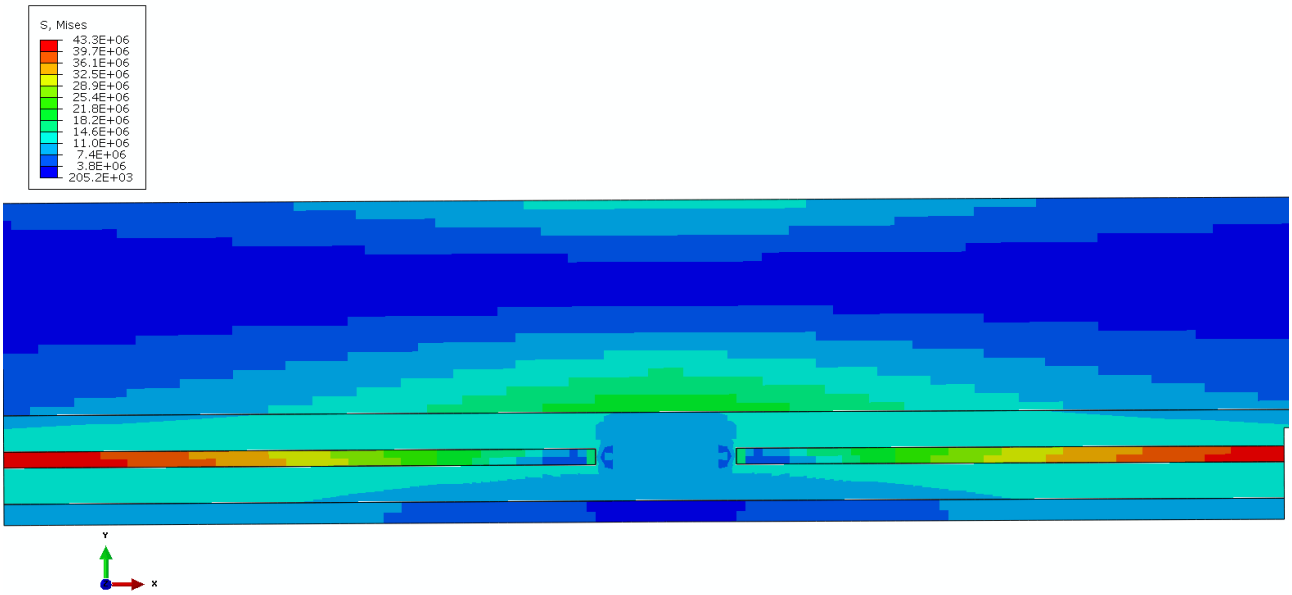

(a)

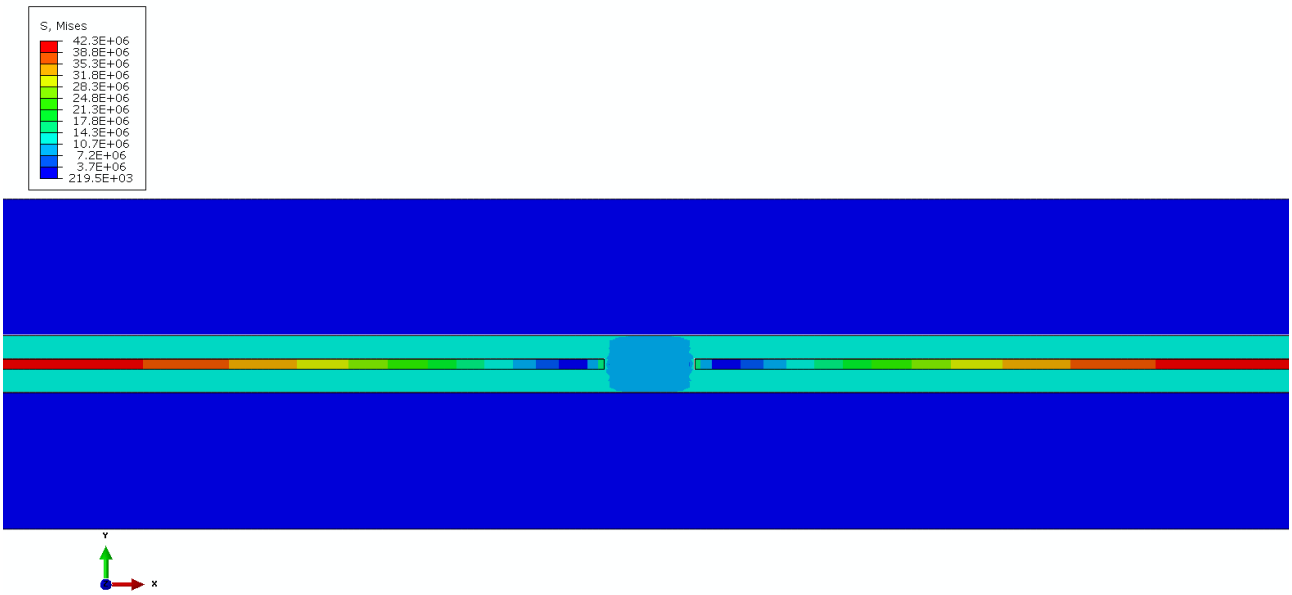

(b)

Fig. 106 The effective von Mises stress values (plotted in [Pa]) predicted by FE simulations for the VSMS275 PV panel (a) and the Panasonic225 PV panel (b).

In the IEC 61215 standard for accelerated aging, the cooling stage is next followed by a heating stage until the temperature reaches 85°C. At the end of the heating step, all the nodes of the two studied PV panels achieve a temperature value equal to 85°C. Consequently, the nodal temperature distributions predicted for both studied PV panels are not presented.

As expected, the vertical nodal displacement reaches the maximum value on the symmetry line and is equal to zero on the frame side because the vertical displacement is constrained to zero. On the symmetry line, the predicted value of vertical deflection is equal to -1.9 mm in the case of VSMS275 PV panel; whereas it can be considered equal to zero in the case of Panasonic225 (in fact 17.9 µm).

In agreement with FE predictions under NOCT, the vertical displacement has a higher value when the bottom layer of the PV panel is made in Tedlar, which is the case of the VSMS275 PV panel.

The horizontal displacement (denoted U_1) values predicted by the FE simulations are presented in Fig. 88 for the zone between two adjacent PV cells. The nodal temperatures are equal to 85°C everywhere in the PV panels and, thus they are not presented there. The zone of interest is far from the symmetry line of PV panel and from the metallic frame side.

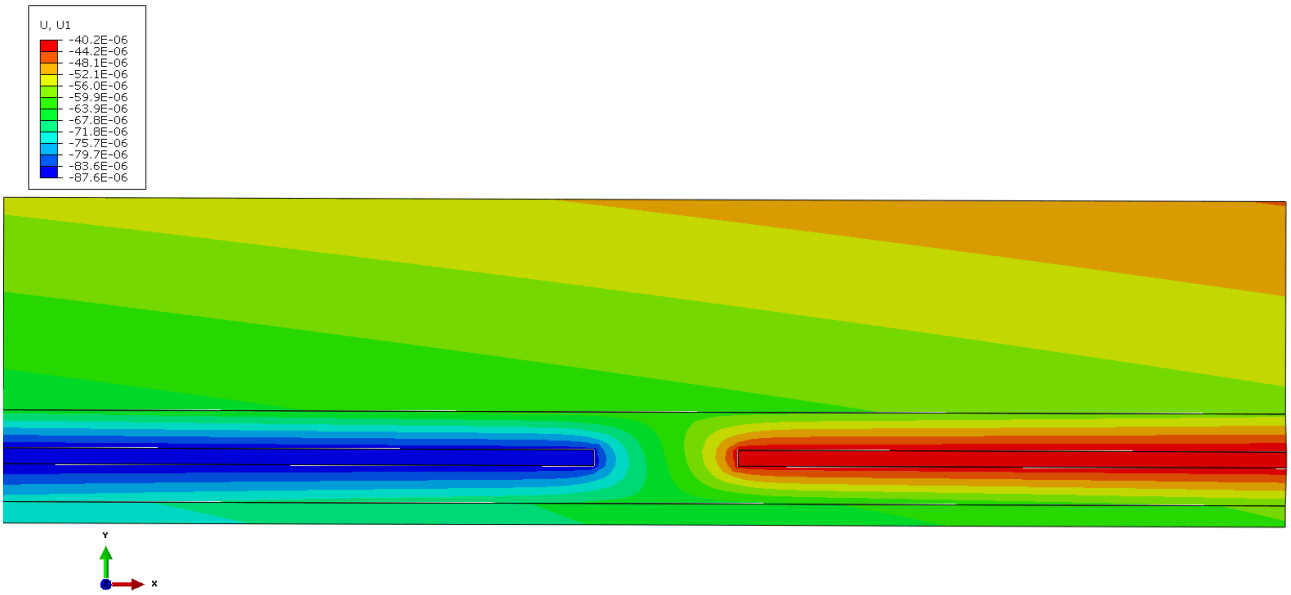

(a)

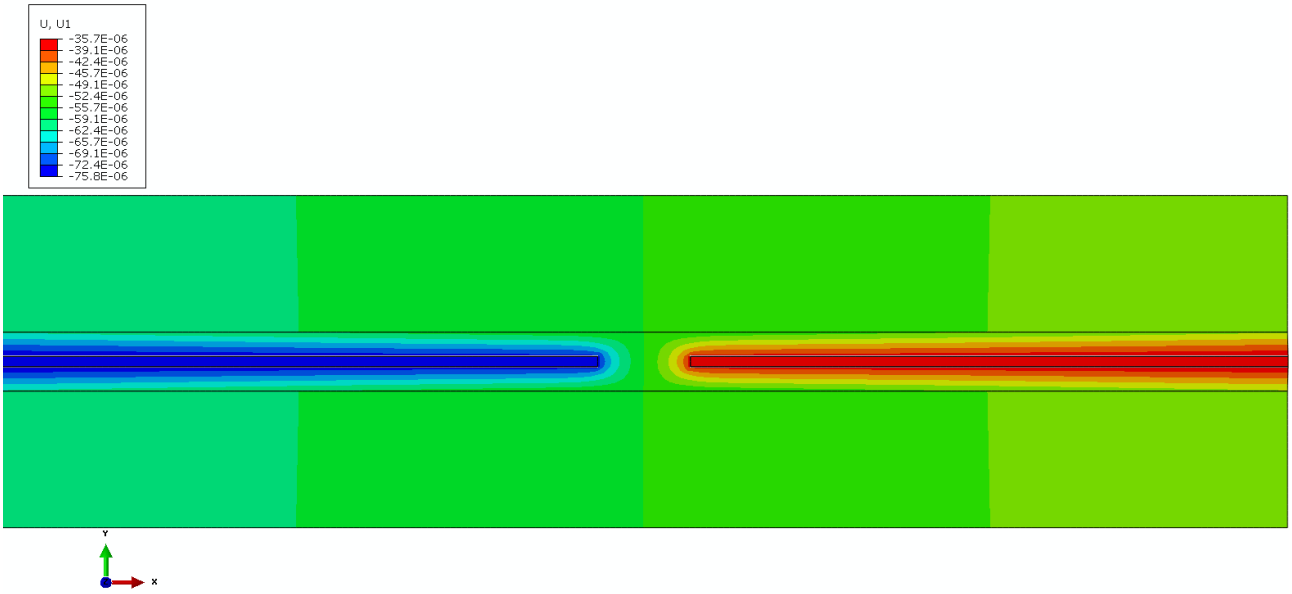

(b)

Fig. 107 Horizontal component of nodal displacement U_1 (plotted in [m])predicted by FE simulations for the VSMS275 PV panel (a) and the Panasonic225 PV panel (b).

In agreement with FE predictions under NOCT, the layers expand freely in the opposite direction to x-direction as seen in Fig. 88. Therefore, the PV cells move away from each other and the gap increases.

In the case of VSMS275 PV panel, the initial gap of 2 mm becomes 2.04444 mm, leading to a predicted gap increase of 44.44 µm. In the case of Panasonic225 PV panel, the initial gap of 2 mm becomes 2.03627 mm, leading to a gap increase of 36.27 µm.

These values of change of the cell gap width can be compared to the experimental value of 44 µm found in the experimental work of Eitner et al. [71]. It should be noted that the specimens used by Eitner et al. [71] possessed a backsheet.

Consequently, our predicted values are in agreement with the experimental ones of Eitner et al. [71] specially in the case of VSMS275 PV panel.

With the increase of temperature, the different layers expand; but the different materials of the layers have not the same CTE values. Hence, some layers expand faster than other ones. Without freedom to expand as required, some layers are then subjected to traction ($\sigma_{11} > 0$); while some others will be subjected to compression ($\sigma_{11} < 0$).

The normal stress component σ_{11} is plotted at the end of heating step in Fig. 89 for both PV panels. In Fig. 89a, the backsheet is subjected to compression stresses while the front glass layer is subjected to bending. The stress states in different layers of VSMS275 PV panel are clearly different with the ones predicted in the layers of Panasonic225 PV Panel.

In Fig. 89b, the normal stress component σ_{11} is distributed symmetrically with respect to the average line of the PV panel. As in the predictions under NOCT, which correspond also to heating step, the PV cells are subjected to tensile stresses. The normal stress distribution across the thickness was next plotted in Fig. 90. The stress values plotted in Fig. 90 are predicted at the end of the heating stage for both PV panels.

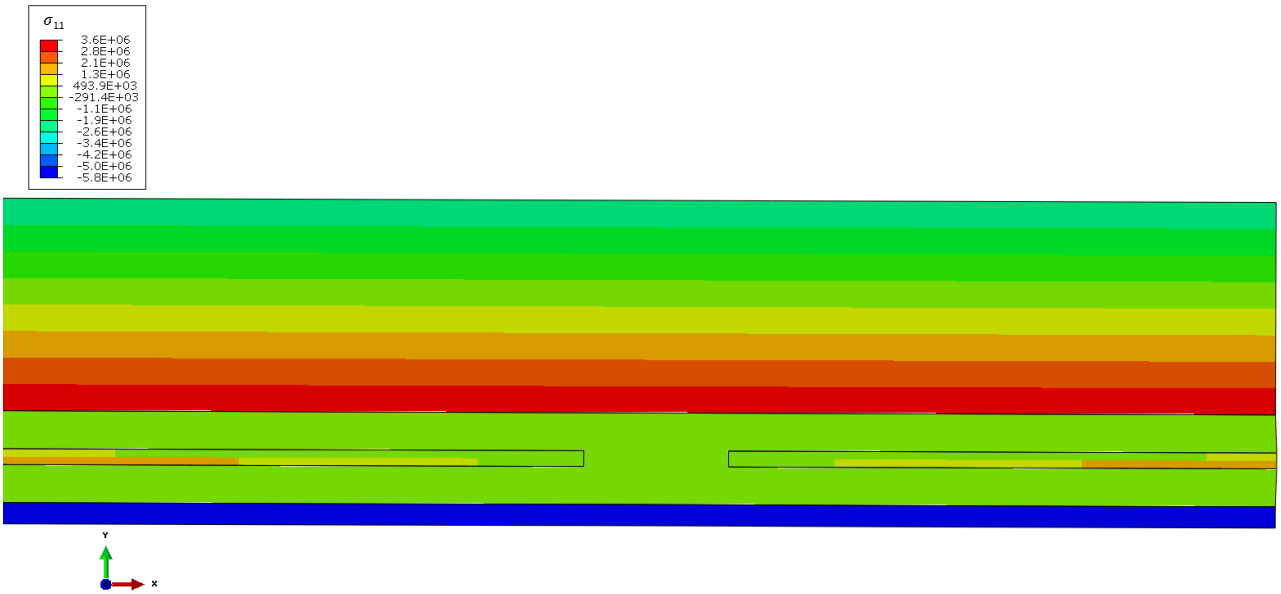

(a)

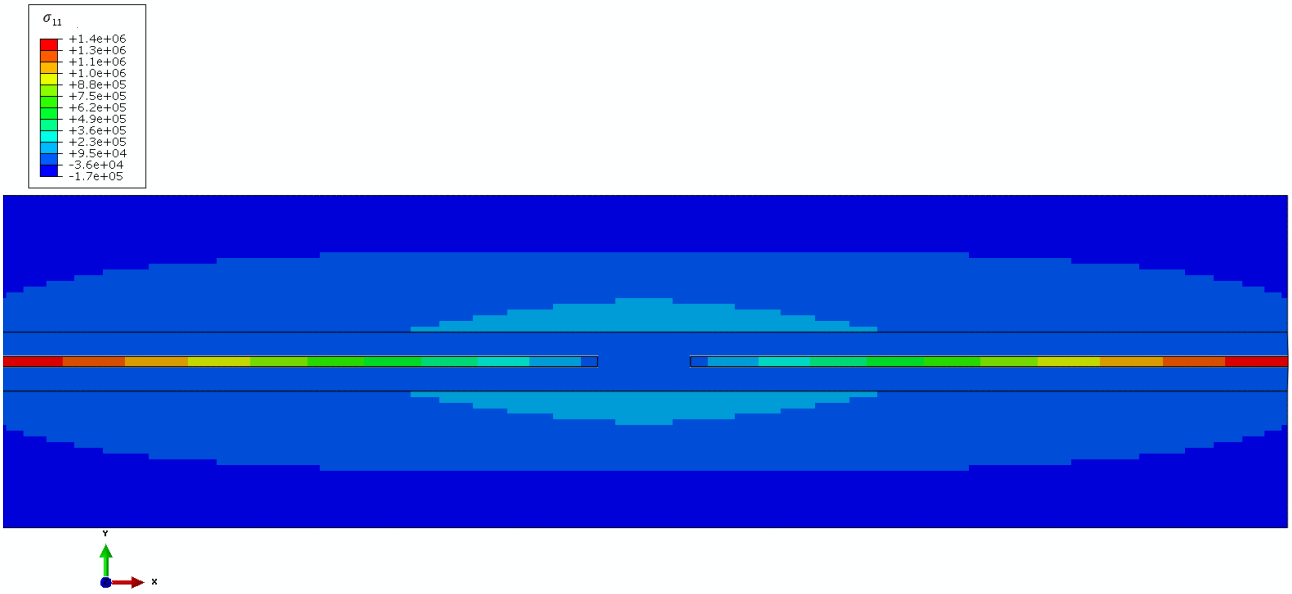

(b)

Fig. 108 Normal component σ_{11} of Cauchy stress tensor (plotted in [Pa]) predicted by FE simulations for the VSMS275 PV panel (a) and the Panasonic225 PV panel (b).

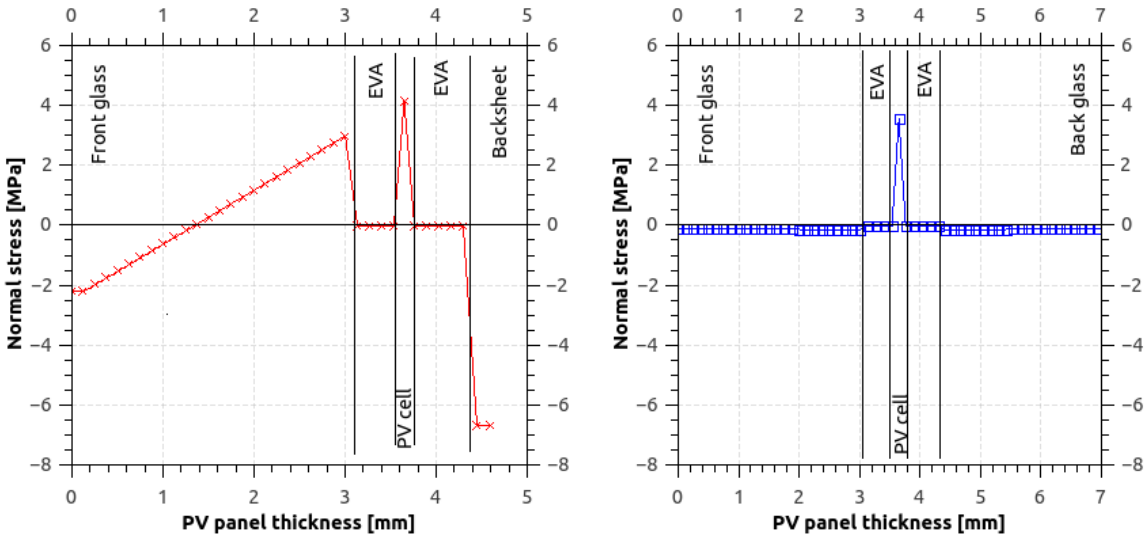

(b) (b)

Fig. 109 Distribution of the normal stress (σ_{11}in [MPa]) through the PV panel thickness after the heating stage in the case of the VSMS275 PV panel (a) and the Panasonic225 PV panel (b).

In the two studied PV panels, the normal stress reaches a maximum value of 4 MPa (in tension) in the layer corresponding to the PV cells. Furthermore, for the VSMS275 PV panel, the front glass layer is subjected to a linear variation of the normal stress, σ_{11}, corresponding to a bending behavior.

However, the layer corresponding to the backsheet experiences a normal stress value of -7 MPa (in compression) for the VSMS275 PV panel, Fig. 90a. Consequently, it can be concluded that these stress variations are due to the backsheet and they may lead over time to damages at the glass-encapsulant and encapsulant-backsheet interfaces. This last result is in agreement with the work of Park [66].

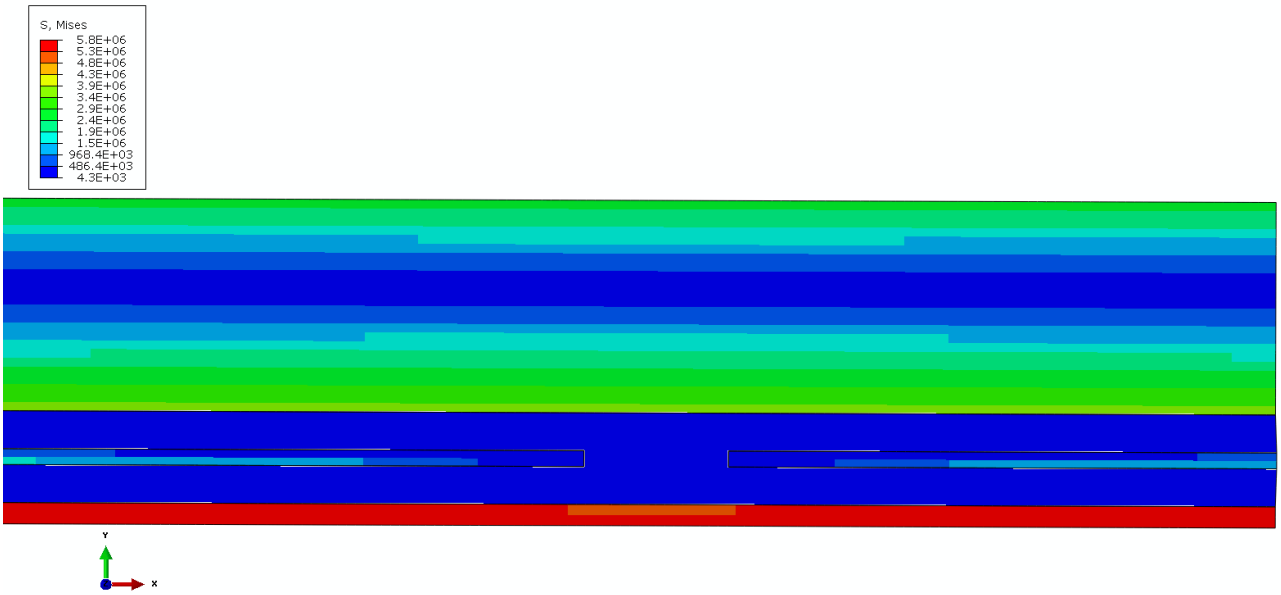

(a)

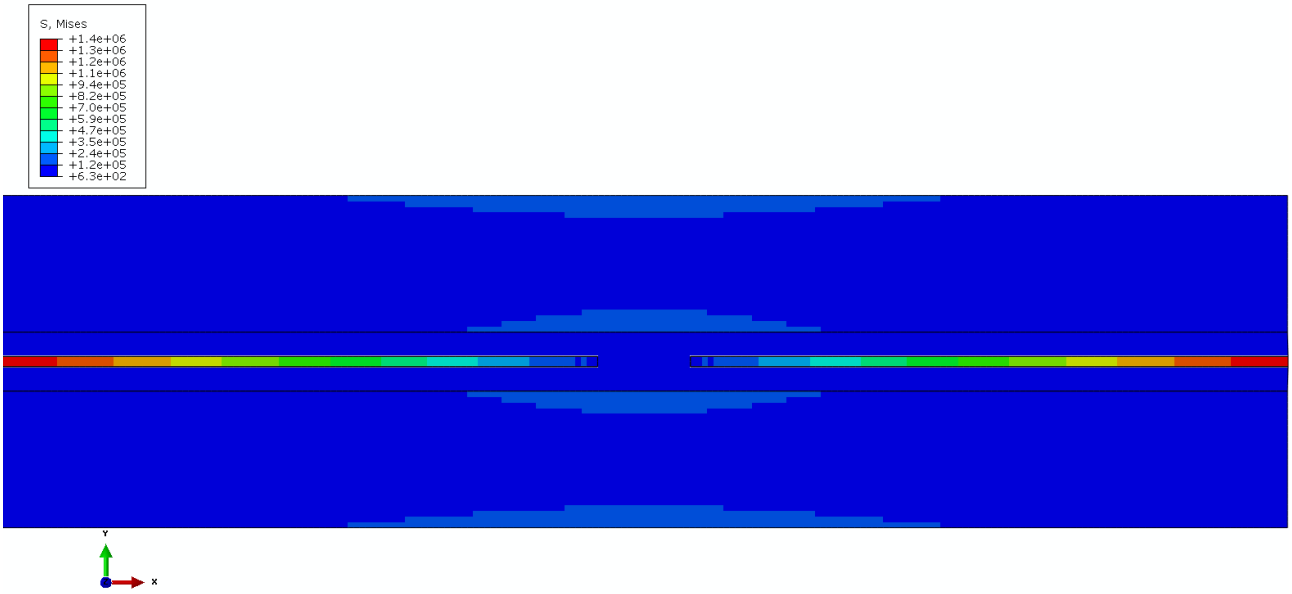

(b)

Fig. 110 Effective von Mises stress values (plotted in [Pa]) predicted by FE simulations at the end of the heating stage for: VSMS275 PV panel (a) and Panasonic225 PV panel (b).

To complete the analysis of stress states, the effective stress defined in the sense of von Mises is plotted in Fig. 91 for the two studied PV panels. One can see that the effective von Mises stress values are almost equal to the ones of normal stress σ_{11} presented in Fig. 91. The other components of Cauchy stress tensor (σ_{22} and σ_{12}) remain close to zero, that is the reason why they are not presented.

5.4. Conclusion

FE simulations of the thermo-mechanical behavior of two commercial PV panels (a mono-facial and a bi-facial one) were conducted under different thermal conditions: NOCT and TCT. The thermal boundary conditions for NOCT were taken from the multi-physical modeling developed in the previous chapter. For the TCT, the thermal conditions were defined in agreement with the IEC 61215 standard for accelerated aging.

In agreement with the literature, the thermoelastic behavior of EVA was accounted for in our FE simulations; whereas all the other materials are assumed to behave as linear elastic materials.

It was found that the distances between two adjacent PV cells predicted under the different thermal conditions are mainly in agreement with the experimental results of Eitner et al.[71]. Furthermore, the stress levels are always higher in the PV cells than in the other layers. However, the stress states are very different across the PV panel thickness in particular for the PV panel with a backsheet. On the contrary, the commercial bi-facial PV panel present almost always weak stress levels in glass and EVA layers.

In the case of the commercial mono-facial PV panel, the normal stress σ_{11} (along the width of the PV panels) present strong variations in our FE predictions. One may think that these stress variations result in damages (and possibly delamination) along the width of the PV panels at the interfaces between the layers.

These FE predictions seem to be in agreement with the experimental results of Park et al. [66] on the occurrence of delamination.

Finally, the negative value of temperature used in the IEC 61215 standard for accelerated aging could be too extreme and lead to high levels of stress. These conditions may not be representative of in-field conditions.

6. General conclusion

The aim of the study presented in this manuscript is to develop a coupled multi-physics numerical model that predicts the thermal behavior of PV panels under various conditions, using only the intrinsic geometrical, thermal, optical and electrical properties of the materials involved and without using the yield relations provided by the manufacturers in their datasheets. The model was also destined to the prediction of the mechanical response of the PV panel.

The model's core was developed using a finite difference approach with an implicit time integration rule to calculate the temperature. some other explicit approaches where used for the optical and electrical parts of the model.

The materials composing the panel were appropriately defined using values from the literature and from the data shared by the manufacturer. The temperature change affecting the materials' properties was taken into account in the model as the calculation is recursive.

The model was then validated under nominal operating conditions, and it was concluded that the model predicts the thermal response of the panel within the margin of fluctuation defined by the manufacturers for three commercial panels.

A parametric study was then conducted by imposing different irradiance conditions on the panel. It was noticed that:

- Imposing the panel to a higher irradiance leads to a rise of the temperature of the panel, which leads to a decrease in the electrical yield of the PV panel, and thus a decrease in the electrical power that can be generated.

- The temperature can rise to dangerous levels for the materials composing the PV panel, especially the polymer encapsulating the PV-cell. Even if the melting of the encapsulant can be avoided, it was noticed that the yield of the PV panel at 3 suns is higher than the yield of the panel at 4 suns.

It was suggested that, even using solar concentrators, one should not go over the value of 2 suns, as it is safe for the materials composing the PV panel, and offers a higher irradiance than the case of 1 sun.

A possible solution to the rise of temperature associated to the 3-4 suns cases, is the use of fans to cool the panel. The fans use some of the produced energy to lower the temperature of the panel, and thus should increase the yield and the electrical energy produced. A study must be conducted to find the optimal point where the electrical consumption might be beneficial to the final electrical production.

The model was also used to study the behavior of bifacial panels, and it was adjusted to take into account the solar irradiance that can be absorbed by the back of the panel. The model was validated under nominal operating conditions, and then the response of the panel was studied under real time conditions.

The QEERI institute provided the meteorological conditions in their test site, and the model's response was studied for a sunny and a cloudy day input conditions. It was observed that the model reacted well to the different changes of irradiance and ambient temperature, as well as the wind conditions.

The manufacturer of the bifacial PV panel proposes a new setup of the panel, a little bit different from the horizontally tilted classical way of setup that is usually used for the PV panels, where the PV panel is installed vertically on the ground. This setup can be interesting for locations where the diffuse solar irradiances and the ground reflectance are high.

The model was then used to determine the mechanical response of the PV panels under nominal conditions, and also under thermal fatigue cycling.

A comparison against experimental results was conducted to validate the model under these conditions. The stresses that are created might be the cause of the delamination happening between the different layers of the panel in its life time.

To go further in this work, it is imperative to study the response of the panel under real time conditions, to determine the micro-stresses that are created in the PV panel in the different time of day, such as a sudden change of temperature caused by meteorological changes (such as the passing of clouds or a change in wind direction or velocity).

Bibliography

[1] E. u$νη Κανελλ$\acute\alpha$κη, “An estimation of technical and energy: an application to European industries,” 2016.
[2] X. Xu, K. Vignarooban, B. Xu, K. Hsu, and A. M. Kannan, “Prospects and problems of concentrating solar power technologies for power generation in the desert regions,” *Renew. Sustain. Energy Rev.*, vol. 53, pp. 1106–1131, Jan. 2016.
[3] “See the world’s largest solar thermal energy facility,” *Bechtel Corporate*. [Online]. Available: https://www.bechtel.com/projects/ivanpah-solar-electric-generating-system/. [Accessed: 12-Jun-2019].
[4] “Noor Ouarzazate Solar Complex - Power Technology | Energy News and Market Analysis.” [Online]. Available: https://www.power-technology.com/projects/noor-ouarzazate-solar-complex/. [Accessed: 12-Jun-2019].
[5] “SPE_GMO2016_full_version.pdf.” .
[6] “best-research-cell-efficiencies.20191106.pdf.” [Online]. Available: https://www.nrel.gov/pv/assets/pdfs/best-research-cell-efficiencies.20191106.pdf. [Accessed: 26-Nov-2019].
[7] “Introduction to Solar Radiation.” [Online]. Available: https://www.newport.com/t/introduction-to-solar-radiation. [Accessed: 26-Nov-2019].
[8] D. C. Jordan and S. R. Kurtz, “Photovoltaic degradation rates—an analytical review,” *Prog. Photovolt. Res. Appl.*, vol. 21, no. 1, pp. 12–29, 2013.
[9] E. Skoplaki and J. A. Palyvos, “On the temperature dependence of photovoltaic module electrical performance: A review of efficiency/power correlations,” *Sol. Energy*, vol. 83, no. 5, pp. 614–624, May 2009.
[10] D. L. Evans and L. W. Florschuetz, “Cost studies on terrestrial photovoltaic power systems with sunlight concentration,” *Sol. Energy*, vol. 19, no. 3, pp. 255–262, Jan. 1977.
[11] W. H. McAdams, *Heat transmission*, 3rd ed. Malabar, Fla: R.E. Krieger Pub. Co, 1985.
[12] R. J. Cole and N. S. Sturrock, “The convective heat exchange at the external surface of buildings,” *Build. Environ.*, vol. 12, no. 4, pp. 207–214, Jan. 1977.
[13] M. Mattei, G. Notton, C. Cristofari, M. Muselli, and P. Poggi, “Calculation of the polycrystalline PV module temperature using a simple method of energy balance,” *Renew. Energy*, vol. 31, no. 4, pp. 553–567, Apr. 2006.
[14] G. Notton, C. Cristofari, M. Mattei, and P. Poggi, “Modelling of a double-glass photovoltaic module using finite differences,” *Appl. Therm. Eng.*, vol. 25, no. 17–18, pp. 2854–2877, Dec. 2005.
[15] P. Berdahl and M. Martin, “Emissivity of clear skiest,” p. 2.
[16] T. Schott and A. Zeidler, “PV-System Analysis,” in *Advances In Solar Energy Technology*, Elsevier, 1988, pp. 457–460.
[17] W. C. Swinbank, “Long-wave radiation from clear skies,” *Q. J. R. Meteorol. Soc.*, vol. 89, no. 381, pp. 339–348, Jul. 1963.
[18] S. Armstrong and W. G. Hurley, “A thermal model for photovoltaic panels under varying atmospheric conditions,” *Appl. Therm. Eng.*, vol. 30, no. 11–12, pp. 1488–1495, Aug. 2010.
[19] A. D. Jones and C. P. Underwood, “A thermal model for photovoltaic systems,” *Sol. Energy*, vol. 70, no. 4, pp. 349–359, 2001.
[20] J. P. Holman, *Heat transfer*. McGraw-Hill, 1989.
[21] J. C. Sánchez Barroso, N. Barth, J. P. M. Correia, S. Ahzi, and M. A. Khaleel, “A computational analysis of coupled thermal and electrical behavior of PV panels,” *Sol. Cells Storage*, vol. 148, pp. 73–86, Apr. 2016.
[22] S. P. Aly, S. Ahzi, N. Barth, and B. W. Figgis, “Two-dimensional finite difference-based model for coupled irradiation and heat transfer in photovoltaic modules,” *Sol. Energy Mater. Sol. Cells*, 2017.
[23] N. Barth, J. P. M. de Correia, S. Ahzi, and M. A. Khaleel, “Thermal Analysis of Solar Panels,” in *Proceedings of the TMS Middle East — Mediterranean Materials Congress on Energy and Infrastructure Systems (MEMA 2015)*, I. Karaman, R. Arróyave, and E. Masad, Eds. Cham: Springer International Publishing, 2015, pp. 441–450.

[24] M. Usama Siddiqui, A. F. M. Arif, L. Kelley, and S. Dubowsky, “Three-dimensional thermal modeling of a photovoltaic module under varying conditions,” *Sol. Energy*, vol. 86, no. 9, pp. 2620–2631, Sep. 2012.
[25] R. Vaillon, L. Robin, C. Muresan, and C. Ménézo, “Modeling of coupled spectral radiation, thermal and carrier transport in a silicon photovoltaic cell,” *Int. J. Heat Mass Transf.*, vol. 49, no. 23–24, pp. 4454–4468, Nov. 2006.
[26] L. Weiss, M. Amara, and C. Ménézo, “Impact of radiative-heat transfer on photovoltaic module temperature: Impact of radiative-heat transfer on photovoltaic module temperature,” *Prog. Photovolt. Res. Appl.*, vol. 24, no. 1, pp. 12–27, Jan. 2016.
[27] R. Hull, *Properties of Crystalline Silicon*. IET, 1999.
[28] M. A. de Blas, J. L. Torres, E. Prieto, and A. García, “Selecting a suitable model for characterizing photovoltaic devices,” *Renew. Energy*, vol. 25, no. 3, pp. 371–380, Mar. 2002.
[29] D. Petreu, “MODELLING AND SIMULATION OF PHOTOVOLTAIC CELLS,” vol. 49, no. 1, p. 6, 2008.
[30] J. Zhao and M. A. Green, “Optimized antireflection coatings for high-efficiency silicon solar cells,” *IEEE Trans. Electron Devices*, vol. 38, no. 8, pp. 1925–1934, Aug. 1991.
[31] D. A. Clugston and P. A. Basore, “PC1D version 5: 32-bit solar cell modeling on personal computers,” in *Conference Record of the Twenty Sixth IEEE Photovoltaic Specialists Conference - 1997*, 1997, pp. 207–210.
[32] W. J. Yang, Z. Q. Ma, X. Tang, C. B. Feng, W. G. Zhao, and P. P. Shi, “Internal quantum efficiency for solar cells,” *Sol. Energy*, vol. 82, no. 2, pp. 106–110, Feb. 2008.
[33] L. M. Fraas and L. D. Partain, *Solar cells and their applications*. Hoboken, N.J.: Wiley, 2010.
[34] C. Hua and C. Shen, “Study of maximum power tracking techniques and control of DC/DC converters for photovoltaic power system,” in *PESC 98 Record. 29th Annual IEEE Power Electronics Specialists Conference (Cat. No.98CH36196)*, 1998, vol. 1, pp. 86–93 vol.1.
[35] W. De Soto, S. A. Klein, and W. A. Beckman, “Improvement and validation of a model for photovoltaic array performance,” *Sol. Energy*, vol. 80, no. 1, pp. 78–88, Jan. 2006.
[36] H.-L. Tsai, “Complete PV model considering its thermal dynamics,” *J. Chin. Inst. Eng.*, vol. 36, no. 8, pp. 1073–1082, Dec. 2013.
[37] J. C. S. Barroso, J. P. M. Correia, N. Barth, S. Ahzi, and M. A. Khaleel, “A PSO algorithm for the calculation of the series and shunt resistances of the PV panel one-diode model,” in *2014 International Renewable and Sustainable Energy Conference (IRSEC)*, 2014, pp. 1–6.
[38] N. Barth, R. Jovanovic, S. Ahzi, and M. A. Khaleel, “PV panel single and double diode models: Optimization of the parameters and temperature dependence,” *Sol. Cells Storage*, vol. 148, pp. 87–98, Apr. 2016.
[39] T. Dittrich, *Materials Concepts for Solar Cells*. IMPERIAL COLLEGE PRESS, 2014.
[40] Liu Chun-xia and Liu Li-qun, “An improved perturbation and observation MPPT method of photovoltaic generate system,” in *2009 4th IEEE Conference on Industrial Electronics and Applications*, Xian, China, 2009, pp. 2966–2970.
[41] A. Safari and S. Mekhilef, *Incremental Conductance MPPT With Direct Control Method Using Cuk Converter*. .
[42] J. Ahmad, “A fractional open circuit voltage based maximum power point tracker for photovoltaic arrays,” in *2010 2nd International Conference on Software Technology and Engineering*, 2010, vol. 1, pp. V1-247-V1-250.
[43] S. Dietrich, M. Pander, M. Sander, S. H. Schulze, and M. Ebert, “Mechanical and thermomechanical assessment of encapsulated solar cells by finite-element-simulation,” presented at the Reliability of Photovoltaic Cells, Modules, Components, and Systems III, 2010, vol. 7773, p. 77730F.
[44] M. Paggi, S. Kajari-Schröder, and U. Eitner, “Thermomechanical deformations in photovoltaic laminates,” *J. Strain Anal. Eng. Des.*, vol. 46, no. 8, pp. 772–782, Nov. 2011.

[45] M. Paggi, I. Berardone, A. Infuso, and M. Corrado, “Fatigue degradation and electric recovery in Silicon solar cells embedded in photovoltaic modules,” *Sci. Rep.*, vol. 4, 2014.
[46] O. O. Ogbomo, E. H. Amalu, N. N. Ekere, and P. O. Olagbegi, “Effect of operating temperature on degradation of solder joints in crystalline silicon photovoltaic modules for improved reliability in hot climates,” *Sol. Energy*, vol. 170, pp. 682–693, Aug. 2018.
[47] J. Kurnik, M. Jankovec, K. Brecl, and M. Topic, “Outdoor testing of PV module temperature and performance under different mounting and operational conditions,” *Sol. Energy Mater. Sol. Cells*, vol. 95, no. 1, pp. 373–376, Jan. 2011.
[48] S. Kajari-Schršder, I. Kunze, and M. Kšntges, “Criticality of Cracks in PV Modules,” *Energy Procedia*, vol. 27, pp. 658–663, 2012.
[49] D. Chianese *et al.*, “Analysis of weathered c-Si PV modules,” in *Proceedings of 3rd World Conference on Photovoltaic Energy Conversion*, 2003, vol. 3, pp. 2922-2926 Vol.3.
[50] P. Sánchez-Friera, M. Piliougine, J. Peláez, J. Carretero, and M. Sidrach de Cardona, “Analysis of degradation mechanisms of crystalline silicon PV modules after 12 years of operation in Southern Europe,” *Prog. Photovolt. Res. Appl.*, vol. 19, no. 6, pp. 658–666, Sep. 2011.
[51] S. Z. Aljoaba, A. M. Cramer, S. A. Rawashdeh, and B. L. Walcott, “Thermoelectrical Modeling of Wavelength Effects on Photovoltaic Module Performance—Part II: Parameterization,” *IEEE J. Photovolt.*, vol. 3, no. 3, pp. 1034–1037, Jul. 2013.
[52] “1-Optical Coating and Materials.pdf.” [Online]. Available: https://www.cvilaseroptics.com/file/general/1-Optical%20Coating%20and%20Materials.pdf. [Accessed: 07-Apr-2017].
[53] Y. Lee and A. A. O. Tay, “Finite Element Thermal Analysis of a Solar Photovoltaic Module,” *Energy Procedia*, vol. 15, pp. 413–420, 2012.
[54] R. E. Bird, “A simple, solar spectral model for direct-normal and diffuse horizontal irradiance,” *Sol. Energy*, vol. 32, no. 4, pp. 461–471, Jan. 1984.
[55] E. F. Schubert, *Light-Emitting Diodes*. Leiden: Cambridge University Press, 2006.
[56] A. B. Sproul and M. A. Green, “Experimental measurement of the intrinsic carrier concentration of silicon,” in *IEEE Conference on Photovoltaic Specialists*, 1990, pp. 380–385 vol.1.
[57] N. D. Arora, J. R. Hauser, and D. J. Roulston, “Electron and hole mobilities in silicon as a function of concentration and temperature,” *IEEE Trans. Electron Devices*, vol. 29, no. 2, pp. 292–295, 1982.
[58] “(9) (PDF) Illumination Source Identification Using a CMOS Optical Microsystem,” *ResearchGate*. [Online]. Available: https://www.researchgate.net/publication/3090810_Illumination_Source_Identification_Using_a_CMOS_Optical_Microsystem. [Accessed: 11-Jan-2019].
[59] M. A. Green, “Solar cell fill factors: General graph and empirical expressions,” *Solid-State Electron.*, vol. 24, no. 8, pp. 788–789, Aug. 1981.
[60] “Mise en page 1 - 130430_voltec_solar_datasheet_tarka_fr2.pdf.” [Online]. Available: http://www.kogybox.com/uploads/assets/voltec_solar/130430_voltec_solar_datasheet_tarka_fr2.pdf. [Accessed: 05-Apr-2017].
[61] “Microsoft Word - 6802.0036 BP350J_C 01_10.doc - BP-350J.pdf.” [Online]. Available: https://www.solarelectricsupply.com/media/custom/upload/BP-350J.pdf. [Accessed: 05-Apr-2017].
[62] “BP 585 - BPSolar85w.pdf.” [Online]. Available: http://www.electricsystems.co.nz/documents/BPSolar85w.pdf. [Accessed: 05-Apr-2017].
[63] “(9) (PDF) QEERI Solar Test Facility 5-Year Report,” *ResearchGate*. [Online]. Available: https://www.researchgate.net/publication/324438287_QEERI_Solar_Test_Facility_5-Year_Report. [Accessed: 13-Jan-2019].
[64] J. A. Coakley, “REFLECTANCE AND ALBEDO, SURFACE,” in *Encyclopedia of Atmospheric Sciences*, Elsevier, 2003, pp. 1914–1923.
[65] M. Knausz *et al.*, “Thermal expansion behavior of solar cell encapsulation materials,” *Polym. Test.*, vol. 44, no. Supplement C, pp. 160–167, 2015.

[66] N. C. Park, J. S. Jeong, B. J. Kang, and D. H. Kim, “The effect of encapsulant discoloration and delamination on the electrical characteristics of photovoltaic module,” *Microelectron. Reliab.*, vol. 53, no. 9–11, pp. 1818–1822, Sep. 2013.
[67] G. Oreski and G. M. Wallner, “Evaluation of the aging behavior of ethylene copolymer films for solar applications under accelerated weathering conditions,” *Sol. Energy*, vol. 83, no. 7, pp. 1040–1047, Jul. 2009.
[68] “Abaqus 6.13 Documentation.” [Online]. Available: http://dsk.ippt.pan.pl/docs/abaqus/v6.13/index.html. [Accessed: 12-Mar-2019].
[69] H. Zhou *et al.*, “Interface engineering of highly efficient perovskite solar cells,” *Science*, vol. 345, no. 6196, pp. 542–546, Aug. 2014.
[70] “IEC 61215-2 Terrestrial photovoltaic (PV) modules – Design qualification and type approval – Part 2: Test procedures.” .
[71] U. Eitner, M. Köntges, and R. Brendel, “Use of digital image correlation technique to determine thermomechanical deformations in photovoltaic laminates: Measurements and accuracy,” *Sol. Energy Mater. Sol. Cells - Sol. ENERG MATER Sol. CELLS*, vol. 94, pp. 1346–1351, 2010.
[72] M. Owen-Bellini, J. Zhu, T. R. Betts, and R. Gottschalg, “Thermo-mechanical stresses of silicon photovoltaic modules,” *13th Photovolt. Sci. Appl. Technol.*, 2017.

List of figures

List of tables

List of annexes

Annex A: Markov matrix in the case of a 5 layers PV module (29 x 29)

$$
M=\begin{bmatrix}
0 & 0 & 0 & 0 & 0 & 0 & 0 & 0 & 0 & 0 & 0 & 0 & 0 & 0 & 0 & 0 & 0 & 0 & 0 & 0 & 0 & 0 & 0 & 0 & 0 & 0 & 0 & 0 & 0 \\
R1 & 0 & 0 & 0 & 0 & 0 & 0 & 1\text{-}R1 & 0 & 0 & 0 & 0 & 0 & 0 & 0 & 0 & 0 & 0 & 0 & 0 & 0 & 0 & 0 & 0 & 0 & 0 & 0 & 0 & 0 & 0 \\
1\text{-}R1 & 0 & 0 & 0 & 0 & 0 & 0 & R1 & 0 & 0 & 0 & 0 & 0 & 0 & 0 & 0 & 0 & 0 & 0 & 0 & 0 & 0 & 0 & 0 & 0 & 0 & 0 & 0 & 0 & 0 \\
0 & 0 & 0 & 0 & 0 & 0 & 0 & 0 & R2 & 0 & 0 & 0 & 0 & 0 & 0 & 0 & 0 & 0 & 1\text{-}R2 & 0 & 0 & 0 & 0 & 0 & 0 & 0 & 0 & 0 & 0 & 0 \\
0 & 0 & 0 & 0 & 0 & 0 & 0 & 0 & 0 & R3 & 0 & 0 & 0 & 0 & 0 & 0 & 0 & 0 & 0 & 1\text{-}R3 & 0 & 0 & 0 & 0 & 0 & 0 & 0 & 0 & 0 & 0 \\
0 & 0 & 0 & 0 & 0 & 0 & 0 & 0 & 0 & 0 & R4 & 0 & 0 & 0 & 0 & 0 & 0 & 0 & 0 & 0 & 1\text{-}R4 & 0 & 0 & 0 & 0 & 0 & 0 & 0 & 0 & 0 \\
0 & 0 & 0 & 0 & 0 & 0 & 0 & 0 & 0 & 0 & 0 & R5 & 0 & 0 & 0 & 0 & 0 & 0 & 0 & 0 & 0 & 1\text{-}R5 & 0 & 0 & 0 & 0 & 0 & 0 & 0 & 0 \\
0 & 0 & 0 & 0 & 0 & 0 & 0 & 0 & 0 & 0 & 0 & 0 & 0 & 0 & 0 & 0 & 0 & 0 & 0 & 0 & 0 & 0 & 1\text{-}A1 & 0 & 0 & 0 & 0 & 0 & 0 & 0 \\
0 & 0 & 0 & 0 & 0 & 0 & 0 & 0 & 0 & 0 & 0 & 0 & 0 & 0 & 0 & 0 & 0 & 0 & 0 & 0 & 0 & 0 & 0 & 1\text{-}A2 & 0 & 0 & 0 & 0 & 0 & 0 \\
0 & 0 & 0 & 0 & 0 & 0 & 0 & 0 & 0 & 0 & 0 & 0 & 0 & 0 & 0 & 0 & 0 & 0 & 0 & 0 & 0 & 0 & 0 & 0 & 1\text{-}A3 & 0 & 0 & 0 & 0 & 0 \\
0 & 0 & 0 & 0 & 0 & 0 & 0 & 0 & 0 & 0 & 0 & 0 & 0 & 0 & 0 & 0 & 0 & 0 & 0 & 0 & 0 & 0 & 0 & 0 & 0 & 1\text{-}A4 & 0 & 0 & 0 & 0 \\
0 & 0 & 0 & 0 & 0 & 0 & 0 & 0 & 0 & 0 & 0 & 0 & 0 & 0 & 0 & 0 & 0 & 0 & 0 & 0 & 0 & 0 & 0 & 0 & 0 & 0 & 1\text{-}A5 & 0 & 0 & 0 \\
0 & 0 & A1 & 0 & 0 & 0 & 0 & 0 & 0 & 0 & 0 & 0 & 1 & 0 & 0 & 0 & 0 & 0 & 0 & 0 & 0 & 0 & A1 & 0 & 0 & 0 & 0 & 0 & 0 & 0 \\
0 & 0 & 0 & A2 & 0 & 0 & 0 & 0 & 0 & 0 & 0 & 0 & 0 & 1 & 0 & 0 & 0 & 0 & 0 & 0 & 0 & 0 & 0 & A2 & 0 & 0 & 0 & 0 & 0 & 0 \\
0 & 0 & 0 & 0 & A3 & 0 & 0 & 0 & 0 & 0 & 0 & 0 & 0 & 0 & 1 & 0 & 0 & 0 & 0 & 0 & 0 & 0 & 0 & 0 & A3 & 0 & 0 & 0 & 0 & 0 \\
0 & 0 & 0 & 0 & 0 & A4 & 0 & 0 & 0 & 0 & 0 & 0 & 0 & 0 & 0 & 1 & 0 & 0 & 0 & 0 & 0 & 0 & 0 & 0 & 0 & A4 & 0 & 0 & 0 & 0 \\
0 & 0 & 0 & 0 & 0 & 0 & A5 & 0 & 0 & 0 & 0 & 0 & 0 & 0 & 0 & 0 & 1 & 0 & 0 & 0 & 0 & 0 & 0 & 0 & 0 & 0 & A5 & 0 & 0 & 0 \\
0 & 0 & 1\text{-}A1 & 0 & 0 & 0 & 0 & 0 & 0 & 0 & 0 & 0 & 0 & 0 & 0 & 0 & 0 & 0 & 0 & 0 & 0 & 0 & 0 & 0 & 0 & 0 & 0 & 0 & 0 & 0 \\
0 & 0 & 0 & 1\text{-}A2 & 0 & 0 & 0 & 0 & 0 & 0 & 0 & 0 & 0 & 0 & 0 & 0 & 0 & 0 & 0 & 0 & 0 & 0 & 0 & 0 & 0 & 0 & 0 & 0 & 0 & 0 \\
0 & 0 & 0 & 0 & 1\text{-}A3 & 0 & 0 & 0 & 0 & 0 & 0 & 0 & 0 & 0 & 0 & 0 & 0 & 0 & 0 & 0 & 0 & 0 & 0 & 0 & 0 & 0 & 0 & 0 & 0 & 0 \\
0 & 0 & 0 & 0 & 0 & 1\text{-}A4 & 0 & 0 & 0 & 0 & 0 & 0 & 0 & 0 & 0 & 0 & 0 & 0 & 0 & 0 & 0 & 0 & 0 & 0 & 0 & 0 & 0 & 0 & 0 & 0 \\
0 & 0 & 0 & 0 & 0 & 0 & 1\text{-}A5 & 0 & 0 & 0 & 0 & 0 & 0 & 0 & 0 & 0 & 0 & 0 & 0 & 0 & 0 & 0 & 0 & 0 & 0 & 0 & 0 & 0 & 0 & 0 \\
0 & 0 & 0 & 0 & 0 & 0 & 0 & 0 & 1\text{-}R1 & 0 & 0 & 0 & 0 & 0 & 0 & 0 & 0 & 0 & R1 & 0 & 0 & 0 & 0 & 0 & 0 & 0 & 0 & 0 & 0 & 0 \\
0 & 0 & 0 & 0 & 0 & 0 & 0 & 0 & 0 & 1\text{-}R2 & 0 & 0 & 0 & 0 & 0 & 0 & 0 & 0 & 0 & R2 & 0 & 0 & 0 & 0 & 0 & 0 & 0 & 0 & 0 & 0 \\
0 & 0 & 0 & 0 & 0 & 0 & 0 & 0 & 0 & 0 & 1\text{-}R3 & 0 & 0 & 0 & 0 & 0 & 0 & 0 & 0 & 0 & R3 & 0 & 0 & 0 & 0 & 0 & 0 & 0 & 0 & 0 \\
0 & 0 & 0 & 0 & 0 & 0 & 0 & 0 & 0 & 0 & 0 & 1\text{-}R4 & 0 & 0 & 0 & 0 & 0 & 0 & 0 & 0 & 0 & R4 & 0 & 0 & 0 & 0 & 0 & 0 & 0 & 0 \\
0 & 0 & 0 & 0 & 0 & 0 & 0 & 0 & 0 & 0 & 0 & 0 & 0 & 0 & 0 & 0 & 0 & 0 & 0 & 0 & 0 & 0 & R5 & 0 & 0 & 0 & 0 & 0 & 0 & 1\text{-}R5 \\
0 & 0 & 0 & 0 & 0 & 0 & 0 & 0 & 0 & 0 & 0 & 0 & 0 & 0 & 0 & 0 & 0 & 0 & 0 & 0 & 0 & 1\text{-}R5 & 0 & 0 & 0 & 0 & 0 & 1 & R5 \\
0 & 0 & 0 & 0 & 0 & 0 & 0 & 0 & 0 & 0 & 0 & 0 & 0 & 0 & 0 & 0 & 0 & 0 & 0 & 0 & 0 & 0 & 0 & 0 & 0 & 0 & 0 & 0 & 0 & 0
\end{bmatrix}
$$

Annex B: DATASHEET BP350

bp solar

BP 350

50 Watt Photovoltaic Module

High-efficiency photovoltaic module using silicon nitride multicrystalline silicon cells.

Performance

Rated power (P_{max})	50W
Power tolerance	± 10%
Nominal voltage	12V
Limited Warranty[1]	25 years

Configuration

J	Clear universal frame and standard J-Box

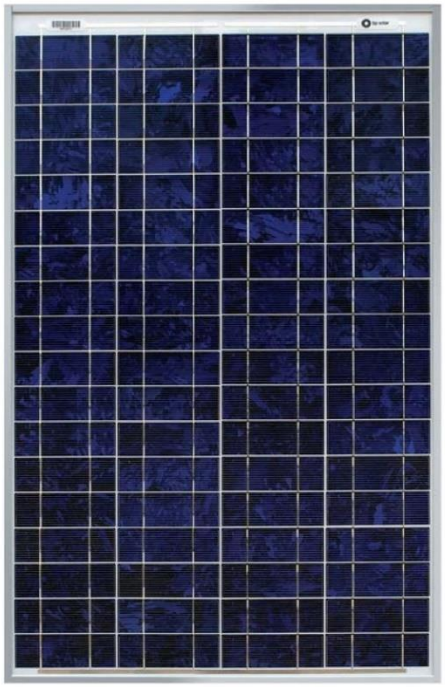

Electrical Characteristics[2]

	BP 350
Maximum power (P_{max})[3]	50W
Voltage at Pmax (V_{mp})	17.5V
Current at Pmax (I_{mp})	2.9A
Warranted minimum P_{max}	45W
Short-circuit current (I_{sc})	3.2A
Open-circuit voltage (V_{oc})	21.8V
Temperature coefficient of I_{sc}	(0.065±0.015)%/ °C
Temperature coefficient of V_{oc}	-(80±10)mV/°C
Temperature coefficient of power	-(0.5±0.05)%/ °C
NOCT (Air 20°C; Sun 0.8kW/m^2; wind 1m/s)	47±2°C
Maximum series fuse rating	20A
Maximum system voltage	50V (U.S. NEC rating)

Mechanical Characteristics

Dimensions	Length: 839mm (33") Width: 537mm (21.1") Depth: 50mm (1.97")
Weight	6.0 kg (13.2 pounds)
Solar Cells	72 cells (42mm x 125mm) in a 4x18 matrix connected in 2 parallel strings of 36 in series
Junction Box	J-Version junction box with 4-terminal connection block; IP 65, accepts PG 13.5, M20, ½ inch conduit, or cable fittings accepting 6-12mm diameter cable. Terminals accept 2.5 to 10mm^2 (8 to 14 AWG) wire.
Diodes	One 9A, 45V Schottky by-pass diode included
Construction	Front: High-transmission 3mm (1/8th inch) tempered glass; Back: White Polyester; Encapsulant: EVA
Frame	Clear anodized aluminum alloy type 6063T6 Universal frame; Color: silver

1. Module Warranty: 25-year limited warranty of 85% power output; 12-year limited warranty of 93% power output; 5-year limited warranty of materials and workmanship. See your local representative for full terms of these warranties.
2. This data represents the performance of typical BP modules, and are based on measurements made in accordance with ASTM E1036 corrected to SRC (STC.)
3. During the stabilization process that occurs during the first few months of deployment, module power may decrease by approx. 1% from typical P_{max}.

6802.0036 BP350J Rev. C 01/10

Quality and Safety

Listed to UL 1703 Standard for safety by Intertek ETL (Class C fire rating)

Approved by Intertek ETL for use in NEC Class 1, Division 2, Groups A to D hazardous locations.

BP350 I-V Curves

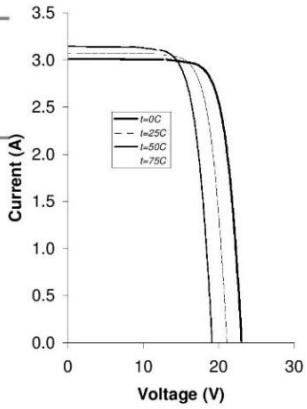

Qualification Test Parameters

Temperature cycling range	-40°C to +85°C (-40°F to 185°F)
Humidity freeze, damp heat	85% RH
Static load front and back (e.g. wind)	50psf (2400 pascals)
Front loading (e.g. snow)	113psf (5400 pascals)
Hailstone impact	25mm (1 inch) at 23 m/s (52mph)

Module Diagram

Dimensions in brackets are in inches. Un-bracketed dimensions are in millimeters.
Overall tolerances ±3mm (1/8")

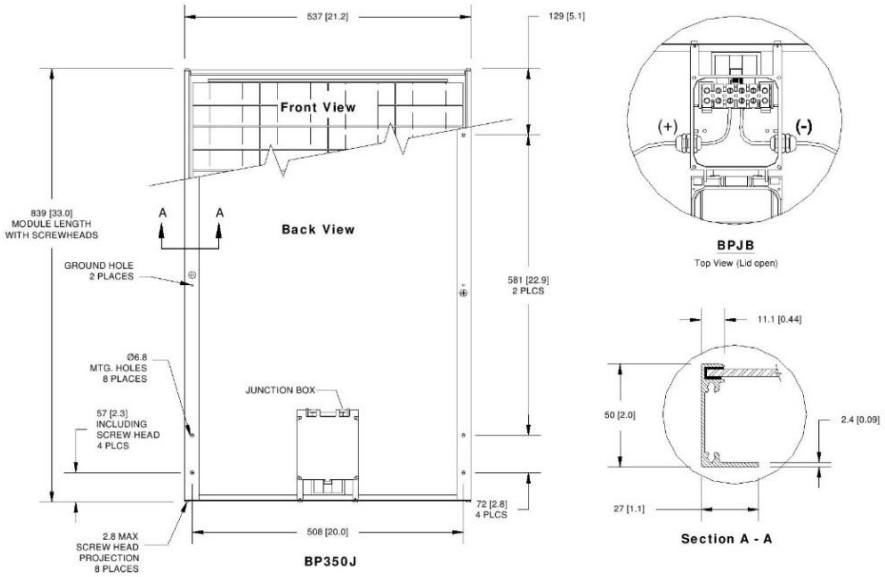

Included with each module: self-tapping grounding screw, instruction sheet, and warranty document.

Note: This publication summarizes product warranty and specifications, which are subject to change without notice. Additional information may be found on our web site: **www.bpsolar.com**

bp solar

6802.0036 BP350J Rev. C 01/10

Annex C: DATASHEET BP585

bp solar

BP 585

85-Watt High-Efficiency
Monocrystalline Photovoltaic Module

The BP 585 photovoltaic module uses the world's leading commercial laser cell processing technology to produce photovoltaic modules with exceptional efficiency. Its premium laser-grooved buried-grid monocrystalline cells provide a premium power performance of 85 watts nominal maximum power and 12 volts of nominal output for DC loads, or with an inverter, AC loads. The BP 585's high efficiency is particularly suited for applications which need maximum energy generation from a limited array area. Applications include utility grid-connected residential and commercial roof systems, building facades, and traditional industrial and remote applications. Modules use our Universal frame, the strongest in the industry.

Available versions include:
BP 585S – Framed module with output cables and polarized connectors
BP 585L – Unframed laminate version of the BP 585S
BP 585U – Framed module with a high-volume Type A junction box
BP 585H – Framed module with our Type B junction box

Proven Materials and Construction

BP Solar's quarter-century of field experience shows in every aspect of these modules' construction and materials:

- Laser patterning and processing minimizes cell front shading, maximizes efficiency;
- Cells are laminated between sheets of ethylene vinyl acetate (EVA) and high-transmissivity low-iron 3mm tempered glass;
- Frame strength exceeds requirements of certifying agencies.

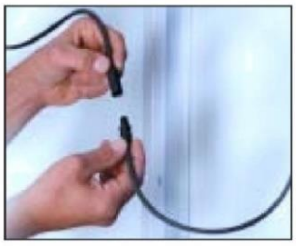

DC Connectors

Output Options

The BP 585 is offered with three output options: Connector-equipped cables and two types of junction box.

BP 585S and BP 585L output is via heavy-duty AWG #12 (3.3mm²) output cables with polarized weatherproof DC-rated connectors which provide reliable low-resistance connections, eliminate wiring errors, and speed installation. Asymmetrical cables enable side-by-side or end-to-end module placement in arrays.

BP 585U output is via our Type A junction box. This junction box is

Clear Anodized Universal Frame

raintight (IP54 rated) and accepts PG13.5 or 1/2" nominal conduit or cable fittings. Its volume (411cc, 25 cubic inches) and 6-terminal connection block enable series or parallel array connections to be made right in the junction box. Options include:

- oversize terminal block which accepts conductors up to 25mm² (AWG #4); standard terminals accept up to 6mm² (AWG #10);
- Solarstate™ charge regulator.

BP 585H output is via our Type B junction box, which is raintight (IP65 rated), features a convenient flip screw-tight lid, and offers the same wiring capabilities as the Type A junction box. It is equipped with a versatile 5-terminal Euro-style connection block. Two cable fittings that accept cable with a diameter between 6-12mm are included with each BP 585H module.

Limited Warranties

- Power output for 25 years;
- Freedom from defects in materials and workmanship for 5 years.

See our website or your local representative for full terms of these warranties.

BP 585

02-3009-3 5/03

Quality and Safety

These modules are manufactured in our ISO 9001-certified factories to demanding specifications. The BP 585S, 585U, and 585H:

- are certified by TÜV Rheinland as Class II equipment for use in systems up to 1000 VDC;
- are listed by Underwriter's Laboratories for electrical and fire safety (Class C fire rating);
- conform to European Community Directives 89/33/EEC, 73/23/EEC, and 93/68/EEC;
- comply with the requirements of IEC 61215, including:
  - repetitive cycling between -40°C and 85°C at 85% relative humidity;
  - simulated impact of 25mm (one-inch) hail at terminal velocity;
  - 2200 VDC frame/cell string isolation test;
  - static loading, front and back, of 2400 pascals (50 psf); front loading (e.g. snow) of 5400 pascals (113 psf).

The BP 585L is recognized by Underwriter's Laboratories for electrical and fire safety. The BP 585U is approved by Factory Mutual Research for application in NEC Class 1, Division 2, Groups C & D hazardous locations.

Electrical Characteristics[1]

	BP 585	BP 580[4]
Maximum power (P_{max})[2]	85W	80W
Voltage at P_{max} (V_{mp})	18.0V	18.0V
Current at P_{max} (I_{mp})	4.72A	4.44A
Warranted minimum P_{max}	80.8W	76W
Short-circuit current (I_{sc})	5.0A	4.7A
Open-circuit voltage (V_{oc})	22.1V	22.0V
Temperature coefficient of I_{sc}	(0.065±0.015)%/°C	
Temperature coefficient of voltage	-(80±10)mV/°C	
Temperature coefficient of power	-(0.5±0.05)%/°C	
NOCT[3]	47±2°C	
Maximum system voltage	600V (U.S. NEC rating) 1000V (TÜV Rheinland rating)	
Maximum series fuse rating	20A (U, H versions) 15A (S, L versions)	

Notes

1. These data represent the performance of typical BP 580 and BP 585 modules as measured at their output terminals. The data are based on measurements made in accordance with ASTM E1036 corrected to SRC (Standard Reporting Conditions, also known as STC or Standard Test Conditions), which are:
   - illumination of 1 kW/m² (1 sun) at spectral distribution of AM 1.5 (ASTM E892 global spectral irradiance);
   - cell temperature of 25°C.
2. During the stabilization process which occurs during the first few months of deployment, module power may decrease approximately 3% from typical P_{max}.
3. The cells in an illuminated module operate hotter than the ambient temperature. NOCT (Nominal Operating Cell Temperature) is an indicator of this temperature differential, and is the cell temperature under Standard Operating Conditions: ambient temperature of 20°C, solar irradiation of 0.8 kW/m², and wind speed of 1m/s.
4. The power of solar cells varies in the normal course of production; the BP 580 is assembled using cells of slightly lower power than the BP 585.

BP 585 I-V Curves

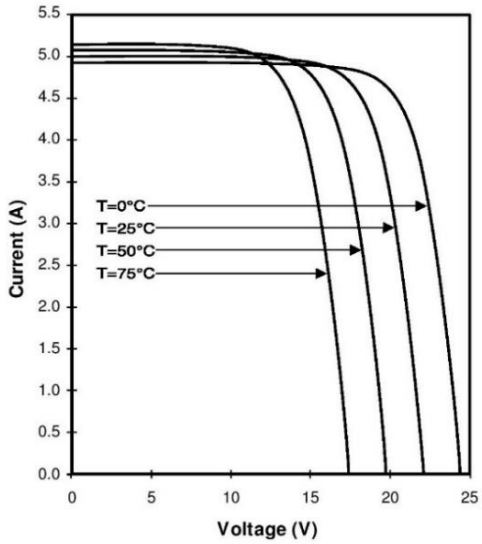

Mechanical Characteristics

Weight		Dimensions
BP 585U, 585S, 585H	7.7 kg (17 pounds)	BP 585U, 585S, 585H: See drawing.
BP 585L	6.1 kg (13.4 pounds)	BP 585L: 1197 [47.1] x 530 [20.9] x 18 [0.7]
		Unbracketed dimensions are in millimeters.
		Bracketed dimensions are in inches.
		Overall tolerances ±3mm (1/8")

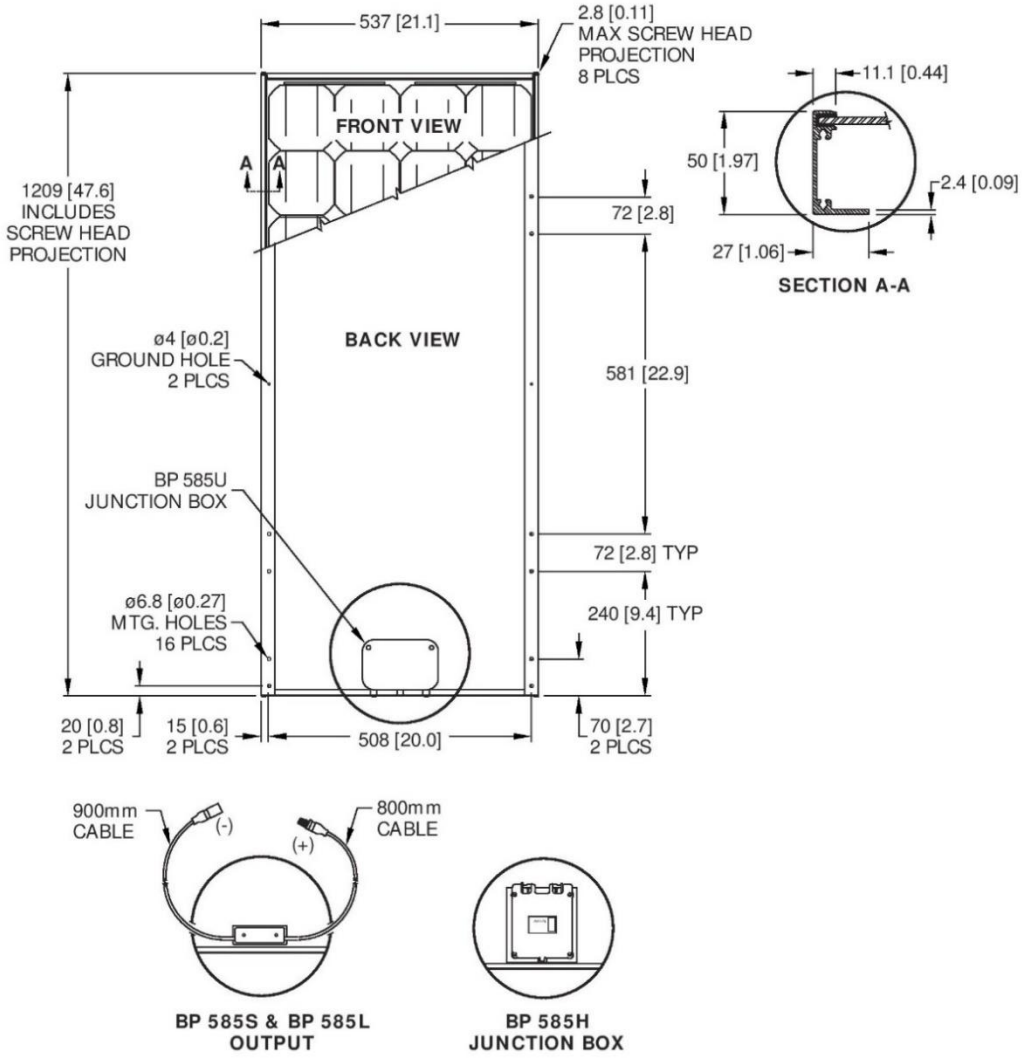

BP 585

Annex D: DATASHEET VSPS and VSMS

TARKA

VSPS AND VSMS PANEL CHARACTERISTICS	
Panel dimensions and weight	1650 x 990 x 42 mm (± 1 mm) / 18 kg
Type of cells	Multicrystalline or monocrystalline silicon
Dimensions and no. of cells/panel	156 x 156 mm / 60 cells (6 x 10)
Solar glass	High transmission, tempered glass, thickness: 3.2 mm
J-Box	Multi Contact - IP 65 • 3 bypass diodes
Connectors and cabling	MC4 Plus certified TÜV - IP68 - Cable length: 2 x 1 m Fast, safe connection with polarizing slot
Encapsulation	High transparence EVA film
Frame	Rustproof anodised aluminium 15 µm • Holes for earth, mounting and drainage
Frame colour	Grey aluminium (optional : black)
Backsheet colour	White (optional : black or clear)
Operating temperature range	-40°C to +85°C
Maximum wind load	2400 Pa
Maximum snow load	5400 Pa
Impact resistance	Hail : 25 mm Ø with impact speed of 83 km/h
Electric safety	Class II

ELECTRICAL DATA

	VSPS					VSMS				
Peak Power Watts (Wp)*	245	250	255	260	265	260	265	270	275	280
Power output tolerance (W)	0 to + 4,99					0 to + 4,99				
Efficiency (%)	15,00 %	15,30 %	15,61 %	15,92 %	16,22 %	15,92 %	16,22 %	16,53 %	16,84 %	17,15 %
Maximum power voltage Vmax (V)*	30,2	30,6	30,8	31,1	31,4	31,3	31,5	31,7	31,7	31,9
Maximum power current Impp (A)*	8,14	8,20	8,28	8,36	8,45	8,32	8,41	8,68	8,72	8,77
Open circuit voltage Voc (V)*	37,5	37,6	37,8	38,0	38,1	38,5	38,6	38,7	39,3	39,5
Short-circuit current Isc (A)*	8,60	8,64	8,70	8,77	8,85	8,69	8,78	9,29	9,35	9,40
Maximum system voltage (V)	1000					1000				
Maximum Reverse Current I_{RM} (A)	16					16				

*Mean values of range modules. * Other power available on request.
Values at Standard Test Conditions (STC): Irradiance 1000W/m² - Air mass AM: 1.5, cell temperature 25°C, EN 60904-3 standard..
Upon request also available in "All Black" and "Transparent".
Poly and Mono also available with EU made cells, conform with French + 10 % FIT regulation.
Calibration by Fraunhofer ISE in Freiburg STC - Class AAA simulator.

TEMPERATURE COEFFICIENTS

	VSPS 245/250/255/260	VSPS 265	VSMS 260/265/270	VSMS 275/280
Power	- 0.409 %/K	- 0.372 %/K	- 0.410 %/K	- 0.395 %/K
Voc	- 107 mV/K	- 115 mV/K	- 128 mV/K	- 116 mV/K
Isc	4.40 mA/K	4.38 mA/K	3.90 mA/K	2.54 mA/K

Ed. 2.1 • december 2014 • Characteristics given for information purposes - Non-binding document.

European production certified by Certisolis, in accordance with the Italian GSE Conto Energia

IEC 61215,
IEC 61730-1 et 2.

VOLTEC solar
So that the future makes sense

Voltec Solar SAS
1 rue des Prés • 67190 DINSHEIM-SUR-BRUCHE • FRANCE
Tel : +33 3 88 49 49 84 • Fax : +33 3 88 49 49 85
info@voltec-solar.com • **www.voltec-solar.com**

Annex E: DATASHEET Panasonic225

Panasonic

Bifacial Photovoltaic Module
VBHN225DJ06

HIT Double 225
Photovoltaic Module

Power per Square meter up to 207.9 Watts


Breezeway: EI Solutions Burbank, CA


Patio Awning: Solar Living Design Lakewood, CO

High Efficiency
HIT™ Double is the world leader in sunlight conversion efficiency, helping customers to enjoy the maximum power per square meter from available space.

Power Guarantee
Panasonic guarantees customers will receive 100% of the panel's rated power (or more) at the time of purchase, enabling owners to generate more kWh per rated watt.

Bifacial Effect
The back face of the panel generates electricity from ambient light reflected off surrounding surfaces, and combines with power from the front face of the panel. Dependant upon system design and site albedo, this results in up to 30% higher power generation (more kWh) per square meter.

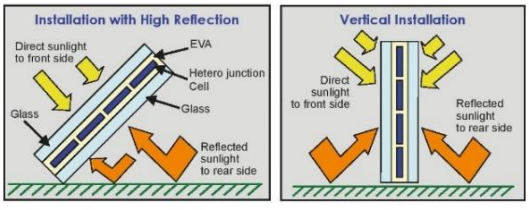

Application Possibilities
- Architectural, Awnings, Balconies, Bus Shelters, BIPV
- Deck & Porch Coverings, Canopies, Carports, Facades
- Fences, Siding, Trellises, Tracking Systems

Proprietary Technology
Our bifacial solar cells are hybrids of single crystalline silicon surrounded by ultra-thin amorphous silicon layers, available solely from Panasonic.

High Temperature Performance
As temperatures rise, the panel produces more electricity than conventional solar panels at the same temperature, for good performance in high temperature sites.

Quality Products
Panasonic is truly committed to quality since it began developing and manufacturing solar PV in 1975. We have been the technology leader, and for decades many satisfied customers have placed their trust in the competence of our unique solar technology.

Brilliant Aesthetics
This panel sets a new aesthetic standard in photovoltaic system design.With a double glass structure that allows brilliant light and shadows to shine through the panels, the solar cells truly appear to be floating in the air. Both residential and commercial customers will enjoy new architectural possibilities.

Panasonic Corporation

HIT Double 225
Photovoltaic Module

Electrical Specifications

		Specifications Including Backside Irradiation Contribution in ISC as a Percent of STC					
Model: VBHN225DJ06	STC	5%	10%	15%	20%	25%	30%
Rated Powr (Pmax)	225W	236W	247W	259W	269W	280W	291W
Maximum Power Voltage (Vpm)	43.2V	43.7V	43.7V	43.7V	43.6V	43.6V	43.6V
Maximu Power Current (Ipm)	5.21A	5.42A	5.67A	5.93A	6.18A	6.43A	6.68A
Open Circuit Voltage (Voc)	52.4V	52.5V	52.6V	52.7V	52.8V	52.9V	53.0V
Short Circuit Current (Isc)	5.54A	5.82A	6.09A	6.37A	6.65A	6.92A	7.20A
Max. System Voltage (Vsys)	600V	——	——	——	——	——	——
Warranted Tolerance	±10%	——	——	——	——	——	——
Series Fuse Rating	15A	——	——	——	——	——	——
Cell Efficiency	20.1%	——	——	——	——	——	——
Module Efficiency	16.0%	——	——	——	——	——	——
Power per Square meter	160.7W	168.6W	176.4W	185.0W	192.1W	200.0W	207.9W

Note: Temperature Coefficient is tentative specification and may be subjected to change in the future.

Temperature Characteristics (VBHN225DJ06)

Temperature (NOCT)	45.8℃
Temp. Coefficient of Pmax	-0.29%/℃
Temp. Coefficient of Voc	-0.124V/℃
Temp. Coefficient of Isc	0.003A/℃

At NOCT (Normal Operating Coditions)

Max. Power(Pmax)	169.6W
Max. Power Voltage (Vmp)	40.9V
Max Power Current (Imp)	4.14A
Open Circuit Voltage (Voc)	49.5V
Short Circuit Voltage (Isc)	4.46A

To Maximize Power

1. Elevate panels above a surface as much as possible.
2. Place panels over light-colored surfaces.
3. Do not allow support rails to shade the panel's back face.

At low irradiance

Max. Power (Pmax)	42.7W
Max. Power Voltage (Vmp)	41.8V
Max Power Current (Imp)	1.02A
Open Circuit Voltage (Voc)	48.9V
Short Circuit Voltage (Isc)	1.11A

Safety Rating & Limited Warranty

Ambient Operating Temperature	-20℃~+40℃
Safety & Rating Certifications	JET IEC61215, IEC61730-1, IEC61730-2
Limited Warranty	Power output: 10 years (90% of Pmin), 25 years (80% fo Pmin) Product workmanship: 10 years (based on guarntee documents)

Mechanical Specifications

Internal Bypass Diodes	3 Bypass Diodes
Module Area	1.4 ㎡
Module Weight	24 kg
Module Dimension	1630 x 862 x 35mm
Cable Lengths/ size	1370, 1370 mm/4.0 sq
Connector	MC3 (PV-KBT/KST-3II-UR)
Statistics load	"50PSF (2400Pa) /112PSF (5400Pa) *Mount on long side only"
Pallet Dimentions	1657×879×150mm
Quantity per pallet/Pallet weight	36pcs/880kg
Quantity per 20FT/40FT container	216 pcs/ 504 pcs

Dependence on Irradiance

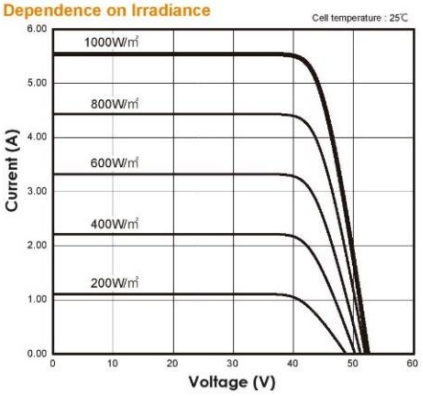

Dimensions Unit : inches (mm)

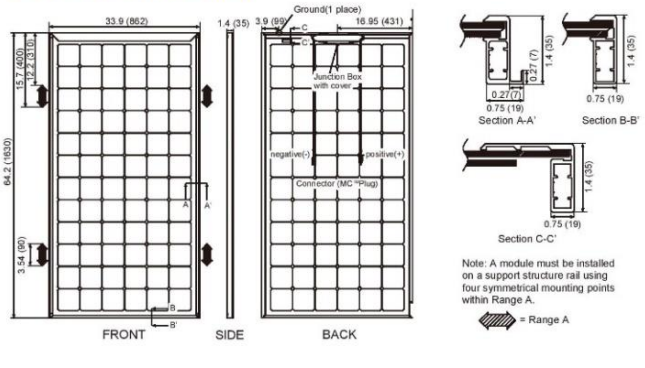

IMPORTANT: The rated power of HIT™ Double is measured under Standard Test Conditions (STC). STC does not account for power produced from the back face of panels. Therefore, HIT Double panels will produce more power than their STC rating, up to 30% more, depending upon the system design and site albedo. Account for the additional power when sizing, selecting system components and wiring.

manufactured by SANYO Electric Co., Ltd.

⚠ CAUTION! Please read the installation manual carefully before using the products.

Please contact

Panasonic Corporation Eco Solutions Company

Solar Business Unit, Energy Systems Business Division
■ Head Office: 1048, Kadoma, Kadoma City, Osaka 571-8686, Japan
■ Tel: +81-6-6900-2720 ■ Fax: +81-6-6900-2820
http://panasonic.net/ecosolutions/solar

Panasonic®